Carbonate mineral nucleation pathways

Ayumi Koishi

To cite this version:

Ayumi Koishi. Carbonate mineral nucleation pathways. Chemical Physics [physics.chem-ph]. Université Grenoble Alpes, 2017. English. NNT : 2017GREAU032 . tel-01701947

HAL Id: tel-01701947

https://theses.hal.science/tel-01701947v1

Submitted on 6 Feb 2018

Communauté
UNIVERSITÉ Grenoble Alpes

THÈSE

Pour obtenir le grade de

DOCTEUR DE LA COMMUNAUTÉ UNIVERSITÉ GRENOBLE ALPES

Spécialité : **Sciences de la Terre, l'Univers et l'Environnement**

Arrêté ministériel : 25 mai 2016

Présentée par

Ayumi KOISHI

Thèse dirigée par **German MONTEZ-HERNANDEZ, chercheur, CNRS**, et
codirigée par **Alejandro FERNANDEZ-MARTINEZ, chercheur, CNRS**

préparée au sein de **l'Institut des Sciences de la Terre**
dans **l'École Doctorale Terre, Univers, Environnement**

Mécanismes de nucléation des carbonates

Carbonate mineral nucleation pathways

Thèse soutenue publiquement le **30 octobre 2017**,
devant le jury composé de :

Madame Encarnacion RUIZ AGUDO
Professeur associé, Universidad de Granada, Rapporteur

Madame Liane G. BENNING
Professeur, GFZ German Research Center for Geosciences, Rapporteur

Monsieur Bruno LANSON
Directeur de Recherche, ISTerre, Président

Monsieur Carlos M. PINA
Professeur associé, Universidad Complutense de Madrid, Examinateur

Monsieur, Laurent J. MICHOT
Directeur de Recherche, Laboratoire PHENIX, Examinateur

Monsieur German MONTES-HERNANDEZ
Chargé de Recherche, ISTerre, Co-Directeur de thèse

Monsieur Alejandro FERNANDEZ-MARTINEZ
Chargé de Recherche, ISTerre, Co-Directeur de thèse

Mécanismes de nucléation des carbonates
Carbonate mineral nucleation pathways

Abstract

Precipitation and dissolution of calcium carbonate ($CaCO_3$) are key processes in both natural and engineered systems due to their intimate association with the Earth's carbon cycle. Precipitation usually occurs on foreign substrates since they lower the energetic barriers controlling nucleation events. This so-called heterogeneous nucleation results from the interplay between the fluid supersaturation and the interfacial energies present at the substrate-nucleus-fluid interfaces. Despite the relevance of interfacial energies for the fate of heterogeneous nucleation, the current literature remains scarce in their absolute values, which limits the accuracy of reactive transport modelling. Of particular relevance to the carbon cycle, the formation of biominerals accounts for a major reservoir of the carbonate minerals in the lithosphere. Recent studies have revealed the existence of multistep nucleation pathways that involve formation of amorphous calcium carbonate (ACC), a metastable intermediate during the early stages of biomineral formation. Such amorphous precursors allow molding of the intricate shapes of biominerals, while their stability and crystallization kinetics are effectively controlled by multiple factors. Elucidating the underlying mechanisms is beneficial for the development of biomimetic materials.

The first goal of this dissertation is to develop a predictive understanding of interfacial energy values as a function of specific physico-chemical properties of the substrates, such as hydrophobicity. This last was investigated using phlogopite mica with and without fluorine substitution yielding hydrophobic and hydrophilic substrates. *In situ* time-resolved Grazing-Incidence Small Angle X-ray Scattering experiments were performed to obtain effective interfacial energy values governing $CaCO_3$ heterogeneous nucleation. Interestingly, the extracted values for both substrates were identical, thus so is the thermodynamic barrier for nucleation, irrespective of surface hydrophobicity. In addition, e*x situ* observations by Atomic Force Microscopy and FTIR indicated that ACC was the primary nucleating phase for both substrates, although surface hydrophobicity seems to control the crystallization kinetics. The hydrophilic substrate was shown to promote the stabilization of ACC, whereas the hydrophobic one favored the crystallization. These results point to the intrinsic structural flexibility of $CaCO_3$ and its advantage in heterogeneous nucleation processes.

The second goal is to provide an atomistic description of the substrate hydrophobicity/hydrophilicity. Water adsorption behavior on phlogopite surface was studied *in situ* using Near-Ambient Pressure X-ray Photoelectron Spectroscopy to investigate the effect of fluorine substitution and the influence of different types of counterions (K^+, Na^+ vs Cs^+). The results of the spectroscopy experiments were further interpreted using molecular dynamics simulations and bond-valence theory. The combination of these techniques showed that the substrate hydrophobicity stemmed from a competition between two factors: hydration of counterions vs that of substrate.

The final goal is to study the molecular mechanisms by which Mg^{2+}, a common impurity in biogenic amorphous precursors, increases the kinetic persistence of ACC. Inelastic Incoherent Neutron Scattering and X-ray Photon Correlation Spectroscopy were combined to elucidate the nanoscale dynamics of water and ions within ACC. The presence of Mg^{2+} was shown to enhance the ionic diffusion within the solid while simultaneously increasing the stiffness of the hydrogen bond network. These counter-intuitive results are addressed by considering the different factors included in the pre-exponential term of the nucleation rate equation within the framework of the classical nucleation theory. Overall, the results point to the importance of water as a kinetic stabilizer, and to the existence of steric barriers that lower the crystallization rate.

Résumé

La précipitation et la dissolution du carbonate de calcium ($CaCO_3$) sont des processus clés dans les systèmes naturels en raison de leur association intime avec le cycle du carbone terrestre. La précipitation se produit généralement sur des substrats étrangers en abaissant les barrières énergétiques qui contrôlent la nucléation. Ce processus appelé nucléation hétérogène résulte d'une interaction entre la sursaturation du fluide et les énergies d'interface entre substrat-noyau-fluide. Malgré l'importance des énergies d'interface sur le devenir de la nucléation hétérogène, la littérature actuelle reste rare dans leurs valeurs absolues, limitant la précision de la modélisation du transport réactif. La formation des biominéraux constitue un réservoir majeur des carbonates dans la lithosphère. Des études récentes ont révélé des nucléations par multi-étapes impliquant la formation du carbonate de calcium amorphe (ACC), un intermédiaire métastable durant les premiers stades de la formation des biominéraux. De tels précurseurs amorphes permettent de réaliser les formes complexes des biominéraux, tandis que leur stabilité et leur cinétique de cristallisation sont contrôlées par de multiples facteurs. L'élucidation des mécanismes sous-jacents est bénéfique pour le développement de matériaux biomimétiques.

Le premier objectif est de développer une compréhension prédictive des valeurs d'énergie d'interface en fonction des propriétés physico-chimiques des substrats, comme l'hydrophobicité. Cette dernière est étudiée en utilisant de la phlogopite avec et sans substitution par le fluor. La technique de diffusion des rayons X aux petits angles en incidence rasante a été employée *in situ* pour obtenir des valeurs d'énergie effective d'interface régissant la nucléation hétérogène du $CaCO_3$. Il est intéressant de noter que les valeurs extraites pour les deux substrats sont identiques, donc leurs barrières de nucléation aussi. La caractérisation *ex situ* par microscopie à force atomique et spectrométrie d'absorption infrarouge a montré que l'ACC se forme en première lieu quelle que soit l'hydrophobicité du substrat, bien que cette dernière contrôle la cinétique de cristallisation. Le substrat hydrophile favorise la stabilisation d'ACC, tandis que le substrat hydrophobe favorise la cristallisation. Ces résultats soulignent la flexibilité structurelle intrinsèque du $CaCO_3$ et son avantage dans les processus de nucléation hétérogènes.

Le deuxième objectif est de fournir une description atomistique de l'hydrophobicité du substrat. L'adsorption d'eau sur la phlogopite a été réalisée *in situ* par spectroscopie de photoélectrons à pression ambiante pour étudier l'effet de la substitution par le fluor et de différents types de contre-ions (K^+, Na^+ vs Cs^+). Ces résultats ont été interprétés par des simulations de dynamique moléculaire et la théorie de bond-valence. La combinaison de ces techniques montre que l'hydrophobicité du substrat provient d'une compétition entre deux facteurs: l'hydratation des contre-ions vs celle du substrat.

Le but final est d'étudier les mécanismes moléculaires par lesquels Mg^{2+}, une impureté chez les précurseurs amorphes biogéniques, augmente la persistance cinétique d'ACC. La technique de diffusion inélastique incohérente des neutrons a été combinée avec la spectroscopie de corrélation de photons X pour élucider la dynamique à l'échelle nanométrique de l'eau et des ions dans les ACC. Les résultats montrent que la présence de Mg^{2+} augmente la diffusion ionique dans le solide tout en amplifiant la rigidité du réseau des liaisons hydrogène. Ces résultats contre-intuitifs sont abordés en considérant différents facteurs cinétiques inclus dans l'équation décrivant le taux de nucléation au sein de la théorie classique de la nucléation. Dans l'ensemble, ces résultats indiquent l'importance de l'eau comme stabilisant cinétique de la structure amorphe et de l'existence de barrières stériques qui abaissent le taux de cristallisation.

Acknowledgements

This PhD thesis would not have seen the light of day without support and guidance of my supervisors, Alejandro Fernandez-Martinez and German Montes-Hernandez. Alex, thank you for sharing with me your knowledge, ideas, scientific network full of inspiring people as well as many memorable moments during the countless number of synchrotron trips. You always inspired me as a person as much as a scientist. Seeing your full dedication to both work and life has been my motivation over the last three years. German, though you might not remember, I in fact owe you a large fraction of my incentive. When I was stuck with my first *in situ* setup in that small, windowless corner, you came in and said ‘what we do goes beyond the chemistry you have ever learned so far’. In a similar vein, Alexander van Driessche deserves a special mention. Sander, you always encouraged me with your humorous ways, insightful comments and colorful outfits. Despite all what I might have said about libraries and mountains, I had truly been the luckiest PhD student, which I owe to three of you.

This work is also a fruit of numerous collaborations. A warm thank you to Laurent Michot for all the pleasant discussions, your contagious humor and addiction to beamtimes; Ian Bourg for your warm welcome to your research group and the guidance in the fascinating world of MD simulations; Carlos Pina and Carlos Pimentel for the AFM measurements and the gourmet tour in Madrid; Virginie Marry for your engagement and hints in the NAP-XPS data analysis; Jean-Jacques Gallet, Fabrice Bournel, Emmanuelle Dubois, Anthony Boucly and Stéphane Tesson for all the hands-on lessons and the ‘pleasant’ night shifts during the NAP-XPS beamtimes; Chong Dai, Andrew Stock and Yandi Hu for sharing the passion for heterogeneous nucleation; Beatrice Ruta, Monica Jimenez-Ruiz and Roberta Poloni, the inspiring and empowering female scientists I am truly grateful to have met in Grenoble; Federico Zontone for your humor and patience with answering my never-ending questions; Byeongdu Lee for sharing your expertise.

Special thanks go to the members of Geochemistry group and ISTerre, particularly Delphine Tisserand for her care in the lab maintenance; Sarah Bureau for her help with the ICP measurements; Nathaniel Findling for the insightful discussions about the synthesis of ACC besides his help with the XRD measurements; Laurent Charlet for his scientific enthusiasm and precious advice on many of my presentation slides; Fabrice Brunet for his comments to the point that always helped to reexamine my ideas; Roland Hellmann for all the enjoyable exchanges over coffee and the fun time in Granada; Rodolphe Pinon for the good chats over green tea besides his IT expertise; Christelle Adoult for her efficient administrative support; Martine Lanson for providing me with her lab equipment and advice.

I am truly thankful to all the precious friends I have made throughout my journey in Lausanne, Princeton and Grenoble, particularly Jasmine, Florian, Boris, Afifa, Katja, Emily, and Ayla for all the good discussions, many cups of coffee and tea, and all kinds of realization and discoveries you brought me; Bin, Van, Johanes, Capucine, Katya, Igor, Margarita, Ana, Elliot, Maor, Claudia, Frans, and my Herculean friends Olesya and Chris for sharing the ups and downs with me during the last three years; my dearest neighbors Cécile, Ollia, and Cookie for many bowls of bonne soupes aux légumes that kept me going, my breakfast buddy Oonagh for our delightful mornings with croissants aux abricots; and JO for his care, patience, encouragements and positive thoughts.

I would like to express my sincere appreciation to Hans-Rudie Pfeifer and Jasquelin Peña, without whom I would have not been here today as an aspiring scientist.

Last but not least, I thank my whole family, particularly my father who has always been my silent supporter and inspiring figure.

十七

行き詰りは環境のせいではない
自分の心の行き詰りである

観音正寺　ことわざの道

Table of Contents

Chapter 5 Surface hydrophobicity and properties of interfacial water 101

Chapter 6 Nanoscopic dynamics of amorphous calcium carbonate: understanding the mechanisms controlling the crystallization kinetics 129

APPENDIX

List of Figures

List of Tables

Chapter 1

Introduction

1.1. The calcium carbonate system

The calcium carbonate ($CaCO_3$) reservoir occupies a significant fraction in the network of global geochemical cycles (Sigg et al., 1992) and acts as major sink of atmospheric and anthropogenic CO_2 (Milliman, 1993; Feely et al., 2004; Sabine, 2004). Once transported into the hydrosphere, environmental factors such as the temperature, pH, ionic force and atmospheric or subsurface CO_2 partial pressure control $CaCO_3$ dissolution and precipitation reactions, which in turn regulates the composition of natural waters, their alkalinity, and the solubility of other solid phases. The dissolution-precipitation cycling of $CaCO_3$ is not limited to the formation of inorganic minerals and alteration of rocks, but it is also affected by the formation of biominerals, mainly by marine organisms, in an intimate binding of carbonate species and organic moieties that provides protective and structural functionalities (Mann, 1993; Mann, 2001; Addadi et al., 2003). The relevance of the $CaCO_3$ cycle also extends to the subsurface chemistry, where contaminant transport via sequestration within solid precipitates takes place. This cycle is further coupled with reduction–oxidation reactions affecting the cycling of other metals (McCarthy and Zachara, 1989; Fujita et al., 2000; Warren et al., 2001; Dong et al., 2005). The $CaCO_3$ system is also of great significance in engineered systems such as geological storage of CO_2 (Chiquet et al., 2007; Espinoza and Santamarina, 2010), scale formation (Söhnel and Garside, 1992; Yang et al., 2001; Chen et al., 2005), and synthesis of biomimetic materials (Sommerdijk and With, 2008; Aizenberg, 2010; Meyers et al., 2013).

1.2. Calcium carbonate mineral nucleation pathways

The $CaCO_3$ system comprises a number of polymorphs in its crystallization process. These include amorphous calcium carbonate (ACC) as well as anhydrous and hydrous crystalline polymorphs such as calcite, aragonite and vaterite for anhydrous phases with calcite being the most stable, and ikaite and monohydrocalcite for hydrous phases (Fig. 1.1). The thermodynamic solubility constants for these crystalline systems are well known, with the exception of vaterite bearing a complex, disordered structure that has not been fully elucidated (Wang and Becker, 2009; Demichelis et al., 2012; Wang and Becker, 2012; Kabalah-Amitai et al., 2013). The solubility constant allows calculating the supersaturation of a given fluid with respect to a given phase. Fluid supersaturation is the main driver towards the formation of a new solid phase. However, it does not directly guide the system toward precipitation, since this begins via nucleation. In order for nucleation to proceed, an energy barrier resulting from the cost of creating an interface between the new phase and the surrounding matrix has to be overcome (Sear, 2007; Yoreo et al., 2017). Indeed, the fate of precipitation in both surface and subsurface systems is largely controlled by nucleation, where saturated or undersaturated solutions percolate in porous media such as rocks, sediments or soils, with a wide distribution of pore size and surface properties. In such settings, it is the interaction of pore surfaces and dissolved ions that determines the physico-chemical factors that in turn govern the reaction. Heterogeneous nucleation (nucleation on a foreign substrate) is indeed the most common mechanism of nucleation in natural and engineered environments, given that the presence of surfaces helps lowering the nucleation barrier (Debenedetti, 1996; Kashchiev, 2000). In spite of its primordial importance in precipitation reactions, the mechanisms and the processes of $CaCO_3$ nucleation, however, are not fully understood. This is mainly due to experimental difficulties impeding our ability to accurately determine (i) the solution composition, where ion-pairs and larger cluster can be present, and (ii) the size of the initial nuclei that is in the order of the nanometer. Another difficulty stems from the fact that heterogeneous nucleation involves a number of unknown or hardly characterizable factors such as surface wettability or surface inhomogeneities on which the nucleation barrier and the nucleation rate depend (Chernov, 1984; Debenedetti, 1996). These difficulties have resulted in the omission of an explicit nucleation term from reactive transport models, which as a consequence may have underestimated or overestimated the amount of precipitation, especially because the rate of heterogeneous nucleation is largely correlated to the specific surface area (Steefel and Van Cappellen, 1990; Noiriel et al., 2012).

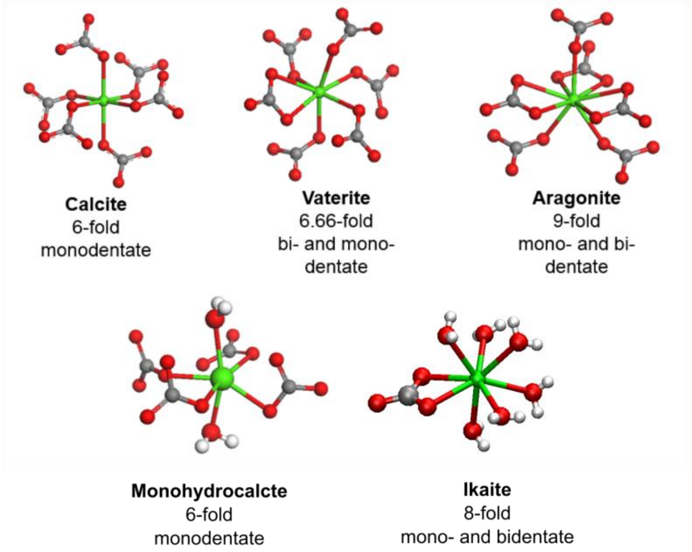

Figure 1.1. Ball-and-stick representation of Ca^{2+} local environment in some of the more common calcium carbonate polymorphs.The carbonate molecule CO_3^{2-}, with D_3h symmetry, can be bound to a Ca^{2+} ion by sharing one or two oxygen atoms with the Ca^{2+} coordination sphere, i.e., through a monodentate or a bidentate ligand, respectively. The Ca^{2+} coordination number and the more common ligand type are shown. The coordination number given for vaterite is an average taken from the different structures that have been proposed. (Adapted from Fernandez-Martinez et al., 2017)

In the following paragraphs, classical nucleation theory (CNT), the most frequently employed, conventional theory describing nucleation, is briefly introduced and then extended to the case of heterogeneous nucleation. Following recent progress of *in situ* and computational studies, a number of observations point out shortcomings of CNT and suggest the existence of alternative pathways to nucleation. Several of such observations and alterative pathways are presented, with a particular emphasis on the case of $CaCO_3$ system where an amorphous precursor pathway formed via 'non-classical' pathways, seems to be the most relevant.

1.3. Classical Nucleation Theory

A theoretical formulation of nucleation was first introduced by Gibbs (1878), based on a competition between an energetic term resulting from the creation of a new phase and another resulting from the creation of an interface. On one hand, creation of the bulk of a new phase results in a gain in chemical potential, $\Delta\mu$. On the other hand, creation of an interface results in an energetic cost proportional to the surface area and to the interfacial free energy α of the interface. During the past century, this theory was further developed by Becker and W. Döring (1935) and others working on the condensation of water droplets from vapor, and it was extended to the nucleation of solid phases from solution and gaseous phases, which was shaped into what is known today as Classical Nucleation Theory (CNT) (Kashchiev, 2000). In short, CNT describes the process of nucleation as the starting point of a first-order phase transition, accompanied by activation energy, from a metastable to a more stable thermodynamic state (Kashchiev, 2000). For comparison, spinodal decomposition, another phase transition process, does not involve an actitation energy.

The thermodynamic driving force to nucleation is the excess free energy Δg between the state of the system before and after nucleation, where the free energy of the initial state (solution) is greater than that of the final state (sum of the new phase plus the final solution). Using the known thermodynamic expression, this is the same as to say that the driving force is the excess chemical potential $\Delta\mu$ between the actual and equilibrium activity products (Kashchiev, 2000; Kashchiev and van Rosmalen, 2003).

$$\Delta\mu = K_{\mathrm{B}}T\ln(\mathrm{IAP}) - K_{\mathrm{B}}T\ln\left(K_{\mathrm{sp}}\right) = K_{\mathrm{B}}T\ln\left(\frac{\mathrm{IAP}}{K_{\mathrm{sp}}}\right) = K_{\mathrm{B}}T\sigma \qquad (1.1)$$

where K_B is the Boltzmann constant, T is the temperature, IAP is the ion activity product, K_{sp} is the solubility constant, and σ is the supersaturation. For a given reaction, IAP and K_{sp} are defined as:

$$aA + bB + \ldots + nN \rightarrow A^{a}B^{b}\ldots N^{n}$$

$$\begin{aligned} \mathrm{IAP} &= (A)^{a}(B)^{b}(C)^{c}\ldots(N)^{n} \\ K_{\mathrm{sp}} &= (A)^{a}_{\mathrm{equil}}()^{b}_{\mathrm{equil}}(C)^{c}_{\mathrm{equil}}\cdots(N)^{n}_{\mathrm{equil}} \end{aligned} \tag{1.2}$$

where $(N)^{n}$ and $(N)_{\mathrm{equil}}{}^{\mathrm{n}}$ denote the actual and equilibrium activities of an ion N, respectively. The free energy of the system decreases proportionally to the number of molecules constituting the nucleus (the new phase), scaling with its volume, giving rise to the first term describing nucleation process that is the change in the free energy of the bulk solution Δg_{b}:

$$\Delta g_{b} = -\frac{\frac{4}{3}\pi r^{3}}{\Omega}\Delta\mu \tag{1.3}$$

where, Ω is the molecular volume and r is the radius of the nucleus for the case of a spherical nucleus for simplicity. Note that this term is negative, thus energetically favorable. The molecules sitting at surface of the nucleus, however, carry less entropy than those in the solution and are less tightly bounded than those in the bulk of the nucleus, giving rise to a non-negligible positive contribution to the free energy of the system that is the interfacial energy α (DeYoreo and Vekilov, 2003; De Yoreo and Whitelam, 2016). This signifies a cost that the system has to overcome during the formation of the nucleus, scaling with its surface area, giving rise to the second term describing nucleation process that is the change in the free energy related to the surface Δg_{s}:

$$\Delta g_{s} = 4\pi r^{2}\alpha \tag{1.4}$$

The change of the free energy of the system before and after the nucleation event Δg_{b} is therefore:

$$\Delta g_{\mathrm{n}} = \Delta g_{\mathrm{b}} + \Delta g_{\mathrm{s}} = -\frac{\frac{4}{3}\pi r^{3}}{\Omega}\Delta\mu + 4\pi r^{2}\alpha \tag{1.5}$$

On the course of the formation of the nucleus, the quadratic term is more important at small sizes, while the cubic term eventually dominates at larger sizes, leading to a free-energy barrier with a peak at a critical radius r_{c} (Fig. 1.2):

$$r_{\mathrm{c}} = \frac{2\Omega\alpha}{\Delta\mu} = \frac{2\Omega\alpha}{K_{\mathrm{B}}T\sigma} \tag{1.6}$$

Nucleation is a fluctuational process since only the nuclei with size $r > r_c$ can grow spontaneously. It is therefore the free energy of the nucleus at the top of the barrier that determines the rate of nucleation (Sear, 2007).

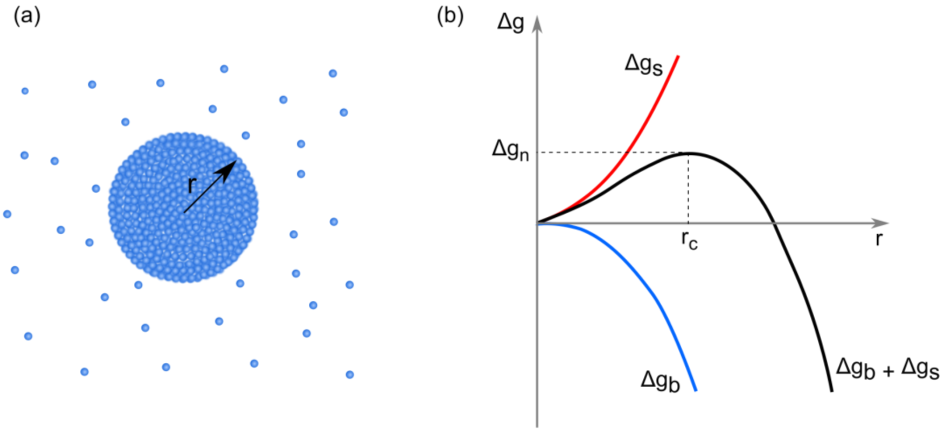

Figure 1.2. Classical nucleation theory. **(a)** Formation of a spherical cluster of radius r from a solution leads to the changes in the free energy shown in **(b)**. The sum of the bulk (Δg_b) and surface (Δg_s) terms (energetically favorable and unfavorable, respectively) results in a free energy barrier of height Δg_n, with a maximum at the critical radius r_c, that the system must overcome via thermal fluctuations in order for the cluster to grow spontaneously.

The kinetics of nucleation are governed by the frequency of successive and reversible attachments (and detachments) f of single ions or molecules (i.e. monomers) to and from the clusters (new phase) of various sizes. With $[n]$ being a cluster of n monomers, the chain reaction follows as: $[1] \leftrightarrow [2] \leftrightarrow \cdots \leftrightarrow [n - 1] \leftrightarrow [n] \leftrightarrow [n + 1] \leftrightarrow \cdots$. This occurs by diffusion from the solute to the nucleus or by transfer of solute across the interface between the nucleus and the solution (Pina and Putnis, 2002; Kashchiev and van Rosmalen, 2003). The nucleation rate J_n, the number of the nucleus formed per unit of volume and time, is thus proportional to the barrier height divided by $K_B T$:

$$J_n = A\exp\left(\frac{\Delta g_n}{K_B T}\right) = A\exp(-\frac{B\Omega^2\boldsymbol{\alpha}'^{3}}{{K_B}^3 T^3 \boldsymbol{\sigma}^{2}}) \tag{1.7}$$

where B is the shape factor which equates to $16\pi/3$ for a spherical nucleus, and the pre-exponential factor A depends on various kinetic factors such as f. More specifically, when the nucleation barrier is high enough compared to the thermal energy, $K_B T$, the metastable state of the system contains thermal fluctuations that are well described by a Boltzmann distribution. Sometimes, one of these fluctuations will reach and overcome the critical size. It can then continue to grow so as to become more and more stable. CNT indeed assumes that the system reaches a steady-state where stable nuclei then appear at a rate J_n:

$$J_{\mathrm{n}} = A\exp(-\frac{\Delta g_{\mathrm{n}}}{K_{\mathrm{B}}T}) = f^{*}ZC_{0}\exp(-\frac{\Delta g_{\mathrm{n}}}{K_{\mathrm{B}}T}) \tag{1.8}$$

where f^* is the rate at which a critical cluster grows, Z is the Zeldovich factor and C_0 is the concentration of particles (ions) in the system. The Zeldovich factor accounts for the energy profile around the critical size (Z is proportional to dg_{n}/dr). Critical clusters experience random size variations that cause some of them to re-dissolve and fall out of the stable region (Kashchiev, 2000). The Zeldovich factor accounts for the probability that only some of these clusters will continue to grow, which effectively decreases the nucleation rate given by $f^*\cdot C_0\cdot\exp(-\Delta g/k_{\mathrm{B}}T)$. The factor f^* depends on the nucleus growth mechanism. As shown by Clouet (2010), under the assumption that that the critical cluster growth is controlled by the long-range diffusion of solute, the nucleus growth rate can be expressed as:

$$f^{*} = 4\pi r\frac{D}{\Omega}\frac{x^{0}}{y^{e}} \tag{1.9}$$

where x^0 and y^{e} are fractions of atoms diffusing in the metastable (initial) and stable (final) regions, respectively, and D is the diffusion coefficient of the particles (under the approximation that the diffusion of a single species is limiting the growth process). This expression links therefore the diffusivity of the species being added to the growing cluster to the nucleation rate.

1.4. Heterogeneous nucleation

In nature, as in engineered media, mineral precipitation occurs inside the pores of rocks, soils and sediments (Prieto, 2014), where in general, the presence of a surface lowers the interfacial free energy (Debenedetti, 1996; De Yoreo and Whitelam, 2016). Let us start by describing the heterogeneous nucleation in the framework of CNT. For simplicity, we assume that the nucleus is a hemisphere of radius r, as shown in Figure 1.3. Eq. (1.5) then becomes:

$$\Delta g_{\mathrm{n}} = \Delta g_{\mathrm{b}} + \Delta g_{\mathrm{s}} = -\frac{\frac{2}{3}\pi r^{3}}{\Omega}\Delta\mu + 2\pi r^{2}\alpha' \tag{1.10}$$

where α' is an effective interfacial free energy, resulting from a combination of three interfacial free energies of the interfaces between liquid-crystal (α_{lc}), liquid-substrate (α_{ls}) and substrate-crystal (α_{sc}). With θ being the contact angle formed between the nucleus and the substrate, α' can be expressed as a function of θ:

$$\alpha'(\theta) = \alpha_{lc}\frac{2(1-\cos\theta) - \sin^2\theta\left(\frac{\alpha_{ls}-\alpha_{sc}}{\alpha_{lc}}\right)}{2^{1/3}(2-3\cos\theta+\cos^3\theta)^{2/3}} \tag{1.11}$$

where $0° < \theta < 180°$. For an ideal hemispherical nucleus, $\theta = 90°$. Eq. (1.11) can thus become:

$$\alpha' = \alpha_{lc} - \frac{1}{2}(\alpha_{ls} - \alpha_{sc}) \tag{1.12}$$

Accordingly, new expressions for the critical radius and the nucleation rate are:

$$r_\mathrm{c} = \frac{2\Omega\alpha'}{\Delta\mu} = \frac{2\Omega\alpha'}{K_\mathrm{B}T\sigma} \tag{1.13}$$

and

$$J_\mathrm{n} = \exp\left(\frac{\Delta g_\mathrm{n}}{K_\mathrm{B}T}\right) = A\exp(-\frac{8\pi\Omega^2\alpha'^3}{3{K_\mathrm{B}}^3T^3\sigma^2}) \tag{1.14}$$

Heterogeneous nucleation as described here by CNT differs from homogeneous nucleation only by the presence of the function of θ (Turnbull and Vonnegut, 1952; Sear, 2007). Since nucleation occurs on a foreign surface that is hardly characterizable (Chernov, 1984; Debenedetti, 1996), if the surface possesses a wide range of contact angles θ, as pointed up by Sear (2007), then additionally there will be a distribution of α'. Furthermore, as will be discussed in section 1.5, both homogeneous and heterogeneous nucleation processes could follow the so-called multistep pathways that are beyond the considerations of CNT. Such complexities have resulted in a lack of mechanistic studies of $CaCO_3$ heterogeneous nucleation. This emphasizes the need for a predictive capability of the heterogeneous nucleation behavior with respect to a range of surface properties, which is one of the main goals of this Ph.D. thesis.

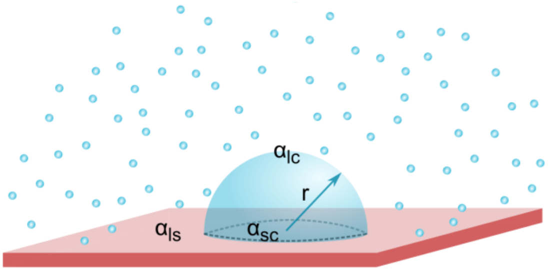

Figure 1.3. Heterogeneous formation of a hemispherical nucleus at a foreign substrate with three interfacial free energies α exerting at interfaces of liquid-crystal (lc), liquid-substrate (ls) and substrate-crystal (sc).

1.5. Multistep nucleation pathways

Over the last two decades, the development of advanced characterization tools, both experimental and computational, has provided evidence that CNT does not account for all of the complex nucleation pathways observed during nucleation of $CaCO_3$. Gebauer et al. (2008) showed using potentiometric titration and ultra-centrifugation techniques that solution composition is more complex than what the current thermodynamic models account for, and that other aqueous species larger than ion-pairs, are present in the solution before nucleation occurs (Gebauer et al., 2008). These species, called 'pre-nucleation clusters' are postulated to be the building blocks of $CaCO_3$ amorphous precipitates (amorphous calcium carbonate, ACC), via aggregation. Questions remain open regarding their thermodynamic stability and therefore their existence as stable aqueous species. Some authors propose that they could be kinetically stabilized species, with lifetimes long enough allowing their experimental observation and characterization (Wallace et al., 2013). Since then, computational studies have revealed the formation of multiple aqueous species, named accordingly by different authors (e.g., dense liquid phases (Wallace et al., 2013), dynamically ordered liquid-like oxyanion polymers (Demichelis et al., 2011), polymer-induced liquid precursors (Bewernitz et al., 2012), etc.), which seemingly represent different states during the course of condensation of the $Ca\text{-}CO_3\text{-}H_2O$ system. Note that the concept of a polymer-induced liquid precursor (PILP) had been introduced in the early 2000's by the group of L. Gower (Gower and Odom, 2000; Gower, 2008). It is possible that some of these intermediate states represent true local free energy minima, representing so called 'magic-number' clusters (Stoyanov, 1973; Stoyanov, 1979). It is therefore legitimate to say, as the current consensus, that there exist nucleation pathways comprising more than one barrier to overcome, along with a number of local minima corresponding to the formation of clusters with different sizes and probably different structural arrangements (Fig. 1.4).

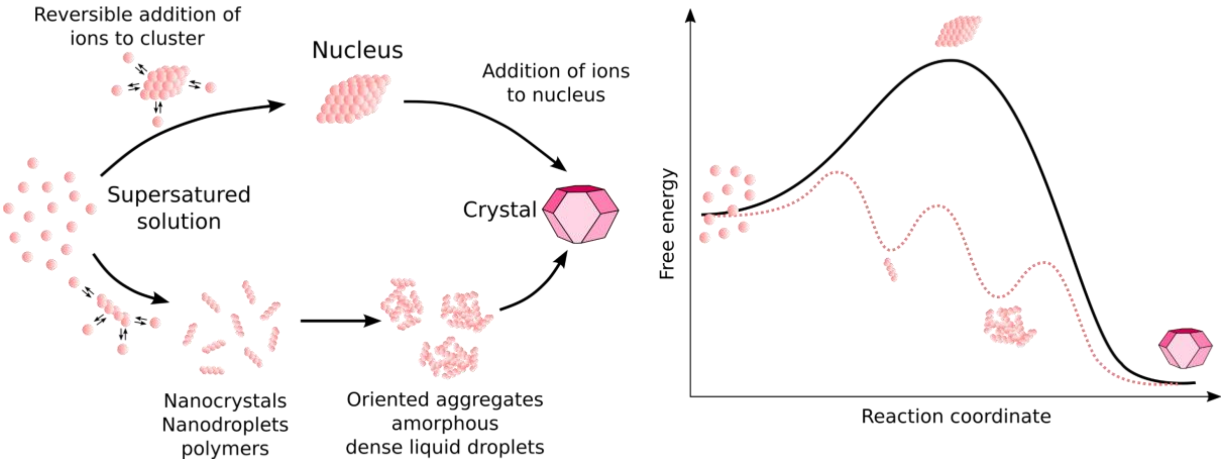

Figure 1.4. Classical and multistep (non-classical) nucleation pathways. (Courtesy: Dr. Alexander van Driessche)

The aggregation processes of these aqueous species are therefore a fundamental part of the nucleation process (Gebauer et al., 2008; Dey et al., 2010; Nudelman et al., 2010; Demichelis et al., 2011; Habraken et al., 2013; De Yoreo et al., 2015). Together with computational efforts, *in situ* techniques such as *in situ* TEM or AFM and synchrotron-based *in situ* scattering techniques are certainly the major contributors to the onset of alternative formulations to CNT, allowing for the observation of nucleation events at work. For example, Nielsen et al. (2014) observed the formation of ACC and vaterite from solution that brought about the formation of more stable crystalline phases both directly via direct transformation and indirectly presumably via dissolution and re-precipitation. The aggregation phenomena following the initial formation of the aqueous precursors, whether pre-nucleation clusters or dense liquid phases, has been described to occur in most cases via spinodal decomposition. This barrier-free mechanism implies a spontaneous separation of a rich Ca-CO_3-H_2O phase from the solution, and it is present in conditions of relatively high fluid supersaturations (Wolf et al., 2008; Bewernitz et al., 2012; Wallace et al., 2013; Stephan E.Wolf and Gower, 2017). Further condensation, via dehydration, of the Ca-CO_3-H_2O dense liquid phase results in the formation of ACC, a known precursor of many biominerals (Addadi et al., 2003).

In the light of the rise of multistep nucleation pathways, the major drawback of CNT has been pointed out to lay in the so-called capillary approximation. Macroscopic concepts such as surface and volume are applied to molecular-scale objects and the interfacial energies are assumed to be independent on the size of the nucleus (Prieto, 2014). In relation to this, it is also assumed that the interface between the nucleus and the solution is zero-width (Lutsko, 2017). Yet, it is worth noting that, even though these weak points are widely accepted, the methods by which parameters are estimated are often disregarded, to the extent where *surface energy* obtained directly from contact angles or adsorption calorimetry are interchangeable replaced for *interfacial energy/tension* obtained from nucleation rate or induction time measurements, with solely the latter being truly relevant in modeling nucleation kinetics (Prieto, 2014).

For a comprehensive overview on these topics, one may refer to De Yoreo and Whitelam (2016) and Van Driessche et al. (2017).

1.6. The amorphous precursor strategy

Amorphous calcium carbonate (ACC), together with amorphous silica and amorphous calcium phosphate, is probably the most frequently observed precursor to crystalline phases in biomineral systems. $CaCO_3$-based biominerals are found abundantly in marine organisms such as sea urchins, mollusks, sponges, corals and crustaceans and are used for structural purposes (coral skeletons and sea urchin tests), protection (sea urchin spines, mollusk shells, crustacean carapaces) and mechanical purposes (sea urchin teeth). They possess enhanced properties with respect to their purely inorganic couterparts, such as reduced brittleness of calcite biominerals used for protection purposes and the enhanced mechanical strength of the aragonite found in nacreous layer of mollusk shells (Nudelman et al., 2006; Nudelman and Sommerdijk, 2012). The uniqueness of such biomineral structures comes also from their spatially controlled crystallization, resulting in the development of specific crystal faces, orientation and location, which requires a precise control over both the nucleation and growth processes (Navrotsky, 2004). Such properties and abilities are inspiring and can provide a basis for the fabrication of novel synthetic materials for biomedical, industrial, and technological purposes such as bone implants, nanowires, nanoparticles, crystalline optical materials, and semi-conductors. The key to determine the functional responses is the interplay of structure, organization and dynamics (Mann, 1993; Mann, 2001).

The ‘amorphous precursor strategy’ refers to the approach by which organisms make use of the flexibility of amorphous phases before crystallization (Addadi et al., 2003), to fill pore spaces, control crystallization and to regulate the chemistry of the final $CaCO_3$ polymorph. Biogenic ACC presents a vast multitude of shapes (Fig. 1.5a) and has been shown to transform into calcite in sea urchin larval spicule (Beniash et al., 1997; Politi et al., 2008; Vidavsky et al., 2014) and into aragonite in the formation of mollusk larval shells (Weiss et al., 2002), to give a few representative examples. However, little remains known about the factors involved in the polymorph selection mechanisms as well as the relevance of ACC structures with respect to the different structural characteristics of the final products (Gebauer et al., 2010; Fernandez-Martinez et al., 2013; Fernandez-Martinez et al., 2017). Its amorphous character, and therefore its isotropic nature, allow for materials to function equally well in all orientations during the early stages of formation, in spite of the inherent instability (Weiner et al., 2003). Also, its high solubility, relative to the crystalline polymorphs, is referred as an advantage for the organisms that make use of it, to form ACC as temporary storage of $CaCO_3$. Both in vivo and in vitro studies show that stable ACC are hydrated and becomes dehydrated as transformation into crystalline $CaCO_3$ proceeds, which, together with the considerable fraction of magnesium, phosphate, as well as proteins found inside or in close vicinity of ACC, elucidates that there might exist specific mechanisms involved in stabilization, destabilization, and transformation of ACC. From the energetic point of view, it has been suggested that the formation of ACC, the least stable precipitate (Fig. 1.5b) (Radha et al., 2010), as the precursor phase has to do with the lowering of interfacial free energy relative to the formation of crystalline phases (Navrotsky, 2004).

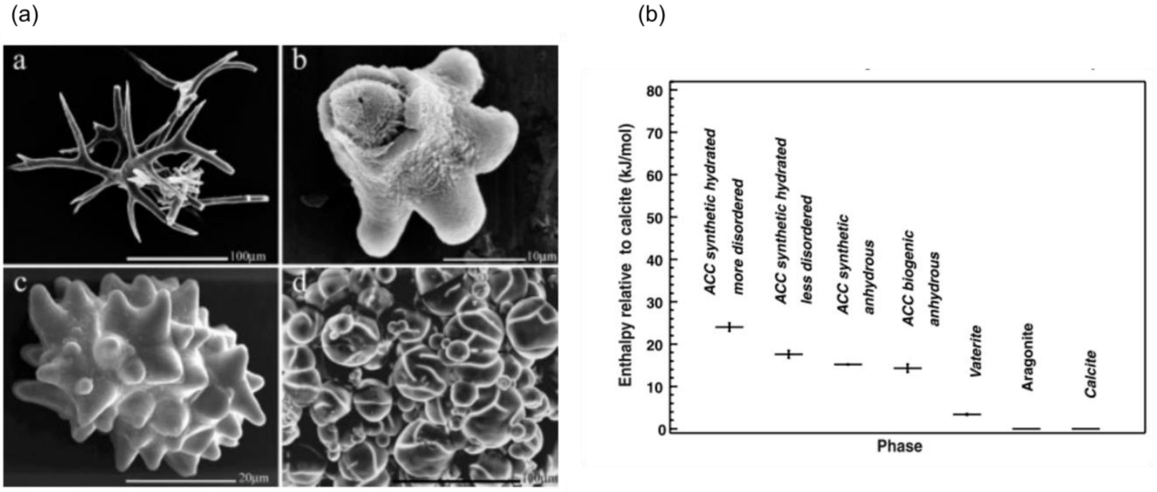

Figure 1.5. Amorphous precursors and relative enthalpy data of $CaCO_3$ system. **(a)** SEM images of various skeletal parts composed of stable ACC. a: Body spicules from *Pyura pachydermatina*, b: Cross-section of a broken tunic spicule from *Pyura pachydermatina*, c: Cystolith from the leaves of *Ficus microcarpa*, d: Granule from storage structure of *Orchestia cavimana*. (Addadi et al. 2003) **(b)** Relative energetic stabilities of different calcium carbonate phases with respect to calcite. (Radha et al., 2010)

References

Addadi L., Raz S. and Weiner S. (2003) Taking advantage of disorder: Amorphous calcium carbonate and its roles in biomineralization. *Adv. Mater.* **15**, 959–970.

Aizenberg J. (2010) New Nanofabrication Strategies: Inspired by Biomineralization. *MRS Bull.* **35**, 323–330.

Becker R. and W. Döring (1935) Kinetische behandlung der keimbildung in übersättingten dampfen [Kinetic theory of nucleation in supersaturated vapors]. *Ann. Phys.* **24**, 719–752.

Beniash E., Aizenberg J., Addadi L. and Weiner S. (1997) Amorphous calcium carbonate transforms into calcite during sea urchin larval spicule growth. *Proc. R. Soc. B Biol. Sci.* **264**, 461–465.

Bewernitz M. a., Gebauer D., Long J., Cölfen H. and Gower L. B. (2012) A Metastable Liquid Precursor Phase of Calcium Carbonate and its Interactions with Polyaspartate. *Faraday Discuss.* **159**, 291–312.

Chen T., Neville A. and Yuan M. (2005) Calcium carbonate scale formation - Assessing the initial stages of precipitation and deposition. *J. Pet. Sci. Eng.* **46**, 185–194.

Chernov A. A. (1984) *Modern crystallography III: crystal growth*., Springer-Verlag.

Chiquet P., Broseta D. and Thibeau S. (2007) Wettability alteration of caprock minerals by carbon dioxide. *Geofluids* **7**, 112–122.

Clouet E. (2010) Modeling of Nucleation Processes. In *ASM Handbook Vol. 22A, Fundamentals of Modeling for Metals Processing* (eds. D. U. Furrer and S. L. Semiatin). pp. 203–219.

Debenedetti P. G. (1996) *Metastable Liquids: concepts and principles*., Princeton University Press, Princeton, New Jersey.

Demichelis R., Raiteri P., Gale J. D. and Dovesi R. (2012) A new structural model for disorder in vaterite from first-principles calculations. *CrystEngComm* **14**, 44–47.

Demichelis R., Raiteri P., Gale J. D., Quigley D. and Gebauer D. (2011) Stable prenucleation mineral clusters are liquid-like ionic polymers. *Nat. Commun.* **2**.

Dey A., Bomans P. H., Muller F. A., Will J., Frederik P. M., de With G. and Sommerdijk N. A. (2010) The role of prenucleation clusters in surface-induced calcium phosphate crystallization. *Nat. Mater.* **9**, 1010–1014.

DeYoreo J. J. and Vekilov P. G. (2003) Principles of Crystal Nucleation and Growth. *Rev. Mineral. Geochemistry* **54**, 57–93.

Dong W., Ball W. P., Liu C., Wang Z., Stone A. T., Bai J. and Zachara J. M. (2005) Influence of calcite and dissolved calcium on uranium(VI) sorption to a Hanford subsurface sediment. *Environ. Sci. Technol.* **39**, 7949–7955.

Van Driessche A. E. S., Kellermeier M., Benning L. G. and Gebauer D. eds. (2017) *New Perspectives on Mineral Nucleation and Growth: From Solution Precursors to Solid Materials*., Springer.

Espinoza D. N. and Santamarina J. C. (2010) Water-CO2-mineral systems: Interfacial tension, contact angle, and diffusionImplications to CO2 geological storage. *Water Resour. Res.* **46**, 1–10.

Feely R. a, Sabine C. L., Lee K., Berelson W., Kleypas J., Fabry V. J. and Millero F. J. (2004) Impact of anthropogenic CO2 on the CaCO3 system in the oceans. *Science* **305**, 362–366.

Fernandez-Martinez A., Kalkan B., Clark S. M. and Waychunas G. a. (2013) Pressure-induced polyamorphism and formation of “aragonitic” amorphous calcium carbonate. *Angew. Chemie - Int. Ed.* **52**, 8354–8357.

Fernandez-Martinez A., Lopez-Martinez H. and Wang D. (2017) Structural Characteristics and the Occurrence of Polyamorphism in Amorphous Calcium Carbonate. In *New Perspectives on Mineral Nucleation and Growth: From Solution Precursors to Solid Materials* (eds. A. E. S. Van Driessche, M. Kellermeier, L. G. Benning, and D. Gebauer). Springer.

Fujita Y., Ferris F. G., Lawson R. D., Colwell F. S. and Smith R. W. (2000) Calcium Carbonate Precipitation by Ureolytic Subsurface Bacteria. *Geomicrobiol. J.* **17**, 305–318.

Gebauer D., Gunawidjaja P. N., Ko J. Y. P., Bacsik Z., Aziz B., Liu L., Hu Y., Bergström L., Tai C.-W., Sham T.-K., Edén M. and Hedin N. (2010) Proto-calcite and proto-vaterite in amorphous calcium carbonates. *Angew. Chemie - Int. Ed.* **49**, 8889–8891.

Gebauer D., Völkel A., Cölfen H., Volkel A. and Colfen H. (2008) Stable prenucleation calcium carbonate clusters. *Science* **322**, 1819–1822.

Gibbs J. W. (1878) On the Equilibrium of Heterogeneous Substances. *Trans. Connect. Acad.* **3**, 108-248-524.

Gower L. B. (2008) Biomimetic model systems for investigating the amorphous precursor pathway and its role in biomineralization. *Chem. Rev.* **108**, 4551–4627.

Gower L. B. and Odom D. J. (2000) Deposition of calcium carbonate films by a polymer-induced liquid-precursor (PILP) process. *J. Cryst. Growth* **210**, 719–734.

Habraken W. J. E. M., Tao J., Brylka L. J., Friedrich H., Bertinetti L., Schenk A. S., Verch A., Dmitrovic V., Bomans P. H. H., Frederik P. M., Laven J., van der Schoot P., Aichmayer B., de With G., DeYoreo J. J. and Sommerdijk N. A. J. M. (2013) Ion-association complexes unite classical and non-classical theories for the biomimetic nucleation of calcium phosphate. *Nat. Commun.* **4**.

Kabalah-Amitai L., Mayzel B., Kauffmann Y., Fitch A. N., Bloch L., Gilbert P. U. P. A. and Pokroy B. (2013) Vaterite crystals contain two interspersed crystal structures. *Science* **340**, 454–457.

Kashchiev D. (2000) *Nucleation: Basic Theory with Applications*., Butterworth-Heinemann, Oxford.

Kashchiev D. and van Rosmalen G. M. (2003) Review: Nucleation in solutions revisited. *Cryst. Res. Technol.* **38**, 555–574.

Lutsko J. F. (2017) Novel Paradigms in Nonclassical Nucleation Theory. In *New Perspectives on Mineral Nucleation and Growth: From Solution Precursors to Solid Materials* (eds. A. E. S. Van Driessche, M. Kellermeier, L. G. Benning, and D. Gebauer). Springer. pp. 25–41.

Mann S. (2001) *Biomineralization: Principles and Concepts in Bioinorganic Materials Chemistry*., Oxford University Press, New York.

Mann S. (1993) Molecular tectonics in biomineralization and biomimetic materials chemistry. *Nat. Lett.* **365**, 499–505.

McCarthy J. F. and Zachara J. M. (1989) Subsurface transport of contaminants: binding to mobile and immobile phases in groundwater aquifers. *Environ. Sci. Technol.* **23**, 496–502.

Meyers M. A., McKittrick J. and Chen P.-Y. (2013) Structural Biological Materials: Critical Mechanics-Materials Connections. *Science* **339**, 773–779.

Milliman J. D. (1993) Production and accumulation of calcium carbonate in the ocean: budget of a nonsteady state. *Global Biogeochem. Cycles* **7**, 927–957.

Navrotsky A. (2004) Energetic clues to pathways to biomineralization: precursors, clusters, and nanoparticles. *Proc. Natl. Acad. Sci. U. S. A.* **101**, 12096–12101.

Nielsen M. H., Aloni S. and De Yoreo J. J. (2014) In situ TEM imaging of CaCO3 nucleation reveals coexistence of direct and indirect pathways. *Science* **345**, 1158–1162.

Noiriel C., Steefel C. I., Yang L. and Ajo-Franklin J. (2012) Upscaling calcium carbonate precipitation rates from pore to continuum scale. *Chem. Geol.* **318–319**, 60–74.

Nudelman F., Gotliv B. A., Addadi L. and Weiner S. (2006) Mollusk shell formation: Mapping the distribution of organic matrix components underlying a single aragonitic tablet in nacre. *J. Struct. Biol.* **153**, 176–187.

Nudelman F., Pieterse K., George A., Bomans P. H., Friedrich H., Brylka L. J., Hilbers P. A., de With G. and Sommerdijk N. A. (2010) The role of collagen in bone apatite formation in the presence of hydroxyapatite nucleation inhibitors. *Nat. Mater.* **9**, 1004–1009.

Nudelman F. and Sommerdijk N. A. J. M. (2012) Biomineralization as an inspiration for materials chemistry. *Angew. Chemie - Int. Ed.* **51**, 6582–6596.

Pina C. M. and Putnis A. (2002) The kinetics of nucleation of solid solutions from aqueous solutions: A new model for calculating non-equilibrium distribution coefficients. *Geochim. Cosmochim. Acta* **66**, 185–192.

Politi Y., Metzler R. A., Abrecht M., Gilbert B., Wilt F. H., Sagi I., Addadi L., Weiner S. and Gilbert P. U. P. A. (2008) Transformation mechanism of amorphous calcium carbonate into calcite in the sea urchin larval spicule. *Proc. Natl. Acad. Sci. U. S. A.* **105**, 17362–17366.

Prieto M. (2014) Nucleation and supersaturation in porous media (revisited). *Mineral. Mag.* **78**, 1437–1447.

Radha A. V., Forbes T. Z., Killian C. E., Gilbert P. U. P. A. and Navrotsky A. (2010) Transformation and crystallization energetics of synthetic and biogenic amorphous calcium carbonate. *Proc. Natl. Acad. Sci. U. S. A.* **107**, 16438–16443.

Sabine C. L. (2004) The Oceanic Sink for Anthropogenic CO2. *Science* **305**, 367–371.

Sear R. P. (2007) Nucleation: theory and applications to protein solutions and colloidal suspensions. *J. Phys. Condens. Matter* **19**, 33101.

Sigg L., Stumm W. and Behra P. (1992) *CHIMIE DES MILIEUX AQUATIQUES : Chimie des Eaux Naturelles et des Interfaces dans l'Environnement*., Masson.

Söhnel O. and Garside J. (1992) *Precipitation—Basic Principles and Industrial Applications*., Butterworth-Heinemann.

Sommerdijk N. a J. M. and With G. De (2008) Biomimetic CaCO3 Mineralization using Designer Molecules and Interfaces. *Chem. Rev.* **108**, 4499–4550.

Steefel C. I. and Van Cappellen P. (1990) A new kinetic approach to modeling water-rock interaction: The role of nucleation, precursors, and Ostwald ripening. *Geochim. Cosmochim. Acta* **54**, 2657–2677.

Stephan E.Wolf and Gower L. B. (2017) Challenges and perspectives of the polymer-induced liquid-precursor process: the pathway from liquid-condensed mineral precursors to mesocrystalline products. In *New Perspectives on Mineral Nucleation and Growth: From Solution Precursors to Solid Materials* (eds. A. E. S. Van Driessche, M. Kellermeier, L. G. Benning, and D. Gebauer). Springer. pp. 43–75.

Stoyanov S. (1979) Nucleation theory for high and low supersaturations. In *Current topics in materials science, Vol. 3* (ed. E. Kaldis). North-Holland, Amsterdam. pp. 421–462.

Stoyanov S. (1973) On the atomistic theory of nucleation rate. *Thin Solid Films* **18**, 91–98.

Turnbull D. and Vonnegut B. (1952) Nucleation Catalysis. *Ind. Eng. Chem.* **44**, 1292–1298.

Vidavsky N., Addadi S., Mahamid J., Shimoni E., Ben-Ezra D., Shpigel M., Weiner S. and Addadi L. (2014) Initial stages of calcium uptake and mineral deposition in sea urchin embryos. *Proc. Natl. Acad. Sci. U. S. A.* **111**, 39–44.

Wallace A. F., Hedges L. O., Fernandez-Martinez A., Raiteri P., Gale J. D., Waychunas G. A., Whitelam S., Banfield J. F. and De Yoreo J. J. (2013) Microscopic evidence for liquid-liquid separation in supersaturated CaCO3 solutions. *Science* **341**, 885–889.

Wang J. and Becker U. (2012) Energetics and kinetics of carbonate orientational ordering in vaterite calcium carbonate. *Am. Mineral.* **97**, 1427–1436.

Wang J. and Becker U. (2009) Structure and carbonate orientation of vaterite (CaCO3). *Am. Mineral.* **94**, 380–386.

Warren L. A., Maurice P. A., Parmar N. and Ferris F. G. (2001) Microbially Mediated Calcium Carbonate Precipitation: Implications for Interpreting Calcite Precipitation and for Solid-Phase Capture of Inorganic Contaminants. *Geomicrobiol. J.* **18**, 93–115.

Weiner S., Levi-Kalisman Y., Raz S. and Addadi L. (2003) Biologically formed amorphous calcium carbonate. *Connect. Tissue Res.* **44**, 214–218.

Weiss I. M., Tuross N., Addadi L. and Weiner S. (2002) Mollusc larval shell formation: Amorphous calcium carbonate is a precursor phase for aragonite. *J. Exp. Zool.* **293**, 478–491.

Wolf S. E., Leiterer J., Kappl M., Emmerling F. and Tremel W. (2008) Early homogenous amorphous precursor stages of calcium carbonate and subsequent crystal growth in levitated droplets. *J. Am.*

Chem. Soc. **130**, 12342–12347.

Yang Q., Liu Y., Gu A., Ding J. and Shen Z. (2001) Investigation of Calcium Carbonate Scaling Inhibition and Scale Morphology by AFM. *J. Colloid Interface Sci.* **240**, 608–621.

De Yoreo J. and Whitelam S. (2016) Nucleation in atomic, molecular, and colloidal systems. In *MRS Bulletin* pp. 357–360.

De Yoreo J. J., Gilbert P. U. P. A., Sommerdijk N. A. J. M., Penn R. L., Whitelam S., Joester D., Zhang H., Rimer J. D., Navrotsky A., Banfield J. F., Wallace A. F., Michel F. M., Meldrum F. C., Colfen H., Dove P. M., Cölfen H. and Dove P. M. (2015) Crystallization by particle attachment in synthetic, biogenic, and geologic environments. *Science* **349**, aaa6760-1-aaa6760-9.

Yoreo J. J. De, Sommerdijk N. A. J. M. and Dove P. M. (2017) Nucleation Pathways in Electrolyte Solutions. In *New Perspectives on Mineral Nucleation and Growth: From Solution Precursors to Solid Materials* (eds. A. E. S. Van Driessche, M. Kellermeier, L. G. Benning, and D. Gebauer). Springer. pp. 1–24.

Chapter 2

State of the art and research questions

2.1. Heterogeneous nucleation of $CaCO_3$

Research question #1
Effect of substrate hydrophobicity on $CaCO_3$ heterogeneous nucleation

2.1.1. Thermodynamics of heterogeneous nucleation

Most current studies of $CaCO_3$ nucleation focus on the homogeneous domain, where the effects of solution pH, co-ions (Mg^{2+}, phosphates, etc.), and of a variety of organic macromolecules over the crystallization pathways are addressed. Occasionally, some studies do mention the possibility of predominant occurrence of heterogeneous nucleation, commenting for instance that the nucleation and subsequent growth were observed mostly on the membrane of the TEM fluid cell (Nielsen et al., 2014) or on the glass wall (Nassif et al., 2005), although the implications of these observations tend to be disregarded in the discussion. In most cases, it is simply unknown whether or not heterogeneous nucleation dominated in a given system, unless it is intentionally studied. In fact, since any physical boundary (macromolecules, spectator ions, vessel walls to mixing apparatus, etc.) can in principle induce nucleation heterogeneously, it is indeed extremely difficult to conduct a truly homogeneous nucleation experiment (Wolf et al., 2008). One must note that it remains unknown whether it is a systematic effect for any given surface to lower the nucleation barrier. The likelihood of heterogeneous nucleation is associated to the lowering of effective interfacial energy α' (see eq. 1.10), thus of the nucleation barrier, provided the weight (cubic exponent) of α' on which nucleation rate depends on (eq. 1.14). Predicting the likelihood of heterogeneous nucleation on a given surface should take into account the physico-chemical factors controlling the values of each component of α', i.e., the three interfacial energies (α_{lc}, α_{sc} and α_{ls}). Given the impossibility of measuring, for every system of interest, each and every single interfacial energy values independently, a predictive understanding of the trends of interfacial energy values needs to be built based on physico-chemical concepts. Establishing an atomistic theory of the heterogeneous nucleation, including the understanding of the effects of molecular details on the nucleation barriers, is the ultimate goal. This Ph.D. thesis aims at contributing to this end.

The dominance of heterogeneous over homogeneous nucleation occurs when the effective interfacial energy, α', is lower than the α_{lc} that controls homogeneous nucleation. In the simple case of a hemispherical nucleus forming on a substrate (eq. 1.12):

$$\alpha' < \alpha_{lc} \;\Rightarrow\; -\frac{1}{2}(\alpha_{ls} - \alpha_{sc}) < 0 \;\Rightarrow\; \alpha_{ls} > \alpha_{sc} \tag{2.1}$$

For heterogeneous nucleation to occur, then, the substrate should show a preference to be wetted by the crystal, rather than by water. A high value of α_{ls} implies a hydrophobic substrate. The values of α_{sc} depend on crystal chemistry differences between the substrate and the nuclei, such as lattice mismatch or the strength of the covalent bonds at the interface (Pimentel et al., 2013). Substrate hydrophobicity has been investigated mostly on organic interfaces, such as self-assembled monolayers with various functionalities (see section 2.1.2). A question arises, however, as to whether the effects of substrate hydrophobicity alone are being addressed, since functionalization of substrates may naturally result in a gap of α_{sc} between different substrates under comparison. Furthermore, additional factors such as structural flexibility and compressibility of the organic monolayers are inevitably present (Cooper et al., 1998; Duffy and Harding, 2004; Freeman et al., 2008).

To this point, mineral substrates may be more successfully used in view of gaining a predictive understanding of heterogeneous nucleation for the $CaCO_3$ system. Unlike organic monolayers, they are rigid, well-characterized, and can provide varying hydrophobicity that is inherent to the structure itself (see section 2.2). Table 2.1 lists selected values of interfacial energies found in the literature from both homogeneous and heterogeneous nucleation experiments, as well as direct measurements and computational simulations for comparison. The values reported from homogeneous nucleation experiments for the pure system seem coherent with those reported from heterogeneous nucleation experiments performed on mineral substrates, with the latter being significantly lower than the former, which indicates that heterogeneous nucleation seem to be energetically more favorable. While the values reported by Dousi et al. (2003) are comparable to those of the heterogeneous nucleation experiments with mineral substrates, values reported by Hamm et al. (2014), using organic substrates, are as high as those from homogeneous nucleation experiments and yielded similar values for different substrates despite the trend observed for the promotion of nucleation (see section 2.1.2 for discussion). It is also noteworthy that the value obtained by calorimetric analysis (Forbes et al., 2011) as well as those from computational simulation are much higher than those from homogeneous nucleation experiments, suggesting that these methods do not measure ‘equivalent’ interfaces (Prieto, 2014). Indeed, the crystal faces exposed to the solution in calorimetric analyses are probably ill-controlled, which could result in systematically higher values due to the presence of high energy crystal faces. It must be emphasized, however, that still very few values are reported in the literature, which makes it challenging to establish comprehensive trends of values of interfacial energies as a function of mineral composition, structure, etc. **The first goal, therefore, is to perform heterogeneous nucleation experiments of $CaCO_3$ on two substrates (1 and 2) of different hydrophobic character ($\alpha_{ls1} \neq \alpha_{ls2}$) with similar surface structure ($\alpha_{sc1} \approx \alpha_{sc2}$), allowing to study the effect of the substrate hydrophobicity independently.** To this end, phlogopite mica was selected as substrates, with varying hydrophobicity by fluorine substitution of octahedral OH group, which yields minimum differences in surface structure. Based on the results of previous studies, **we hypothesize that the more hydrophobic substrate will show a lower barrier to nucleation, thus yielding a distinctively lower value for the effective interfacial energy.**

Table 2.1. Selected values of interfacial energy/surface tension obtained by various methods

	(mJ/m^2)	
Homogeneous nucleation		
calcite - water	98	(Söhnel and Mullin, 1982)
calcite - water	83	(Söhnel and Mullin, 1978)
calcite - water	97	(Bennema and Söhnel, 1990)
calcite – water (additive: alcohol)	43	(Manoli and Dalas, 2000)
Heterogeneous nucleation		
quartz	36 (calcite) 27 (ACC)	(Fernandez-Martinez et al., 2013a)
muscovite mica	41 (calcite) 24 (vaterite)	(Li et al., 2014)
quartz	47 (calcite) 32 (vaterite)	
carboxylated polymers	30-32 (calcite)	(Dousi et al., 2003)
C16–COOH	81 (calcite)	(Hamm et al., 2014)
C16–SH	86 (calcite)	
C11–SH	91 (calcite)	
C11–PO_4	95 (calcite)	
Direct method		
muscovite mica - water	107	(Bailey and Kay, 1967; Bailey and Price, 1970)
muscovite mica - water	7	(Christenson, 1993)
muscovite mica – electrolyte solutions	4.6	(Pashley, 1981)
calcite - water	1480	(Forbes et al., 2011)
Computational simulation		
calcite (1014) - water	160	(de Leeuw and Parker, 1998)
calcite (1014) - water	412	(Bruno et al., 2013)

For heterogeneous nucleation data, effective interfacial energy values are reported.

2.1.2. Heterogeneous nucleation: A molecular view of the electrolyte-substrate interface

Intrinsic and extrinsic surface properties, such as the type of the adsorbed ions or surface charge distribution, induce dramatic changes in the structure and dynamics of interfacial water (see section 2.2). Naturally, this might affect the values of the interfacial energies between the fluid and the formed crystals (α_{lc}) as well as the fluid and the substrate (α_{ls}). The value of the effective interfacial energy (α') depends therefore on a large variety of physico-chemical factors that influence the wetting of surfaces. In particular, hydrophobic surfaces are postulated to bear weak interactions with water, which results in attracting cations due to the net deficiency of accepted H-bonds (Scatena et al., 2001; Pratt and Pohorille, 2002). Although some studies have pointed to an increase of the liquid-substrate interfacial energy (α_{ls}) when electrolyte ions are located near the interface (Butkus and Grasso, 1998), it is not clear whether this effect is universal. Interestingly, authors note that this effect was particularly true with increasing the hydrophobicity of substrates, which presumably can be explained by the attraction of cations.

Heterogeneous nucleation studies have predominantly been performed on organic interfaces, often using surfaces coated with self-assembled monolayers. A study by Giuffre et al. (2013) demonstrated that charge-neutral substrates (i.e. hydrophobic) promoted nucleation of calcite as compared to negatively charged substrates since the hydrophobic surface would favor to form a new interface between the substrate and calcite crystals rather than to maintain the contact with the solution (Fig. 2.1a (A-D)). This result implies that one way to overcome the increased α_{ls} on a hydrophobic surface is to nucleate a new phase. On the contrary, some studies reported promoted nucleation of calcite on negatively charged or carboxyl-terminated (present in dissociated form of >COOH above pH 7, >COO$^-$, thus negatively charged) substrates (Dousi et al., 2003; Hu et al., 2012), owing to the strong attraction of Ca^{2+} atoms. Similar observations were reported by Hamm et al. (2014) where substrates exhibiting strong binding strength to calcite were shown to promote calcite nucleation. Such classical behavior on carboxylated substrates seems somewhat contradictory to the existence of stabilized ACC by carboxyl groups (Guillemet et al., 2006; Ihli et al., 2013), although a study by Kim et al. (2007) reports that carboxylated substrates induced faster crystallization of the deposited ACC film over hydrophobic substrates. Moreover, Aizenberg et al. (1999) report that nucleation was even suppressed on hydrophobic substrates. Reflecting contrasting observations, Giuffre et al. (2013) suggest that there must be a reversal in the nucleation rate at a certain supersaturation σ for any two substrates, since nucleation barriers are constant for a given substrate–liquid–crystal system, provided that nucleation proceeds in a classical manner (Fig. 2.1a (E)). This also points up the importance of reporting the values for interfacial energy for a given system under study, and this is even more so since absolute values of interfacial energy are very scarce in the literature. From the perspective of the H-bond asymmetry (see section 2.2 and Fig. 2.2b), promotion of nucleation on charge-negative substrates seems in fact consistent with the same observation on charge-neutral substrates since the latter also displays a negative field. In this context, the degree of attraction of Ca^{2+} may be dependent on the σ as suggested by Giuffre et al. (2013) such that at relatively low σ, water molecules would form strong oriented hydrogen bonds with the substrate which then alleviates the negatively-charged surface while for hydrophobic surfaces negative charge is created by the contact with water. Along with the dependence on the supersaturation, it is to note that classical behavior reported in some of the studies above could be due to the observation methods such as optical microscopy that do not allow for the detection of primary nuclei.

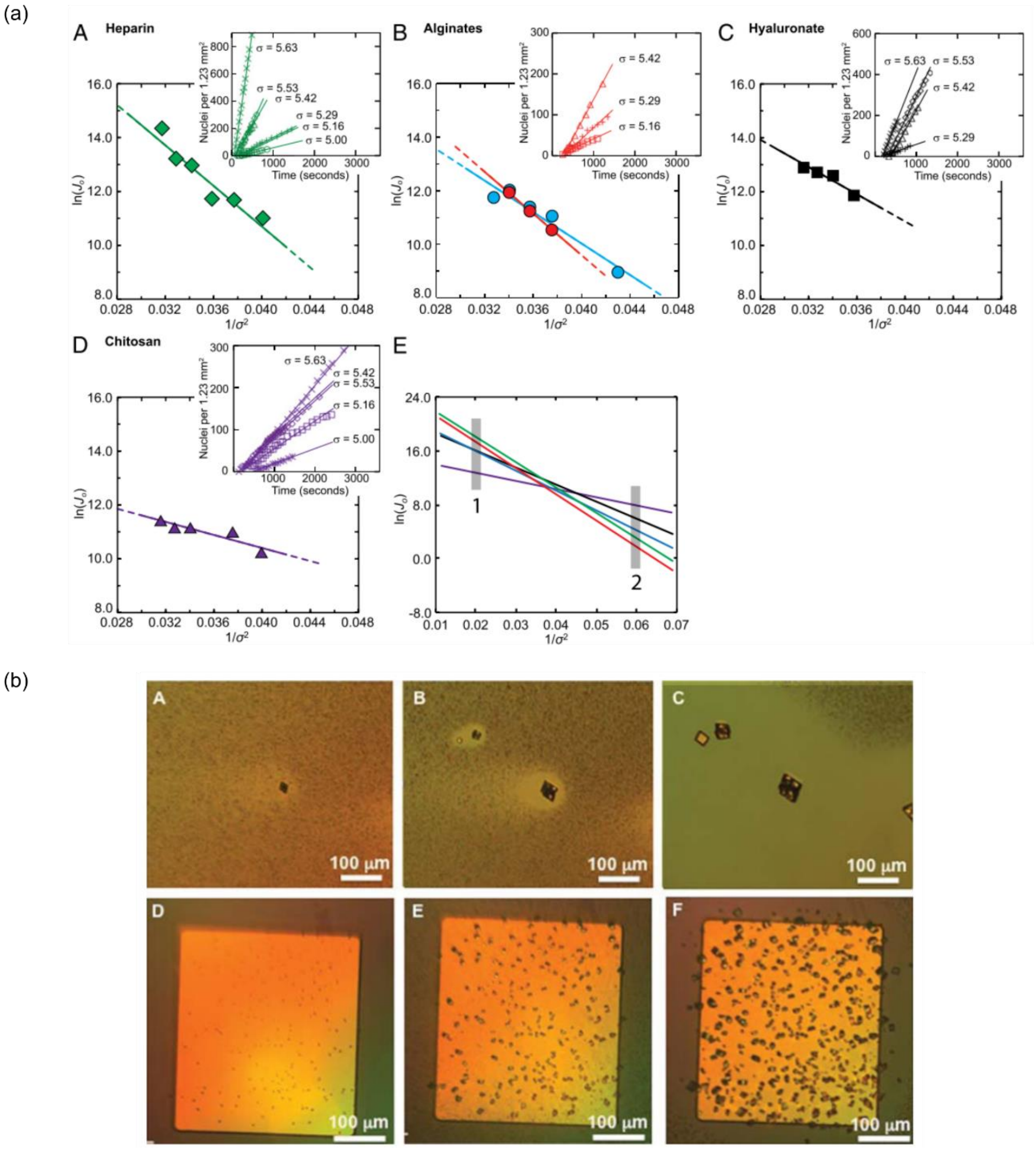

Figure 2.1. Examples of studies on heterogeneous nucleation of $CaCO_3$. **(a)** Calcite steady-state nucleation rates obey classical nucleation theory and show substrate specific dependence on B (slope), a proxy for the thermodynamic barrier to nucleation. (A) Heparin, B = 376 ± 60; (B) LG alginate (red circles), B = 390 ± 11 and HG alginate (blue circles), B = 294 ± 45; (C) Hyaluronate, B = 253 ± 58; and (D) chitosan, B = 121 ± 22. (E) Trends in A–D extrapolated to (1) large and (2) small

supersaturations predicts reversal in relative order of nucleation rates. (Giuffre et al., 2013) **(b)** (A–C) Still images from movie showing the pathway of calcite formation during diffusion of carbonate into $CaCl_2$ solution on an OH-terminated SAM. The appearance of ACC is followed by nucleation of calcite and concomitant dissolution of the ACC film. Frame times are 830 s, 1,892 s and 3,742 s. (D–F) Still images from movie showing the pathway of calcite formation during diffusion of carbonate into $CaCl_2$ solution on carboxyl-terminated SAM. Frame times are 280 s, 700 s and 1500 s. (Hu et al., 2012)

If the nucleation of calcite was enough to compensate the increased α_{ls} due to the hydrophobic effect, then to what extent can α_{lc} affect the fate of heterogeneous nucleation? As already mentioned, the formation of ACC as an intermediate entity would help lowering the interfacial energy relative to the formation of crystalline phases (Navrotsky, 2004). This seems plausible since the structure of ACC includes water, thus contributing to the lowering of α_{lc}. A study by Xu et al. (2004) is in line with this rationale, where OH-terminated substrates (i.e. hydrophilic) displayed inhibiting effects toward the transformation of ACC, to which authors attribute the interaction between the hydrophilic substrates and the water molecules within the ACC. Hu et al. (2012) also showed that ACC particles were deposited on OH-terminated substrates after being homogeneously nucleated. Authors demonstrate that further ACC dissolution resulted in the indirect precipitation of calcite, in contrast to carboxyl-terminated substrates on which direct precipitation of calcite was observed (Fig. 2.1b). On the other hand, a study by Pouget et al. (2009) using cryo-TEM reported that the nucleation of crystalline phases (vaterite and calcite) took place within the ACC deposited on the organic interface (stearic acid monolayer), although authors also note that the initial formation of ACC seems independent of the substrate and occurred homogeneously by aggregation of ion clusters.

It is yet curious that the initial formation of ACC is often regarded as resulting from homogeneous nucleation. From the point of view that there might also be a competition between α_{sc} and $\alpha_{lc,}$ nucleating calcite would be favored on a hydrophobic surface for the reduction of α_{sc}, while for the reduction of α_{lc}, ACC could be the preferred phase to nucleate (and not only to deposit), even though this is probably scaled by the magnitude of the surface hydrophobicity as well as the supersaturation. Although results shown above are inspiring, it is challenging to identify individual factors that are controlling the nucleation, since the effects of substrate hydrophobicity might not be addressed directly (section 2.1.1). Nevertheless, there exists increasing evidence, observed for the $CaCO_3$ system, of nucleation and crystallization behaviors that fall out of the classical pathway. Given the relevance of heterogeneous nucleation, **the second goal is to ascertain the possibility that multistep nucleation pathways could be present during the heterogeneous nucleation of $CaCO_3$. On the basis of the hydrous nature of ACC and consideration of α_{sc}, we hypothesize that ACC would form more favorably on hydrophilic substrate while crystalline polymorphs would favor hydrophobic substrate, which in both cases lowers the value of α_{sc}.**

2.2. Surface hydrophobicity and properties of interfacial water

Research question #2

Atomistic view of surface hydrophobicity: what does define the hydrophobic properties of fluorinated phlogopite bearing adsorbed cations?

As described in the previous section, surface hydrophobicity is one of the most important physicochemical properties to be considered in order to ascertain the likelihood of heterogeneous nucleation. It can considerably influence the structure and the dynamics of the interfacial water as will be discussed below, which in turn determines the nature of interaction. Geochemists have long studied the properties of interfacial water, in particular the so-called electrical double layer (EDL) at the solid-water interface (Sposito, 2004). The presence of EDL is a ubiquitous characteristic to a wide range of systems, both natural or engineered, that contain water and colloids, nanoparticles, or nanopores (Sposito, 2004; Bourg et al., 2017), and it has been of particular importance in the scope of understanding and predicting sorption behaviors and mechanisms of ions, contaminants and organic substances (Damaskin and Frumkin, 1974; Brown et al., 1999; Sposito, 2004). EDL model integrates the concepts of surface charge, electrical potential decay, as well as the distribution of water and electrolyte ions that screen the surface charge as a function of pH and electrolyte concentration (Brown, 2001). Although consideration of hydrophobic mineral (as will be discussed below) and organic (Scatena et al., 2001; Pratt and Pohorille, 2002; Elhadj et al., 2006; Stephenson et al., 2008) interfaces can be found in the literature, such insights of interfacial water behaviors have rarely been integrated into the framework of heterogeneous nucleation. Yet, there exist fundamental features of interfacial water structure and dynamics that are applicable and beneficial to the development of a predictive understanding of heterogeneous nucleation.

One of the widely acknowledged characteristics of a hydrophobic surface, in comparison to a hydrophilic one, is the depletion of the interfacial water density (Schwnedel et al., 2003; Steitz et al., 2003; Poynor et al., 2006; Janecek and Netz, 2007; Maccarini et al., 2007). For a talc-water interface, a representative hydrophobic mineral, the water density is reported to be depleted by ~0.8 Å as compared to hydrophilic muscovite mica interface (Fig. 2.2a) and this is associated to the total number of hydrogen bonds (J. Wang et al., 2009). Surface hydrophobicity is also reflected by the orientational ordering of interfacial water molecules. At the water-muscovite interface, the H_2O dipoles point toward the muscovite surface, donating hydrogen bonds to the surface oxygens which are the strong interaction sites (Wang et al., 2006), while at the water-talc interface, they point toward the liquid phase, with H-O-H plane forming an average angle of ~60° with the surface (J. Wang et al., 2009). At the water-vapor interface, which can be viewed as hydrophobic due to its weak interfacial interactions, it is known that the orientational distribution of water molecules and their density along the normal direction to the interface lead to electrical asymmetry (Stillinger, 1973; Pratt and Pohorille, 2002), resulting in a positive electric field on the vapor side and a negative field on the water side due to an unbalanced number of accepted and donated H-bonds at the interface. Following this rationale and the observation that there exists a net deficiency of accepted H-bonds (Fig. 2.2b), J. Wang et al. (2009) predict that hydrophobic talc surface would preferably attract cations, which could have a tremendous implication for heterogeneous nucleation behavior. While the opposite would hold at hydrophilic muscovite mica interface (i.e. a net deficiency of donated H-bonds, thus net positive charge), the interaction between the surface ions and water molecules might change the scenario.

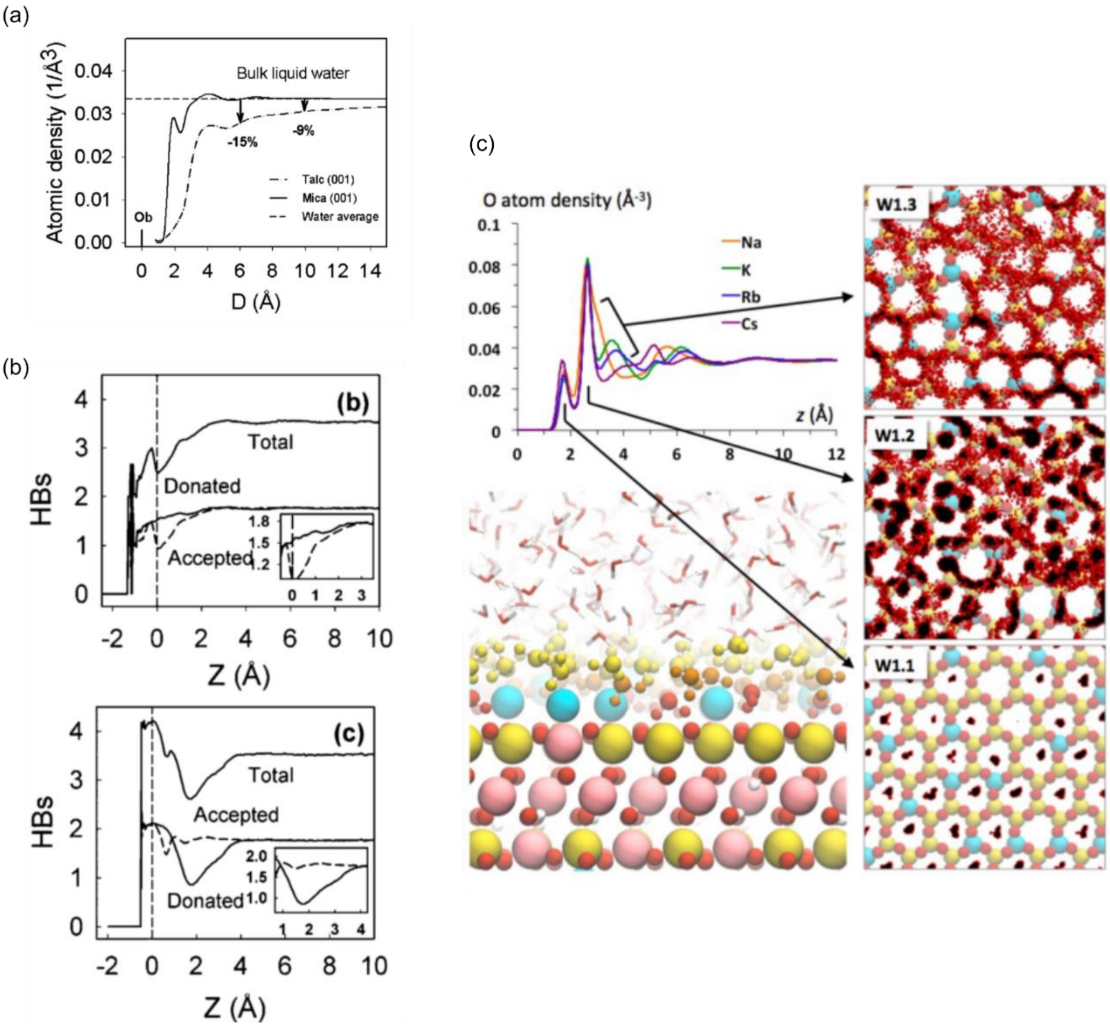

Figure 2.2. Examples of studies on interfacial water properties. **(a)** Cumulative average water density as a function of distance from the surface at talc (001) and mica (001). The zero position is defined as the average *Z*-coordinate of the surface bridging oxygens. (J. Wang et al., 2009) **(b)** Average number of hydrogen bonds and their donor/acceptor components for talc (001) and mica (001) annotated as b and c in the original paper. (J. Wang et al., 2009) **(c)** Top left: water O density profile as a function of distance from the mica surface for Na-, K-, Rb-, and Cs-bearing mica. Bottom left: MD simulation snapshot of the mica-water interface. Right: *xy* density maps of water molecules in sub-layers. (Bourg et al., 2017)

At the muscovite-water interface, it is the presence of K^+ ions that contributes to the net positive charge since water molecules hydrating K^+ ions do not donate H-bonds to the surface oxygens, thus resulting in the net deficiency of donated H-bonds (J. Wang et al., 2009). When the mineral surface interacts with water containing electrolyte ions, however, the resulting structure and energetics of EDL, in particular the Stern layer, the very first two water monolayers in which surface complexation of adsorbed ions is predominant (Sposito, 2004), depend largely on the nature of the electrolyte ions, in addition to the surface topography, surface charge distribution, and hydrogen bonding. At the muscovite mica-water interface, one of the most extensively studied model examples, smaller alkali metals such as Na and Li prefer to form outer-sphere surface complexes at the triad sites, whereas larger alkali metals such as Cs, Rb or K would favor to form inner-sphere surface complexes at the cavity sites (Bourg et al., 2017). The structure and distribution of interfacial water are strongly templated by the distribution of alkali metals and the basal oxygen atoms. It is known that there exit three sub-layers of water, each forming two, one or no hydrogen bonds with the basal surface, located at different heights from the surface (Park and Sposito, 2002; Wang et al., 2005; Bourg and Sposito, 2011; Sakuma and Kawamura, 2011; Bourg et al., 2017). The first sub-layer water molecules generally occupy siloxane cavities that are unoccupied by the inner-sphere surface complexes; the second sub-layer molecules sit atop basal oxygen atoms and the third sub-layer molecules sit loosely above the Si-O-Si/Al rings (Fig. 2.2c). It is noteworthy that the third sub-layer changes its height depending on the adsorbed cations. Additionally, some of the adsorbed cations can display outward shifting as increasing the number of surface water molecules (Wang et al., 2005), which in turn affects the H-bonding arrangements of interfacial water. Interestingly, a computational study by Rotenberg et al. (2011) demonstrated that the surface hydrophobicity is determined by the competition between adhesion of water molecules to the surface and cohesion in between the water molecules. Extrapolating this result to a mica-water interface with adsorbed cations, a competition for the water molecules between the substrate and the cations would significantly control the substrate hydrophobicity.

The occurrence of substitutions in many of the silicate and alumino-silicate minerals must also be noted as a source of permanent charge, altering the wetting properties. Of particular interest is the phyllosilicate group where a number of possibilities exist for both cationic (Si^{4+}, Al^{3+}, Li^+, Fe^{2+}, Mg^{2+}) and anionic (F^-, OH^-, O^{2-}) substitutions (Demyanova and Tressaud, 2009). In particular, fluorine substitution of octahedral OH group has been extensively studied for both trioctahedral and dioctahedral micas including phlogopite and muscovite in terms of natural occurrence, OH-F distribution or local charge balance (Robert et al., 1993; Papin et al., 1997; Robert et al., 1999). Whether naturally occurring or synthetized, when OH^- is substituted by F^-, the mineral surface exhibits hydrophobic properties, thus altering the interfacial water structure. A study by Michot et al. (1994) demonstrate that, OH^- being the only hydrophilic sites for talc, fluorination suppresses the specific interactions, confirming the hydrophobicity of the Si-O-Si region on the basal surface. A computational study by Rotenberg et al. (2011) also reports that when exposed to a low relative humidity, the fluorine substitution in talc lowered the adsorption energy $\Delta\mu_{\mathrm{ads}}$ to -3.5 kcal/mol, while for hydroxylated talc it was -5.9 kcal/mol, equivalent to the formation of a hydrogen bond between a water molecule and the structural OH^- (~$10K_BT$). Hydrophobic effects were also observed in the interlayer water of smectite in a study by Dazas et al. (2013), showing that the fluorinated smectites, when compared to the hydroxylated counterpart, not only reduced the interlayer water content by ~30%, but also reduced the positional disorder of the interlayer water molecules. Fluorine substitutions with varying OH/F ratio in mica minerals are commonplace in nature because of the similarity in ionic radii (Wedepohl, 1978; Petersen et al., 1982). Despite the environmental relevance resulting from this natural abundance, still very few studies examine the effect of fluorine substitution on water-mica interface.

In the previous section 2.1, substrate hydrophobicity has been described as an important factor controlling the likelihood of heterogeneous nucleation from thermodynamic point of view. However, as discussed above, the concept of surface hydrophobicity involves a great deal of molecular complexity caused by multiple factors such as the type of electrolytes, surface topology, charge distribution and the resulting H-bonds arrangements. Therefore, an atomistic description of heterogeneous nucleation should include a depiction of the loci of nucleation within the EDL, the effect of the water depletion on cluster formation and other related details. And the foremost question to be addressed is the detailed picture of the interfacial water structure. **The phlogopite mica substrates used here exhibit structural complexity, involving OH and F functional groups, that alters the permanent charges due to their structural substitutions and a variety of resulting water adsorption sites. These factors can be responsible for the hydrophobic properties of the surface. A fundamental question posed is: what does define the hydrophobic properties of fluorinated phlogopite bearing adsorbed cations? We hypothesize, based on interaction sites present at OH- and F-phlogopite, that substrate hydrophobicity is defined through a competition between the hydration properties of counterions and inherent structural hydrophobicity.**

2.3. Amorphous calcium carbonate: an intermediate in the $CaCO_3$ crystallization processes

Research question #3

Linking the atomistic dynamics and crystallization kinetics in ACC: how does the presence of water and Mg^{2+} control ACC crystallization kinetics?

Heterogeneous nucleation of the $CaCO_3$ system has been review in sections 2.1 and 2.2, with a particular focus on the effect of substrate hydrophobicity and the possibility of multistep nucleation, together with its atomistic depiction of the interface in contact with electrolyte solutions. The focus of section 2.3 is amorphous calcium carbonate, a metastable intermediate in the multistep nucleation of $CaCO_3$.

2.3.1. Structure of amorphous calcium carbonate and polyamorphism

Understanding the links between the structural characteristics of ACC and those of $CaCO_3$ crystalline polymorphs is of great interest in order to ascertain possible polymorph selection mechanisms (Fernandez-Martinez et al., 2017). Despite its disordered nature, insights on ACC short-range structure can be obtained by several methods, including ^{13}C and ^{43}Ca NMR spectroscopy, X-ray absorption spectroscopy (XAS), high-energy X-ray scattering combined with pair distribution function (PDF) analyses and Reverse Monte Carlo (RMC) simulations.

The local order of biogenic ACC has been described mainly by EXAFS spectroscopy which provides coordination symmetry, bond distances, and the nature and the number of the nearest neighboring atoms around Ca^{2+}. It has been shown that the ACC present in sea urchin embryos and freshwater snail shell has short-range order that resembles that of calcite and of aragonite, respectively (Hasse et al., 2000; Marxen et al., 2003; Politi et al., 2006), though the studies reporting aragonitic ACC need to be revised carefully due to the short energy range of EXAFS data and the high number of parameters used in the fits. Levi-Kalisman et al. (2002) reported that the local order of biogenic ACC can be different for different ACC samples, demonstrating distinct EXAFS spectra for each of the three biogenic ACC studied. Neumann and Epple (2007), on the other hand, suggest that monohydrocalcite seems to be the best model for a larger group of biogenic ACC. For synthetic ACC, Gebauer et al. (2010) showed using XAS and ^{13}C NMR that different proto-structured ACC can be achieved by controlling the pH of the saturated solution, with proto-vaterite produced at a starting pH of 9.80 and proto-calcite at a starting pH of 8.75. Furthermore, Fernandez-Martinez et al. (2013b) showed that a first-order phase transition occurs when synthetic ACC is subjected to high pressures (~10 GPa), showing a transition from calcite-vaterite-like ACC to *aragonitic* ACC.

Such occurrence of different short-range order structures for a given stoichiometry is referred to as polyamorphism, the amorphous analogue to polymorphism. Fernandez-Martinez et al. (2017) point out that the relevance of polyamorphism actually depends on the subsequent crystallization mechanisms of ACC: dissolution-reprecipitation or solid-state transformation. In the former case, as recently demonstrated by *in situ* TEM (Nielsen et al., 2014), the proto-structure, if any, of ACC seems no longer relevant since the dissolution of ACC precursors occurs resulting in an increase of the supersaturation and a subsequent precipitation of crystalline polymorphs of lower solubility. Solid-state transformation has been observed for both biogenic ACC (Politi et al., 2008; Gong et al., 2012) and synthetic ACC (Ihli et al., 2014), in which case pre- (for biogenic) or proto- (for synthetic) structures may remain relevant. Proto-structured ACC were demonstrated to be pH dependent (Gebauer et al., 2010), to which the authors relate the pH-dependence of the solubility of prenucleation clusters (Gebauer et al., 2008), suggesting the structural preservation from clusters, to proto-structured ACC, and to crystalline phases (Gebauer et al., 2014). Zou et al. (2015), on the other hand, showed that there exists size-dependent solubility that controls the polymorph selection. Cartwright et al. (2012) stress that the question as to how biogenic ‘pre-structured’ ACC and synthetic ‘proto-structured’ ACC can be related still remains open. Indeed, true determination of polyamorphs is not simple, considering the presence of inorganic and organic impurities, such co-ions (Mg^{2+}, Na^{2+}, Sr^{+}, Ba^{+}, etc.), proteins, carboxylic acids, polyphosphates, as well as the varying contents of water in biogenic ACC. Some of these points are reviewed in the following sections.

2.3.2. Water as structural component

The structural characteristics of ACC including the topology of H_2O, Ca^{2+} and CO_3^{2-} binding is of interest in order to know how inorganic and organic impurities can be incorporated (Fernandez-Martinez et al., 2017). So far, biogenic ACC is found in two states: hydrous or anhydrous, with the latter being the transient phase before the onset of crystallization. A considerable number of studies show that the water is present ensuring ACC structural integrity. Indeed, from the thermodynamic point of view, water has been referred to as the key to the structural stability of ACC (Raiteri and Gale 2010). Goodwin et al. (2010) proposed a nanoporous structure of ACC that is charge-separated into Ca^{2+}-rich and Ca^{2+}-deficient channels, with water molecules and carbonate ions locate within the latter. This structure was later shown to be unstable and thus would result in homogeneous distribution of density and charge within a few simulation steps (Singer et al., 2012). Homogeneous nature of ACC, at the nanometer scale, is also supported by other computational studies (Raiteri and Gale, 2010; Wallace et al., 2013; Cobourne et al., 2014). Nevertheless, it seems to be the distribution of water ‘species’, as will be discussed below, within the ‘homogeneous’ ACC that might control the kinetic property.

The majority of water is present as a molecular entity (Nebel et al., 2008). A minor fraction of hydroxyl groups is reported to be present in synthetic ACC, presumably due to the highly alkaline medium used for the synthesis (Michel et al., 2008; Nebel et al., 2008) and they seem to be thermally stable (Schmidt et al., 2014). Schmidt et al. (2014) showed three types of water molecules by combining NMR spectroscopy and thermogravimetric analysis (TGA): a translationally rigid structural H_2O; a restrictedly mobile H_2O; fluidlike mobile H_2O. Another study combining PDF and NMR spectroscopy by Michel et al. (2008) also noted that there are both mobile and rigid structural water components, with half of the latter undergoing restricted motion on a millisecond time scale. On the contrary, mobile water molecules were reported to be absent in the close vicinity of carbonate groups in biogenic ACC from lobster gastrolitsh (Reeder et al., 2013). Authors suggest that the mobile component of water molecules may only reside near the particle surfaces or as fluid inclusions in pores with limited access to carbonate ions as opposed to synthetic ACC, where mobile H_2O might facilitate the transport and structural rearrangement of the carbonate framework. Indeed, water molecules and carbonate ions seem to be closely coupled via formation of hydrogen bonds. To this point, Saharay et al. (2013) demonstrated by computational simulation that the fraction of H-bonds donated from water molecules to CO_3^{2-} increased upon dehydration, together with increased local ordering resulting in denser packing of neighboring atoms. Farhadi-Khouzani et al. (2016) also noted that the water molecules induce dipole moment across carbonate groups upon heating above 45 °C, seen in FTIR spectra of proto-aragonite ACC, which in turn resulted in the de-shielding in NMR spectra due to electron removal from the central C atoms. It is therefore the location of carbonate groups and the mobility of water molecules in their close vicinity that seem to determine the persistence of ACC. It is to note that, in spite of all the efforts devoted to the study of the structural characteristics of ACC, only few studies have addressed its dynamical properties, such as those using NMR (Michel et al., 2008; Singer et al., 2012; Saharay et al., 2013; Schmidt et al., 2014). Studying the dynamic characteristics of ACC is not only important for an accurate description of the potential energy landscape controlling the configurational space of its structure, but also for atomistic dynamics that are intimately related to the easiness of solid-state nucleation, i.e., nucleation from ACC to a crystalline $CaCO_3$ polymorph without the need of passing through a dissolution-precipitation process.

2.3.3. Dynamics of structural water and kinetic control of additives

Biogenic ACC, unlike its synthetic counterpart, persists for several days to even months under adequate conditions before crystallizing, as manifested by studies where the crystallization of biogenic ACC was tracked (Beniash et al., 1997; Addadi et al., 2003; Raz et al., 2003; Politi et al., 2004). In the process of forming crystalline phases, the formation of transient ACC, namely anhydrous ACC for its low water content compared to stable, hydrous one, has been relatively well-documented in various species (Beniash et al., 1997; Weiss et al., 2002; Raz et al., 2003; Politi et al., 2004). On a particular note, Weiner et al. (2003) showed that almost all the known biogenic ACC deposits have significant amounts of magnesium and/or phosphorus, and where tested, they also contained occluded proteins. Since the kinetic persistence of ACC seems to be strongly related to the retained structural water (Raiteri and Gale, 2010), the question then arises on the mechanisms by which these additives act on the dynamics of structural water.

As for inorganic additives, the role of Mg^{2+} has perhaps been the most extensively studied. The concentration of Mg^{2+} in biogenic ACC ranges from 0 up to ~30 mol% (Addadi et al., 2003; Weiner et al., 2003). Some studies have attributed the increased kinetic persistence of ACC to the presence of Mg^{2+} (Loste et al., 2003; Rodriguez-Blanco et al., 2012; Purgstaller et al., 2016), to which presumably, the existence of a high barrier for dehydration of the Mg^{2+} ion can be attributed (Hamm et al., 2010). Calorimetry analysis also revealed that ACC with ~10% of Mg^{2+} content is energetically the most stable and this proportion of Mg^{2+} is equivalent to the average Mg^{2+} content found in biogenic ACC (Radha et al., 2012). Authors suggest that the incorporation of Mg^{2+} could be thermodynamically imposed, since incorporation of Mg^{2+} into calcite at low concentration seems energetically favorable (Bischoff, 1998). D. Wang et al. (2009), to this point, suggest that the presence of organic acids, such as carboxyl groups, in certain conformation and electrostatic potential topology, can increase Mg^{2+} uptake in ACC, to the extent of high-Mg-calcite and dolomite, whose synthesis is rarely successful in the laboratory. Raz et al. (2003) note, on the other hand, that Mg^{2+} seems to be indispensable for the formation of transient ACC that later transforms to calcite in sea urchin larval spicules containing ~ 5 mol% of Mg^{2+}. Additionally, Politi et al. (2010) showed that Mg^{2+} ions distorts the host structure of $CaCO_3$ and thus inhibits its crystallization, where a shortening of the Mg-O bond length was observed as compared to crystalline anhydrous $MgCO_3$ minerals. Whether or not it is thermodynamically driven, these examples highlight the relevance of Mg^{2+} in the stabilization of ACC.

How is the enhanced kinetic persistence of ACC reflected in its crystallization process? An *in situ* study by Purgstaller et al. (2016) showed that with high Mg^{2+} initial concentration (> ~17 mol%, pH 8.3), the formation of Mg^{2+}-bearing ACC was observed as a precursor to Mg-calcite yielding up to 20 mol% of Mg^{2+}, while lower initial concentration yielded Mg-calcite precipitation directly. Given the high content of Mg^{2+} in the Mg-calcite with respect to that of Mg^{2+}-bearing ACC as well as the hydration energy of Mg^{2+}, the authors suggest that the formation of Mg-calcite took place via dissolution and re-precipitation of the amorphous phase. A comparable observation was made by Rodriguez-Blanco et al. (2012) with 10 mol% Mg which yielded calcite formation via an amorphous phase. Similar results were also obtained by Wang et al. (2012) where it is suggested that the formation of aragonite seem to have been kinetically inhibited due to the rapidly increased supersaturation with respect to ACC. These observations, along with the known kinetic barrier of Mg^{2+} inhibition of calcite formation (Lippmann, 1973; Berner, 1975; Davis et al., 2000), have long been associated to the hydration energy of Mg^{2+}. Reflective of this, a recent simulation by Raiteri et al.

(2015) also demonstrated that, for a preformed $MgCO_3$ ion pair, Mg^{2+} exhibited only 6-fold coordination with 5 water oxygen atoms and 1 carbonate oxygen atom where no water exchange was observed within the timeframe accessible to MD simulation (50 ns), while carbonate exhibited relatively fast rotation around the central carbon atom. The authors also suggest that the water exchange dynamics around Mg^{2+} can be relatively slow. Interestingly, on the other hand, Radha and Navrotsky (2015) report that the adsorption enthalpy of rigid structural water was more exothermic for ACC (−62.1 ± 0.7 kJ/mol) than for pure amorphous magnesium carbonate (AMC) (−58.5 ± 0.6 kJ/mol, 100 mol% Mg^{2+}), despite the fact that the hydration enthalpy is expected to be ionic size-dependent. To this point, authors rationalize that Mg‒O octahedra in AMC could be more relaxed than Ca-O in ACC, which explains the lower hydration enthalpy, where they refer to a study by Xu et al. (2013). This last suggests the existence of additional barrier, beside the hydration energy of Mg^{2+}, which prevents Mg^{2+} and CO_3^{2-} from forming a long-range structure, resulting from the spatially limited configuration of carbonate groups due to the compacted Mg-O octahedral structure in the crystalline magnesite at ambient conditions. These results emphasize the extent to which Mg^{2+} can affect the crystallization pathways of $CaCO_3$ system, although, more specific investigation is needed on how Mg^{2+} contributes to retain structural water during the course of the crystallization of ACC.

In addition to Mg^{2+}, a variety of macromolecules has been shown to contribute to the kinetic persistence of ACC (Aizenberg et al., 1996; Ihli et al., 2013; Tobler et al., 2014; Tobler et al., 2015). To name an example, SM50, a common matrix protein from sea urchin embryonic spicule, was shown to hinder the dehydration of ACC, in particular at the outer rim of the spicule (Gong et al., 2012). Interestingly, authors note that this is where SM50, together with other proteins, has been found to locate uniformly along the spicule, as part of the extracellular matrix (Urry et al., 2000; Seto et al., 2004). Such stabilization of ACC embedded or in contact with the extracellular organic matrix has also been reported by others (Shechter et al., 2008; Bentov et al., 2010). Some authors point out that limited diffusion and reduced solubility of ACC could be the key in such processes (Gal et al., 2013; Gal et al., 2014). Another factor contributing to the stabilization of biogenic ACC may be the confinement effect since biomineralization often occurs inside the cellular compartments where membranes or phospholipid bilayers with associated macromolecules delimit the site of the mineralization (Whittaker et al., 2016). It has been shown indeed that the spatial restraints stabilize amorphous phases and reduce nucleation rates of crystalline biominerals (Loste et al., 2004; Stephens et al., 2010; Tester et al., 2014; Wang et al., 2014). In addition to the plausible physico-chemical reactions involved between ACC and proteins, all these results underline the occurrence and the relevance of nucleation and the consecutive crystallization in contact with a foreign surface (i.e. heterogeneous nucleation).

Amorphous structure, even being solid, is dynamic by nature in that it undergoes structural rearrangements followed by crystallization. This dynamic character is demonstrated to be closely related to that of water it contains, in close association to the presence of its additives, interfaces and spatial limitations, as discussed above. As noted in section 1.3 (see eq. 1.8), the solid-state dynamics in the nucleation of ACC to a crystalline $CaCO_3$ polymorph are controlled not only by the thermodynamic barrier dictated by CNT, but also by the pre-exponential kinetic factor (*A*), which includes the Zeldovich factor and atomic diffusivity of the Ca^{2+} and CO_3^{2-} ions. Within an amorphous solid, this diffusivity can be conceptualized as the number of atomic re-arrangements that the system undergoes per unit of time, as a result of Brownian dynamics. The Zeldovich factor is the factor dictating how many of these re-arrangements will be successful, and will translate into the formation of a crystalline nucleus. **The goal therefore is to establish the relationship between the nanoscopic dynamics of ACC and its kinetic persistence: how does the presence of Mg^{2+} (known to increase ACC kinetic persistence) affect its dynamic properties? Given its hydration energy, we hypothesize that Mg^{2+} enhances the persistence of ACC via formation of strong hydrogen bond network and in doing so creates barrier for structural rearrangements.**

2.4. Summary of research questions and hypotheses

Research question #1

The effect of substrate hydrophobicity on $CaCO_3$ heterogeneous nucleation

Previous research has highlighted the substantial role of the substrate hydrophobicity as an enhancer of heterogeneous nucleation. This has been explained in section 2.1 and it is summarized in eq. (2.1).

a) The first research goal is to perform heterogeneous nucleation experiments of $CaCO_3$ on two substrates (1 and 2) of different hydrophobic character ($\alpha_{ls1} \neq \alpha_{ls2}$) with similar surface structure ($\alpha_{sc1} \approx \alpha_{sc2}$), allowing to study the effect of the substrate hydrophobicity independently.

   Hypothesis: **Hydrophobic substrate would show a lower barrier to nucleation, thus yielding a distinctively lower value for the effective interfacial energy α'.**

b) The second research goal is to ascertain the possibility that multistep nucleation pathways could be present during the heterogeneous nucleation of $CaCO_3$.

   Hypothesis: On the basis of the hydrous nature of ACC and a particular consideration of α_{sc}, **ACC would form more favorably on hydrophilic substrate while crystalline polymorphs would favor hydrophobic substrate, which in both cases lowers the value of α_{sc}.**

Research question #2

Atomistic view of surface hydrophobicity: what does define the hydrophobic properties of fluorinated phlogopite bearing adsorbed cations?

Solid-water interface develops an electrical double layer that is sensitive to the types of counterions and topology of substrates. The phlogopite mica substrates used in this Ph.D. thesis comprise OH and F functional groups, that alters the permanent charges due to their structural substitutions and a variety of resulting adsorption sites for water and counterions, within which several factors can be responsible for their hydrophobic property.

Hypothesis: **Surface hydrophobicity is defined through a competition between the hydration properties of counterions and inherent structural hydrophobicity.**

Research question #3

Linking the atomistic dynamics and crystallization kinetics in ACC: how does the presence of water and Mg^{2+} control ACC crystallization kinetics?

Stability of ACC is enhanced by the presence of Mg^{2+}, in close association with water, both of which are known as thermodynamic and kinetic stabilizers. The solid-state dynamics of nucleation of ACC to a crystalline $CaCO_3$ polymorph are controlled by the pre-exponential kinetic factor (A) which includes the Zeldovich factor and atomic diffusivity of the Ca^{2+} and CO_3^{2-} ions, in addition to the thermodynamic barrier. Within an amorphous solid, this diffusivity can be conceptualized as the number of atomic re-arrangements that the system undergoes per unit of time, as a result of Brownian dynamics, in which the Zeldovich factor dictates the probability of successful structural re-arrangements into the formation of a crystalline nucleus. A link between the nanoscopic dynamics in ACC and its kinetic persistence needs to be established.

Hypothesis: **Mg^{2+} enhances the persistence of ACC via formation of strong hydrogen bond network and in doing so creates barrier for structural rearrangements.**

2.5. Dissertation organization

The following chapter (Chapter 3) provides a brief summary of the theory and application of both the experimental and theoretical techniques that play a major role in the subsequent research chapters.

Chapter 4 is devoted to the study of $CaCO_3$ heterogeneous nucleation (research question #1), where the focus is to determine the effect of substrate hydrophobicity by using hydroxylated and fluorinated phlogopite micas in order to obtain values of effective interfacial energies, usable to reactive transport modeling, and to ascertain the possibility of the occurrence of multistep nucleation pathways during the heterogeneous nucleation of $CaCO_3$. *In situ* nucleation experiments by time-resolved Grazing-incidence Small Angle X-ray Scattering are combined to *ex situ* characterizations by Atomic Force Microscopy and ATR-FTIR spectroscopy.

As an extension to Chapter 4, Chapter 5 aims at providing an atomistic description of mineral-water interface (research question #2) with a particular emphasis on the substrate hydrophobicity caused by (i) F and OH functional groups present in the phlogopite substrates used in Chapter 4 and (ii) adsorbed counterions (K^+, Na^+ and Cs^+). Water adsorption behavior will be examined by Near-Ambient Pressure XPS, and the results are further investigated by classical Molecular Dynamics simulations combined with bond-valence theory.

The focus of Chapter 6 is amorphous calcium carbonate (ACC), a metastable intermediate in the multistep nucleation of $CaCO_3$ (research question #3). The goal is to elucidate the link between the dynamic character of ACC and its crystallization kinetics in presence of Mg^{2+}, a thermodynamic and kinetic stabilizer among other additives and factors. By a unique combination of X-ray Photon Correlation Spectroscopy and Inelastic Incoherent Neutron Scattering, this chapter examines specifically the dynamics of hydrogen bond network and the ionic diffusivity within the solid ACC doped with various contents of Mg^{2+}.

The final chapter of the dissertation (Chapter 7) recalls the research questions and outlines the key results of the three research chapters. It also includes new hypotheses resulting from this work.

References

Addadi L., Raz S. and Weiner S. (2003) Taking advantage of disorder: Amorphous calcium carbonate and its roles in biomineralization. *Adv. Mater.* **15**, 959–970.

Aizenberg J., Addadi L., Weiner S. and Lambert G. (1996) Stabilization of amorphous calcium carbonate by specialized macromolecules in biological and synthetic precipitates. *Adv. Mater.* **8**, 222–226.

Aizenberg J., Black A. J., Whitesides G. M., Aizenberg J. and Black A. J. (1999) Control of crystal nucleation by patterned self-assembled monolayers. *Nature* **398**, 495–498.

Bailey A. I. and Kay S. M. (1967) A Direct Measurement of the Influence of Vapour, of Liquid and of Oriented Monolayers on the Interfacial Energy of Mica. *Proc. R. Soc. A Math. Phys. Eng. Sci.* **301**, 47–56.

Bailey A. I. and Price A. G. (1970) Interfacial Energies of Clean Mica and of Monomolecular Films of Fatty Acids Deposited on Mica, in Aqueous and Non-Aqueous Media. *Spec. Discuss. Faraday Soc.* **1**, 118–127.

Beniash E., Aizenberg J., Addadi L. and Weiner S. (1997) Amorphous calcium carbonate transforms into calcite during sea urchin larval spicule growth. *Proc. R. Soc. B Biol. Sci.* **264**, 461–465.

Bennema P. and Söhnel O. (1990) Interfacial surface tension for crystallization and precipitation from aqueous solutions. *J. Cryst. Growth* **102**, 547–556.

Bentov S., Weil S., Glazer L., Sagi A. and Berman A. (2010) Stabilization of amorphous calcium carbonate by phosphate rich organic matrix proteins and by single phosphoamino acids. *J. Struct. Biol.* **171**, 207–215.

Berner R. A. (1975) The role of magnesium in the crystal growth of calcite and aragonite from sea water. *Geochim. Cosmochim. Acta* **39**, 489–504.

Bischoff W. D. (1998) Dissolution Enthalpies of Magnesian Calcites. *Aquat. Geochem.* **4**, 321–336.

Bourg I. C., Lee S. S., Fenter P. and Tournassat C. (2017) Stern Layer Structure and Energetics at Mica-Water Interfaces. *J. Phys. Chem. C* **121**, 9402–9412.

Bourg I. C. and Sposito G. (2011) Molecular dynamics simulations of the electrical double layer on smectite surfaces contacting concentrated mixed electrolyte (NaCl-CaCl2) solutions. *J. Colloid Interface Sci.* **360**, 701–715.

Brown G. E. (2001) How Minerals React with Water. *Science* **294**, 67–70.

Brown G. E., Henrich V. E., Casey W. H., Clark D. L., Eggleston C., Felmy A., Goodman D. W., Grtzel M., Maciel G., Mccarthy M. I., Nealson K. H., Sverjensky D. A., Toney M. F. and Zachara J. M. (1999) Metal Oxide Surfaces and Their Interactions with Aqueous Solutions and Microbial Organisms Microbial Organisms. *Chem. Rev.* **99**, 77–174.

Bruno M., Massaro F. R., Pastero L., Costa E., Rubbo M., Prencipe M. and Aquilano D. (2013) New estimates of the free energy of calcite/water interfaces for evaluating the equilibrium shape and nucleation mechanisms. *Cryst. Growth Des.* **13**, 1170–1179.

Butkus M. A. and Grasso D. (1998) Impact of Aqueous Electrolytes on Interfacial Energy. *J. Colloid Interface Sci.* **200**, 172–181.

Cartwright J. H. E., Checa A. G., Gale J. D., Gebauer D. and Sainz-Díaz C. I. (2012) Calcium carbonate polyamorphism and its role in biomineralization: How many amorphous calcium carbonates are there? *Angew. Chemie - Int. Ed.* **51**, 11960–11970.

Christenson H. K. (1993) Adhesion and surface energy of mica in air and water. *J. Phys. Chem.* **97**, 12034–12041.

Cobourne G., Mountjoy G., Rodriguez-Blanco J. D., Benning L. G., Hannon A. C. and Plaisier J. R. (2014) Neutron and X-ray diffraction and empirical potential structure refinement modelling of magnesium stabilised amorphous calcium carbonate. *J. Non. Cryst. Solids* **401**, 154–158.

Cooper S. J., Sessions R. B. and Lubetkin S. D. (1998) A new mechanism for nucleation beneath monolayer films? *J. Am. Chem. Soc.* **120**, 2090–2098.

Damaskin B. B. and Frumkin A. N. (1974) Potentials of zero charge, interaction of metals with water and adsorption of organic substances-III. The role of the water dipoles in the structure of the dense part of the electric double layer. *Electrochim. Acta* **19**, 173–176.

Davis K. J., Dove P. M. and Yoreo J. J. De (2000) The role of Mg2+ as an impurity in calcite growth. **290**, 1134–1137.

Dazas B., Lanson B., Breu J., Robert J. L., Pelletier M. and Ferrage E. (2013) Smectite fluorination and its impact on interlayer water content and structure: A way to fine tune the hydrophilicity of clay surfaces? *Microporous Mesoporous Mater.* **181**, 233–247.

Demyanova L. P. and Tressaud A. (2009) Fluorination of alumino-silicate minerals: The example of lepidolite. *J. Fluor. Chem.* **130**, 799–805.

Dousi E., Kallitsis J., Chrissanthopoulos A., Mangood A. H. and Dalas E. (2003) Calcite overgrowth on carboxylated polymers. *J. Cryst. Growth* **253**, 496–503.

Duffy D. M. and Harding J. H. (2004) Simulation of organic monolayers as templates for the nucleation of calcite crystals. *Langmuir* **20**, 7630–7636.

Elhadj S., De Yoreo J. J., Hoyer J. R. and Dove P. M. (2006) Role of molecular charge and hydrophilicity in regulating the kinetics of crystal growth. *Proc. Natl. Acad. Sci. U. S. A.* **103**, 19237–19242.

Farhadi-Khouzani M., Chevrier D. M., Zhang P., Hedin N. and Gebauer D. (2016) Water as the Key to Proto-Aragonite Amorphous CaCO3. *Angew. Chemie - Int. Ed.* **55**, 8117–8120.

Fernandez-Martinez A., Hu Y., Lee B., Jun Y.-S. and Waychunas G. A. (2013a) In Situ Determination of Interfacial Energies between Heterogeneously Nucleated CaCO3 and Quartz Substrates: Thermodynamics of CO2 Mineral Trapping. *Environ. Sci. Technol.* **47**, 102–109.

Fernandez-Martinez A., Kalkan B., Clark S. M. and Waychunas G. a. (2013b) Pressure-induced polyamorphism and formation of “aragonitic” amorphous calcium carbonate. *Angew. Chemie -*

Int. Ed. **52**, 8354–8357.

Fernandez-Martinez A., Lopez-Martinez H. and Wang D. (2017) Structural Characteristics and the Occurrence of Polyamorphism in Amorphous Calcium Carbonate. In *New Perspectives on Mineral Nucleation and Growth: From Solution Precursors to Solid Materials* (eds. A. E. S. Van Driessche, M. Kellermeier, L. G. Benning, and D. Gebauer). Springer. pp. 77–92.

Forbes T. Z., Radha A. V. and Navrotsky A. (2011) The energetics of nanophase calcite. *Geochim. Cosmochim. Acta* **75**, 7893–7905.

Freeman C. L., Harding J. H. and Duffy D. M. (2008) Simulations of calcite crystallization on self-assembled monolayers. *Langmuir* **24**, 9607–9615.

Gal A., Habraken W., Gur D., Fratzl P., Weiner S. and Addadi L. (2013) Calcite crystal growth by a solid-state transformation of stabilized amorphous calcium carbonate nanospheres in a hydrogel. *Angew. Chemie - Int. Ed.* **52**, 4867–4870.

Gal A., Kahil K., Vidavsky N., Devol R. T., Gilbert P. U. P. A., Fratzl P., Weiner S. and Addadi L. (2014) Particle accretion mechanism underlies biological crystal growth from an amorphous precursor phase. *Adv. Funct. Mater.* **24**, 5420–5426.

Gebauer D., Gunawidjaja P. N., Ko J. Y. P., Bacsik Z., Aziz B., Liu L., Hu Y., Bergström L., Tai C.-W., Sham T.-K., Edén M. and Hedin N. (2010) Proto-calcite and proto-vaterite in amorphous calcium carbonates. *Angew. Chemie - Int. Ed.* **49**, 8889–8891.

Gebauer D., Kellermeier M., Gale J. D., Bergström L. and Cölfen H. (2014) Pre-nucleation clusters as solute precursors in crystallisation. *Chem. Soc. Rev.* **43**, 2348–2371.

Gebauer D., Völkel A., Cölfen H., Volkel A. and Colfen H. (2008) Stable prenucleation calcium carbonate clusters. *Science* **322**, 1819–1822.

Giuffre A. J., Hamm L. M., Han N., De Yoreo J. J. and Dove P. M. (2013) Polysaccharide chemistry regulates kinetics of calcite nucleation through competition of interfacial energies. *Proc. Natl. Acad. Sci. U. S. A.* **110**, 9261–9266.

Gong Y., Killian C., Olson I., Appathurai N. P., Amasino A., Martin M., Holt L., Wilt F. and Gilbert P. (2012) Phase transitions in biogenic amorphous calcium carbonate. *Proc. Natl. Acad. Sci. U. S. A.* **109**, 6088–6093.

Goodwin A. L., Michel F. M., Phillips B. L., Keen D. A., Dove M. T. and Reeder R. J. (2010) Nanoporous structure and medium-range order in synthetic amorphous calcium carbonate. *Chem. Mater.* **22**, 3197–3205.

Guillemet B., Faatz M., Gro F., Wegner G., Gnanou Y. and Berland A. P. (2006) Nanosized Amorphous Calcium Carbonate Stabilized by Poly(ethylene oxide)-b-poly(acrylic acid) Block Copolymers. *Langmuir*, 1875–1879.

Hamm L. M., Giuffre A. J., Han N., Tao J., Wang D., De Yoreo J. J. and Dove P. M. (2014) Reconciling disparate views of template-directed nucleation through measurement of calcite nucleation kinetics and binding energies. *Proc. Natl. Acad. Sci. U. S. A.* **111**, 1304–1309.

Hasse B., Ehrenberg H., Marxen J. C., Becker W. and Epple M. (2000) Calcium carbonate modifications in the mineralized shell of the freshwater snail Biomphalaria glabrata. *Chem. Eur. J.* **6**, 3679–3685.

Hu Q., Nielsen M. H., Freeman C. L., Hamm L. M., Tao J., Lee J. R. I., Han T. Y. J., Becker U., Harding J. H., Dove P. M. and De Yoreo J. J. (2012) The thermodynamics of calcite nucleation at organic interfaces: Classical vs. non-classical pathways. *Faraday Discuss.* **159**, 509–523.

Ihli J., Kim Y. Y., Noel E. H. and Meldrum F. C. (2013) The effect of additives on amorphous calcium carbonate (ACC): Janus behavior in solution and the solid state. *Adv. Funct. Mater.* **23**, 1575–1585.

Ihli J., Wong W. C., Noel E. H., Kim Y.-Y., Kulak A. N., Christenson H. K., Duer M. J. and Meldrum F. C. (2014) Dehydration and crystallization of amorphous calcium carbonate in solution and in air. *Nat. Commun.* **5**.

Janecek J. and Netz R. R. (2007) Interfacial Water at Hydrophobic and Hydrophilic Surfaces: Depletion versus Adsorption. *Langmuir* **23**, 8417–8429.

Kim Y. Y., Douglas E. P. and Gower L. B. (2007) Patterning inorganic (CaCO3) thin films via a polymer-induced liquid-precursor process. *Langmuir* **23**, 4862–4870.

de Leeuw N. H. and Parker S. C. (1998) Surface Structure and Morphology of Calcium Carbonate Polymorphs Calcite, Aragonite, and Vaterite: An Atomistic Approach. *J. Phys. Chem. B* **102**, 2914–2922.

Levi-Kalisman Y., Raz S., Weiner S., Addadi L. and Sagi I. (2002) Structural Differences Between Biogenic Amorphous Calcium Carbonate Phases Using X-ray Absorption Spectroscopy. *Adv. Funct. Mater.* **12**, 43–48.

Li Q., Fernandez-Martinez A., Lee B., Waychunas G. A. and Jun Y. S. (2014) Interfacial energies for heterogeneous nucleation of calcium carbonate on mica and quartz. *Environ. Sci. Technol.* **48**, 5745–5753.

Lippmann F. (1973) Crystal Chemistry of Sedimentary Carbonate Minerals. In *Sedimentary Carbonate Minerals. Minerals, Rocks and Inorganic Materials (Monograph Series of Theoretical and Experimental Studies), vol. 6.* Springer, Berlin, Heidelberg. pp. 5–96.

Loste E., Park R. J., Warren J. and Meldrum F. C. (2004) Precipitation of calcium carbonate in confinement. *Adv. Funct. Mater.* **14**, 1211–1220.

Loste E., Wilson R. M., Seshadri R. and Meldrum F. C. (2003) The role of magnesium in stabilising amorphous calcium carbonate and controlling calcite morphologies. *J. Cryst. Growth* **254**, 206–218.

Maccarini M., Steitz R., Himmelhaus M., Fick J., Tatur S., Wolff M., Grunze M., Janecek J. and Netz R. R. (2007) Density depletion at solid-liquid interfaces: A neutron reflectivity study. *Langmuir* **23**, 598–608.

Manoli F. and Dalas E. (2000) Spontaneous precipitation of calcium carbonate in the presence of ethanol, isopropanol and diethylene glycol. *J. Cryst. Growth* **218**, 359–364.

Marxen J. C., Becker W., Finke D., Hasse B. and Epple M. (2003) EARLY MINERALIZATION IN BIOMPHALARIA GLABRATA: MICROSCOPIC AND STRUCTURAL RESULTS. *J. Moll. Stud.* **69**, 113–121.

Michel F. M., MacDonald J., Feng J., Phillips B. L., Ehm L., Tarabrella C., Parise J. B. and Reeder R. J. (2008) Structural characteristics of synthetic amorphous calcium carbonate. *Chem. Mater.* **20**, 4720–4728.

Michot L. J., Villieras F., Francois M., Yvon J., Le Dred R. and Cases J. M. (1994) The Structural Microscopic Hydrophilicity of Talc. *Langmuir* **10**, 3765–3773.

Nassif N., Gehrke N., Pinna N., Shirshova N., Tauer K., Antonietti M. and Cölfen H. (2005) Synthesis of stable aragonite superstructures by a biomimetic crystallization pathway. *Angew. Chemie - Int. Ed.* **44**, 6004–6009.

Navrotsky A. (2004) Energetic clues to pathways to biomineralization: precursors, clusters, and nanoparticles. *Proc. Natl. Acad. Sci. U. S. A.* **101**, 12096–12101.

Nebel H., Neumann M., Mayer C. and Epple M. (2008) On the Structure of Amorphous Calcium CarbonatesA Detailed Study by Solid-State NMR Spectroscopy. *Inorg. Chem.* **47**, 7874–7879.

Neumann M. and Epple M. (2007) Monohydrocalcite and its relationship to hydrated amorphous calcium carbonate in biominerals. *Eur. J. Inorg. Chem.*, 1953–1957.

Nielsen M. H., Aloni S. and De Yoreo J. J. (2014) In situ TEM imaging of CaCO3 nucleation reveals coexistence of direct and indirect pathways. *Science* **345**, 1158–1162.

Papin Ä., Sergent J. and Robert J. (1997) Intersite OH-F distribution in an Al-rieh synthetie phlogopite. *Eur. J. Mineral.* **9**, 501–508.

Park S.-H. and Sposito G. (2002) Structure of Water Adsorbed on a Mica Surface. *Phys. Rev. Lett.* **89**, 85501.

Pashley R. M. (1981) DLVO and hydration forces between mica surfaces in Li+, Na+, K+, and Cs+ electrolyte solutions: A correlation of double-layer and hydration forces with surface cation exchange properties. *J. Colloid Interface Sci.* **83**, 531–546.

Petersen E. U., Essene E. J., Peacor D. R. and Valley J. W. (1982) Fluorine end-member micas and amphiboles. *Am. Mineral.* **67**, 538–544.

Pimentel C., Pina C. M. and Gnecco E. (2013) Epitaxial growth of calcite crystals on dolomite and kutnahorite (104) surfaces. *Cryst. Growth Des.* **13**, 2557–2563.

Politi Y., Arad T., Klein E., Weiner S. and Addadi L. (2004) Sea Urchin Spine Calcite Forms via a Transient Amorphous Calcium Carbonate Phase. *Science* **306**, 1161–1164.

Politi Y., Batchelor D. R., Zaslansky P., Chmelka B. F., Weaver J. C., Sagi I., Weiner S. and Addadi L. (2010) Role of magnesium ion in the stabilization of biogenic amorphous calcium carbonate: A structure-function investigation. *Chem. Mater.* **22**, 161–166.

Politi Y., Levi-Kalisman Y., Raz S., Wilt F., Addadi L., Weiner S. and Sagi I. (2006) Structural characterization of the transient amorphous calcium carbonate precursor phase in sea urchin embryos. *Adv. Funct. Mater.* **16**, 1289–1298.

Politi Y., Metzler R. A., Abrecht M., Gilbert B., Wilt F. H., Sagi I., Addadi L., Weiner S. and Gilbert P. U. P. A. (2008) Transformation mechanism of amorphous calcium carbonate into calcite in the sea urchin larval spicule. *Proc. Natl. Acad. Sci. U. S. A.* **105**, 17362–17366.

Pouget E. M., Bomans P. H., Goos J. A., Frederik P. M. and Sommerdijk N. A. (2009) The Initial Stages of Template-Controlled CaCO3 Formation Revealed by Cryo-TEM. *Science* **323**, 1455–1458.

Poynor A., Hong L., Robinson I. K., Granick S., Zhang Z. and Fenter P. A. (2006) How Water Meets a Hydrophobic Surface. *Phys. Rev. Lett.* **97**, 266101–266104.

Pratt L. R. and Pohorille A. (2002) Hydrophobic Effects and Modeling of Biophysical Aqueous Solution Interfaces Hydrophobic Effects and Modeling of Biophysical Aqueous Solution Interfaces. *Chem. Rev.* **102**, 2671–2692.

Prieto M. (2014) Nucleation and supersaturation in porous media (revisited). *Mineral. Mag.* **78**, 1437–1447.

Purgstaller B., Mavromatis V., Immenhauser A. and Dietzel M. (2016) Transformation of Mg-bearing amorphous calcium carbonate to Mg-calcite - In situ monitoring. *Geochim. Cosmochim. Acta* **174**, 180–195.

Radha A. V., Fernandez-Martinez A., Hu Y., Jun Y.-S., Waychunas G. A. and Navrotsky A. (2012) Energetic and structural studies of amorphous Ca1−xMgxCO3·nH2O (0⩽x⩽1). *Geochim. Cosmochim. Acta* **90**, 83–95.

Radha A. V and Navrotsky A. (2015) Direct Experimental Measurement of Water Interaction Energetics in Amorphous Carbonates MCO3 (M = Ca, Mn, and Mg) and Implications for Carbonate Crystal Growth. *Cryst. Growth Des.* **15**, 70–78.

Raiteri P., Demichelis R. and Gale J. D. (2015) Thermodynamically Consistent Force Field for Molecular Dynamics Simulations of Alkaline-Earth Carbonates and Their Aqueous Speciation. *J. Phys. Chem. C* **119**, 24447–24458.

Raiteri P. and Gale J. D. (2010) Water is the key to nonclassical nucleation of amorphous calcium carbonate. *J. Am. Chem. Soc.* **132**, 17623–17634.

Raz S., Hamilton P. C., Wilt F. H., Weiner S. and Addadi L. (2003) The transient phase of amorphous calcium carbonate in sea urchin larval spicules: The involvement of proteins and magnesium ions in its formation and stabilization. *Adv. Funct. Mater.* **13**, 480–486.

Reeder R. J., Tang Y., Schmidt M. P., Kubista L. M., Cowan D. F. and Phillips B. L. (2013) Characterization of Structure in Biogenic Amorphous Calcium Carbonate: Pair Distribution Function and Nuclear Magnetic Resonance Studies of Lobster Gastrolith. *Cryst. Growth Des.* **13**, 1905–1914.

Robert J.-L., Beny J.-M., Della Ventura G. and Hardy M. (1993) Fluorine in micas: Crystal-chemical control of the OH-F distribution between trioctahedral and dioctahedral sites. *Eur. J. Mineral.* **5**, 7–18.

Robert J. L., Della Ventura G. and Hawthorne F. C. (1999) Near-infrared study of short-range disorder of OH and F in monoclinic amphiboles. *Am. Mineral.* **84**, 86–91.

Rodriguez-Blanco J. D., Shaw S., Bots P., Roncal-Herrero T. and Benning L. G. (2012) The role of pH and Mg on the stability and crystallization of amorphous calcium carbonate. *J. Alloys Compd.* **536**, S477–S479.

Rotenberg B., Patel A. J. and Chandler D. (2011) Molecular explanation for why talc surfaces can be both hydrophilic and hydrophobic. *J. Am. Chem. Soc.* **133**, 20521–20527.

Saharay M., Yazaydin A. O. and Kirkpatrick R. J. (2013) Dehydration-induced amorphous phases of calcium carbonate. *J. Phys. Chem. B* **117**, 3328–3336.

Sakuma H. and Kawamura K. (2011) Structure and dynamics of water on Li+-, Na+-, K+-, Cs+-, H3O+-exchanged muscovite surfaces: A molecular dynamics study. *Geochim. Cosmochim. Acta* **75**, 63–81.

Scatena L. F., Brown M. G. and Richmond G. L. (2001) Water at Hydrophobic Surfaces: Weak Hydrogen Bonding and Strong Orientation Effects. *Science* **292**, 908–912.

Schmidt M. P., Ilott A. J., Phillips B. L. and Reeder R. J. (2014) Structural Changes upon Dehydration of Amorphous Calcium Carbonate. *Cryst. Growth Des.* **14**, 938–951.

Schwnedel D., Hayashi T., Dahint R., Pertsin A., Grunze M., Steitz R. and Shchreiber F. (2003) Interaction of watr with slef-assembled monolayers: Neutron reflectivity measurements of the water density in the interface region. *Langmuir* **19**, 2284–2293.

Seto J., Zhang Y., Hamilton P. and Wilt F. (2004) The localization of occluded matrix proteins in calcareous spicules of sea urchin larvae. *J. Struct. Biol.* **148**, 123–130.

Shechter A., Glazer L., Cheled S., Mor E., Weil S., Berman A., Bentov S., Aflalo E. D., Khalaila I. and Sagi A. (2008) A gastrolith protein serving a dual role in the formation of an amorphous mineral containing extracellular matrix. *Proc. Natl. Acad. Sci. U. S. A.* **105**, 7129–7134.

Singer J. W., Yazaydin A. Ö., Kirkpatrick R. J. and Bowers G. M. (2012) Structure and Transformation of Amorphous Calcium Carbonate: A Solid-State 43Ca NMR and Computational Molecular Dynamics Investigation. *Chem. Mater.* **24**, 1828–1836.

Söhnel O. and Mullin J. W. (1978) A method for the determination of precipitation induction periods. *J. Cryst. Growth* **44**, 377–382.

Söhnel O. and Mullin J. W. (1982) Precipitation of calcium carbonate. *J. Cryst. Growth* **60**, 239–250.

Sposito G. (2004) *The Surface Chemistry of Natural Particles*., Oxford University Press.

Steitz R., Gutberlet T., Hauss T., Klösgen B., Krastev R., Schemmel S., Simonsen A. C. and Findenegg G. H. (2003) Nanobubbles and their precursor layer at the interface of water against a hydrophobic substrate. *Langmuir* **19**, 2409–2418.

Stephens C. J., Ladden S. F., Meldrum F. C. and Christenson H. K. (2010) Amorphous calcium carbonate is stabilized in confinement. *Adv. Funct. Mater.* **20**, 2108–2115.

Stephenson A. E., DeYoreo J. J., Wu L., Wu K. J., Hoyer J. and Dove P. M. (2008) Peptides enhance magnesium signature in calcite: insights into origins of vital effects. *Science* **322**, 724–727.

Stillinger F. H. (1973) Structure in Aqueous Solutions of Nonpolar Molecules from the Standpoint of Scaled-Particle Theory. *J. Sol. Chem.* **2**, 141–158.

Tester C. C., Whittaker M. L. and Joester D. (2014) Controlling nucleation in giant liposomes. *Chem. Commun.* **50**, 5619–5622.

Tobler D. J., Blanco J. D. R., Dideriksen K., Sand K. K., Bovet N., Benning L. G. and Stipp S. L. S. (2014) The Effect of Aspartic Acid and Glycine on Amorphous Calcium Carbonate (ACC) Structure, Stability and Crystallization. *Procedia Earth Planet. Sci.* **10**, 143–148.

Tobler D. J., Rodriguez-Blanco J. D., Dideriksen K., Bovet N., Sand K. K. and Stipp S. L. S. (2015) Citrate effects on amorphous calcium carbonate (ACC) structure, stability, and crystallization. *Adv. Funct. Mater.* **25**, 3081–3090.

Urry L. A., Hamilton P. C., Killian C. E. and Wilt F. H. (2000) Expression of spicule matrix proteins in the sea urchin embryo during normal and experimentally altered spiculogenesis. *Dev. Biol.* **225**, 201–213.

Wallace A. F., Hedges L. O., Fernandez-Martinez A., Raiteri P., Gale J. D., Waychunas G. A., Whitelam S., Banfield J. F. and De Yoreo J. J. (2013) Microscopic evidence for liquid-liquid separation in supersaturated CaCO3 solutions. *Science* **341**, 885–889.

Wang D., Hamm L. M., Giuffre A. J., Echigo T., Rimstidt J. D., Yoreo J. J. De, Grotzinger J. and Dove P. M. (2012) Revisiting geochemical controls on patterns of carbonate deposition through the lens of multiple pathways to mineralization. *Faraday Discuss.* **159**, 371–386.

Wang D., Wallace A. F., De Yoreo J. J. and Dove P. M. (2009) Carboxylated molecules regulate magnesium content of amorphous calcium carbonates during calcification. *Proc. Natl. Acad. Sci. U. S. A.* **106**, 21511–21516.

Wang J., Kalinichev A. G. and Kirkpatrick R. J. (2009) Asymmetrie hydrogen bonding and orientational ordering of water at hydrophobic and hydrophilic surfaces: A comparison of water/vapor, water/talc, and water/mica interfaces. *J. Phys. Chem. C* **113**, 11077–11085.

Wang J., Kalinichev A. G. and Kirkpatrick R. J. (2006) Effects of substrate structure and composition on the structure, dynamics, and energetics of water at mineral surfaces: A molecular dynamics modeling study. *Geochim. Cosmochim. Acta* **70**, 562–582.

Wang J., Kalinichev A. G., Kirkpatrick R. J. and Cygan R. T. (2005) Structure, energetics, and dynamics of water adsorbed on the muscovite (001) surface: a molecular dynamics simulation. *J. Phys. Chem. B* **109**, 15893–15905.

Wang Y. W., Christenson H. K. and Meldrum F. C. (2014) Confinement increases the lifetimes of hydroxyapatite precursors. *Chem. Mater.* **26**, 5830–5838.

Wedepohl K. H. ed. (1978) *Handbook of Geochemistry: Vol. II/1.*, Springer-Verlag.

Weiner S., Levi-Kalisman Y., Raz S. and Addadi L. (2003) Biologically formed amorphous calcium carbonate. *Connect. Tissue Res.* **44**, 214–218.

Weiss I. M., Tuross N., Addadi L. and Weiner S. (2002) Mollusc larval shell formation: Amorphous calcium carbonate is a precursor phase for aragonite. *J. Exp. Zool.* **293**, 478–491.

Whittaker M. L., Dove P. M. and Joester D. (2016) Nucleation on surfaces and in confinement. *MRS Bull.* **41**, 388–392.

Wolf S. E., Leiterer J., Kappl M., Emmerling F. and Tremel W. (2008) Early homogenous amorphous precursor stages of calcium carbonate and subsequent crystal growth in levitated droplets. *J. Am. Chem. Soc.* **130**, 12342–12347.

Xu J., Yan C., Zhang F., Konishi H., Xu H. and Teng H. H. (2013) Testing the cation-hydration effect on the crystallization of Ca-Mg-CO3 systems. *Proc. Natl. Acad. Sci. U. S. A.* **110**, 17750–17755.

Xu X., Han J. T. and Cho K. (2004) Formation of Amorphous Calcium Carbonate Thin Films and Their Role in Biomineralization. *Chem. Mater.* **16**, 1740–1746.

Zou Z., Bertinetti L., Politi Y., Jensen A. C. S., Weiner S., Addadi L., Fratzl P. and Habraken W. J. E. M. (2015) Opposite Particle Size Effect on Amorphous Calcium Carbonate Crystallization in Water and during Heating in Air. *Chem. Mater.* **27**, 4237–4246.

Chapter 3

Fundamentals: experimental and theoretical methods

This chapter aims at providing a brief summary of the theory and application of both the experimental and theoretical techniques that play a major role in the subsequent research chapters. The experimental techniques described here include X-ray Photon Correlation Spectroscopy (XPCS), Near-Ambient Pressure X-ray Photoelectron Spectroscopy (NAP-XPS), Grazing-incidence Small Angle X-ray Spectroscopy (GISAXS) and Inelastic Incoherent Neutron Scattering (IINS). The theoretical approaches include Molecular Dynamics (MD) simulations and Bond-Valence analysis.

3.1. X-ray Photon Correlation Spectroscopy (XPCS)

XPCS has been recently developed as an extension to the dynamical light scattering (DLS), taking advantages of the short wavelengths of X-rays to probe dynamics at the atomic and nanoscale, with negligible multiple-scattering (Hippert et al., 2006). Since its introduction, XPCS has played an important role in establishing a relationship between the kinetics and the structure of systems out of equilibrium. The following paragraphs provide the most fundamental information needed to interpret the data from a user's point of view. For a more complete theoretical description of the XPCS technique, useful resources are available in the literature (Dierker et al., 1995; Stephenson et al., 2009; Madsen et al., 2015).

Coherent light scattered from a disordered system gives rise to a random diffraction or 'speckle' pattern. This is well illustrated with the example of the double slit experiment. A coherent source gives rise to an interference pattern where fringes are present under the Gaussian envelope. As the coherence of the beam is decreased, more incoherent 'background' is observed (Fig. 3.1). The interference pattern resulting from the sum of such scattered waves, even with a random set of phases, corresponds to the exact spatial arrangement of the particles in the system under study. Therefore, if the particle positions were to fluctuate, so does the speckle pattern.

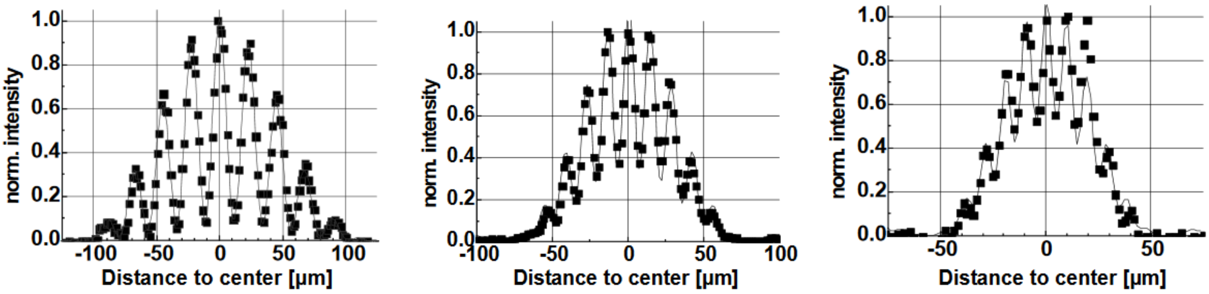

Figure 3.1. Example of interference fringe pattern obtained from a double pinhole at three different X-ray energies, from left to right: 6 keV, 10 keV and 14 keV. A higher degree of incoherence is observed at higher energy. The extrapolation for a 100% incoherent source would be a Gaussian, with no fringes. (Leitenberger et al., 2003)

Let us consider a coherent beam of cross section ξ^2 and incident wave vector $\boldsymbol{k}$, scattered with outgoing wave vector $\boldsymbol{k'}$ from a disordered sample. The instantaneous intensity at a given point in the far field can be written as the square of a total field $E(\boldsymbol{Q}, t)$:

$$I(\boldsymbol{Q},t) = |E(\boldsymbol{Q},t)|^2 = \left|\sum_n \exp[i\boldsymbol{Q}\cdot\boldsymbol{r}_n(t)]f_n(\boldsymbol{Q})\right|^2 \tag{3.1}$$

Here, $f_n(\boldsymbol{Q})$ is the scattering amplitude of the n-th scatterer located at position $\boldsymbol{r}_n(t)$, and $\boldsymbol{Q} = \boldsymbol{k'} - \boldsymbol{k}$ is the momentum transfer. The sum is taken over scatterers in the coherence volume, spanned by the transverse and longitudinal coherence lengths, and the beam is assumed to be fully coherent. For clarity we omit the Lorentz factor and the Thomson scattering length r_0^2 in eq. (3.1). A measurement of the intensity will naturally be a time average $<I(\boldsymbol{Q}, t)>_T$ taken over the acquisition time T. However, it does not involve any statistical ensemble average. If the system is non-ergodic, i.e., it has static random disorder, $<I(\boldsymbol{Q}, t)>_T$ will display, as a function of $\boldsymbol{Q}$, distinct and sharp (angular size λ/ξ) variations in intensity, known as ‘speckles’. If, on the other hand, the system is ergodic with fluctuation timescales that are much shorter than the counting time, the measured time average is equivalent to an ensemble average and $<I(\boldsymbol{Q}, t)>_T$ can be replaced by the usual ensemble average, denoted by $<I(\boldsymbol{Q}, t)>$. It is to note that the use of 2D detectors is indispensable, which makes it possible to probe such fluctuations at a given time in a statistical way, in particular for non-ergodic systems such as glasses that undergo ageing phenomena. The statistics are made over all the speckles collected in the detector, at each given time t, or during a short time interval Δt during which the ageing is not significant (Ruta et al., 2014).

In real space, such dynamical processes are explained by the van Hove distribution function which defines the probability of finding a particle at position $\boldsymbol{r}$ at time t, given that there was a particle (itself or another) at the origin at time $t = 0$:

$$G(\boldsymbol{r},t) = \frac{1}{N}\langle\sum_{i=1}^{N}\sum_{j=1}^{N}\delta\left(\boldsymbol{r}+\boldsymbol{r_j}(0)-\boldsymbol{r_i}(t)\right)\rangle \tag{3.2}$$

where < > denotes an ensemble average, δ( ) is the three-dimensional Dirac delta function, and $\boldsymbol{r}_i(t)$ is the time dependent position coordinates for a set of N particles with $i = 1,\ldots,N$. $G(\boldsymbol{r}, t)$ can be divided into two parts called 'self' $G_s(\boldsymbol{r}, t)$ when $i = j$ and 'distinct' $G_d(\boldsymbol{r}, t)$ when $i \neq j$:

$$\begin{aligned} G(\boldsymbol{r},t) &= G_s(\boldsymbol{r},t) + G_d(\boldsymbol{r},t) \\ &= \frac{1}{N}\langle\sum_{i=1}^{N}\delta(\boldsymbol{r}+\boldsymbol{r_i}(0)-\boldsymbol{r_i}(t))\rangle + \frac{1}{N}\langle\sum_{i\neq j}^{N}\delta(\boldsymbol{r}+\boldsymbol{r_j}(0)-\boldsymbol{r_i}(t))\ \rangle \end{aligned} \tag{3.3}$$

The former describes the average motion of the particle located initially at the origin at time $t = 0$, while the latter describes the relative motions of the remaining $N – 1$ particles. Note that by XPCS, unlike incoherent scattering techniques that measure the self-part only, one measures $G(\boldsymbol{r}, t)$, the probability that *any atom* is found at position $\boldsymbol{r}$ at time t, provided that an atom was at $\boldsymbol{r} = 0$ (origin) at $t = 0$.

As already mentioned, if the spatial arrangement of the scatterers changes with time, the corresponding speckle pattern will also change, thus a measurement of the intensity fluctuations of the speckles can reveal the dynamics of the system. The measurement of temporal intensity correlations by X-ray photon correlation spectroscopy is identical in nature to a photon correlation spectroscopy (PCS or Dynamic Light Scattering, DLS) experiments that employ visible coherent light, commonly found in many laboratories. Temporal correlations can be quantified with the help of the normalized intensity correlation function $g(\boldsymbol{Q}, t)$. If the system is ergodic the (time averaged) intensity correlation function can be written in terms of the (ensemble averaged) time correlation functions of the scattered field.

As illustrated in Figure 3.2, time-resolved speckle patterns, collected on a 2D detector, provides the intensity fluctuations $I(\boldsymbol{Q}, t)$ at a given $\boldsymbol{Q}$, containing the information on the dynamics of structural rearrangements. This is evaluated by computing intensity autocorrelation function:

$$g^{(2)}(\Delta t,\boldsymbol{Q}) = \frac{< I(t,\boldsymbol{Q})I(t+\Delta t,\boldsymbol{Q}) >}{< I(t,\boldsymbol{Q}) >^2} \tag{3.4}$$

where <…> denotes the ensemble average (circular average in this case) at a given $\boldsymbol{Q}$. $g^{(2)}$ is related to density fluctuation by:

$$g^{(2)}(\Delta t, \boldsymbol{Q}) = 1 + c|f(\boldsymbol{Q}, \Delta t)|^2 \tag{3.5}$$

where $f(\boldsymbol{Q}, \Delta t) = \int G(\boldsymbol{r}, \Delta t)e^{-\boldsymbol{q}\boldsymbol{r}}d\boldsymbol{r}$ is the intermediate structure factor (density autocorrelation function), dynamical counterpart of static structure factor $S(\boldsymbol{Q})$, and c is a setup-dependent, coherence factor. Note that the function $f(\boldsymbol{Q}, \Delta t)$ itself is also the Fourier transform (FT) of the van Hove correlation function (eq. 3.2) in the spatial domain. To extract dynamical information, $g^{(2)}$ is fitted by the Kohlrausch–Williams–Watts (KWW) model at a given $\boldsymbol{Q}$:

$$g^{(2)}(\Delta t) \ = \ 1 \ + \ c * \exp(-2 * \left(\frac{\Delta t}{\tau}\right)\beta) \tag{3.6}$$

where τ is the relaxation (structural rearrangement) time and β is the decay shape factor (Madsen et al., 2015).

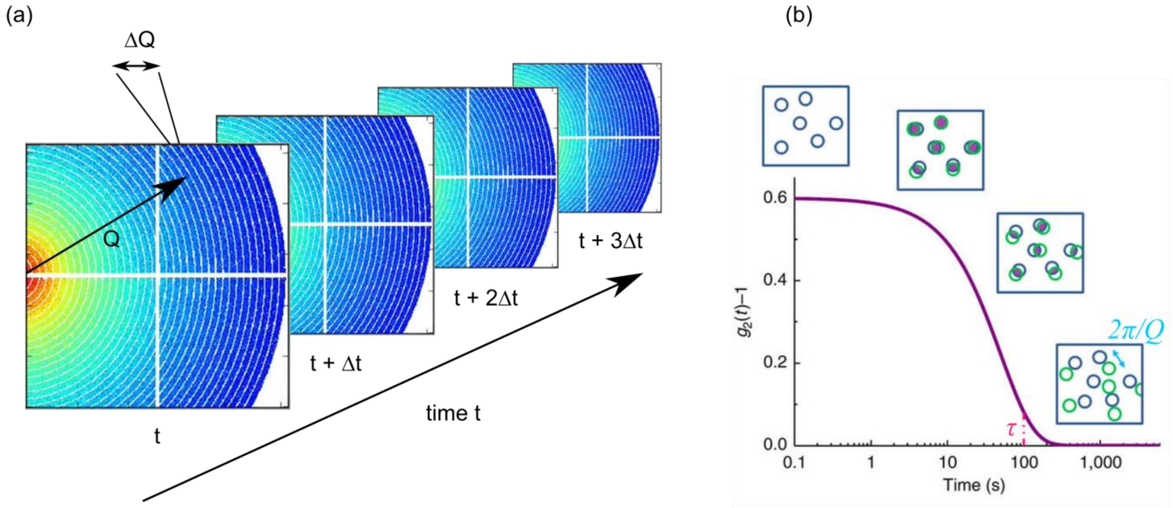

Figure 3.2. Schematic illustrations of XPCS measurement and data analysis. **(a)** Time-resolved 2D speckle patterns, from which intensity autocorrelation functions are computed for a given Q by circularly averaging within width ΔQ. **(b)** Schematic illustration of intensity autocorrelation function $g_2(Q, t)$ and structural relaxation where blue and green circles are the initial and the final states, respectively, of a system under study. (Adapted ftom Giordano and Ruta, 2016)

3.2. Near-Ambient Pressure X-ray Photoelectron Spectroscopy (NAP-XPS)

3.2.1. Electronic structure of atoms

The discovery of the photoelectric effect and related observations indicated that electromagnetic radiation is adsorbed or emitted at certain wavenumbers, implying that only certain energy states are permitted (Einstein, 1905). A detailed view of atomic structure and energy levels was provided by the introduction of quantum mechanics dealing with the Schrödinger equation:

$$E\psi = -\frac{\hbar^2}{2m}\nabla^2 + V\psi \tag{3.7}$$

where ψ is the wavefunction for a wave-like particle of mass m in a three-dimensional system with energy E, $\hbar = h/2\pi$ with Planck constant h, and ∇^2 Laplacian operator $\partial^2/(\partial x)^2 + \partial^2/(\partial y)^2 + \partial^2/(\partial z)^2$. A wavefunction ψ is a quantum analogue to the electron trajectories demonstrated in classical physics, and it contains internal dynamics and motions of the electrons relative to the nucleus. The process of solving the Schrodinger equation by a number of constraints and boundary conditions which must be satisfied to obtain the solution appropriate to the physical situation, gives rise to quantum numbers. Principal quantum number (n = 1, 2, 3 …) determines the energy level of electrons belonging to the same shell (K, L, M …, respectively). The energy level increases as n increases. Angular momentum quantum number (l = 0, 1, 2, …, n - 1) determines the subshell (s, p, d …, respectively), or the shape of the volume of space occupied by electrons, within the same shell with the same value of n (Dirac, 1981). Figure 3.3 schematically represents electron shells and subshells.

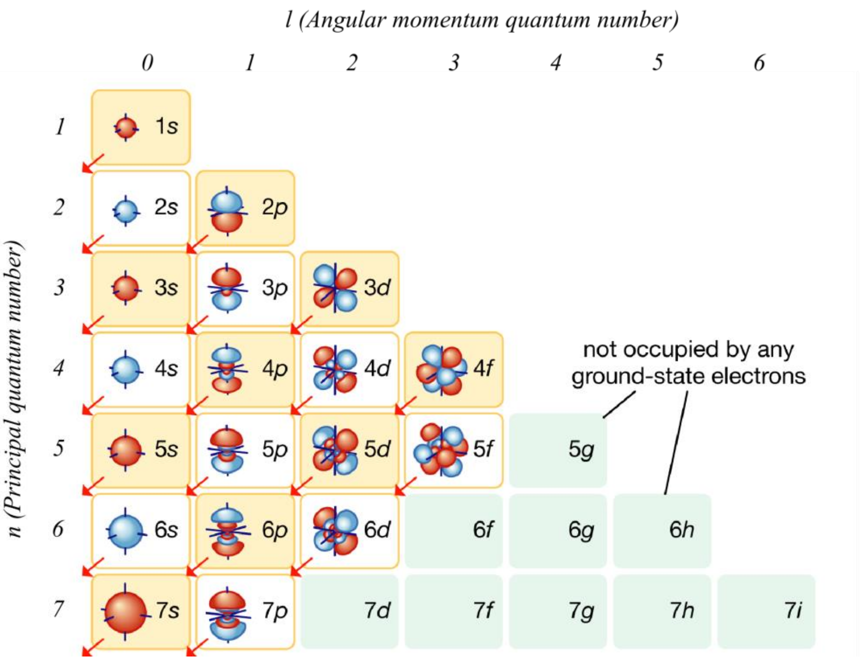

Figure 3.3. Electron shells and subshells representation. Red arrows indicate the semi-irregular order of filling. (Adapted from Encyclopedia Britannica, Inc., 2012)

Relative orientation and the resulting interaction between the spin magnetic moment of the electron (±½) and the magnetic field arising from the orbital angular momentum can give rise to the splitting the energy levels (spin-orbit coupling) (Fig. 3.4). An example of this is the splitting of 2*p* (l = 1) orbital into $2p_{3/2}$ and $2p_{1/2}$ energy levels with the total angular momentum (vector sum of its orbital and spin momenta) $j = l + ½$ and $l – ½$, respectively. This splitting can be observed when $l > 1$ (*p*, *d*, *f* …) and low-*j* level lies below high-*j* level in energy.

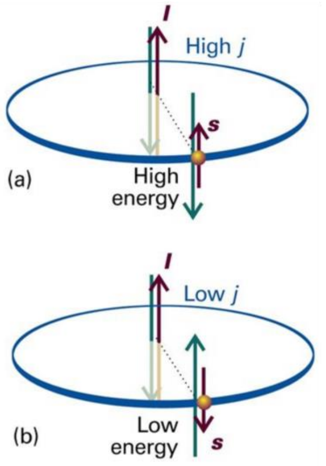

subshell	*j*		area ratio
s	1/2		-
p	1/2	3/2	1:2
d	3/2	5/2	2:3
f	5/2	7/2	3:4

Figure 3.4. Spin-orbit coupling as a result of magnetic interaction between spin and orbital magnetic moments (*s* and *l*, respectively). The total angular momentum *j* is the vector sum of *s* and *l*, and is high when the two angular momenta are close to parallel **(a)** and is low when opposed **(b)**. (Adapted from Atkins and de Paula, 2014)

3.2.2. General principles

Derivative of photoelectric effect, X-ray Photoelectron Spectroscopy (XPS) measures the kinetic energy of outgoing photoelectron upon core ionization by X-ray radiation (Atkins and de Paula, 2014). Due to the extremely short elastic mean free path of electrons travelling through condensed matter, XPS provides information exclusively from the top few atomic layers (up to ~10 nm). Because energy is conserved, the energy of the incoming photon hv must be equal to the sum of the binding energy BE of the sample and the kinetic energy of the photoelectron:

$$h\nu = \frac{1}{2}m_e v^2 + \text{BE}\ (+\ \phi) \tag{3.8}$$

where ϕ is the work function of the sample. Knowing the frequency v of the incident photon, and the measured kinetic energy of the outgoing photoelectron, the BE can be deduced. BE is specific not only to element but also sensitive to chemical state of element, electronic structure and band structure (Fig. 3.5a). A photoelectron spectrometer consists of a photon source, an electrostatic analyzer and an electron detector (Fig. 3.5b). The different kinetic energies of the photoelectrons can be detected due to the deflection of the electron path caused by the charged plates of the analyzer which is dependent of the electron speed (thus kinetic energy). XPS can be performed using either laboratory X-ray sources (Mg or Al anode) or synchrotron X-ray radiation. The latter source has an advantage of high photon flux, flexibility of X-ray energy and polarizability.

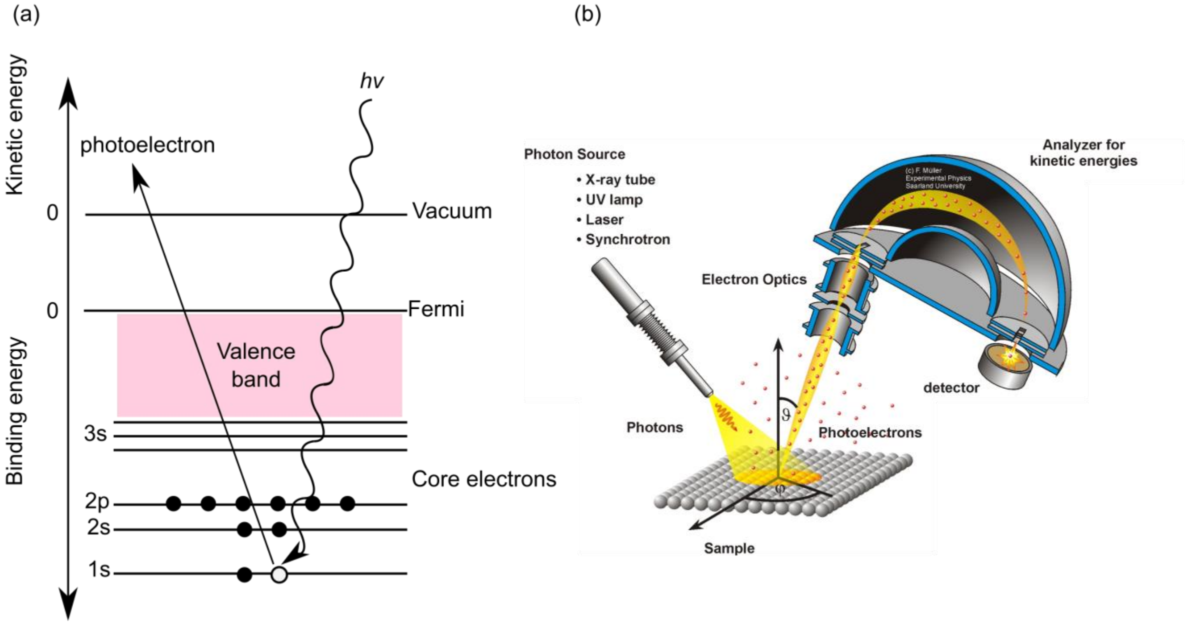

Figure 3.5. Schematic illustrations of XPS measurements. **(a)** Energy levels from core electrons, valence band, Fermi to vacuum (free electron). **(b)** Schematic representation of a photoelectron spectrometer. (© F. Müller, Saarlandes University)

3.2.3. Near-Ambient Pressure X-ray Photoelectron Spectroscopy and its application

Near-Ambient Pressure X-ray Photoelectron Spectroscopy (NAP-XPS) allows performing XPS measurements at ambient pressures (Salmeron and Schlögl, 2008). The greatest technical challenge at elevated pressure is the scattering of electrons by gas molecules which attenuates the photoelectron signal. This has been overcome by the development of differential pumping technique. The spectroscopy chamber at ambient pressure is separated from the analyzer at ultra-high vacuum ($< 10^{-10}$ mbar, UHV) through differentially pumped lens system, in which the electrons are focused onto the apertures between the pumping stages, thus increasing the transmission of electrons (Fig. 3.6).

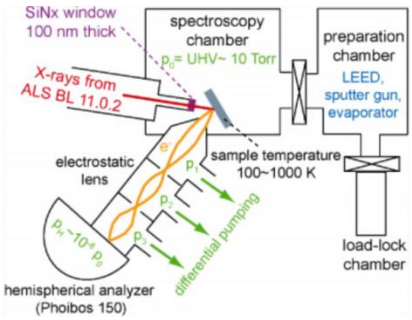

Figure 3.6. Schematic illustration of the ambient pressure XPS spectrometer at ALS beamline 11.0.2. (Yamamoto et al., 2008)

The development of NAP-XPS has widened the scope of applications, ranging from industrial catalysis to environmental science, involving various surfaces in presence of gases and vapors. Under conventional XPS in UHV, such interfacial studies with adsorbed molecules have been performed by cooling the samples to cryogenic temperatures. The plausibility of such interfaces, however, remained unclear regarding whether they represent an equilibrium structure or kinetically-trapped metastable structure. Examples of recent studies beneficiating from NAP-XPS are: adsorption of water films on metal and mineral surfaces, water structure of ice through melting transition, and redox chemistry of various oxide surfaces (Salmeron and Schlögl, 2008).

3.3. Grazing-incidence Small Angle X-ray Scattering

3.3.1. General principles

Grazing-incidence Small Angle X-ray Scattering (GISAXS) combines the grazing incidence diffraction (X-ray reflectivity) and the classical small angle scattering (SAXS) (Renaud et al., 2003). As shown in Figure 3.7, the advantages of the grazing incidence geometry reside in the scattering information obtained independently for both *xy*-direction (along the interface) and *z*-direction (normal to the interface). The incoming and exiting wave vectors ($\boldsymbol{k}_i$ and $\boldsymbol{k}_f$) form the incident and reflected beam angles (α_i and α_f) along the out-of-plane direction and the scattered angle (2θ) along the in-plane direction. The corresponding momentum transfer $\boldsymbol{q}_x$, $\boldsymbol{q}_y$ and $\boldsymbol{q}_z$ are therefore defined as:

$$\begin{aligned} \boldsymbol{q}_x &= k_0\left[\cos(\alpha_f)\cos(2\theta) - \cos(\alpha_i)\right] \\ \boldsymbol{q}_y &= k_0\left[\sin(2\theta)\cos(\alpha_f)\right] \\ \boldsymbol{q}_z &= k_0\left[\sin(\alpha_f) \pm \sin(\alpha_i)\right] \end{aligned} \tag{3.9}$$

where $k_0 = 2\pi/\lambda$.

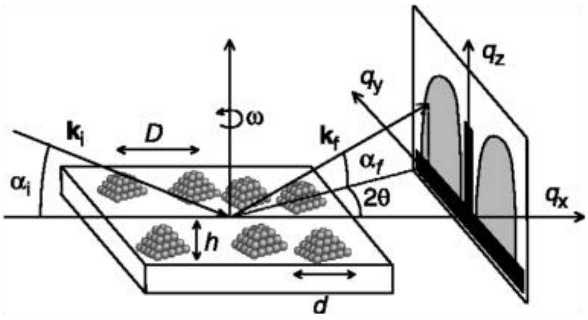

Figure 3.7. Schematic representation of GISAXS in real- and reciprocal-space geometry. Respectively, k_i and k_f are the incident and the scattered wave vectors, α_i and α_f are the incidence and reflected beam angles along the out-of-plane and 2θ is the scattered angle along the in-plane direction. (Renaud et al., 2003)

Similarly to SAXS, the GISAXS intensity is related primary to heterogeneities of the electron density within the sample (Guinier, 1963). In the two-media approximation, this is called “contrast” between particles of density ρ_1 embedded in a matrix (ex. solution) of density ρ_2:

$$\Delta\rho^2 = (\rho_1 - \rho_2)^2 \tag{3.10}$$

In addition to the number of particles scattered N and their volume V_p per volume V illuminated by X-ray beam, the intensity is also inflected by the structure factor $S(\boldsymbol{q})$ and the form factor $P(\boldsymbol{q})$:

$$I(\boldsymbol{q}) = \frac{N}{V}\Delta\rho^2 {V_p}^2 P(\boldsymbol{q}) S(\boldsymbol{q}) \tag{3.11}$$

There exists an analogy between the scattering by an atom (an assembly of electrons) and by a particle (an assembly of atoms). In the former case, the total structure factor $F(\boldsymbol{q})$ results from the waves scattered by all the atoms in the unit cell (lattice interference) and is defined through Fourier transformation (FT) as:

$$F(\boldsymbol{q}) = \sum_j^N f_j(\boldsymbol{q}) e^{i\boldsymbol{q}\boldsymbol{r}_j} \tag{3.12}$$

where $f_j(\boldsymbol{q})$ is the atomic form factor for an atom j, which itself is the FT of atomic electron density. The scattered intensity $I(\boldsymbol{q})$ equates to the squared modulus of $F(\boldsymbol{q})$. By analogy, for the small-angle scattering, the structure factor $S(\boldsymbol{q})$ results from the inter-particle interference which is the FT of inter-particle pair correlation function $g(\boldsymbol{r}) - 1$:

$$S(\boldsymbol{q}) = 1 + 4\pi\rho_0 \int [g(\boldsymbol{r}) - 1] \frac{\sin(\boldsymbol{q}\boldsymbol{r})}{\boldsymbol{q}\boldsymbol{r}} \boldsymbol{r}^2 \mathrm{d}\boldsymbol{r} \tag{3.13}$$

where ρ_0 is the particle number density and $g(\boldsymbol{r})$ is the probability of finding another scatterer at position $\vec{r}$ provided that there is a scatterer at the origin. The square brackets denote the average over all conformations and orientations. It is to note that in GISAXS, because reactions of interest occur at the interface, one will instead refers to the inter-particle interference in the xy-direction $S(\boldsymbol{q}_{\parallel})$. The form factor $P(\boldsymbol{q})$ is the FT of the probability distribution function $P(\vec{r})$:

$$P(\boldsymbol{q}) = \int \mathrm{d}\vec{r} e^{i\boldsymbol{q}\boldsymbol{r}} P(\boldsymbol{r}) \tag{3.14}$$

where $P(\vec{r})$ represents the probability of finding another scatterer at a distance $\vec{r}$ away in a given volume such as a particle. In practice, one employs instead the distance (pair) distribution function $p(\boldsymbol{r})$:

$$P(\boldsymbol{q}) = \frac{1}{R}\int_0^R \mathrm{d}\boldsymbol{r}\,\frac{\sin(\boldsymbol{qr})}{\boldsymbol{qr}}\,p(\boldsymbol{r}) \tag{3.15}$$

where R is the radius of the object of interest and $p(\boldsymbol{r})$ represents the distribution of distances r between all pairs of points within the object. For common shape objects, $p(\boldsymbol{r})$ is available in the literature and some examples are shown Figure 3.8.

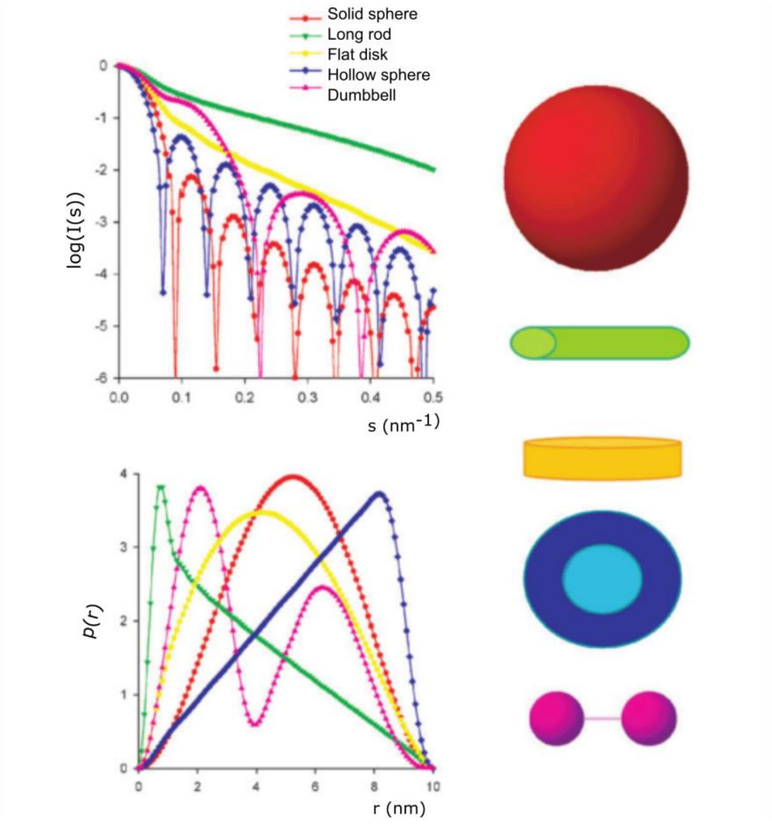

Figure 3.8. Scattering intensities and distance distribution functions of geometrical bodies. Scattered intensity (top) and the corresponding distance distribution function $p(r)$ (bottom) of solid sphere, long rod, flat disk, hollow sphere and dumbbell. (Adapted from Svergun and Koch, 2003)

For spherically symmetric particles, the scattered intensity from such particles can be expressed as a simple multiplication of the form factor $P(\boldsymbol{q})$ by the structure factor $S(\boldsymbol{q})$ as shown in Figure 3.9. When particles are correlated, the so-called long-range Bragg peak appears at $2\pi/D$ where D is the inter-particle distance.

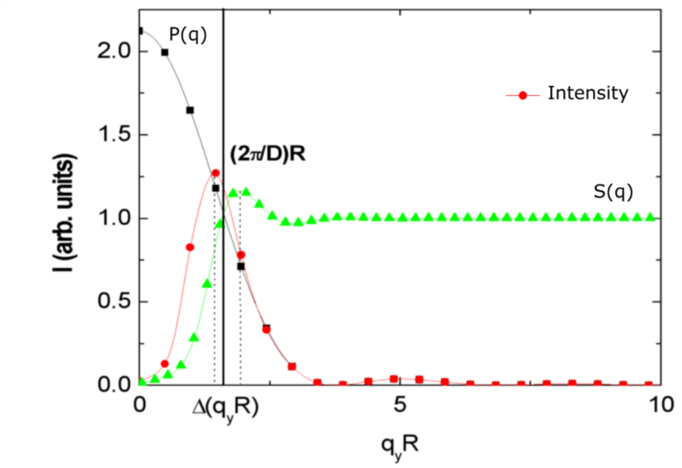

Figure 3.9. Intensity as the product of the form factor $P(q)$ by the structure factor $S(q)$ for centrosymmetric, correlated particles. (Adapted from Baruchel et al., 1993)

3.3.2. Data analysis

The GISAXS data are usually treated within the Distorted-Wave Born Approximation (DWBA), due to the existence of multiple-scattering effects at the particle interfaces with the substrate and the air or the surrounding medium (Renaud et al., 2003; Renaud et al., 2009). This is especially true when considering out-of-plane scattering, where multiple scattering across multiple interfaces can be as strong as the scattering from the particle. However, these effects are minimized when considering in-plane $\boldsymbol{q}_{xy}$ (substrate) scattering. The GISAXS data analyzed in this thesis aims to describe the nucleation and growth of particles across the substrate plane. In this specific case, multiple scattering at interfaces is minimized, and the scattering can be analyzed within the Born Approximation. One-dimensional curves are therefore obtained from the 2D detector by performing cuts and integrating intensity along the $\boldsymbol{q}_{xy}$ direction, parallel to the substrate plane. Such one-dimensional scattering curves can then be analyzed using the classical SAXS analysis principles and approximations.

Guinier approximation

When there is no interaction between particles with sufficiently large particle separation, the system can be treated on a basis of a single-averaged, isolated particle. In such conditions, and in the range where $\boldsymbol{q}R \ll 1$ holds (with R being the particle radius), the scattered intensity is related to the radius of gyration R_g, the effective size of the scattered "particle'', irrespective of their shape. This is known as Guinier's law:

$$I(\boldsymbol{q}) = I_0 \mathrm{e}^{\left(-\frac{\boldsymbol{q}^2 R_g{}^2}{3}\right)} \tag{3.16}$$

where I_0 is the absolute intensity at $\boldsymbol{Q} = 0$ (Guinier and Fournet, 1955). If the Guinier's law applies, in the range where $\boldsymbol{q}R \ll 1$ (data at the very small angle is necessary), a plot of $\ln(I(\boldsymbol{q}))$ vs $\boldsymbol{q}^2$ should be linear and its slope is therefore related to the R_g by $-R_g^2/3$.

The Porod's limit

When considering correlations over distances $\boldsymbol{r} \ll D$ if D is typical lengths in the sample, or $\boldsymbol{q} \gg D^{-1}$, solely the interface between the two media will give rise to the scattered intensity due to $\Delta\rho^2 \neq 0$. If sharp interface is present between particles, the integrated surface area per unit volume S/V is related to the scatted intensity by:

$$\frac{S}{V} = \frac{1}{2\pi\Delta\rho^2 V} \lim_{\boldsymbol{q}\to\infty} \boldsymbol{q}^4 I(\boldsymbol{q}) \tag{3.17}$$

The Porod plot, $\log(I(\boldsymbol{q}))$ vs $\log(\boldsymbol{q})$, therefore will generate a slope of -4. The slope can be deviated, referring to rough interfaces of the so-called "fractal dimension" D of the scattering objects, as slope $\sim 1/\boldsymbol{q}^{6-D}$. Fractal nature, that is the structure of the object is independent of the characteristic length scale of observation (Teixeira, 1988), can be divided into either mass fractal or surface fractal scaling. The former refers to the type of aggregation of the primary particles, while the latter refers to the boundary surface of a particle or aggregate (Besselink et al., 2016). For $\boldsymbol{q}^{-x}$, $1 < x < 3$ is obtained with mass fractals and $3 < x < 4$ with surface fractals (Fig. 3.10).

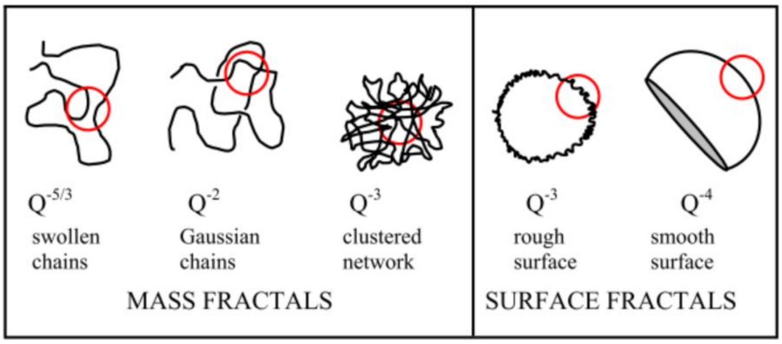

Figure 3.10. Porod exponents for mass fractals and surface fractals. (Hammouda, 2008)

The invariant

In two-phase approximation, the invariant Q is a useful quantity that, independently of the details of the structure, relates the scattered intensity to the total scattered volume by:

$$Q = \int_0^\infty I(\boldsymbol{q})\boldsymbol{q}^2 \mathrm{d}\boldsymbol{q} = 2\pi^2\phi(1-\phi)\Delta\rho^2 \tag{3.18}$$

where ϕ is the volume fraction of one phase, and 1 - ϕ is that of the other. If $\Delta\rho$ is known, Q can be compared to the phase-separated amount of material, provided the composition. If $\Delta\rho$ is constant, Q can still be used as a quantity proportional to the total scattered volume, such as the volume of precipitate. A precise determination of Q requires data taken over the full range of the SAXS data from small $\boldsymbol{q}$ limit to the beginning of the WAXS region. In high-$\boldsymbol{q}$ range, in particular, because the scattered intensity is weak in addition to the background subtraction, experimental precision can be a limiting factor.

For derivation of the invariant Q, resources are available in the literature (Amemiya and Shinohara, 2011; Melnichenko et al., 2012; Gommes, 2016).

3.4. Inelastic Incoherent Neutron Scattering (IINS)

3.4.1. Inelastic neutron scattering (INS)

INS constitutes the major fraction of neutron scattering, allowing observations of various excitations of condensed matter in a wide range of excitation energy (Fig. 3.11) (Squires, 1996).

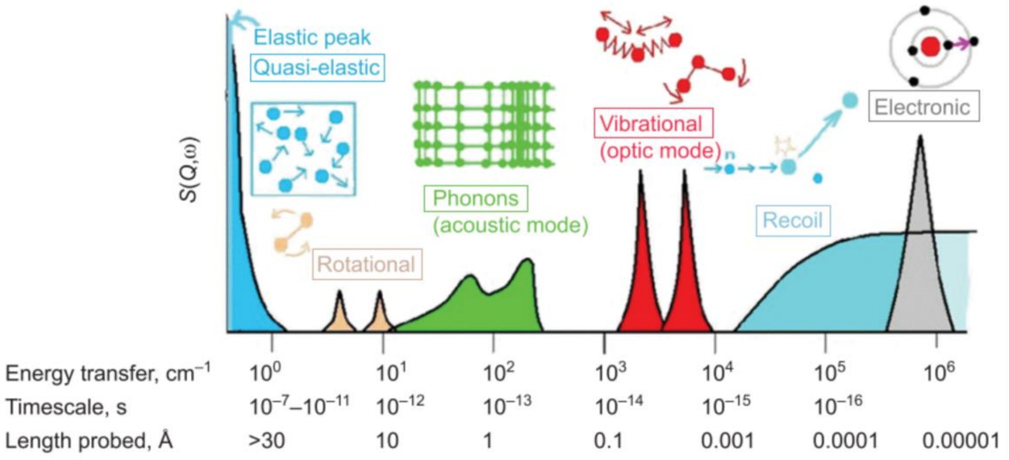

Figure 3.11. An hypothetical spectrum of typical excitations in condensed matter seen by inelastic nuclear scattering. (Parker and Collier, 2016)

A neutron is characterized by its wave vector $\boldsymbol{k}$ and the spin state σ (the latter is ignored with unpolarized neutrons). In a process of inelastic scattering, the two quantities of interest are the momentum transfer $\boldsymbol{Q}$ and the energy transfer $\hbar\omega$ from the neutrons to the sample:

$$\boldsymbol{Q} = \boldsymbol{k}_i - \boldsymbol{k}_f \tag{3.19}$$

$$\hbar\omega = \frac{\hbar^2}{2m}(\boldsymbol{k}_i{}^2 - \boldsymbol{k}_f{}^2) \tag{3.20}$$

where $\boldsymbol{k}_i$ is the initial (incident) wave vector and $\boldsymbol{k}_f$ is the final (exiting) wave vector. In practice, as a function of $\boldsymbol{k}_f$ given their $\boldsymbol{k}_i$, INS measures the number of scattered neutrons per solid angle and energy unit, or the double differential cross-section:

$$\frac{\mathrm{d}^2\sigma}{\mathrm{d}\Omega\mathrm{d}\omega} = \frac{\boldsymbol{k}_f}{\boldsymbol{k}_i}[b_{\mathrm{coh}}{}^2 S_{\mathrm{coh}}(\boldsymbol{Q},\omega) + b_{\mathrm{inc}}{}^2 S_{\mathrm{inc}}(\boldsymbol{Q},\omega)] \tag{3.21}$$

where Ω is the solid angle, b_{coh} and b_{inc} are the coherent and incoherent scattering lengths, $S_{\mathrm{cof}}(\boldsymbol{Q}, \omega)$ and $S_{\mathrm{inc}}(\boldsymbol{Q}, \omega)$ are the coherent and incoherent scattering functions (dynamical structure factor), respectively. Coherent scattering gives rise to interference fringes at discrete values of $\boldsymbol{Q}$ (as a result of summation of the wave amplitudes from the scattering centers) referring to the distribution of atoms in the lattice. Its scattering cross section is indeed expressed as:

$$\left(\frac{\mathrm{d}\sigma}{\mathrm{d}\Omega}\right)_{\mathrm{coh}} = \langle b\rangle^2 \sum_{ij} \mathrm{e}^{-\boldsymbol{Q}\cdot(\boldsymbol{r}_i-\boldsymbol{r}_j)} \tag{3.22}$$

where < > denotes the average. Incoherent scattering, on the other hand, is independent of $\boldsymbol{Q}$, thus arises as a flat background of the interference fringes. Its cross section is expressed as:

$$\left(\frac{\mathrm{d}\sigma}{\mathrm{d}\Omega}\right)_{\mathrm{inc}} = (\langle b^2\rangle - \langle b\rangle^2)N \tag{3.23}$$

where N is the number of atoms in the system. Note that if all the nuclei were identical, only the coherent scattering would be observable. The scattering functions are expressed as:

$$S_{\mathrm{coh}}(\boldsymbol{Q},\omega) = \frac{1}{2\pi\hbar}\iint G_{\mathrm{d}}(\vec{r},t)e^{i(\vec{Q}\cdot\vec{r}-\omega t)}\mathrm{d}\vec{r}\,\mathrm{d}t \tag{3.24}$$

$$S_{\mathrm{inc}}(\boldsymbol{Q},\omega) = \frac{1}{2\pi\hbar}\iint G_{\mathrm{s}}(\vec{r},t)e^{i(\vec{Q}\cdot\vec{r}-\omega t)}\mathrm{d}\vec{r}\,\mathrm{d}t \tag{3.25}$$

where G_{d} and G_{s} are the distinct- and self-correlation functions describing correlations between different particles and the particle itself, respectively. Therefore, coherent INS probes collective excitation such as phonons and magnons, while incoherent INS explores local single-particle excitations when an object rattles at its location, such as molecular vibrations.

3.4.2. Inelastic Incoherent Neutron Scattering (IINS) as a probe of hydrogen dynamics

Hydrogen is a strong spin-incoherent scatterer with an exceptionally large incoherent scattering cross-section (Table 3.1).

Table 3.1. Coherent σ_{coh} and incoherent σ_{inc} cross-section values for selected elements and isotopes

Element	**Thermal neutrons**	
	σ_{coh} (barn)	σ_{inc} (barn)
^{1}H	1.76	80.3
^{2}H	5.59	2.05
^{nat}C	5.55	0.001
^{nat}Ca	2.78	0.05
^{nat}O	4.23	0.0008

$\sigma = 4\pi|b|^2$ where b is the scattering length. (Dianoux and Lander, 2003)

Given the relative abundance of ^{1}H with respect to ^{2}H (~10^{-4}), all the scattering can be considered as arising via the incoherent scattering cross-section, and in this case, one can observe using an appropriate instrument the density of states of the excitation spectrum. The dynamical properties of the H-bonding network can be studied via the observation of librational modes, namely twist, wag and rock, occurring at excitation energies between 300 and 1100 cm^{-1} (37 - 137 meV). Librational motions are characterized by the intermolecular interactions of water molecules, and are thus probes the hindered rotation of H-bonding network (Han and Zhao, 2011) (Fig. 3.12).

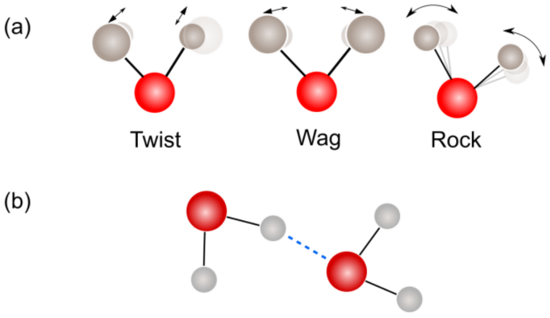

Figure 3.12. Libration of water molecules. **(a)** Librational modes (twisting, wagging and rocking). **(b)** Hydrogen bonding dynamics (dotted blue line) hinders the librational modes.

3.5. Molecular Dynamics simulations

In molecular dynamics (MD) simulations, the equilibrium and dynamical properties of a classical many-body system are computed (Frenkel and Smit, 2002). The term classical implies that the motions of every constituent particle in the simulation are ruled by the laws of classical mechanics, most importantly, the Newton’s second law of motion:

$$\boldsymbol{F} = m\boldsymbol{a} \tag{3.26}$$

where $\boldsymbol{a}$ is the acceleration, m is the particle mass and $\boldsymbol{F}$ is the force experienced by the particle. The trajectory of every atom in the system considered, or the evolution of the position and the velocity of each atom at each time step of the simulation, results from the interaction potentials between atoms and molecules since the force they exert results from the gradient of the potential energy. For a given system with N atoms, the potential energy can be divided into terms including individual atoms, pairs, triplets, etc., among which, the pair potential is the major consideration in the simulation (Allen and Tildesley, 1987). For a non-bonded atom pair ij separated by $\boldsymbol{r}_{ij} = |\boldsymbol{r}_i - \boldsymbol{r}_j|$, the effective pair potential $V_{2,\mathrm{eff}}$ can be parametrized as follows:

$$V_{2,eff}(\boldsymbol{r}_{ij}) = 4\varepsilon_{ij}[(\sigma_{ij}/\boldsymbol{r}_{ij})^{12} - (\sigma_{ij}/\boldsymbol{r}_{ij})^{6}] + \frac{z_i z_j}{4\pi\varepsilon_0 \boldsymbol{r}_{ij}} \tag{3.27}$$

The first term refers to the van der Waals force represented by Lennard-Jones 12-6 potential for short-range dipole-dipole interactions, and the second term refers to the Coulomb potential energy for long-range ionic interactions. The Lennard-Jones potential (Fig. 3.13) for an atom pair ii is characterized by a long-range attractive tail of the form $-1/\boldsymbol{r}^6$, a negative well of depth ε_{ii} and a steep repulsive wall at $\boldsymbol{r} < \sigma_{ii}$. The Coulomb potential energy involves the charge z, and the vacuum permittivity ε_0 ($8.854\times10^{-12}\,\mathrm{C^2J^{-1}m^{-1}}$).

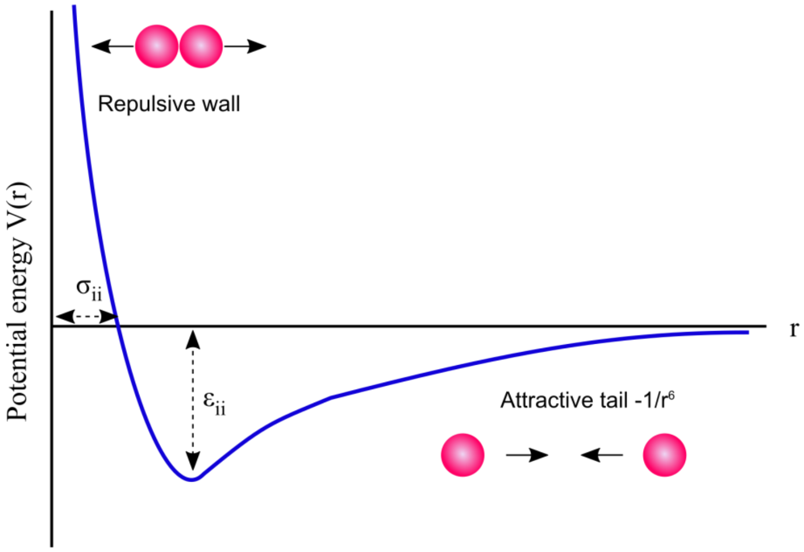

Figure 3.13. The Lennard-Jones 12-6 potential for an atom pair *ii*.

In order to reduce the number of parameters, the following combinations rules are used in practice (Allen and Tildesley, 1987):

$$\varepsilon_{ij} = \sqrt{\varepsilon_{ii} * \varepsilon_{jj}}\ ;\ \sigma_{ij} = \frac{\sigma_{ii}+\sigma_{jj}}{2} \tag{3.28}$$

A truncation radius is often set as 12 Å for van der Waals interaction. For bonded atoms or molecules such as water in particular, the bond stretch, angle bend as well as torsional rotation must also be taken accounted for the total potential energy. There are a large number of force fields and water models, with different parametrizations of the energy potential, developed to reproduce the geometry and dynamics or selected properties of different structures of interest. In this work, the CLAYFF force field (Cygan et al., 2004) and SPC water model (Berendsen, H.J.C., Postma, J.P.M., van Gunsteren, W.F., Herman, 1981) were used. The choice was made based on the wide range of successful applications of this force-field on mineralogical studies, particularly on clay and mica minerals (Wang et al., 2006; Cygan et al., 2009; Kalinichev et al., 2010).

The initial positions can be chosen according to a compatible structure one aims to simulate, often from experimental structures. The initial velocities, on the other hand, are determined randomly from a Maxwell-Boltzmann distribution corresponding to the desired temperature, with the magnitude of the velocity vector $\boldsymbol{v} = [v^2_x + v^2_y + v^2_y]^{1/2}$ that is scaled in such a way that the total momentum is zero.

At thermal equilibrium, the temperature and the velocities are related as:

$$\langle \boldsymbol{v}^2{}_{\propto} \rangle = K_{\mathrm{B}} T/m \tag{3.29}$$

where $\boldsymbol{v}_{\alpha}$ is the α-component of the velocity of a given particle of mass m. One can then compute an instantaneous temperature at time t:

$$K_{\mathrm{B}} T(t) = \sum_{i=1}^{N} \frac{m \boldsymbol{v}^2{}_{\propto,i}(t)}{3N} \tag{3.30}$$

where 3N is the number of degrees of freedom. Given the initial positions and the velocities, the attempt is then made in order to obtain the positions and the velocities at a later time $t + \delta t$. For this purpose, various integration algorithms have been designed, among which Verlet algorism is perhaps the most widely used (Allen and Tildesley, 1987; Frenkel and Smit, 2002). In this last, the advancement of the positions is achieved by:

$$\boldsymbol{r}(t+\delta t) = 2\boldsymbol{r}(t) - \boldsymbol{r}(t-\delta t) + \delta t^2 \boldsymbol{a}(t) \tag{3.31}$$

where $\boldsymbol{r}$ is the position and $\boldsymbol{a}$ is the acceleration. This results from summing the following equations obtained by Taylor expansion about $\boldsymbol{r}(t)$:

$$\begin{aligned} \boldsymbol{r}(t+\delta t) &= \boldsymbol{r}(t) + \delta t \boldsymbol{v}(t) + \frac{1}{2}\delta t^2 \boldsymbol{a}(t) + \cdots \\ \boldsymbol{r}(t-\delta t) &= \boldsymbol{r}(t) - \delta t \boldsymbol{v}(t) + \frac{1}{2}\delta t^2 \boldsymbol{a}(t) - \cdots \end{aligned} \tag{3.32}$$

Note that the velocities have been eliminated in the eq. (3.31) as a result of the addition and are indeed unnecessary to compute the trajectories themselves. They can still be obtained by:

$$\boldsymbol{v}(t) = \frac{\boldsymbol{r}(t+\delta t) - \boldsymbol{r}(t-\delta t)}{2\delta t} \tag{3.33}$$

Given a property of interest A that is a function of a particular point in phase space ($\boldsymbol{\Gamma}$), as the system evolves in time t, so does the $\boldsymbol{\Gamma}$ and thus $A(\boldsymbol{\Gamma})$. An experimentally observable A_{obs} is therefore nothing but the time average of $A(\boldsymbol{\Gamma})$ taken over a long time interval:

$$A_{\text{obs}} = \langle A \rangle_{\text{time}} = \lim_{t_{\text{obs}} \to \infty} \frac{1}{t_{\text{obs}}} \int_0^{t_{\text{obs}}} A\big(\boldsymbol{\Gamma}(t)\big) \mathrm{d}t \tag{3.34}$$

The ultimate goal of a MD simulation is to derive a property of interest that is comparable to a macroscopic scale measurement (~10^{23} atoms). A typical MD simulation however deals with 10^4 to 10^5 atoms for computational reasons. Also, instead of extending the integration to infinite time (eq. 3.34), one performs an average over a long finite time t_{obs} where equations of motion are solved on a step-by-step basis. Or, a large finite number τ_{obs} of time steps, each of which has the length δt defined as $t_{\text{obs}}/\tau_{\text{obs}}$ are taken:

$$A_{\text{obs}} = \langle A \rangle_{\text{time}} = \frac{1}{\tau_{\text{obs}}} \sum_{\tau=1}^{\tau_{\text{obs}}} A(\boldsymbol{\Gamma}(\tau)) \tag{3.35}$$

In order to cope with the complexity of $A(\boldsymbol{\Gamma}(\tau))$ for a large system, one considers an ensemble average, where an ensemble is a collection of points $\boldsymbol{\Gamma}$ in phase space. These points are distributed according to a probability density $\rho(\boldsymbol{\Gamma})$ determined by the fixed macroscopic parameters such as NPT, NVT, etc., and such distribution is denoted as ρ_{ens}. Under the conditions where the probability density $\rho_{\text{ens}}(\boldsymbol{\Gamma})$ for the ensemble of question remains the same as the system evolves (i.e. in equilibrium) and the ergodicity holds (i.e. all the trajectories are different sections of a single long trajectory passing through all the state points ($\boldsymbol{r}$, $\boldsymbol{p}$)), the ensemble average will be equal to the time average:

$$A_{\mathrm{obs}} = \langle A \rangle_{\mathrm{ens}} = \frac{1}{\tau_{\mathrm{obs}}} \sum_{\tau=1}^{\tau_{\mathrm{obs}}} A(\boldsymbol{\Gamma}(\tau)) \tag{3.36}$$

3.6. Bond-valence model

The bond valence model arises as a quantitatively accurate version of the Pauling's second rule (Pauling, 1929). This last, known as the electrostatic valency principle, states that the strength of a bond can be calculated by the valence of the atom divided by its coordination number (C.N.) to its closest neighbors. In reality, polyhedra can bear distortions due to structural relaxation, resulting in shortened or elongated bond lengths. It is evident that a shorter bond involves more of the valence electron density than a longer one. The correlation between the length and the bond strength has been established by combining numerous empirical results and computational predictions of inorganic crystal structures, from which the bond-valence model has been formulated (Brown and Altermatt, 1985):

$$s_{ij} = \exp(R_0 - R_{ij}/B) \tag{3.37}$$

where s_{ij} is the bond valence between atoms i and j, R_{ij} is their distance, and R_0 and B are the empirically obtained parameters. The bond-valence model has further been extended to hydrogen bonds by using experimental data obtained with neutron diffraction on ice structure (Bickmore et al., 2009). Table 3.2 summarizes the parameters R_0 and B used in the present work.

Table 3.2. Bond-valence parameters

		$\boldsymbol{R_0}$	$\boldsymbol{B}$
Si	O	1.624	0.37
Al	O	1.651	0.37
Mg	O	1.693	0.37
K	O	2.132	0.37
Na	O	1.803	0.37
Cs	O	2.417	0.37
H	O	0.907	0.28 (R < 1.05 Å)
		0.569	0.94 (1.05 Å ≤ R ≤ 1.70 Å)
		0.99	0.59 (R > 1.70 Å)

(Brown and Altermatt, 1985; Bickmore et al., 2009)

References

Allen M. P. and Tildesley D. J. (1987) *Computer Simulation of Liquids*., University Press.

Amemiya Y. and Shinohara Y. (2011) Small-Angle X-ray Scattering Basics & Applications. *Cherion Sch. 2010 @ SPring-8*.

Atkins P. and de Paula J. (2014) *Atkins' Physical Chemistry*., Oxford University Press.

Baruchel J., Hodeau J.-L., Lehmann M. S., Regnard J.-R. and Schlenker C. eds. (1993) *Neutron and Synchrotron Radiation for Condensed Matter Studies Vol. II: Applications to Solid State Physics and Chemistry*., Springer-Verlag.

Berendsen, H.J.C., Postma, J.P.M., van Gunsteren, W.F., Herman J. (1981) Interaction models for water in relation to protein hydration. In *Intermolecular Forces.* pp. 331–342.

Besselink R., Stawski T. M., Van Driessche A. E. S. and Benning L. G. (2016) Not just fractal surfaces, but surface fractal aggregates: Derivation of the expression for the structure factor and its applications. *J. Chem. Phys.* **145**, 211908.

Bickmore B. R., Rosso K. M., Brown I. and Kerisit S. (2009) Bond-valence constraints on liquid water structure. *J. Phys. Chem. A* **113**, 1847–1857.

Brown I. D. and Altermatt D. (1985) Bond-Valence Parameters Obtained from a Systematic Analysis of the Inorganic Crystal Structure Database. *Acta Crystallogr.* **244**, 244–247.

Cygan R. T., Greathouse J. A., Heinz H. and Kalinichev A. G. (2009) Molecular models and simulations of layered materials. *J. Mater. Chem.* **19**, 2470–2481.

Cygan R. T., Liang J.-J. J. and Kalinichev A. G. (2004) Molecular Models of Hydroxide, Oxyhydroxide, and Clay Phases and the Development of a General Force Field. *J. Phys. Chem. B* **108**, 1255–1266.

Dianoux A. J. and Lander G. eds. (2003) *ILL Neutron Data Booklet*. Second., OCP Science.

Dierker S. B., Pindak R., Fleming R. M., Robinson I. K. and Berman L. (1995) X-Ray Photon-Correlation Spectroscopy Study of Brownian-Motion of Gold Colloids in Glycerol. *Phys. Rev. Lett.* **75**, 449–452.

Dirac P. A. M. (1981) *The principles of quantum mechanics*., Clarendon Press.

Einstein A. (1905) Concerning an heuristic point of view toward the emission and transformation of light. *Am. J. Phys.* **17**.

Frenkel D. and Smit B. (2002) *Understanding molecular simulation: from algorithms to applications*., Academic press.

Giordano V. M. and Ruta B. (2015) Unveiling the structural arrangements responsible for the atomic dynamics in metallic glasses during physical aging. *Nat. Commun.* **7**, 1–8.

Gommes C. J. (2016) Small-angle scattering and scale-dependent heterogeneity. *J. Appl. Crystallogr.* **49**, 1162–1176.

Guinier A. (1963) *X-Ray Diffraction in Crystals, Imperfect Crystals, and Amorphous Bodies*., W. H.

Freeman and Company.

Guinier A. and Fournet G. (1955) *Small-angle scattering of X-rays*., John Wiley & Sons.

Hammouda B. (2008) Probing Nanoscale Structures - the SANS toolbox.

Han K.-L. and Zhao G.-J. (2011) *Hydrogen Bonding and Transfer in the Excited State*., John Wiley & Sons Ltd.

Hippert F., Geissler E., Hodeau J. L., Lelièvre-Berna E. and Regnard J. R. eds. (2006) *Neutron and X-ray Spectroscopy*., Springer.

Kalinichev A. G., Padma Kumar P. and James Kirkpatrick R. (2010) Molecular dynamics computer simulations of the effects of hydrogen bonding on the properties of layered double hydroxides intercalated with organic acids. In *Philosophical Magazine* pp. 2475–2488.

Leitenberger W., Wendrock H., Bischoff L., Panzner T., Pietsch U., Grenzer J. and Pucher A. (2003) Double pinhole diffraction of white synchrotron radiation. In *Physica B: Condensed Matter* pp. 63–67.

Madsen A., Fluerasu A. and Ruta B. (2015) Structural Dynamics of Materials Probed by X-Ray Photon Correlation Spectroscopy. In *Synchrotron Light Sources and Free-Electron Lasers* (eds. E. Jaeschke, S. Khan, J. R. Schneider, and J. B. Hastings). Springer International Publishing, Chicago. pp. 1–21.

Melnichenko Y. B., He L., Sakurovs R., Kholodenko A. L., Blach T., Mastalerz M., Radliński A. P., Cheng G. and Mildner D. F. R. (2012) Accessibility of pores in coal to methane and carbon dioxide. *Fuel* **91**, 200–208.

Parker S. F. and Collier P. (2016) Applications of Neutron Scattering in Catalysis Where atoms are and how they move Neutron Properties and their Applications. *Johnson Matthey Technol. Rev* **60**, 132–144.

Pauling L. (1929) The principles determining the structure of complex ionic crystals. *J. Am. Chem. Soc.* **51**, 1010–1026.

Renaud G., Lazzari R. and Leroy F. (2009) Probing surface and interface morphology with Grazing Incidence Small Angle X-Ray Scattering. *Surf. Sci. Rep.* **64**, 255–380.

Renaud G., Revenant C., Barbier A., Noblet M., Ulrich O., Jupille J., Borensztein Y., Henry C. R., Deville J., Scheurer F., Mane-mane J. and Fruchart O. (2003) Real-Time Monitoring of Growing Nanoparticles. *Science* **300**, 1416–1419.

Ruta B., Baldi G., Chushkin Y., Rufflé B., Cristofolini L., Fontana A., Zanatta M. and Nazzani F. (2014) Revealing the fast atomic motion of network glasses. *Nat. Commun.* **5**.

Salmeron M. and Schlögl R. (2008) Ambient pressure photoelectron spectroscopy: A new tool for surface science and nanotechnology. *Surf. Sci. Rep.* **63**, 169–199.

Squires G. L. (1996) *Introduction to the theory of thermal neutron scattering*., Dover Publications.

Stephenson G. B., Robert A. and Grübel G. (2009) X-ray spectroscopy: Revealing the atomic dance. *Nat. Mater.* **8**, 702–703.

Svergun D. I. and Koch M. H. J. (2003) Small-angle scattering studies of biological macromolecules in solution. *Reports Prog. Phys.* **66**, 1735–1782.

Teixeira J. (1988) Small-angle scattering by fractal systems. *J. Appl. Crystallogr.* **21**, 781–785.

Wang J., Kalinichev A. G. and Kirkpatrick R. J. (2006) Effects of substrate structure and composition on the structure, dynamics, and energetics of water at mineral surfaces: A molecular dynamics modeling study. *Geochim. Cosmochim. Acta* **70**, 562–582.

Yamamoto S., Bluhm H., Andersson K., Ketteler G., Ogasawara H., Salmeron M. and Nilsson A. (2008) In situ x-ray photoelectron spectroscopy studies of water on metals and oxides at ambient conditions. *J. Phys. Condens. Matter* **20**, 184025.

Chapter 4

Heterogeneous nucleation of calcium carbonate: effect of surface hydrophobicity

4.1. Introduction

The dissolution-precipitation cycling of $CaCO_3$ regulates the composition of natural waters, their alkalinity, and the solubility of other solid phases, thus regulating the precipitation of a wide range of minerals, alteration of rocks, as well as transport and sequestration of contaminants in the subsurface (McCarthy and Zachara, 1989; Fujita et al., 2000; Warren et al., 2001; Dong et al., 2005). From calcareous biominerals, which accounts for a biotic sink of CO_2 (Lowenstam and Weiner, 1989; Morse et al., 2007; Sanders and Henson, 2014), to the majority of inorganically formed carbonates, the very first step, nucleation, stems from the interactions of ions with a surrounding matrix of either organic or inorganic origin. This process, known as heterogeneous nucleation, involves complex physico-chemical fluid-nucleus-substrate interactions, of which the precise mechanisms and the factors controlling the process remain elusive. Besides its relevance to natural systems, understanding this complex process is also of great relevance to improve our control over geological storage of CO_2 (Chiquet et al., 2007; Espinoza and Santamarina, 2010), scale formation (Söhnel and Garside, 1992; Yang et al., 2001; Chen et al., 2005), and synthesis of biomimetic materials (Sommerdijk and With, 2008; Aizenberg, 2010; Meyers et al., 2013), to list just a few.

Today, although a number of so-called non-classical, multistep, nucleation pathways have been observed (Gebauer and Cölfen, 2011; Stawski et al., 2016; Van Driessche et al., 2017), Classical Nucleation Theory (CNT) makes still the most widely used quantitative formalization of nucleation process. CNT describes nucleation as a stochastic process due to a nucleation barrier that stems from a competition between the chemical potential gained by the formation of a new bulk phase and the cost of creating an interface (Gibbs, 1878; Kashchiev, 2000). Nucleation is therefore an activated physical process, whose energetic barrier is controlled by the interfacial energy and the fluid supersaturation. When nucleation takes place at an interface, as is often the case in both natural and engineered media, for instance inside cellular compartments in case of biomineralization (Lowenstam and Weiner, 1989; Whittaker et al., 2016) or in the pores of rocks, soils and sediments (Prieto, 2014) in case of abiotic formation, the contribution from the interfacial penalty is an effective term, α', resulting from a combination of three interfacial energies exerting at the interfaces between liquid-crystal (α_{lc}), liquid-substrate (α_{ls}) and substrate-crystal (α_{sc}). It is not surprising therefore that the property of the substrate plays a significant role in the fate of heterogeneous nucleation. The dominance of heterogeneous nucleation over homogeneous nucleation occurs when α' is lower than α_{lc} that controls homogeneous nucleation. A study by Fernandez-Martinez et al. (Fernandez-Martinez et al., 2013a) confirmed that the presence of quartz surface contributes to a reduction of α' with respect to α_{lc} for calcite nucleation by a factor of ~3. The question then arises whether, and if so how, one particular surface property rather than another can affect the values of α', thus occurrence of $CaCO_3$ nucleation. In the simple case of a hemispherical nucleus forming on a substrate (θ = 90° in eq. 4.4; see Materials and Methods), the occurrence of heterogeneous nucleation is promoted if:

$$\alpha' < \alpha_{\mathrm{lc}} \;\Rightarrow\; -\frac{1}{2}(\alpha_{\mathrm{ls}} - \alpha_{\mathrm{sc}}) < 0 \;\Rightarrow\; \alpha_{\mathrm{ls}} > \alpha_{\mathrm{sc}}$$

, which suggests that the substrate should show a preference to be wetted by the crystal, rather than by water. A high value of α_{ls} implies a hydrophobic substrate. Indeed, surface hydrophobicity has been shown to be one of the promoting factors for nucleation (Giuffre et al., 2013; Dai et al., 2016). On a particular note, however, the study on barite heterogeneous nucleation by Dai et al. (Dai et al., 2016) showed that nucleation was enhanced when hydrophilic, negatively charged self-assembled monolayers were combined with hydrophobic ones. The rationale for this behavior was deduced to be that ion adsorption provided by the hydrophilic regions on the substrate enhanced the nucleation behavior. Other studies (Pimentel et al., 2013; Li et al., 2014), on the other hand, suggest that a lattice mismatch between the substrate and the precipitate could control the values of α', or more relevantly, the values of α_{sc}. However, absolute values of interfacial energy are scarce in the literature and the disparity among the values reported cannot be neglected (Forbes et al., 2011). Considering that the application of CNT relies on a priori knowledge of thermodynamic parameters including interfacial energies (Kashchiev, 2000), it is necessary to develop a predictive understanding of the dependence of α' values and the nucleation behavior on a given specific physico-chemical property of surface, such as surface hydrophobicity.

This study thus aims at providing (i) a quantitative link between the substrate hydrophobicity and values of the effective interfacial energy and (ii) a mechanistic understanding of how surface hydrophobicity affects heterogeneous nucleation of $CaCO_3$ polymorphs. A set of natural and synthetic phlogopite mica was selected as substrates with different degrees of fluorine substitution for octahedral hydroxyl group, referring to different extents of hydrophobicity. These substitutions are naturally occurring in phyllosilicates (Wedepohl, 1978; Petersen et al., 1982; Demyanova and Tressaud, 2009), and have a strong influence on the wetting behavior of mineral surfaces (Michot et al., 1994; Rotenberg et al., 2011; Dazas et al., 2013). We designed a series of *in situ* experiments using time-resolved Grazing-Incidence Small-Angle X-ray Scattering (GISAXS) technique in an open-flow system. This approach allows us to extract, at the nanoscale, density fluctuations occurring at the substrate-water interface, that is the most relevant information to the heterogeneous nucleation events, from which effective interfacial energy between nucleating particles and mineral surface can be determined, as previously demonstrated for calcium carbonate, iron oxide and barium sulfate systems with mica and quartz as substrates (Jun et al., 2010; Fernandez-Martinez et al., 2013a; Li et al., 2014; Dai et al., 2016). *Ex situ* characterization of the nucleated particles was performed using Atomic Force Microscopy (AFM) for determining their morphological features and by ATR-FTIR for phase identification of the precipitates. This study sheds lights on the role of surface hydrophobicity over the control of heterogeneous nucleation of $CaCO_3$ polymorphs, in particular its mechanisms and nucleation pathways.

4.2. Materials and Methods

4.2.1. Sample preparation

Phlogopite micas were used as substrates for all experiments (Table 4.1). Samples labelled ‘OH phlogopite’ and ‘$F_{0.8}$ phlogopite’ are natural, whereas ‘F phlogopite’ is synthetic. Substrates were cleaved using Scotch® tape in ultra-pure water in order to minimize the splitting force, immediately before each measurement.

Table 4.1. Summary of mica minerals used as substrates for heterogeneous nucleation experiments.

Name	Composition	Source
OH phlogopite	$(K_{0.98}Na_{0.10})(Mg_{2.44}Al_{0.22}Fe_{0.10}Ti_{0.04}\square_{0.2})(Si_3Al_1)O_{10}(OH)_2$	Réserve collection Jussieu, Paris, France
F phlogopite	$KMg_3(AlSi_3O_{10})F_2$	H. C. Materials Corporation, IL, USA
$F_{0.8}$ phlogopite	$(K_{0.96}Na_{0.04})(Mg_{2.74}Fe_{0.16}Al_{0.09}Ti_{0.04})(Si_{2.89}Al_{1.11})O_{10}(OH_{0.46}F_{1.54})$	Muséum national d'Histoire naturelle, Paris, France

OH phlogopite and $F_{0.8}$ phlogopite are natural and F phlogopite is synthetic.

4.2.2. *In situ* time-resolved Grazing-Incidence Small Angle X-ray Scattering (GISAXS)

In situ heterogeneous nucleation experiments were performed on OH and F phlogopite (Table 4.1). Freshly cleaved mica substrates were glued on a sample holder with a small amount of crystal bond (Crystalbond 509, Agar Scientific®) and fixed horizontally in a custom-made fluid cell (for details see Fig. S4.7). Equimolar solutions of $CaCl_2$ and $NaHCO_3$ (Table 4.2) were flowed at a constant rate of 5.7 mL/min using peristatic pumps (model WPX1-NF1/8S4-J8-YP, Welco Co. Ltd., Tokyo, Japan). Both solutions were mixed using a Y-mixer placed at ~15 cm before the inlet of the fluid cell. Before each measurement, the cell and the Teflon tubing were rinsed thoroughly by flowing a 2% HCl solution, followed by ultra-pure water, through the setup.

Table 4.2. Summary of solution chemistry used for heterogeneous nucleation experiments.

Condition	σ_{calcite}	σ_{ACC}	[Ca^{2+}] (mM)	[HCO_3^{2-}] (mM)	pH
I	3.97	2.04	15	15	8.27
II	2.97	1.04	10	10	8.10
III	2.67	0.74	7.5	7.5	8.18
IV	2.21	0.28	5	5	8.29

GISAXS measurements were performed at the 12ID-B beamline located at the Advanced Photon Source (Argonne National Laboratory, USA). An incident X-ray energy of 14 keV and a sample-to-detector distance of 2020 mm were selected to cover a $\boldsymbol{q}$-range of 0.0002 to 0.4 $Å^{-1}$. The incident angle was set slightly lower (α_i = 0.1°) than the critical angle ($\alpha_c \approx 0.14°$ at 14 keV incident energy) for the total reflection from phlogopite, allowing the X-ray beam to be reflected by the substrate. GISAXS patterns were collected every 3 minutes with 30 sec of exposure time, for a time frame of 2 to 5 hours. In order to minimize and (if any) verify beam damage, GISAXS patterns at left and right sides of the irradiated spot were collected every 18 minutes. From time to time, scattering from the solution was also collected in order to monitor the absence of homogeneous nucleation. Supersaturations ($\sigma = \ln(\text{IAP}/K_{\text{SP}})$, where IAP is the ionic activity product and K_{SP} is the solubility constant) with respect to calcite and amorphous calcium carbonate (ACC) were calculated by Phreeqc (Parkhurst and Appelo, 1999) using the solubility constants at 25°C: $K_{\text{SP (calcite)}} = 10^{-8.48}$ (Plummer and Busenberg, 1982) and $K_{\text{SP (ACC)}} = 10^{-7.64}$ (Kellermeier et al., 2014), as well as the pH values of the two reactants measured before each experiment and the concentrations reported in Table 4.2.

GISAXS scattering images were corrected by transmission using a monitor value of the incident intensity on the sample and the scattered intensity at the Kapton peak at high $\boldsymbol{q}$. Horizontal cuts of the scattered intensity were performed along the $\boldsymbol{q}_{xy}$ direction parallel to the plane of the substrate. The intensity along this plane shows an enhancement at the critical angle position, due to the Yoneda-Vineyard effect (Renaud et al., 2009) (Fig. S4.7). For each measurement, the first image (substrate in contact with ultra-pure water, before the mixed solution reaches the fluid cell) was used as background and was subtracted from the rest. The extracted one-dimensional curves ($\boldsymbol{q}_{xy}$ direction) were fitted using the IRENA package installed on Igor Pro 7.02. The 'Unified fit', a simple model based on the unified scattering theory (Beaucage, 1996; Beaucage et al., 2004), was employed in the Guinier region to extract average radius of gyration, R_g. The GISAXS scattered intensity is proportional to the number density of the particles N/V with V the total volume irradiated by the X-ray, the inhomogeneity in the electron densities $\Delta\rho$, as well as the form factor $P(\boldsymbol{q})$ and the structure factor $S(\boldsymbol{q})$:

$$I(\boldsymbol{q}) = \frac{N}{V}\Delta\rho^2 {V_{\text{p}}}^2 P(\boldsymbol{q}) S(\boldsymbol{q}) \tag{4.1}$$

Provided the absence of defined correlations (no observable peaks in the intensity) and the polydispersity of the particles formed, we assume $S(\boldsymbol{q}) = 1$. In the framework of the CNT, heterogeneous nucleation is driven by two opposing factors, the supersaturation σ and the effective interfacial energy α', that determine the height of the nucleation barrier Δg_{n}, which in turn controls the nucleation kinetics. The nucleation rate J_{n} is expressed as:

$$J_n = \exp\left(\frac{\Delta g_n}{K_{\mathrm{B}} T}\right) = A\exp(-\frac{16\pi \Omega^2 \boldsymbol{\alpha'^3}}{3{K_{\mathrm{B}}}^3 T^3 \boldsymbol{\sigma^2}}) \tag{4.2}$$

where K_{B} is the Boltzmann constant, T is the temperature, A is a kinetic factor related to kinetic pathways, Ω is a molecular volume (for the two phases assumed, calcite and ACC, experimentally obtained values were $6.16 \cdot 10^{-29}$ (Markgraf and Reeder, 1985) and $9.37 \cdot 10^{-29}$ m³/mol (Fernandez-Martinez et al., 2013b), respectively). J_{n} is experimentally obtained from the so-called SAXS invariant Q:

$$Q = \int_0^\infty I(\boldsymbol{q})\boldsymbol{q}^2 \mathrm{d}\boldsymbol{q} = 2\pi^2 \phi(1-\phi)\Delta\rho^2 \tag{4.3}$$

where, in a two-phase approximation (i.e. the precipitates and the matrix), ϕ is the fraction volume of one phase and 1-ϕ is that of the other. Since Q is related to the total scattered volume, its evolution is proportional to the nucleation rate J_{n}, provided that the system is nucleation-dominated ($\Delta\rho$ remains constant and the volume of the particles does not evolve over time). A regression analysis of the plot $\ln(J_{\mathrm{n}})$ vs. the inverse of σ^2 provides the coefficient estimate that is proportional to the effective interfacial energy α'. For the σ range used in the present work, linear regression was performed. The term α' is an effective value that comprises three components corresponding to the interfacial energies governing the interface between liquid and crystal (α_{lc}), liquid and substrate (α_{ls}) and substrate and crystal (α_{sc}):

$$\alpha' = \alpha_{lc} \frac{2(1-\cos\theta) - \sin^2\theta(\frac{\alpha_{\mathrm{ls}} - \alpha_{\mathrm{sc}}}{\alpha_{\mathrm{lc}}})}{2^{1/3}(2 - 3\cos\theta + \cos^3\theta)^{2/3}} \tag{4.4}$$

where θ is the angle formed between the substrate and the crystal.

4.2.3. *Ex situ* heterogeneous nucleation experiments

4.2.3.1. Atomic Force Microscopy (AFM)

Ex situ heterogeneous nucleation experiments of $CaCO_3$ were performed on OH and $F_{0.8}$ phlogopite substrates. Freshly cleaved substrates were fixed on a sample holder using a small amount of Araldite epoxy and placed vertically in a freshly mixed, metastable, supersaturated solution (condition IV, Table 4.2). Relatively low supersaturation was chosen to allow sufficient spacing between the heterogeneously nucleated particles after several tests at higher supersaturation conditions. After 15 min of reaction, the substrates were gently rinsed with ethanol to quench the reaction before being mounted in the observation cell of the AFM (Nanoscope IIIa Multimode, Veeco Instruments). Topography, vertical deflection and lateral deflection signals were recorded in contact mode in a closed fluid cell under ethanol, using Bruker SNL-10D tips. The cell was filled with ethanol while data collection in order to quench the reaction while achieving a better resolution than when exposed in air. The scan areas varied between 10 x 10 nm^2 to 14 x 14 μm^2. The scan velocity was set at 5 Hz, and was increased to 61 Hz for high-resolution images. Scan quality yields 512 points per line and 512 lines per image. Data analyses were performed using WSxM 4.0 Beta 8.2 and NanoScope Analysis 1.50. Normal force F_N was calculated using the following equation (Bhushan, 2007):

$$F_\mathrm{N} = K_\mathrm{N} S_\mathrm{Z} V_\mathrm{N} \tag{4.5}$$

where K_N is the normal spring constant (0.06 N/m), S_Z is the sensitivity of the photodetector (m/V) and V_N is the normal voltage (V). For each area scanned, S_Z and V_N values were linearly extrapolated based on the two force distance curves, measured before and after the corresponding scan.

4.2.3.2. Attenuated Total Reflectance Fourier Transform Infrared Spectroscopy (ATR-FTIR)

Ex situ heterogeneous nucleation experiments were performed on OH and F phlogopite under conditions I to IV (Table 4.2). Freshly cleaved substrates were placed vertically in a freshly mixed, metastable, supersaturated solution. The substrates were sampled at 1, 3, 6 hours (1 and 3 hours for conditions I and II), gently quenched with ethanol and characterized by ATR-FTIR (Nicolet iS10). Spectra were collected in the range of 650 – 4000 cm^{-1}, by averaging 500 scans at a resolution of 4 cm^{-1} for each measurement. Experiments were performed at least 3 times for each condition and the averaged data are shown. Under condition III, the closest solution chemistry as the one (condition IV) employed for AFM observation which provides sufficient FTIR signal, nucleation experiments were repeated and the substrates were sampled after 4 days of reaction for a comparison purpose.

4.3. Results

4.3.1. *In situ* time-resolved GISAXS

A representative time-resolved plot of the GISAXS intensity, $I(\boldsymbol{q})$ *vs.* $\boldsymbol{q}$, is shown in Figure 4.1A for the $CaCO_3$ – F phlogopite system under condition I (for solution chemistry see Materials and Methods; Table 4.2). Only the $\boldsymbol{q}$ range where the data display significant statistics is shown (0.004 – 0.15 Å^{-1}, corresponding to a d_{min} of 4.2 nm and a d_{max} of 157 nm). Additional time-resolved plots are provided in Figure S4.1. In general, the scattered intensity increased during the course of the measurement as

$CaCO_3$ formed on the substrate, with varying induction times that depended on the substrates and on the fluid supersaturations. Figure 4.1B shows a representative fit to the data and the so-called Lorentz function, $L = I(\boldsymbol{q})\cdot\boldsymbol{q}^2$, from which a mean particle size (radius of gyration, R_g) and the invariant Q, proportional to the total mass nucleated, are obtained respectively (for details see Materials and Methods).

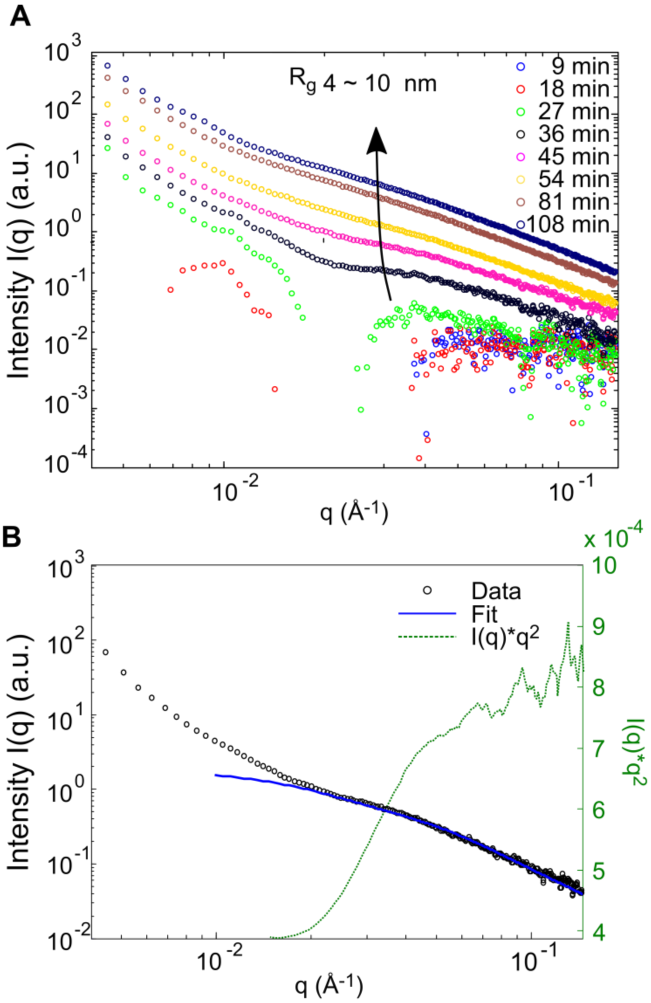

Figure 4.1. (A) Representative evolution of the GISAXS intensity over time and **(B)** representative fit to the data and Lorentz function ($I(\boldsymbol{q})*\boldsymbol{q}^2$). Data shown here are horizontal cuts at the interface for the $CaCO_3$ – F phlogopite system under condition I ($\sigma_{calcite} = 3.97$; $\sigma_{ACC} = 2.04$). The invariant Q is obtained by integrating the curve $I(\boldsymbol{q})*\boldsymbol{q}^2$, which is equivalent to the total mass nucleated.

For both OH and F systems, R_g remained in the same range of values (R_g ~ 5-7 nm) over the duration of the experiments (Figs. 4.2A and 4.2B), with an exception of the F phlogopite system under condition I where an apparent growth of particles was observed reaching a R_g value of 11 nm. Since R_g remains approximately constant for the tested range of conditions, the increase in intensity is attributed to an increase in the number of particles (i.e. the precipitation process is dominated by nucleation). Hence, we can assume that the rate at which the GISAXS invariant Q evolves over time is a good proxy for the nucleation rate. Accordingly, the nucleation rate J_n was obtained for different systems (Fig. S4.2), with which the corresponding effective interfacial free energies (α') were estimated using eq. 4.2 for calcite and amorphous calcium carbonate (ACC), the least and the most soluble phases among those susceptible to nucleate. The obtained values of α' were identical for both surfaces (OH and F phlogopite): $\alpha'_{calcite}$ ~ 33-34 mJ/m^2 and α'_{ACC} ~ 9 mJ/m^2 (Figs. 4.2C and 4.2D). Note that α' values were cross-checked using the induction time deduced from the same invariant *vs*. time curves (Figs. S4.2). As shown in Figure S4.3, the yielded values of α' were very similar to those obtained from J_n, which underlines the robustness of the results and validates the use of the invariant *Q* evolution rate as a valid proxy for the nucleation rate.

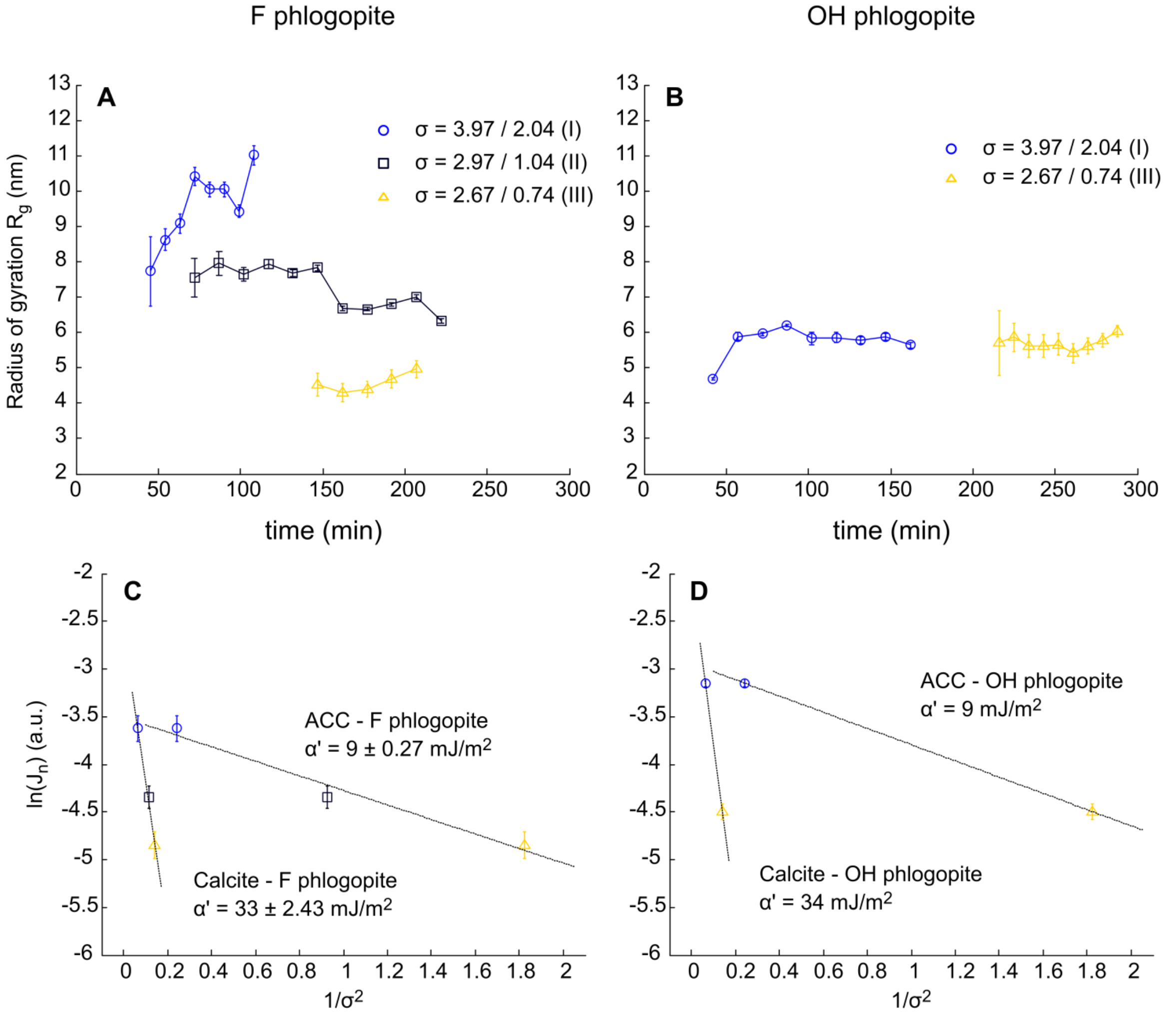

Figure 4.2. (A, B) Evolution of the radius of gyration (R_g) for F and OH phlogopite at different supersaturations ($\sigma_{calcite}$ / σ_{ACC}). **(C, D)** Effective interfacial free energies α' for F and OH phlogopite under the hypotheses that calcite and ACC are the nucleated phases. Error bars represent 90 % confidence interval of J_n. The confidence intervals (2SE) of α' for F phlogopite are calculated from J_n values.

4.3.2. *Ex situ* observation by Atomic Force Microscopy

Figs. 4.3A and 4.3B show a random and dense population of heterogeneously nucleated $CaCO_3$ particles on both substrates after 15 mins of reaction under condition IV. These particles were confirmed to have been heterogeneously nucleated as they were not removable after several scans at a maximum applied force of 50 nN (normal force), besides the fact that the substrates were placed vertically during the reaction time to avoid the deposition of homogeneously nucleated particles, if any. Both surfaces also had a few, large aggregated particles. They were assumed to have been deposited onto the surface after being homogeneously nucleated, since they were very weakly attached to the surface and were readily removed after a few scans at a low loading (normal force ~ 0.5 nN).

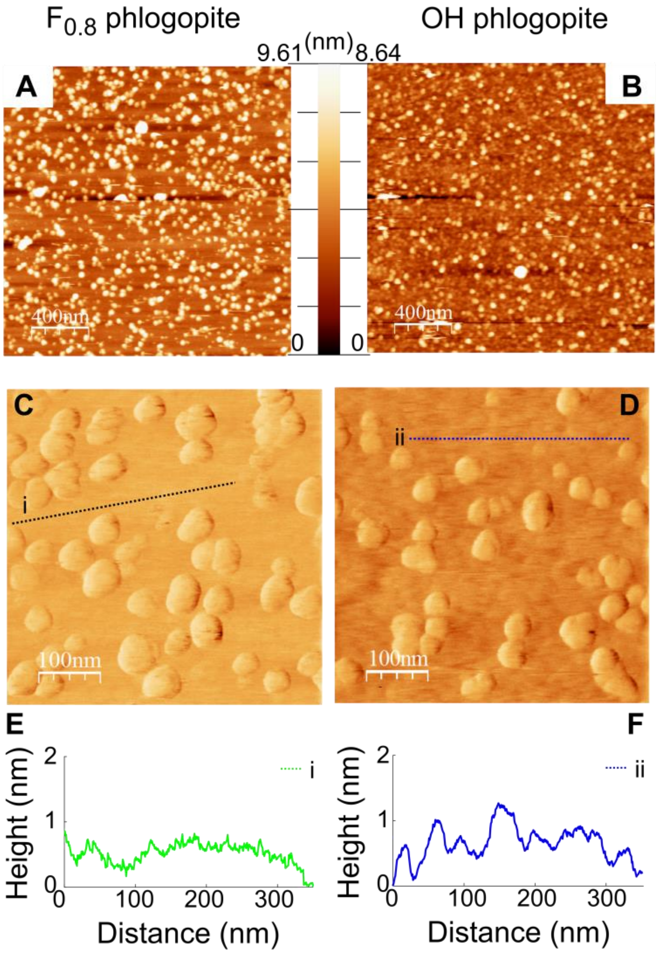

Figure 4.3. Comparison of AFM images between $F_{0.8}$ phlogopite and OH phlogopite after 15 min of reaction under condition IV ($\sigma_{calcite}$ = 2.21; σ_{ACC} = 0.28). **(A, B)** 2 x 2 μm^2 topography with $CaCO_3$ particles heterogeneously nucleated. **(C, D)** 0.5 x 0.5 μm^2 friction images. **(E, F)** Height profiles along the dotted lines shown in C (i) and D (ii).

On average, the particles on OH phlogopite were smaller (20-40 nm wide and 5 nm high) than those nucleated on $F_{0.8}$ phlogopite (40-50 nm wide and 6 nm high). In addition, the friction images and the height profiles clearly show that $F_{0.8}$ phlogopite surface in between the $CaCO_3$ particles remains atomically flat (Figs. 4.3C and 4.3E), while the OH phlogopite surface in between the particles is fully covered by a rather rough precipitate, presumably $CaCO_3$, without a distinct shape (Figs. 4.3D and 4.3F).

Figure 4.4 compares high-resolution images of phlogopite surfaces before and after the heterogeneous nucleation events. Figure 4.4A shows a high-resolution friction image of the clean OH phlogopite surface, obtained under water, before nucleation took place. Its two-dimensional fast Fourier Transform (FFT) (Fig. 4.4B) exhibits a hexagonal pattern and the corresponding unit cell distances, in accordance to the surface structure of this mineral (Kuwahara, 2001). Figure 4.4C shows the $F_{0.8}$ phlogopite surface with a heterogeneously nucleated $CaCO_3$ particle. The high-resolution friction image of the zoomed area (Fig. 4.4D) shows the characteristic surface structure of phlogopite (001) as confirmed by 2D FFT (inset). A friction image of the OH phlogopite surface with heterogeneously nucleated $CaCO_3$ is shown in Figure 4.4E. Conversely, the high-resolution friction image and corresponding 2D FFT of the OH phlogopite surface (Fig. 4.4F) do not display clear evidence of its surface structure. This last further supports the idea that the OH surface is fully covered by heterogeneously formed precipitates, together with the roughness of inter-particle surface as mentioned above. It is to note that the heterogeneously nucleated particles shown in Figure 4.4E have experienced a certain degree of wear and are therefore smaller than the original particles, as a result of our attempt to expose the unaltered OH phlogopite surface (Fig. S4.4).

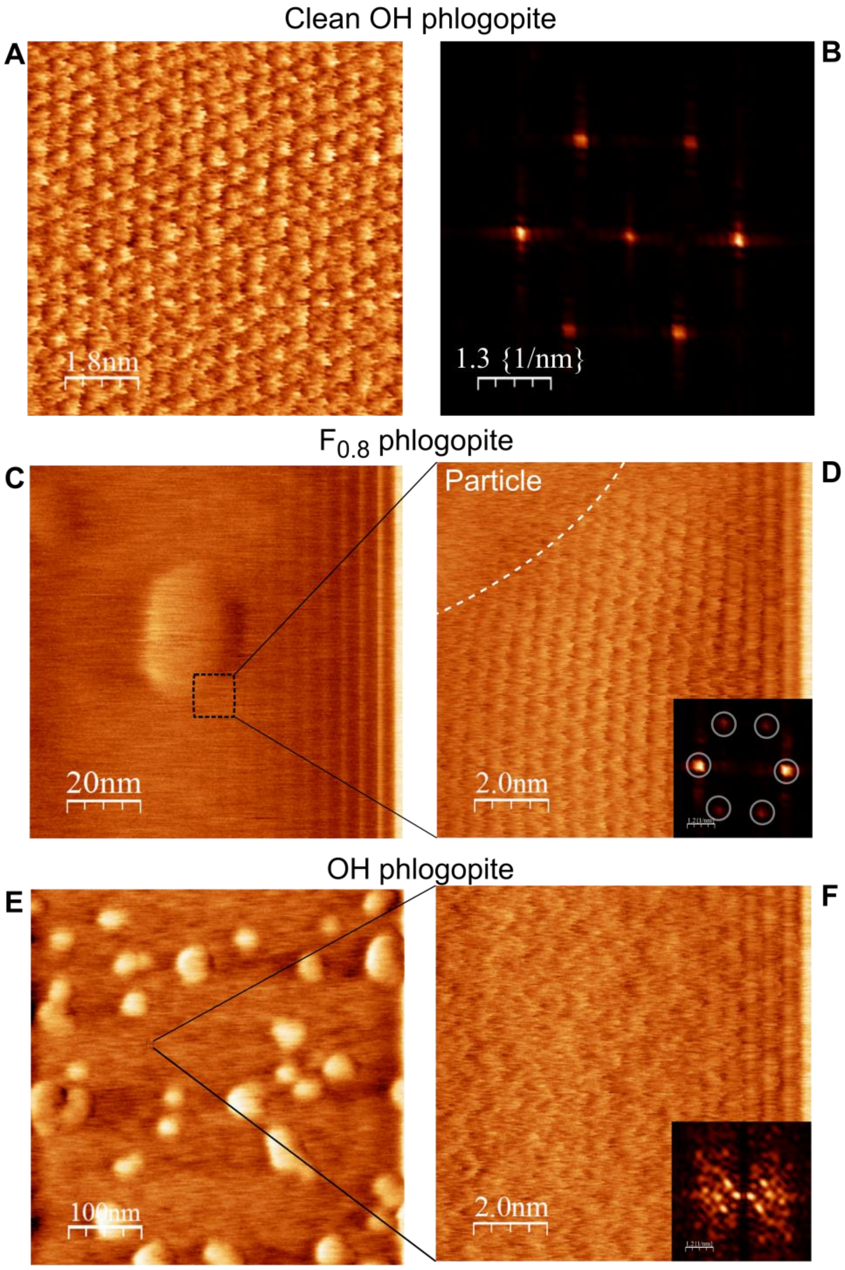

Figure 4.4. High-resolution images of phlogopite surfaces before and after the heterogeneous nucleation events. **(A)** High resolution friction image of a clean OH phlogopite surface under water before the experiment and **(B)** its 2D fast Fourier Transform (FFT) showing a hexagonal pattern. **(C)** High resolution friction image of $F_{0,8}$ phlogopite surface after the experiment with a heterogeneously nucleated $CaCO_3$ particle and **(D)** its high resolution friction image with 2D FFT. **(E)** 0,5x0,5 μm^2 friction image of OH phlogopite surface after the experiment with heterogeneously nucleated $CaCO_3$ particles and **(F)** its high resolution friction image with 2D FFT. Condition IV ($\sigma_{calcite} = 2.21$; $\sigma_{ACC} = 0.28$).

4.3.3. *Ex situ* observation by ATR-FTIR

ATR-FTIR absorbance spectra are shown in Figure 4.5 for F and OH phlogopite before and after nucleation experiments under condition III, the closest solution chemistry as the one employed (condition IV) in AFM observations since no FTIR feature was observable under this condition.

Intensity was normalized to the unity within the x-axis limit shown in each figure. Figure 4.5A compares the spectra of bear OH and F phlogopite before nucleation experiments, where OH phlogopite is characterized by a doublet peak at ~3711 and ~3670 cm^{-1}, attributed to the structural (octahedral) hydroxyl group (Šontevska et al., 2008; Sijakova-Ivanova and Cukovska, 2016), as well as a small feature of adsorbed water between 3600 and 3000 cm^{-1} (inset). F phlogopite lacks such features, in accordance with previous studies (Gianfagna et al., 2007; Scordari et al., 2013). Regions below 1000 cm^{-1} remained dominated by the strong signals from phlogopite after nucleation experiments, consequently peak assignments for $CaCO_3$ polymorphs were performed from 1800 to 1200 cm^{-1}. Spectra of ACC are typically characterized by a split peak of the asymmetric stretch of CO_3^{2-} (v_3) at ~1417 and ~1475 cm^{-1} (Addadi et al., 2003; Loste et al., 2003; Hodson et al., 2015; Demény et al., 2016), accompanied by a peak of in-plane bending (δ) of O-H, arising from the structural water of ACC (Loste et al., 2003; Rodriguez-Blanco et al., 2011; Demény et al., 2016). Such features were clearly observed on OH phlogopite at 1, 3, 6 hours (Fig. 4.5C) up to 4 days (Fig. S4.5A). On F phlogopite, on the other hand, the split peak of v_3 has an additional feature at 1400 cm^{-1}, corresponding to calcite (Addadi et al., 2003; Fleet et al., 2004; Demény et al., 2016). Given the presence of δ O-H at 1645 cm^{-1} at 1h, the nucleated phase is assigned to be a mixture of ACC and calcite. The spectra at 3 and 6h are tentatively assigned as a mixture of vaterite and calcite provided the absence of δ O-H and the shape of the v_3 peak (Hodson et al., 2015). The transformation of ACC to vaterite on F phlogopite was further supported by its 4-day spectrum that exhibits out-of-plane and in-plane bending of CO_3^{2-} (v_2 and v_4, respectively) corresponding to these phases (715, 742, and 874 cm^{-1}, data not shown) as well as the shape of the v_3 split peak (Sato and Matsuda, 1969; Noel et al., 2013) as shown in Figure S4.5A. Under conditions I and II (Fig. S4.5B), the spectra evolve in the same directions as condition III, but reactions proceed faster.

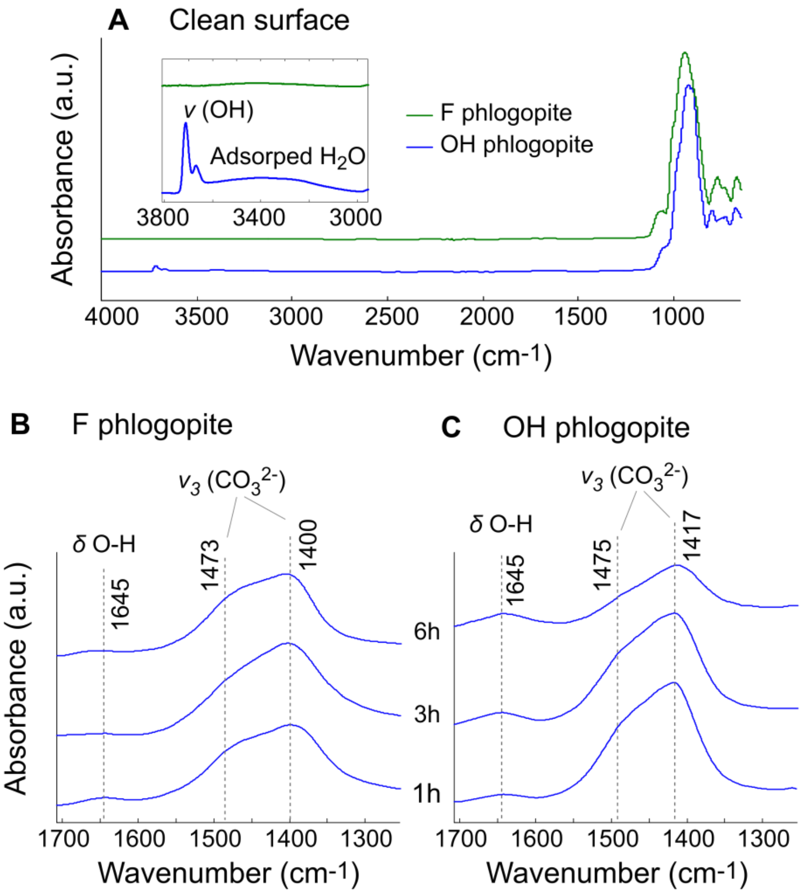

Figure 4.5. ATR-FTIR absorbance spectra **(A)** before and **(B, C)** after 1, 3, and 6 hours of reaction under condition III (σ_{calcite} = 2.67; σ_{ACC} = 0.74) for F and OH phlogopite. Intensity is normalized to the unity within the x-axis limits shown.

4.4. Discussion

4.4.1. Effect of surface hydrophobicity on α' values

The *in situ* time-resolved GISAXS experiments show that all systems were dominated by nucleation under the experimental conditions investigated (Figs. 4.2A and 4.2B). A quite narrow range of R_g values (~ 4 to 11 nm) was obtained and particle growth was only clearly observed for F phlogopite under condition I (Fig. 4.2A). The relatively simple method (i.e. Guinier approximation) used here to determine R_g values does not yield any information about the polydispersity, thus resulting in particle size values with relatively large error bars. In this regard, we specify that a precise analysis of the particle size is not the goal of this study. Within the framework of CNT, nevertheless, the size of primary particles is inversely proportional to the supersaturation (Kashchiev, 2000). This seems to hold only for the F phlogopite system and exclusively during the early stages of the reaction (< 45 min) for conditions I and II (Fig. 4.2A). This suggests that (i) the observed particles are not the critical nuclei and/or (ii) a complex nucleation pathway, involving intermediate entities, could be present. Indeed, though with very low counts (poor statistics), a plateau was observed in the high $\boldsymbol{q}$ region in some experimental conditions (data not shown), from which the existence of particles with a smaller size can be inferred, in which case, the nanometer-scale particles (~ 4 to 11 nm) observed here would have resulted from instantaneous aggregation of those smaller particles. In any case, the trends of the nucleation rates observed in our study can be fitted using the master equation of CNT (eq. 4.2), which suggests that, even if these particles are not the critical nuclei, the aggregation behavior of these particles provides a good proxy to study nucleation events and their properties.

The nucleation rate obtained accordingly yielded identical values of α' for F and OH phlogopite (Figs. 4.2C and 4.2D). This infers that both substrates possess the same barrier for nucleation and thus the nucleation mechanism may be the same, irrespective of surface hydrophobicity, despite our hypothesis that hydrophobicity is beneficial for heterogeneous nucleation, based on previous studies (Giuffre et al., 2013; Dai et al., 2016) as mentioned earlier. In fact, these studies employed substrates coated by different polysaccharides or self-assembled monolayers in order to tune the surface hydrophobicity, where authors did not take into account the changes in the α_{sc} term (interfacial energy between the substrate and the nucleating crystal) that is accompanied when using different functionalities since nuclei sees a different surface structure on a substrate functionalized, for instance, by chitosan than on a substrate functionalized by heparin as in the study by Giuffre et al. (Giuffre et al., 2013). Furthermore, additional factors such as structural flexibility and compressibility of these organic monolayers are inevitably present (Cooper et al., 1998; Duffy and Harding, 2004; Freeman et al., 2008). Considering these elements, in the present study, we employed phlogopite substrates with different OH/F ratios, presenting a high similarity in the surface structures, in an attempt to minimize the differences in α_{sc}, so that the α' values obtained reflects solely the effect of surface hydrophobicity. Provided the distinct morphological differences between F and OH phlogopite (Figs. 4.3C and 4.3D), it is important to recall that heterogeneous nucleation results from a competition between the fluid and the forming crystal for the substrate (eq. 4.4). As clearly demonstrated by our AFM observations, the nature of a substrate gives rise to particular interactions for a given crystal-substrate-fluid system. AFM and FTIR observations provide further insights into this last point.

4.4.2. Surface hydrophobicity controls the kinetic persistence of ACC

The roughness of the OH phlogopite surface determined by AFM in between the heterogeneously nucleated particles (Figs. 4.3D and 4.3F) indicated the presence of a continuous layer that is only partially removable (Fig. S4.4). Supported by the formation of ACC observed by FTIR (Fig. 4.5C), this continuous layer seen by AFM can be identified as a layer of ACC. On the contrary, the $F_{0.8}$ phlogopite shows a contrasting behavior: a bare surface was found between the heterogeneously nucleated particles (Figs. 4.3C and 4.3E). The formation of ACC was observed on F phlogopite at early stage of nucleation (Fig. 4.5B), which is further supported by the formation of vaterite (Fig. S4.5A) which usually forms via ACC (Pouget et al., 2010; Radha et al., 2010; Xiao et al., 2010; Rodriguez-Blanco et al., 2011). This consequently points to a shorter lifetime of the ACC layer on F phlogopite as compared to that on OH phlogopite as schematized in Figure 4.6, and this enhanced metastability of the ACC layer may also explains the promoted particle growth on this substrate, presumably through a dissolution-reprecipitation process. A plausible scenario for the enhanced kinetic persistence of ACC on OH phlogopite could be the promoted formation of hydrogen bonds between the water molecules of ACC and the basal oxygen atoms of the substrate provided its hydrophilicity.

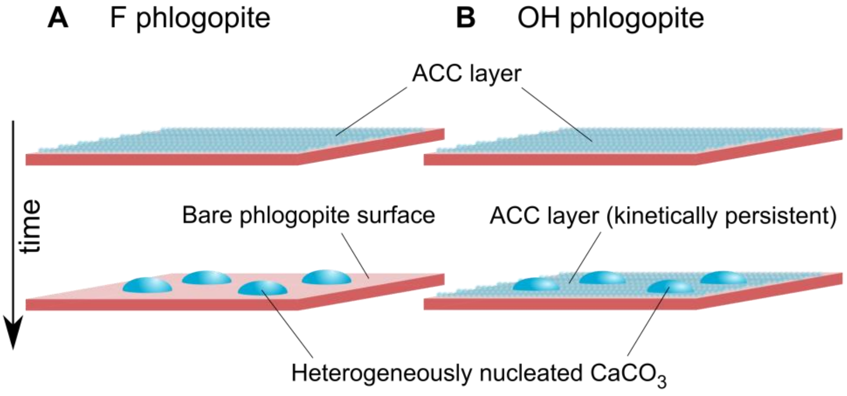

Figure 4.6. Schematic representation of **(A)** F phlogopite surface and **(B)** OH phlogopite surface covered with heterogeneously nucleated $CaCO_3$.

It is important to note that the *in situ* and *ex situ* experimental setups seemingly resulted in discrepancies regarding size and particle density between GISAXS and AFM study, which is also reported by Li et al. (2014) in similar experiments. Although the results complement each other, the degree of heterogeneous nucleation observed by the *ex situ* AFM study would have given rise to a higher scattering in particular from the larger particles (low $\boldsymbol{q}$) in the GISAXS patterns, even despite the difference in the proved size ranges (Fig. S4.6). This shall be attributed to the differences in the evolution of induction times resulting from the differences in the hydrodynamics of each experiment (*in situ* open flow *vs. ex situ* static) as one of the most relevant factors. Another non-negligible factor could be the use of ethanol in *ex situ* observations as quenching regent. In particular, AFM observation was performed under ethanol in addition to the quenching beforehand. These factors possibly increased the supersaturation at the interface and accelerated the crystallization process as compared to the *in situ* GISAXS experiments. This also explains the disparity in the kinetics of the ACC layer on F phlogopite between AFM and FTIR observations: rapid crystallization (< 15 min) on AFM images (Figs. 4.3 and 4.4) vs. the observation of ACC by FTIR after 1 hour (Fig. 4.5). Nevertheless, the relative stability of ACC on OH phlogopite with respect to F phlogopite remains valid.

4.4.3. Can there be thermodynamic contributions to the stability of ACC controlled by surface hydrophobicity?

Surface hydrophobicity does not seem to affect the absolute values of α', as discussed above. The effective interfaciale energy, however, results from a complex interplay between the three interfacial energies exerting at the interface between substrate, nuclei and solution, which also depends on the contact angle between the substrate and the nuclei (eq. 4.4). To further investigate the thermodynamic contributions to the stability of ACC controlled by surface hydrophobicity, a three-dimensional thermodynamic diagram for the three different interfacial free energies (Fig. 4.7) was built for each system using eq. 4.4 by making certain assumptions. First, we employ a hemispherical model for the heterogeneously nucleated particles when calcite was considered to be the formed polymorph, which makes $\theta = 90°$. For ACC, taking into account its hydrous character, θ is supposed to be very low on a hydrophilic OH phlogopite and is set to $\theta = 5°$, according to the contact angle values reported for hydrophilic muscovite mica (Bailey and Price, 1970; Christenson, 1993). A hypothetical, higher value of $\theta = 50°$ was selected for F phlogopite considering its hydrophobic character and hydrous nature of ACC. Since the value of the interfacial free energy of the solid-solid interface (substrate-crystal) α_{sc}, is experimentally the most difficult to measure and is therefore rarely reported in the literature, α_{sc} is plotted as the dependent variable (vertical axis) and α_{lc} and α_{ls} as the independent variables. Then, to evaluate the values of α_{sc}, representative, i.e. coherent, values were selected from the literature, such that $\alpha_{ls\text{-}OH} < \alpha_{ls\text{-}F}$ and $\alpha_{lc\text{-}ACC} < \alpha_{lc\text{-}calcite}$ (see red and blue lines in Fig. 4.7).

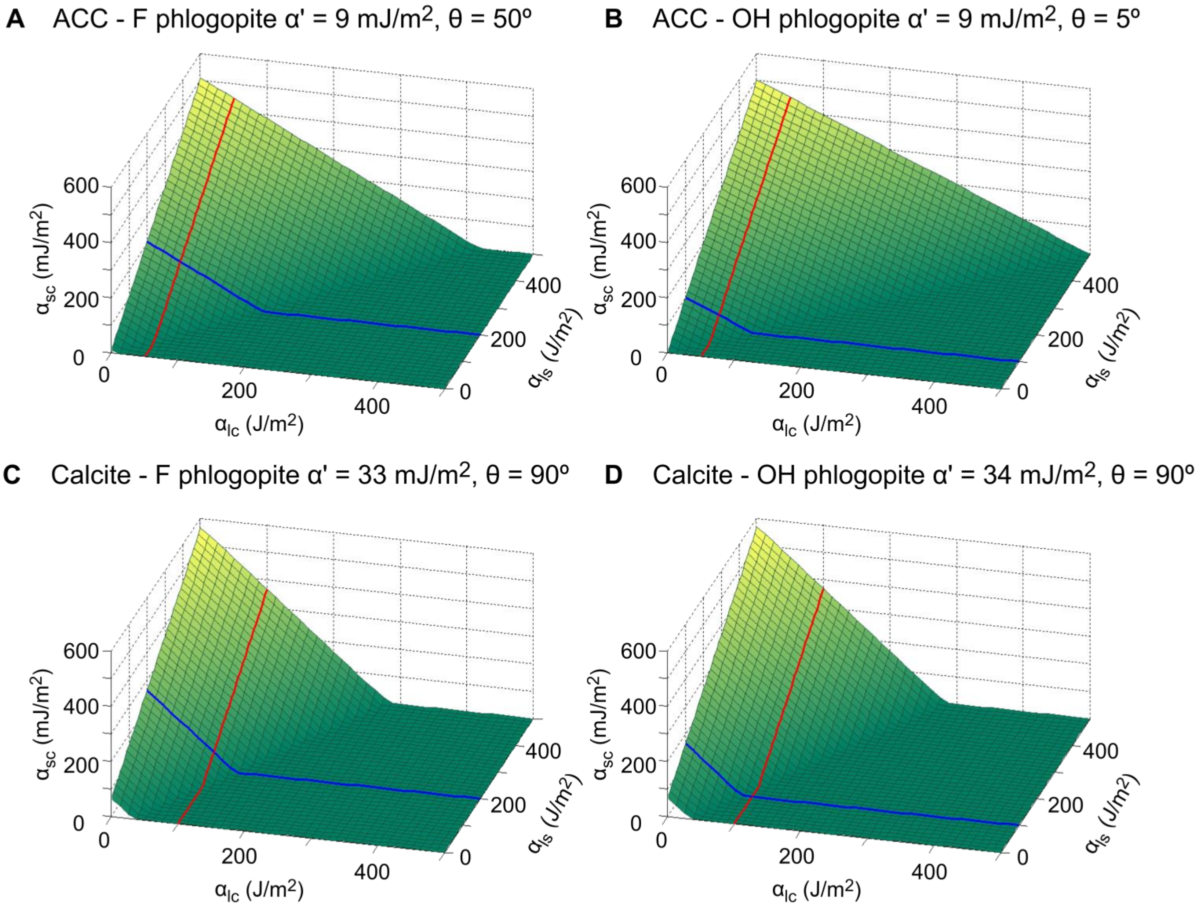

Figure 4.7. Interfacial free energy surfaces for **(A)** ACC – F phlogopite system, **(C)** ACC- OH phlogopite system , **(B)** Calcite – F phlogopite system and **(D)** Calcite – OH phlogopite system.The value of α_{sc} (substrate - crystal) is plotted as a function of different values for α_{lc} (liquid - crystal)' α_{ls} (liquid - substrate), using the value of the effective interfacial energy α' obtained from the GISAXS experiments. θ was set as 50° and 90° for ACC and calcite, respectively, for F phlogopite and 5° and 90° for ACC and calcite, respectively, for OH phlogopite. The red and the blue lines refer to representative values found in the literature.

One must note, however, a significant discrepancy in the values of α_{lc} and α_{ls} reported in the literature. For instance, α_{ls} values for water - muscovite mica range from ~3-5 mJ/m^2 (Pashley, 1981; Christenson, 1993) to 107 mJ/m^2 (Bailey and Kay, 1967; Bailey and Price, 1970). Contributing factors to such a discrepancy may be the roughness of the surface after cleavage, freshness of the cleaved surface, or the presence of K_2CO_3 adsorbates formed on air-cleaved mica (Christenson and Thomson, 2016). The value of α_{lc} for water – $CaCO_3$ also varies, and in addition, depends on the faces and the polymorphs considered. A calorimetric approach yielded 1480 mJ/m^2 (Forbes et al., 2011), while much lower values were obtained from homogeneous and heterogeneous nucleation experiments. Examples include a value of 98 mJ/m^2 for homogeneous calcite nucleation (Söhnel and Mullin, 1982); 43 mJ/m^2 for homogeneous vaterite nucleation in presence of alcohols (Manoli and Dalas, 2000); 30-32 mJ/m^2 for heterogeneous calcite nucleation on carboxylated polymers (Dousi et al., 2003); 36

mJ/m^2 for heterogeneous calcite nucleation on quartz (Fernandez-Martinez et al., 2013a) and 24-47 mJ/m^2 for heterogeneous vaterite and calcite nucleation on muscovite mica and quartz (Li et al., 2014). Computational studies yielded values ranging from 160 (de Leeuw and Parker, 1998) to 412 mJ/m^2 (Bruno et al., 2013) for the most stable (1014) calcite face. Although the plane of nucleation is expected to be related to surface wetting properties (Chevalier, 2014) or to the surface tension (Chevalier and Guenoun, 2016), it remains unknown from our AFM images (Figs. 4.3C and 4.3D). Epitaxial growth of calcite on muscovite mica (001) has been observed to be promoted due to the presence of K_2CO_3, except for the freshly cleaved mica (Stephens et al., 2010), though this is not applicable to our case since cleavage was performed under ultra-pure water.

A close inspection of these diagrams infers that the preference of ACC for the hydrophilic substrate demonstrated here experimentally is also reflected in this thermodynamic diagram. The α_{sc} value obtained (crossing point of the red and blue lines) for ACC on the OH phlogopite (Fig. 4.7B) is lower than that for the F phlogopite (Fig. 4.7A). Also, the α_{sc} value for calcite on the F phlogopite (Fig. 4.7C) is lower than that for ACC (Fig. 4.7A), which implies another thermodynamic driver for crystallization via the minimization of all the interfacial free energies (ACC would form first, but it would crystallize to calcite to minimize the value of α_{sc}). For the OH system (Figs. 4.7B and 4.7D), the α_{sc} value for calcite on the OH phlogopite is negative (negative values in Figure. 4.7 have been set to zero), which indicates a non-physical situation. Given the absence of calcite on OH phlogopite according to the FTIR observations (Figs. 4.5C), this may infer that (i) calcite cannot nucleate directly on OH phlogopite, and its formation proceeds always via an amorphous intermediate (ACC) or (ii) wrong estimations for α_{ls} and α_{lc} are used. Given the uncertainties in the values of all the interfacial free energies as discussed above, we cannot give more weight to one of these two possibilities, and both remain plausible. Overall, nucleation of ACC seems more prone on OH phlogopite than on F phlogopite (Figs. 4.7A and 4.7B). In fact, as long as $\alpha_{lc\text{-}ACC} < \alpha_{lc\text{-}calcite}$, which seems to be a reasonable hypothesis, α_{sc} is always found to be lower for calcite than for ACC when $\alpha_{ls} = 100$ mJ/m^2. This would also have occurred for F phlogopite if a higher value of α_{lc} was selected, although the energetic preference for calcite over ACC wouldn't have changed. Sensitivity tests (data not shown) showed that the resulting interfacial energy values are more sensitive to the θ values than to the α' values. Increasing α' is followed by an incremental increase in the slope of the 3D surface, whereas increasing θ is followed by a more abrupt change in the tilt of the surface (Fig. 4.7), which limits or extends the range of non-physical values of α_{sc}.

4.4.4. Limitation in the application of CNT

Our results are based on the conceptual model of CNT and under the so-called capillary approximation that the initially formed nuclei have the same structural nature as the final crystal. However, studies in the last decade report that nucleation process follows a multistep pathway involving pre-nucleation clusters, supposedly, of different structural nature than those of the crystalline polymorphs, although their exact structural description has not been achieved yet (Gebauer et al., 2008; Gebauer and Cölfen, 2011). It is therefore reasonable to conceive nucleation as a continuous structural evolution, with initially formed clusters that subsequently form liquid polymers of evolving density due to continuous dehydration (Demichelis et al., 2011; Wallace et al., 2013). These polymers would eventually form an amorphous phase or a solid polymorph. Under these assumptions of a continuous evolution, the geometry of the surface plotted in Figure 4.7 would also show a continuous evolution depending on the exact nature of the nucleated phase (a cluster, a polymer, or a dense liquid), so as the effective interfacial energy. These results underline the limitation of macroscopic values such as surface tension (Ruckenstein and Djikaev, 2005), which are presumably over predicted for small clusters (Christoffersen et al., 1991), and of the capillary approximation used in CNT (Kashchiev, 2000).

4.5. Conclusion

The presence of an interface is ubiquitous and the surface property such as surface hydrophobicity is one of the major factors affecting the heterogeneous nucleation behaviors relevant to numerous processes from biomineralization to subsurface reactive transport and scale formation. Contrary to the initial hypotheses, the *in situ* GISAXS experiments yielded almost identical values for the effective interfacial energy for both the hydrophilic and the hydrophobic substrates (33-34 and 9 mJ/m^2 for calcite and ACC, respectively). Thus, the nucleation barrier is the same, irrespective of the surface hydrophobicity, and so is the nucleation pathway, as confirmed by the formation of ACC layer on both substrates. Interestingly, however, the fate of this ACC layer is kinetically controlled by the surface hydrophobicity. The hydrophilic substrate enhanced its kinetic persistence as compared to hydrophobic one, presumably by the interactions between the water molecules of ACC and the hydrophilic substrate and by the reduction of the interfacial penalty between the nuclei and the substrate (α_{sc}).

The distinctive morphological differences observed, together with the identical values for the effective interfacial free energies obtained, point to the fact that the $CaCO_3$ system has a great 'structural flexibility', which allows it to nucleate on substrates of contrastingly hydrophobicity. This ability to adapt to the substrate properties could be reflected by the different binding environments, thus different energetic minima, present in $CaCO_3$ crystals themselves. For instance, Ca^{2+} and CO_3^- can bind through either monodentate (one oxygen atom shared) or bidentate (two oxygen atoms shared) ligands and it is known that each polymorph has different proportions of such ligands (100% monodentate in calcite and ~50% in ACC and aragonite). Furthermore, the binding structure of $CaCO_3$ unit is different for hydrous polymorphs. For instance, isolated, hydrated ion pairs are present in the ikaite structure whereas one H_2O molecule is hosted by each $CaCO_3$ unit in monohydrocalcite. In addition to this, ACC, due to its inherent structural disorder, offers even more options for the forming solid to adapt to a variety of substrate environments. This structural variability reflects a complex potential energy surface with many local minima in the configuration space, supporting the observed ability to adapt to remarkably different environments such as those provided by OH and F phlogopite substrates, as shown here. Perhaps, a system bearing no poly(a)morphs such as NaCl can be a good candidate to discern this hypothesized ‘structural flexibility’ as one of the major parameters governing the pathways and ability to nucleate heterogeneously.

This work provides a mechanistic view of $CaCO_3$ heterogeneous nucleation on phlogopite substrates with different hydrophobicity, showing that the nature of the nucleating solid, the existence of an amorphous precursor, and its ‘structural flexibility’ are key for predicting the nucleation behavior.

Supporting information

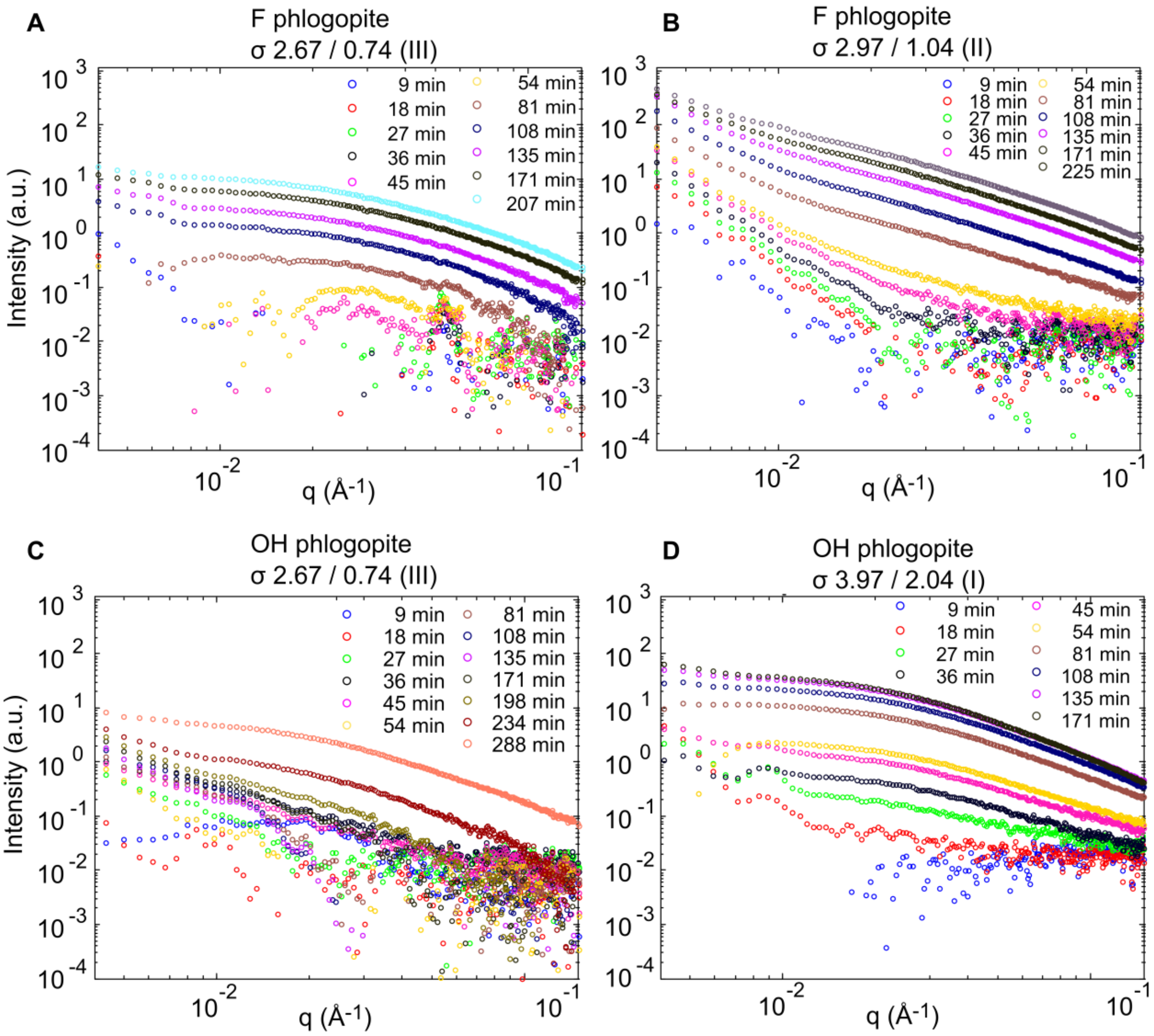

Figure S4.1. Evolution of 1D GISAXS pattern along the interface for **(A, B)** $CaCO_3$ – F phlogopite and **(C, D)** $CaCO_3$ - OH phlogopite systems at different supersaturations ($\sigma_{calcite}$ / σ_{ACC}).

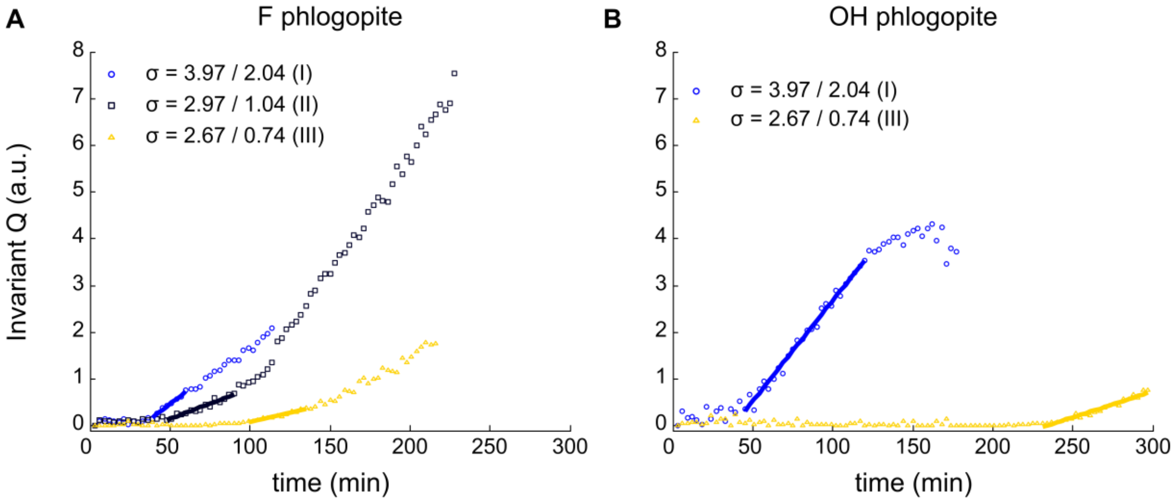

Figure S4.2. Evolution of GISAXS invariant *Q* for **(A)** F phlogopite and **(B)** OH phlogopite at different supersaturations (σ_{calcite} / σ_{ACC}). Linear regressions are performed on the data rage shown by the straight lines, from which the slopes are used to estimate the nucleation rate J_{n} and the *x*-intercepts to estimate the induction time T_{n}.

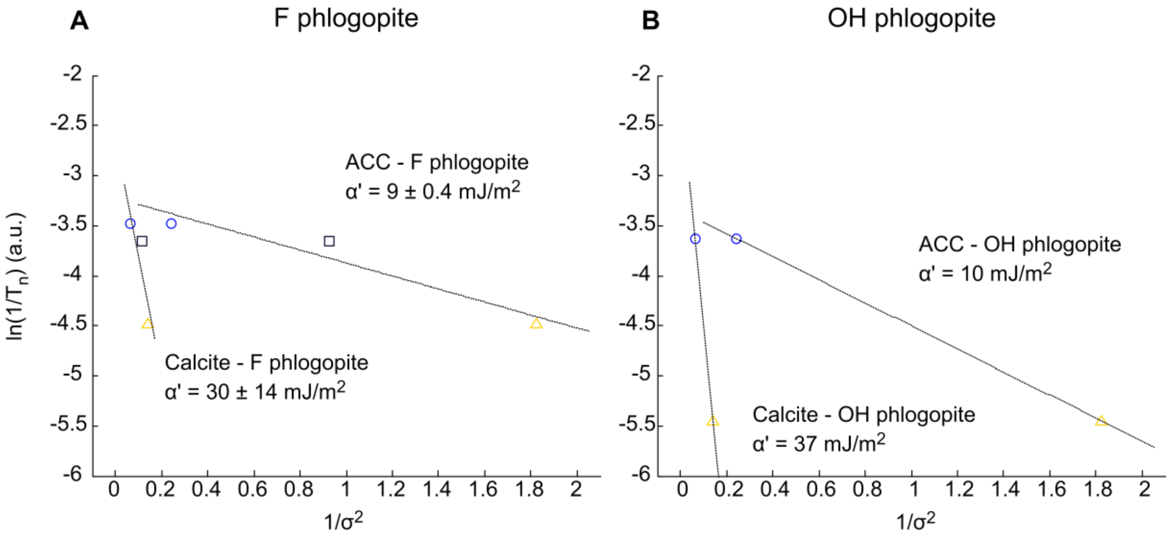

Figure S4.3. Effective interfacial energies *α'* for calcite and ACC estimated based on the induction time T_n (Fig. S4.2), for **(A)** CaCO3 - F phlogopite and **(B)** CaCO3 - OH phlogopite. The confidence intervals (2SE) of *α'* for F phlogopite are calculated from the T_n values.

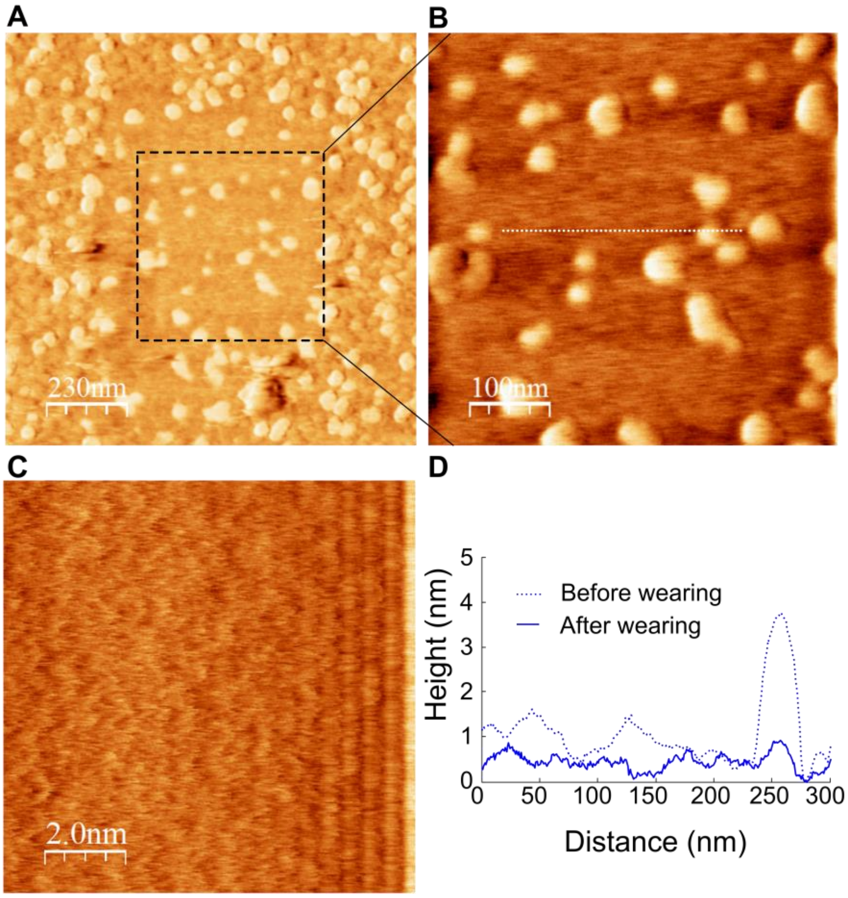

Figure S4.4. Wear of $CaCO_3$ precipitate. **(A)** 1.15 x 1.15 µm^2 friction image of OH phlogopite covered with $CaCO_3$ particles after 16 scan lines at an applied force of 50.4 nN. **(B)** Friction image of the zoomed area. **(C)** High resolution friction image of the phlogopite surface. **(D)** Height profiles before and after wearing along the dotted line shown in B.

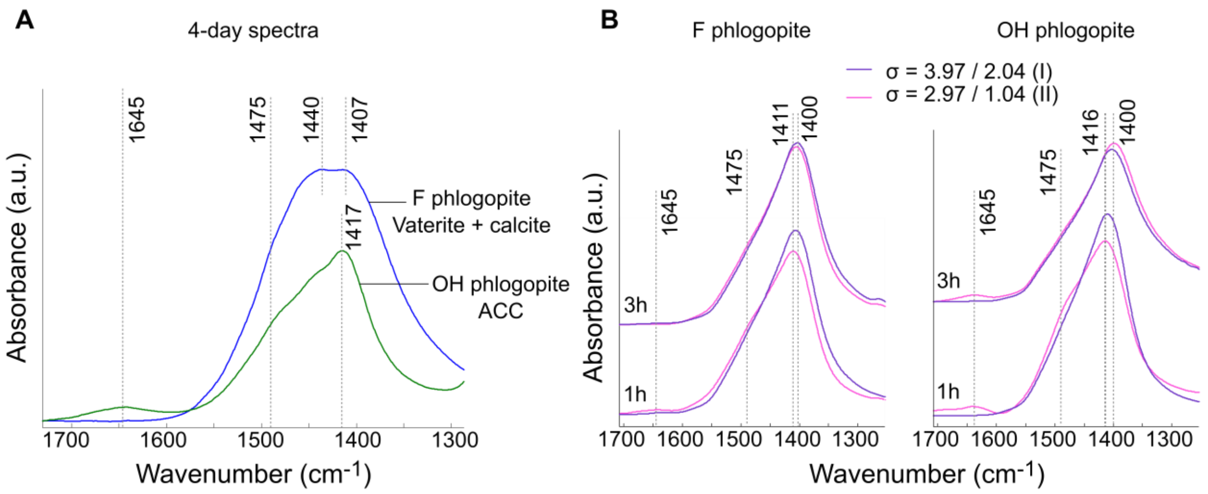

Figure S4.5. (A) ATR-FTIR spectra of F and OH phlogopite after 4 days under condition III. **(B)** ATR-FTIR spectra of F and OH phlogopite after 1 and 3 hours under conditions I and II.

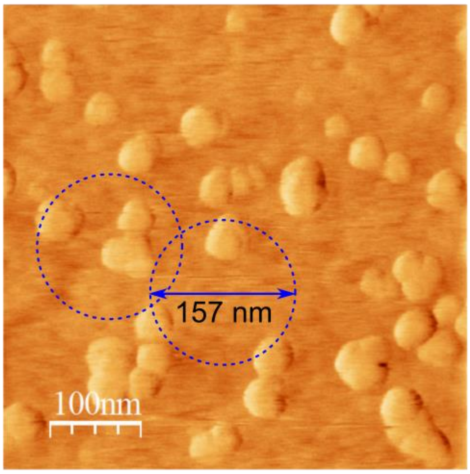

Figure S4.6. Size-range proved by *in situ* GISAXS (shown by circles) as compared to a typical size range proved by AFM.

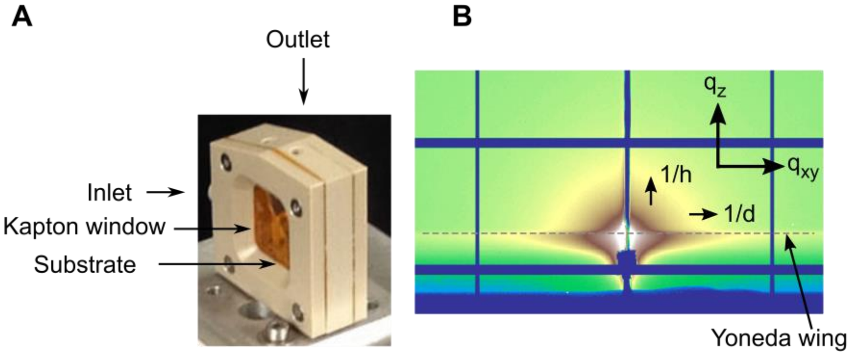

Figure S4.7. Custom-made fluid cell used for GISAXS measurements and a representative intensity pattern. **(A)** Cell is equipped with Kapton windows and inlet/outlet for solutions. Substrate glued on a sample holder is slid horizontally at the bottom of the cell through slits created for its purpose. **(B)** The dotted line indicates the so-called Yoneda wing (anomalous reflection).

References

Addadi L., Raz S. and Weiner S. (2003) Taking advantage of disorder: Amorphous calcium carbonate and its roles in biomineralization. *Adv. Mater.* **15**, 959–970.

Aizenberg J. (2010) New Nanofabrication Strategies: Inspired by Biomineralization. *MRS Bull.* **35**, 323–330.

Bailey A. I. and Kay S. M. (1967) A Direct Measurement of the Influence of Vapour, of Liquid and of Oriented Monolayers on the Interfacial Energy of Mica. *Proc. R. Soc. A Math. Phys. Eng. Sci.* **301**, 47–56.

Bailey A. I. and Price A. G. (1970) Interfacial Energies of Clean Mica and of Monomolecular Films of Fatty Acids Deposited on Mica, in Aqueous and Non-Aqueous Media. *Spec. Discuss. Faraday Soc.* **1**, 118–127.

Beaucage G. (1996) Small-Angle Scattering from Polymeric Mass Fractals of Arbitrary Mass-Fractal Dimension. *J. Appl. Crystallogr.* **29**, 134–146.

Beaucage G., Kammler H. K. and Pratsinis S. E. (2004) Particle size distributions from small-angle scattering using global scattering functions. *J. Appl. Crystallogr.* **37**, 523–535.

Bhushan B. ed. (2007) *Springer Handbook of Nanotechnology*. 2nd ed., Springer.

Bruno M., Massaro F. R., Pastero L., Costa E., Rubbo M., Prencipe M. and Aquilano D. (2013) New estimates of the free energy of calcite/water interfaces for evaluating the equilibrium shape and nucleation mechanisms. *Cryst. Growth Des.* **13**, 1170–1179.

Chen T., Neville A. and Yuan M. (2005) Calcium carbonate scale formation - Assessing the initial stages of precipitation and deposition. *J. Pet. Sci. Eng.* **46**, 185–194.

Chevalier N. R. (2014) Do surface wetting properties affect calcium carbonate heterogeneous nucleation and adhesion? *J. Phys. Chem. C* **118**, 17600–17607.

Chevalier N. R. and Guenoun P. (2016) Surface Tension Drives the Orientation of Crystals at the Air-Water Interface. *J. Phys. Chem. Lett.* **7**, 2809–2813.

Chiquet P., Broseta D. and Thibeau S. (2007) Wettability alteration of caprock minerals by carbon dioxide. *Geofluids* **7**, 112–122.

Christenson H. K. (1993) Adhesion and surface energy of mica in air and water. *J. Phys. Chem.* **97**, 12034–12041.

Christenson H. K. and Thomson N. H. (2016) The nature of the air-cleaved mica surface. *Surf. Sci. Rep.* **71**, 367–390.

Christoffersen J., Rostrup E. and Christoffersen M. R. (1991) Relation between interfacial surface tension of electrolyte crystals in aqueous suspension and their solubility; a simple derivation based on surface nucleation. *J. Cryst. Growth* **113**, 599–605.

Cooper S. J., Sessions R. B. and Lubetkin S. D. (1998) A new mechanism for nucleation beneath monolayer films? *J. Am. Chem. Soc.* **120**, 2090–2098.

Dai C., Stack A. G., Koishi A., Fernandez-Martinez A., Lee S. S. and Hu Y. (2016) Heterogeneous Nucleation and Growth of Barium Sulfate at Organic–Water Interfaces: Interplay between Surface Hydrophobicity and Ba 2+ Adsorption. *Langmuir* **32**, 5277–5284.

Dazas B., Lanson B., Breu J., Robert J. L., Pelletier M. and Ferrage E. (2013) Smectite fluorination and its impact on interlayer water content and structure: A way to fine tune the hydrophilicity of clay surfaces? *Microporous Mesoporous Mater.* **181**, 233–247.

Demény A., Németh P., Czuppon G., Leél-Őssy S., Szabó M., Judik K., Németh T. and Stieber J. (2016) Formation of amorphous calcium carbonate in caves and its implications for speleothem research. *Sci. Rep.* **6**.

Demichelis R., Raiteri P., Gale J. D., Quigley D. and Gebauer D. (2011) Stable prenucleation mineral clusters are liquid-like ionic polymers. *Nat. Commun.* **2**.

Demyanova L. P. and Tressaud A. (2009) Fluorination of alumino-silicate minerals: The example of lepidolite. *J. Fluor. Chem.* **130**, 799–805.

Dong W., Ball W. P., Liu C., Wang Z., Stone A. T., Bai J. and Zachara J. M. (2005) Influence of calcite and dissolved calcium on uranium(VI) sorption to a Hanford subsurface sediment. *Environ. Sci. Technol.* **39**, 7949–7955.

Dousi E., Kallitsis J., Chrissanthopoulos A., Mangood A. H. and Dalas E. (2003) Calcite overgrowth on carboxylated polymers. *J. Cryst. Growth* **253**, 496–503.

Van Driessche A. E. S., Kellermeier M., Benning L. G. and Gebauer D. eds. (2017) *New Perspectives on Mineral Nucleation and Growth: From Solution Precursors to Solid Materials*., Springer.

Duffy D. M. and Harding J. H. (2004) Simulation of organic monolayers as templates for the nucleation of calcite crystals. *Langmuir* **20**, 7630–7636.

Espinoza D. N. and Santamarina J. C. (2010) Water-CO2-mineral systems: Interfacial tension, contact angle, and diffusion—Implications to CO2 geological storage. *Water Resour. Res.* **46**.

Fernandez-Martinez A., Hu Y., Lee B., Jun Y.-S. and Waychunas G. A. (2013a) In Situ Determination of Interfacial Energies between Heterogeneously Nucleated CaCO3 and Quartz Substrates: Thermodynamics of CO2 Mineral Trapping. *Environ. Sci. Technol.* **47**, 102–109.

Fernandez-Martinez A., Kalkan B., Clark S. M. and Waychunas G. a. (2013b) Pressure-induced polyamorphism and formation of “aragonitic” amorphous calcium carbonate. *Angew. Chemie - Int. Ed.* **52**, 8354–8357.

Fleet M. E., Liu X. and King P. L. (2004) Accommodation of the carbonate ion in apatite: An FTIR and X-ray structure study of crystals synthesized at 2-4 GPa. *Am. Mineral.* **89**, 1422–1432.

Forbes T. Z., Radha A. V. and Navrotsky A. (2011) The energetics of nanophase calcite. *Geochim. Cosmochim. Acta* **75**, 7893–7905.

Freeman C. L., Harding J. H. and Duffy D. M. (2008) Simulations of calcite crystallization on self-assembled monolayers. *Langmuir* **24**, 9607–9615.

Fujita Y., Ferris F. G., Lawson R. D., Colwell F. S. and Smith R. W. (2000) Calcium Carbonate

Precipitation by Ureolytic Subsurface Bacteria. *Geomicrobiol. J.* **17**, 305–318.

Gebauer D. and Cölfen H. (2011) Prenucleation clusters and non-classical nucleation. *Nano Today* **6**, 564–584.

Gebauer D., Völkel A., Cölfen H., Volkel A. and Colfen H. (2008) Stable prenucleation calcium carbonate clusters. *Science* **322**, 1819–1822.

Gianfagna A., Scordari F., Mazziotti-Tagliani S., Ventruti G. and Ottolini L. (2007) Fluorophlogopite from Biancavilla (Mt. Etna, Sicily, Italy): Crystal structure and crystal chemistry of a new F-dominant analog of phlogopite. *Am. Mineral.* **92**, 1601–1609.

Gibbs J. W. (1878) On the Equilibrium of Heterogeneous Substances. *Trans. Connect. Acad.* **3**, 108-248-524.

Giuffre A. J., Hamm L. M., Han N., De Yoreo J. J. and Dove P. M. (2013) Polysaccharide chemistry regulates kinetics of calcite nucleation through competition of interfacial energies. *Proc. Natl. Acad. Sci. U. S. A.* **110**, 9261–9266.

Hodson M. E., Benning L. G., Demarchi B., Penkman K. E. H., Rodriguez-Blanco J. D., Schofield P. F. and Versteegh E. A. A. (2015) Biomineralisation by earthworms - an investigation into the stability and distribution of amorphous calcium carbonate. *Geochem. Trans.* **16**.

Jun Y. S., Lee B. and Waychunas G. A. (2010) In situ observations of nanoparticle early development kinetics at mineral-water interfaces. *Environ. Sci. Technol.* **44**, 8182–8189.

Kashchiev D. (2000) *Nucleation: Basic Theory with Applications*., Butterworth-Heinemann, Oxford.

Kellermeier M., Picker A., Kempter A., Cölfen H. and Gebauer D. (2014) A straightforward treatment of activity in aqueous CaCo3 solutions and the consequences for nucleation theory. *Adv. Mater.* **26**, 752–757.

Kuwahara Y. (2001) Comparison of the surface structure of the tetrahedral sheets of muscovite and phlogopite by AFM. *Phys. Chem. Miner.* **28**.

de Leeuw N. H. and Parker S. C. (1998) Surface Structure and Morphology of Calcium Carbonate Polymorphs Calcite, Aragonite, and Vaterite: An Atomistic Approach. *J. Phys. Chem. B* **102**, 2914–2922.

Li Q., Fernandez-Martinez A., Lee B., Waychunas G. A. and Jun Y. S. (2014) Interfacial energies for heterogeneous nucleation of calcium carbonate on mica and quartz. *Environ. Sci. Technol.* **48**, 5745–5753.

Loste E., Wilson R. M., Seshadri R. and Meldrum F. C. (2003) The role of magnesium in stabilising amorphous calcium carbonate and controlling calcite morphologies. *J. Cryst. Growth* **254**, 206–218.

Lowenstam H. A. and Weiner S. (1989) *On Biomineralization*., Oxford University Press, New York.

Manoli F. and Dalas E. (2000) Spontaneous precipitation of calcium carbonate in the presence of ethanol, isopropanol and diethylene glycol. *J. Cryst. Growth* **218**, 359–364.

Markgraf S. A. and Reeder S. A. (1985) High-temperature structure refinements of calcite and magnesite. *Am. Mineral.* **70**, 590–600.

McCarthy J. F. and Zachara J. M. (1989) Subsurface transport of contaminants: binding to mobile and immobile phases in groundwater aquifers. *Environ. Sci. Technol.* **23**, 496–502.

Meyers M. A., McKittrick J. and Chen P.-Y. (2013) Structural Biological Materials: Critical Mechanics-Materials Connections. *Science* **339**, 773–779.

Michot L. J., Villieras F., Francois M., Yvon J., Le Dred R. and Cases J. M. (1994) The Structural Microscopic Hydrophilicity of Talc. *Langmuir* **10**, 3765–3773.

Morse J. W., Arvidson R. S. and Lüttge A. (2007) Calcium carbonate formation and dissolution. *Chem. Rev.* **107**, 342–381.

Noel E. H., Kim Y.-Y., Charnock J. M. and Meldrum F. C. (2013) Solid state crystallization of amorphous calcium carbonate nanoparticles leads to polymorph selectivity. *CrystEngComm* **15**, 697–705.

Parkhurst B. D. L. and Appelo C. A. J. (1999) User's Guide To PHREEQC (version 2) — a Computer Program for Speciation, and Inverse Geochemical Calculations. *Exch. Organ. Behav. Teach. J.*

Pashley R. M. (1981) DLVO and hydration forces between mica surfaces in Li+, Na+, K+, and Cs+ electrolyte solutions: A correlation of double-layer and hydration forces with surface cation exchange properties. *J. Colloid Interface Sci.* **83**, 531–546.

Petersen E. U., Essene E. J., Peacor D. R. and Valley J. W. (1982) Fluorine end-member micas and amphiboles. *Am. Mineral.* **67**, 538–544.

Pimentel C., Pina C. M. and Gnecco E. (2013) Epitaxial growth of calcite crystals on dolomite and kutnahorite (104) surfaces. *Cryst. Growth Des.* **13**, 2557–2563.

Plummer L. N. and Busenberg E. (1982) The solubilities of calcite, aragonite and vaterite in CO2-H2O solutions between 0 and 90°C, and an evaluation of the aqueous model for the system CaCO3-CO2-H2O. *Geochim. Cosmochim. Acta* **46**, 1011–1040.

Pouget E. M., Bomans P. H. H., Dey A., Frederik P. M., de With G. and Sommerdijk N. A. J. M. (2010) The Development of Morphology and Structure in Hexagonal Vaterite. *J. Am. Chem. Soc.* **132**, 11560–11565.

Prieto M. (2014) Nucleation and supersaturation in porous media (revisited). *Mineral. Mag.* **78**, 1437–1447.

Radha A. V., Forbes T. Z., Killian C. E., Gilbert P. U. P. A. and Navrotsky A. (2010) Transformation and crystallization energetics of synthetic and biogenic amorphous calcium carbonate. *Proc. Natl. Acad. Sci. U. S. A.* **107**, 16438–16443.

Renaud G., Lazzari R. and Leroy F. (2009) Probing surface and interface morphology with Grazing Incidence Small Angle X-Ray Scattering. *Surf. Sci. Rep.* **64**, 255–380.

Rodriguez-Blanco J. D., Shaw S. and Benning L. G. (2011) The kinetics and mechanisms of amorphous calcium carbonate (ACC) crystallization to calcite, viavaterite. *Nanoscale* **3**, 265–271.

Rotenberg B., Patel A. J. and Chandler D. (2011) Molecular explanation for why talc surfaces can be both hydrophilic and hydrophobic. *J. Am. Chem. Soc.* **133**, 20521–20527.

Ruckenstein E. and Djikaev Y. S. (2005) Recent developments in the kinetic theory of nucleation. *Adv. Colloid Interface Sci.* **118**, 51–72.

Sanders R. and Henson S. (2014) Ecological Carbon Sequestration in the Oceans and Climate Change. In *Global Environmental Change* Springer Netherlands. pp. 125–131.

Sato M. and Matsuda S. (1969) Structure of vaterite and infrared spectra. *Zeitschrift fur Krist. - New Cryst. Struct.* **129**, 405–410.

Scordari F., Schingaro E., Ventruti G., Nicotra E., Viccaro M. and Tagliani S. M. (2013) Fluorophlogopite from Piano delle Concazze (Mt. Etna, Italy): Crystal chemistry and implications for the crystallization conditions. *Am. Mineral.* **98**, 1017–1025.

Sijakova-Ivanova T. and Cukovska L. R. (2016) Mineralogical characteristics of phlogopite from Dupen kamen, Republic of Macedonia. *IOSR J. Appl. Geol. Geophys.* **4**, 72–76.

Söhnel O. and Garside J. (1992) *Precipitation—Basic Principles and Industrial Applications*., Butterworth-Heinemann.

Söhnel O. and Mullin J. W. (1982) Precipitation of calcium carbonate. *J. Cryst. Growth* **60**, 239–250.

Sommerdijk N. a J. M. and With G. De (2008) Biomimetic CaCO3 Mineralization using Designer Molecules and Interfaces. *Chem. Rev.* **108**, 4499–4550.

Šontevska V., Jovanovski G., Makreski P., Raškovska A. and Šoptrajanov B. (2008) Minerals from Macedonia. XXI. Vibrational spectroscopy as identificational tool for some phyllosilicate minerals. *Acta Chim. Slov.* **55**, 757–766.

Stawski T. M., van Driessche A. E. S., Ossorio M., Diego Rodriguez-Blanco J., Besselink R. and Benning L. G. (2016) Formation of calcium sulfate through the aggregation of sub-3 nanometre primary species. *Nat. Commun.* **7**.

Stephens C. J., Mouhamad Y., Meldrum F. C. and Christenson H. K. (2010) Epitaxy of calcite on mica. *Cryst. Growth Des.* **10**, 734–738.

Wallace A. F., Hedges L. O., Fernandez-Martinez A., Raiteri P., Gale J. D., Waychunas G. A., Whitelam S., Banfield J. F. and De Yoreo J. J. (2013) Microscopic evidence for liquid-liquid separation in supersaturated CaCO3 solutions. *Science* **341**, 885–889.

Warren L. A., Maurice P. A., Parmar N. and Ferris F. G. (2001) Microbially Mediated Calcium Carbonate Precipitation: Implications for Interpreting Calcite Precipitation and for Solid-Phase Capture of Inorganic Contaminants. *Geomicrobiol. J.* **18**, 93–115.

Wedepohl K. H. ed. (1978) *Handbook of Geochemistry: Vol. II/1.*, Springer-Verlag.

Whittaker M. L., Dove P. M. and Joester D. (2016) Nucleation on surfaces and in confinement. *MRS Bull.* **41**, 388–392.

Xiao J., Wang Z., Tang Y. and Yang S. (2010) Biomimetic mineralization of CaCO3 on a phospholipid monolayer: From an amorphous calcium carbonate precursor to calcite via vaterite. *Langmuir* **26**, 4977–4983.

Yang Q., Liu Y., Gu A., Ding J. and Shen Z. (2001) Investigation of Calcium Carbonate Scaling Inhibition and Scale Morphology by AFM. *J. Colloid Interface Sci.* **240**, 608–621.

Chapter 5

Surface hydrophobicity and properties of interfacial water

5.1. Introduction

The formation of electric double layer (EDL) is ubiquitous whenever there is an electrolyte-solid interface, and its molecular-scale characteristics have been of particular research interest for decades due to the important chemical reactions occurring in it (Brown, 2001). Both the type of dissolved ionic species and the specific properties of the mineral surface play significant role in controlling the EDL properties. The EDL has control over sorption/desorption and precipitation mechanisms involved in a wide range of processes in biology, geology and engineered systems (Damaskin and Frumkin, 1974; Brown et al., 1999; Menzel, 2002; Sposito, 2004; Siretanu et al., 2014). Surface hydrophobicity is one of the most important physicochemical properties of a substrate, due to the significant consequences that it has on the interfacial water structure and dynamics. The hydrophobicity of a surface, at large, has generally been related to an increase of contact angles (Keller et al., 2011; Chevalier, 2014), enhanced precipitation (Tyrrell and Attard, 2002; Giuffre et al., 2013), and depleted interfacial water density (Schwnedel et al., 2003; Steitz et al., 2003; Poynor et al., 2006; Janecek and Netz, 2007; Maccarini et al., 2007). Though hydrophobic effects have been of active interest in areas such as biophysics (Pratt and Pohorille, 2002), it is only in the last decades that computational efforts have provided molecular details of interfacial water configurations at such interfaces. For instance, a study by Wang et al. (2009) demonstrated that the depleted water density at a water-talc interface, a typical neutral-charge mineral, is explained by the reduced number of hydrogen bonds, accompanied by a net deficiency of accepted H-bonds, which potentially attract cations. Rotenberg et al. (2011), on the other hand, demonstrated that talc surface can in fact be either hydrophilic or hydrophobic as a result of competition between adhesion of water molecules to the surface and cohesion in between the water molecules, a vision that is particularly relevant at low relative humidity. Yet, the majority of studies on interfacial water properties have been performed on muscovite mica, notably synthetic, fully hydroxylated muscovite discs in most experimental (Cheng et al., 2001; Schlegel et al., 2006; Lee et al., 2010; Lee et al., 2012; Lee et al., 2013; Gomez and Geiger, 2014) and computational (Park and Sposito, 2002; Wang et al., 2005; Sakuma and Kawamura, 2011; Bourg et al., 2017) studies. This has contributed to a well-documented description of the EDL formed on aqueous electrolyte-muscovite interfaces, highlighting the sensitivity of the interfacial water structure to the type of adsorbed counterions, the relations between their hydration energies and the dynamics within the EDL

(Churakov, 2013; Lee et al., 2013; Fenter and Lee, 2014), or even in pores of different scales (Rotenberg et al., 2007; Bourg and Sposito, 2010; Holmboe and Bourg, 2014), and their lateral distribution with distinct organization according the surface topology and charge distributions (Ricci et al., 2014; Bourg et al., 2017).

Fluorine substitutions in mica minerals are commonplace in nature because of the similarity in ionic radii (Wedepohl, 1978; Petersen et al., 1982) between the OH^- and F^- groups. Of particular interest is the phyllosilicate group where a number of possibilities exist for cationic and anionic substitutions, which has been extensively studied (Robert et al., 1993; Papin et al., 1997; Robert et al., 1999; Demyanova and Tressaud, 2009). Whether naturally occurring or synthetized, when OH^- is substituted by F^-, the mineral surface exhibits hydrophobic properties that alter its interfacial water structure. A study by Dazas et al. (2013) provides an example, using fluorinated smectites that not only reduced the interlayer water content by ~30%, but also reduced the positional disorder of interlayer water molecules as compared to their hydroxylated counterparts. A computational study by Rotenberg et al. (2011) also reports that, when exposed to a low relative humidity, fluorine substitution in talc lowered the adsorption free energy from $\Delta\mu_{ads}$ = -5.9 kcal/mol for hydroxylated talc (corresponding to the formation of a hydrogen bond between a water molecule and the structural OH^- ($\sim 10K_BT$)) to $\Delta\mu_{ads}$ = -3.5 kcal/mol. To this point, Michot et al. (1994) showed that, OH^- being the only hydrophilic sites for talc, fluorination suppresses the specific interactions between water and the OH^- group, which confirms the inherent hydrophobicity of the Si-O-Si basal surface. Despite the environmental and industrial relevance of this source of hydrophobicity for mica minerals, still very few studies have examined the effect of fluorine substitutions on water-mica interfaces and, most importantly, the inherent hydrophobic property of mica caused by fluorine substitution has not yet been linked to the well-studied sensitivity of interfacial water structure upon types of adsorbed counterions.

Here, Near-Ambient Pressure XPS was used to investigate the dynamics of water adsorption and how they are affected by the inherent structural hydrophobicity (OH phlogopite vs. F phlogopite, both with interfacial K^+ exchanged by Na^+) and by the type of the exchanged surface alkali metals (K^+-, Na^+-, vs. Cs^+-exchanged OH phlogopite). Classical MD simulation was used to further examine the surface hydration behavior governed by the three alkali metals and to predict shifts of the binding energies using the bond-valence model. This paper clarifies the role of surface hydrophobicity inherent to the phlogopite structure and the type of alkali metals, and further discusses the mechanisms of surface hydration.

5.2. Materials and Methods

5.2.1. Phlogopite mica

Phlogopite belongs to the phyllosilicate group of minerals, with the chemical formula $KMg_3(Si_3Al)O_{10}(F,OH)_2$. The basic structure of phlogopite is composed of a Mg-octahedral sheet sandwiched between two Si-tetrahedral sheets with one out of four silicon (Si^{4+}) atoms being substituted by aluminium (Al^{3+}) atoms (isomorphic substitution) (Fig. 5.1). The isomorphic substitution results in a net negative charge within the layer. This is balanced by interlayer cations, namely potassium (K), which bind successive tetrahedral-octahedral-tetrahedral (TOT) sheets. Each tetrahedron consists of one Si atom coordinated to four bridging oxygen (Ob) atoms; oxygen atoms coordinated to Al atoms are labelled as Obts (bridging oxygens with tetrahedral substitution). The tetrahedral apical Ob or Obts atoms connect tetrahedral sheets to the octahedral sheets in which octahedrons are connected to each other by sharing edges. The octahedral OH groups are located right above and underneath the interlayer K atoms. In fluorinated phlogopite, these OH groups are substituted by F ions. Phlogopite is one of the common mica minerals, allowing perfect cleavage along the (0 0 1) plane. When cleaved, ideally half of the interlayer K atoms stay with one cleaved surface (basal surface), and the other half with the other one.

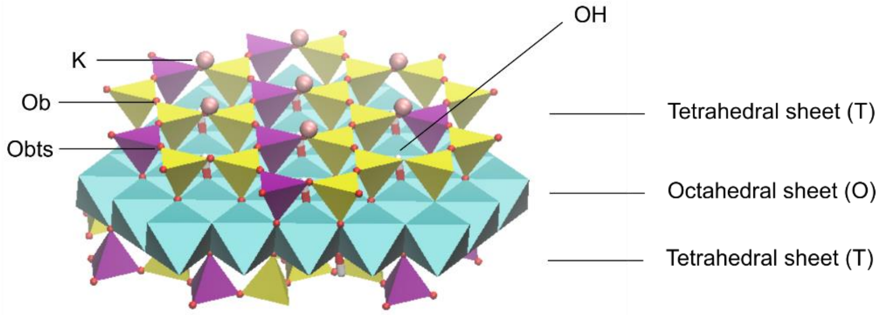

Figure 5.1. Structure of OH phlogopite. Atoms are shown as yellow (Si), pink (Al), cyan (Mg), red (O), white (H), pink spheres (K).

5.2.2. Near-ambient pressure X-ray Photoelectron Spectroscopy (NAP-XPS)

NAP-XPS measurements were performed on OH phlogopite (natural) and F phlogopite (synthetic) as summarized in Table 5.1. For OH phlogopite, counterion exchange was achieved by placing a few drops of 1M KCl, NaCl and CsCl solutions on a freshly cleaved surface, then rinsed with distilled water to remove Cl^- and excessive alkali metals. The same procedure was repeated for F phlogopite with 1M NaCl solution. This preparation yielded K^+-, Na^+- and Cs^+-exchanged OH phlogopite and Na^+-exchanged F phlogopite.

Table 5.1. Summary of phlogopite samples

Name	Composition	Source	Counterion exchange
OH phlogopite	$(K_{0.98}Na_{0.10})(Mg_{2.44}Al_{0.22}Fe_{0.10}Ti_{0.04}\square_{0.2})(Si_3Al_1)O_{10}(OH)_2$	Réserve collection Jussieu, Paris, France	K^+, Na^+, Cs^+
F phlogopite	$KMg_3(AlSi_3O_{10})F_2$	H. C. Materials Corporation, IL, USA	Na^+

OH phlogopite is natural and F phlogopite is synthetic. Counterions were exchanged with K^+, Na^+ and Cs^+ ions for the former and with Na^+ ions for the latter.

The samples were then fixed to an Au plate equipped with a thermocouple using a small amount of silver glue. Phlogopite is an excellent insulator that accumulates positive charges on its surface as the result of X-ray irradiation, which causes substantial shifts in the measured binding energies. To minimize this effect, the phlogopite surface was covered by a metal grid pasted with silver glue, leaving an intact 2 mm hole in the middle for the X-ray to reach the phlogopite surface. NAP-XPS measurements were performed at the TEMPO beamline located at SOLEIL synchrotron (France). Incident X-ray energies of 750 eV and 1200 eV were selected. In situ water adsorption experiments were performed from 0 to 57% relative humidity by gradually introducing distilled water vapor at a constant temperature. The distilled water was previously degassed several times through consecutive freeze-pump-thaw cycles. All the acquired data were calibrated with respect to the C1s reference peak (285.2 eV binding energy) and analyzed using Igor Pro software. Shirley background and Gaussian peak models were used to fit the spectra.

5.2.3. Molecular dynamics simulations

Molecular dynamics (MD) simulations were performed on the supercomputers at the National Energy Research Scientific Computing Center (NERSC) using the code LAMMPS. Three 60-Å thick phlogopite models of $KMg_3(AlSi_3O_{10})(OH)_2$ was built in a 63.84 × 55.26 × 120 $Å^3$ simulation cell with periodic boundary conditions with K^+, Na^+ and Cs^+ as counterions to partially compensate the structural surface charge. Isomorphic substitutions of Si by Al were randomly distributed within the layers, with the only constrain of avoiding neighboring tetrahedral substitutions. Simulations of each model were performed under different hydration states, up to a surface coverage of 3 water monolayers (ML). 1 ML was defined as 5.25 water molecules per surface area of a unit cell (48.997 $Å^2$), according to the density of bulk water. Interatomic interactions were computed in real space up to a distance of 12.0 Å. The CLAYFF force field (Cygan et al., 2004) was used for the phlogopite, the Dang model (Dang, 1995) for alkali metals and SPC water model (Berendsen, H.J.C., Postma, J.P.M., van Gunsteren, W.F., Herman, 1981) for water molecules. All atoms were kept mobile during the simulation, except for a middle K^+ interlayer to avoid drifting of the phlogopite. Each system bearing K^+, Na^+ and Cs^+ with 3 ML water coverage was first equilibrated for 1.5 ns in the NVT ensemble followed by a short (50 ps) equilibration in the NPT ensemble. A simulation was then performed for 1 ns in the NVT ensemble at 298 K, where water molecules were gradually removed for the first 500 ps until the system reached the aimed hydration state. The system was then equilibrated for 250 ps, followed by 250 ps of final simulation (production run) in order to obtain the different properties of interest. The same procedure was repeated for every hydration state aimed, until there were no more water molecules in the system.

In addition to the standard MD simulation outputs (pair distribution functions), we performed bond-valence (BV) analyses in an attempt to predict the shifting trends of binding energies (BE) of an atom under different hydration states of the systems. The bond valence, *s*, is a function of the distance between a pair of atoms, and is defined as:

$$s(r) = \exp\frac{(r_0 - r)}{B} \qquad 5.1.$$

where r is the distance between a pair of atoms i and j, and r_0 and B are empirically determined parameters, specific to a given pair (Brown and Altermatt, 1985). We used $B = 0.37$ and a set of r_0 values reported by Bickmore et al. (2009) for H-O pair and by Brown and Altermatt (1985) for the remaining cation-anion pairs. Using radial distribution functions (RDF) computed during our MD simulation, the *s* of a given pair *ij* was obtained as:

$$s_{ij} = \int_0^{r_1} g(r)s(r)\rho 4\pi r^2 \mathrm{d}r \qquad 5.2.$$

where $g(r)$ is the radial distribution function, r_1 is the first minimum of the $g(r)$, $s(r)$ is the bond valence function, ρ is the number density of atom j in the simulation cell. The BV sum for an atom i was therefore obtained by summing up *s* from all the contributing pairs: *ij*, *ik*, *il*… etc.

5.3. Results

5.3.1. NAP-XPS

NAP-XPS spectra were recorded for the exchanged alkali metals (K3p, Nas2 and Cs4d) as well as for surface oxygens (O1s) to investigate the surface hydration effects. Spectra were also recorded for Si (Si2p) and Mg (Mg2p) to examine the charge transfer effects throughout the phlogopite surface structure upon changes in the surface hydration. The evolution of O1s spectra from ultra-high vacuum (UHV) up to 43 - 57% relative humidity (RH) are shown in Figure 5.2. The data shown are collected at 750 eV incident energy. The non-consistency of the RH between samples reflects the slight difference (a few degrees) in the actual temperature reported by the thermocouple installed on the sample holder. Under UHV conditions, all surfaces displayed a large, broad peak at 533 eV with a small shoulder at 530.5 eV. The peak emerging at 536 eV concomitantly to the increase of RH is characteristic of water vapor (Salmeron and Schlögl, 2008). Above UHV, different peaks corresponding to adsorbed water appeared in the spectra. O1s spectra were fitted using three to four components using the constraint that the same peaks were to be found in the corresponding spectra recorded using 1200 eV incident energy. This cross-validation assumes that, when measured with two different incident energies, only the relative intensities of different components change. Further peak assignments will be reported in the Discussion section.

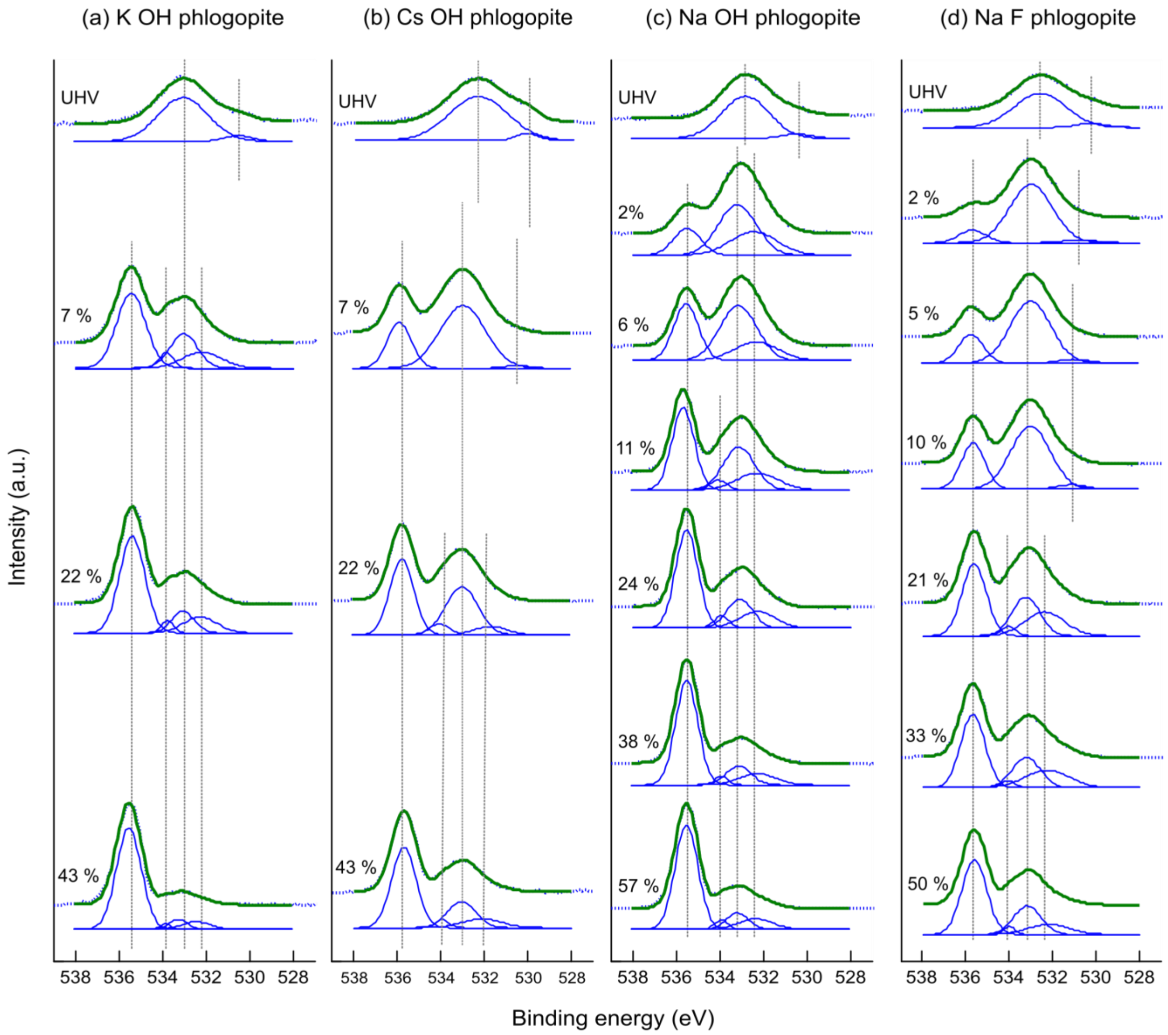

Figure 5.2. O1s NAP-XPS spectra with increasing relative humidity for **(a)** K^+-exchanged OH phlogopite, **(b)** Cs^+-exchanged OH phlogopite, **(c)** Na^+-exchanged OH phlogopite and **(d)** Na^+-exchanged F phlogopite, measured at 750 eV incident X-ray energy. Experimental data are shown as dots and fitted results are shown as solid lines. Vertical dashed lines are inserted at the fitted peak positions as visual aids.

Figure 5.3 shows the evolution of K3p, Cs4d and Na2s spectra. NAP-XPS signals from the alkali metals disappeared at high RH for all systems. As soon as the water vapor was introduced, the Cs4d peak showed a slight shift (~0.8 eV) to a higher BE (Fig. 5.3b), while the Na2s peak, for both OH and F, shifted to a lower BE by 0.5 eV (Figs. 5.3c and 5.3d). No major shift in BE was observed for both Si2p and Mg2p (Fig. S5.1), except for the Si2p spectra at high RH for both Cs^+- and Na^+-systems. For the K^+-system, all K3p, Mg2p and Si2p spectra remained unchanged upon water adsorption (Figs. 5.3a and S5.1).

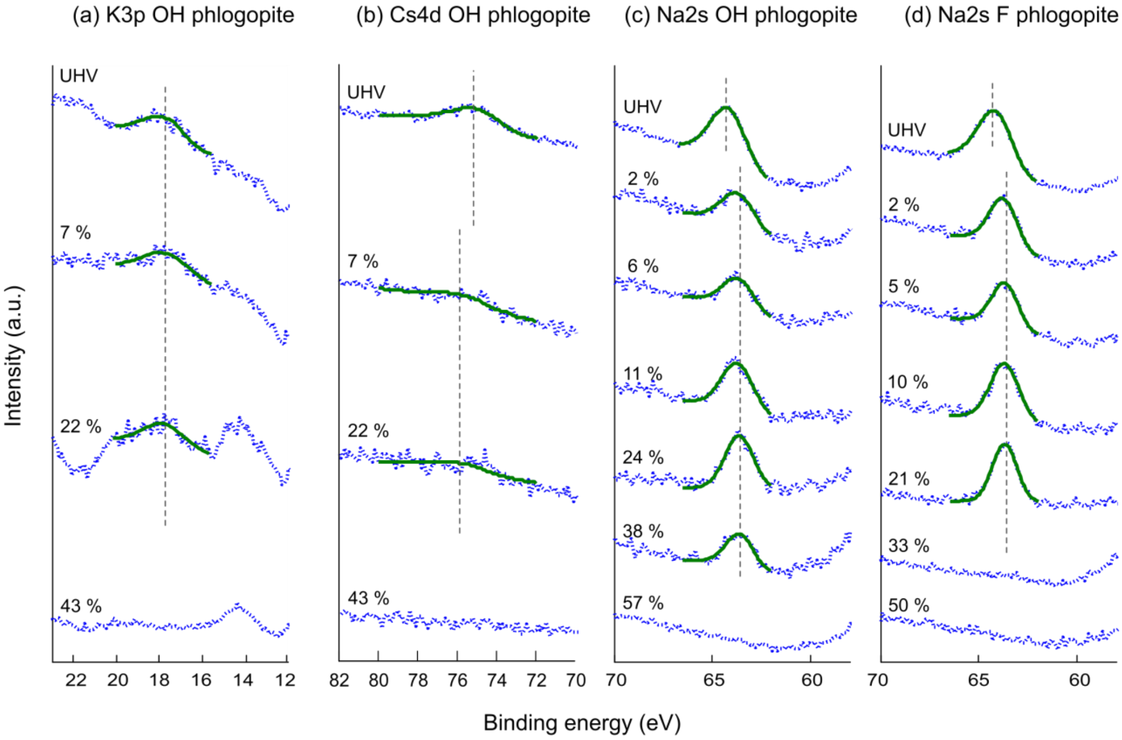

Figure 5.3. K3p, Cs4d and Na2s NAP-XPS spectra with increasing relative humidity for **(a)** K^+-exchanged OH phlogopite, **(b)** Cs^+-exchanged OH phlogopite, **(c)** Na^+-exchanged OH phlogopite and **(d)** Na^+-exchanged F phlogopite. Experimental data are shown as dots and fitted results are shown as solid lines. Vertical dashed lines are inserted at the fitted peak positions as visual aids.

5.3.2. Molecular dynamics simulations

The evolution of the coordination number (CN) for K^+, Na^+ and Cs^+ ions as a function of the hydration state was determined by integrating the first peak of the M (alkali metal)-Ow (water oxygen) radial distribution functions (RDF) (Fig. 5.4). Na^+ has the smallest CN, followed by K^+ and Cs^+. CN for K^+-Ow and Cs^+-Ow exhibited a sharp increase before attaining its equilibrium at about 1 ML coverage, reaching up to 3.5 and 5.8 respectively, while that for Na^+-Ow continuously displayed a gradual increase, leveling at a value of ~2.7.

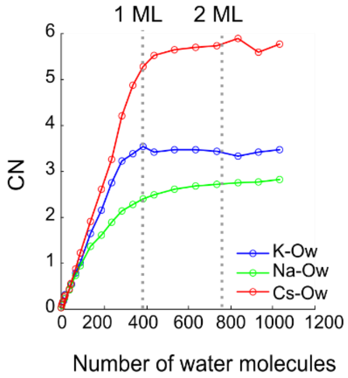

Figure 5.4. Evolution of coordination number for K^+, Na^+ and Cs^+ ions as a function of hydration states. M^+ (alkali metal) – Ow (water oxygen) coordination number (the number of water molecules in the first hydration shell). Vertical dotted lines indicate 1 and 2 ML coverage of water.

Figure 5.5 (left) shows density profiles of K^+, Na^+ and Cs^+ cations in the direction normal to the basal surface, with $z = 0$ corresponding to the average height of the basal O atoms. The distances between the basal O – alkali metals gradually increased as the number of water molecules increased up to 1 ML coverage. At low hydration (0.08 ML), all K^+ and Cs^+ cations and the majority of the Na^+ sit on the top of the ditrigonal cavities (Figs. 5.5a and 5.5c right), preferentially on those with more than one isomorphic substitution, forming inner-sphere surface complexes. In addition, a few Na^+ cations interacted with water molecules located atop basal Obts atoms, forming outer-sphere surface complexes. The number of Na^+ cations sitting atop (i.e. so-called triad sites) forming outer-sphere surface complexes increased at higher hydration states, resulting in a double distribution (Fig. 5.5b left). When ions were present in the ditrigonal cavities, the octahedral OH groups bent to accommodate the adsorbed ions. Otherwise they pointed up, perpendicularly to the basal surface with an intermittent oscillating inclination towards the isomorphic substitution sites.

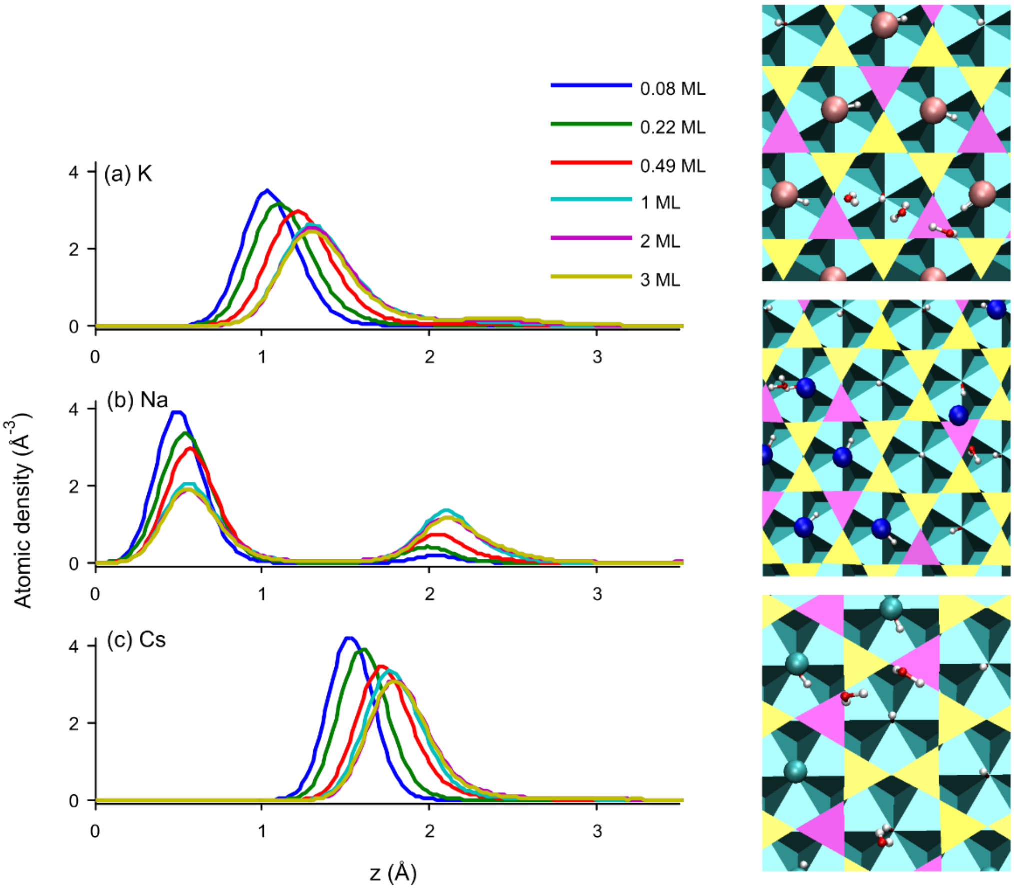

Figure 5.5. Atomic density profiles of alkali metals in the direction normal to the interface and representative snapshots (top view). Left: atomic density profiles of **(a)** K^+, **(b)** Na^+ and **(c)** Cs^+ at different hydration stages (blue: 0.08 ML, green: 0.22 ML, red: 0.49 ML , cyan: 1 ML, purple: 2 ML and yellow: 3 ML). The average height of the basal O atoms was set to $z = 0$. Right: MD simulation snapshots (top views) at 0.08 ML. Atoms are shown as yellow (Si), pink (Al), cyan (Mg), red (O), white (H), pink spheres (K), blue spheres (Na), cyan sphered (Cs).

The density profiles of water oxygen (Ow) atoms for the K^+-, Na^+- and Cs^+- systems at different hydration states are compared in Figure 5.6. The average height of the basal O atoms is set as $z = 0$. At an early stage of hydration (0.08 ML), the distance between the basal surface and the first Ow layer was the closest for the Na^+- system (2.53 Å), followed by Cs^+- (2.56 Å) and K^+- (2.64 Å) systems as indicated by the dotted lines. It then gradually increased as the number of water molecules was increased up to 1 ML coverage. In particular, Na^+-bearing phlogopite displayed the largest shift. Beyond the first Ow layer, K^+- and Cs^+-bearing phlogopite exhibited more structured layering than Na^+- bearing phlogopite.

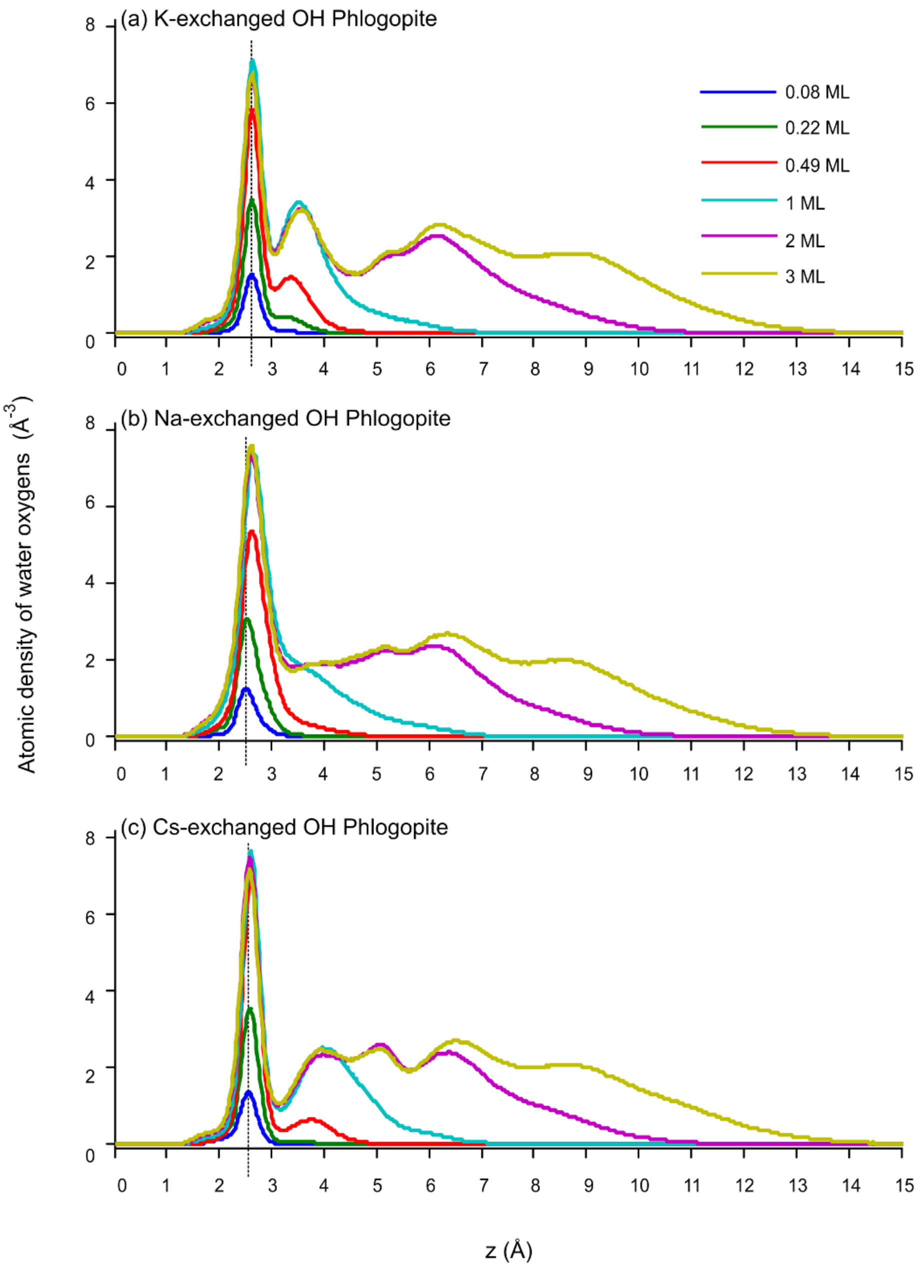

Figure 5.6. Atomic density profiles of water oxygens (Ow) in the direction normal to the interface for **(a)** K^+-, **(b)** Na^+- and **(c)** Cs^+-bearing OH Phlogopite at different hydration stages (blue: 0.08 ML, green: 0.22 ML, red: 0.49 ML , cyan: 1 ML, purple: 2 ML and yellow: 3 ML coverage of water). The average height of the basal O atoms was set to *z* = 0. Dotted lines indicate the positions of the first Ow layer at 0.08 ML.

Figure 5.7 shows MD simulation snapshots (top view) at 0.22 ML coverage with accumulated trajectories drawn at 2.5 ps intervals during the 250 ps of simulation. Na^+ cations were the most mobile (Fig. 5.7a middle), in particular those sitting initially above the ditrigonal cavities with less than two isomorphic substitutions were readily displaced to the edge of the closest Al-tetrahedra (triad sites). Meanwhile, only two K^+ cations (per simulation cell) were displaced from their initial position to another cavity (both cavities near one isomorphic substitution) while no displacement was observed for Cs^+. Ow atoms from the first Ow layer are shown in red, and the others are colored in yellow in Figure 5.7b. The former are more likely to sit near the isomorphic substitutions, in particular for K^+ and Cs^+ systems, whereas the yellow-colored Ow atoms tend to sit above the Si-tetrahedra (Fig. 5.7b left and right).

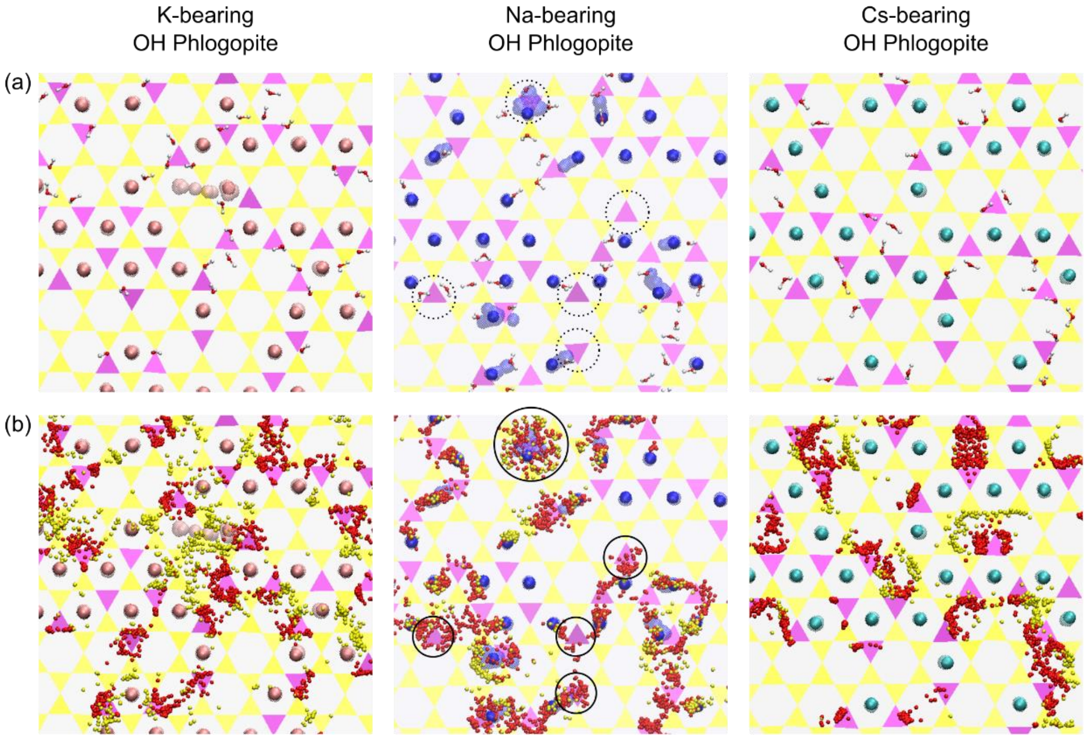

Figure 5.7. MD simulation snapshots at early stage of hydration (0.22 ML) for K^+-, Na^+- and Cs^+-bearing OH Phlogopite. **(a)** Top view with trajectories of alkali metals accumulated during 250 ps of simulation at an interval of 2.5 ps. **(b)** Top view with trajectories of alkali metals and water oxygens (Ow). Ow atoms within the first Ow layer are colored in red and those outside this threshold are colored in yellow. Dotted and solid circles are shown for comparison with snapshots at 2 and 3 ML (Fig. 5.8). Atoms are shown as yellow (Si), pink (Al), red (O), white (H), pink spheres (K), blue spheres (Na), cyan sphered (Cs).

In the same way, top view snapshots at 2 and 3 ML coverage are shown in Figure 5.8 with accumulated trajectories. Na^+-bearing phlogopite has the largest number of Ow atoms within the first Ow layer (colored in red). Many of the Na^+ cations were dislocated and lifted within the bulk water layer (Fig. S5.2b). At 2 ML coverage, a few Cs^+ cations were finally dislocated beyond its original cavity, although the dislocation remains minor even at 3 ML coverage.

(a) K-bearing
OH Phlogopite
2ML

(b) Na-bearing
OH Phlogopite
2 ML

(c) Cs-bearing
OH Phlogopite
2ML

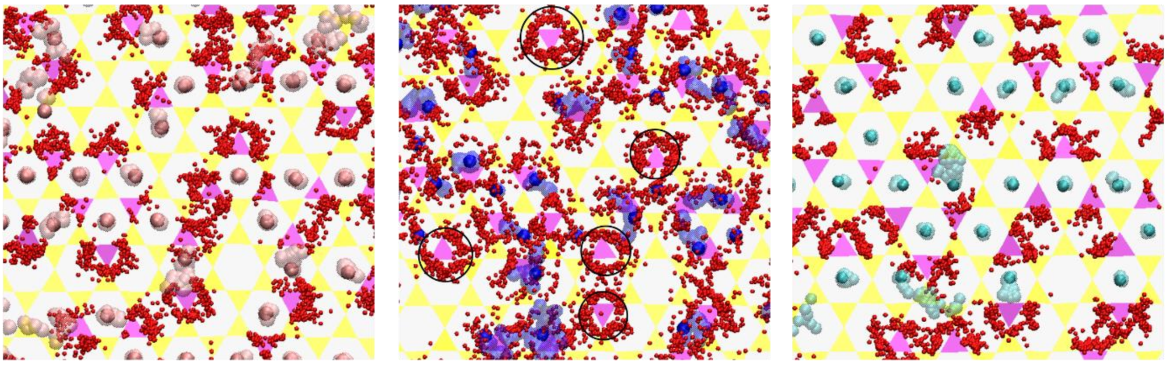

(d) K-bearing
OH Phlogopite
3 ML

(f) Na-bearing
OH Phlogopite
3 ML

(g) Cs-bearing
OH Phlogopite
3 ML

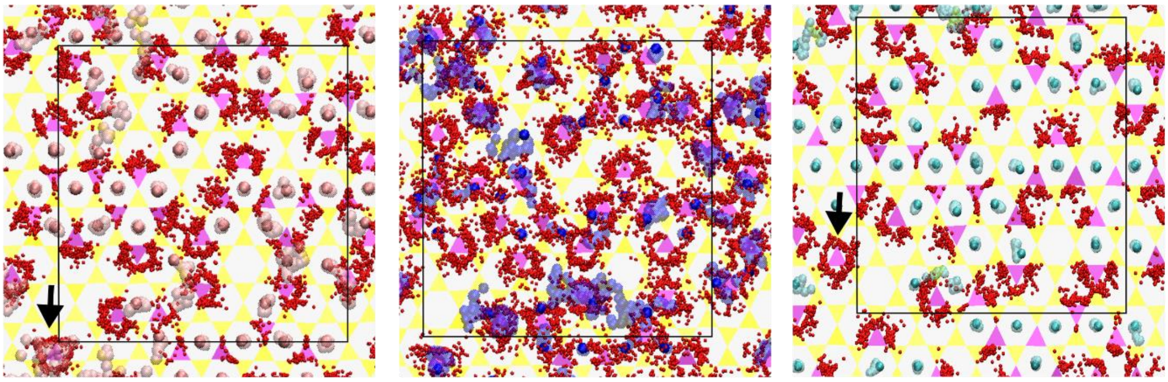

Figure 5.8. MD simulation snapshots with 2 and 3 ML water coverage for **(a, d)** K^+-, **(b, f)** Na^+- and **(c, g)** Cs^+-bearing OH Phlogopite. Top view with trajectories of alkali metals (K^+ (pink), Na^+ (blue) and Cs^+ (cyan)) and water oxygens (red) within the first hydration peak. For visual aid, solid squares in d, f and g indicate the frame by which snapshots are taken at 0.22 and 2 ML. Atoms are shown as yellow (Si), pink (Al), red (O), pink spheres (K), blue spheres (Na), cyan sphered (Cs).

The results of BV analyses are shown in Figure 5.9. The BV sum of the respective alkali metals was calculated based on the individual contributions from the basal bridging oxygens (both with and without isomorphic substitution, denoted as Ob and Obts, respectively) and water oxygens (Ow). The BV sum of Na^+ displayed a continuous increase as a function of hydration states, whereas that of K^+ and Cs^+ displayed a concave upward trend before reaching 1 ML. Generally, the contribution from the basal O atoms decreased with increasing hydration states, at the expense of that from water molecules.

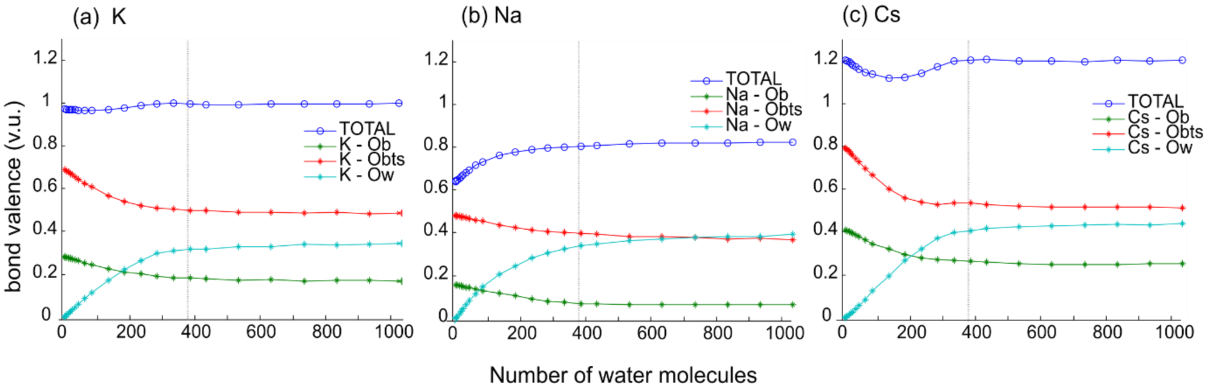

Figure 5.9. Bond-valence sum for **(a)** K^+, **(b)** Na^+ and **(c)** Cs^+, along with the contributions from basal O atoms with and without isomorphic substitutions (Ob and Obts, respectively) and water oxygen (Ow) as a function of hydration stages. Vertical dashed lines indicate 1 ML coverage of water.

The results of BV analyses for the basal Obts atoms (bridging oxygen near tetrahedral substitutions) are shown in Figure 5.10. Contributions from water hydrogen (Hw) atoms, surface alkali metals (M^+) and surface Si and Al atoms were considered. For all the systems, the BV sum of Obts showed an increasing trend with increasing hydration state, resulting from the increasing BV of Obts-Hw pair which was negatively compensated by that of Obts-M^+ pair. Such an increasing trend of the BV sum was not observed for Ob atoms (bridging oxygen without tetrahedral substitutions, data not shown). Although Si and Al atoms were the main contributors to the total BV sum of Obts atoms, no particular trend was observed, except for the slight decreasing trend for the BV of Obts-Al pair.

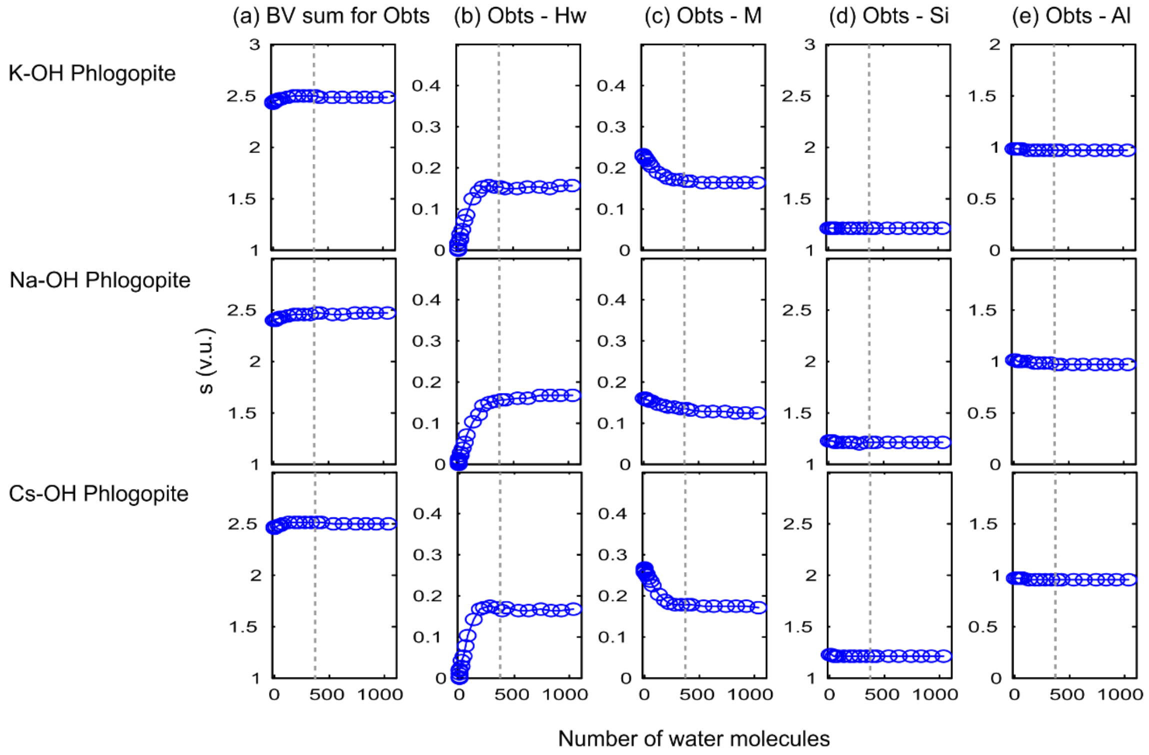

Figure 5.10. Bond-valence analysis of basal O atoms with isomorphic substitutions (Obts) for K^+-, Na^+- and Cs^+-exchanged OH phlogopite. **(a)** BV sum for Obts atoms contributed by **(b)** water hydrogen (Hw) atoms, **(c)** alkali metals (M^+), **(d)** basal Si atoms and **(e)** basal Al atoms. Vertical dashed lines indicate 1 ML coverage of water.

5.4. Discussion

5.4.1. Oxygen species of phlogopite mica

Under UHV, all O1s NAP-XPS spectra exhibited a large broad peak at 533 eV and a small shoulder at lower BE (530.5 eV), indicating that there are at least two distinct bonding environments for O atoms within the phlogopite structure (Fig. 5.2). Negatively charged sites can give rise to a lowering of binding energies (BE) as demonstrated by Zakaznova-Herzog et al. (2005), where a net negative charge in Mg-rich olivine resulted in lowering the O1s binding energies by more than 1 eV as compared to quartz. For phlogopite, surface O atoms are more negatively charged than those in the bulk structure, in particular Obts atoms (bridging oxygen atoms near the isomorphic substitutions), to which the minor component (530.3 eV) is tentatively assigned. On the other hand, some studies observed that the formation of hydroxyl OH groups at metallic and oxide surfaces upon exposure to water brought about a peak at around 530 – 531 eV (Ogasawara et al., 2002; Schiros et al., 2007; Yamamoto et al., 2008; Newberg et al., 2011; Casalongue et al., 2013). Although OH phlogopite has OH groups in the octahedral sheets, the assignment of the 530.3 eV peak to the OH groups does not rationalize for the F phlogopite since all the OH groups are substituted by F^-. Given its broad feature, the main peak can stem from various types O atoms from the bulk structure (from the first ~10 nm) in addition to the surface Ob atoms. This is further confirmed by the area ratio between the main and the minor components of about 13:1. This ratio is of the same order of magnitude as the ratio between the surface Obts and surface Ob plus bulk Ob atoms within the first 10 nm, which is roughly the depth that is probed by XPS.

5.4.2. Effects of surface hydration on bonding environments

A distinct feature upon increasing RH is the appearance of water gas phase signal at 536 eV (Fig. 5.2). Arising from the free, uncoordinated water OH bonds (Ogasawara et al., 2002; Schiros et al., 2010), the signal from the gas phase always occurs at higher binding energies than surface signals due to the differences in the final state relaxation between surface species and gas phase upon core-ionization (Nilsson, 2002). Increasing RH also led to the appearance of new surface components: water monolayer and multilayer arising at 532.2-532.5 eV and 534 eV, respectively, following the nomenclature by previous NAP-XPS water adsorption studies (Yamamoto et al., 2008; Casalongue et al., 2013). Additionally, the main O1s peak (533 eV) shifted to a higher BE for all surfaces except for the K^+-exchanged one, and the Obts peak (530.5 eV) disappeared (K^+- and Na^+-OH phlogopite) or shifted (Cs^+-OH and Na^+-F phlogopite). The shift of the O1s main peak to a higher BE occurred concomitantly with the shift of the exchanged cations (Figs. 5.3b-d): interestingly, Na2s shifted to a lower BE by 0.5 eV (both OH and F phlogopite) while Cs4d shifted to a to a higher BE by ~0.5 eV, though for the latter the shift was relatively small and the signal was weak. These observations suggest that the interactions with the water molecules can be quite different for Na^+ and Cs^+ cations. Indeed, the interaction is much stronger for Na^+ (Lee et al., 2013), provided its small ionic radius and its lower coordination number (Fig. 5.4). This is also well pictured by the double distribution of Na^+ cations (Fig. 5.5b middle), which results from the predominant Na^+-water interaction over that of Na^+-surface (Sakuma and Kawamura, 2011).

The observed changes in the BE of core electrons as a function of hydration state results from the changes in the electronic valence configurations (Nilsson et al., 2015). The direction of the shifts can be interpreted as a charge transfer, either a gain (shift to lower BE) or a loss (shift to higher BE) of valence electron density. The BV analyses (Fig. 5.9) are in good agreement with this. The BV sum for Na^+ exhibits an increasing trend with the hydration state (Fig. 5.9b), implying that the BE shifts to a lower energy, whereas that for Cs^+ decreases at early stages of hydration (Fig. 5.9c), suggesting that the BE shifts to a higher energy. It is to note that the major contribution to the increasing BV sum for Na^+ arises from the BV of Na-Ow (water oxygen) pair, in agreement with the strong hydration of Na^+ mentioned earlier. The decreasing trend of the BV sum for Cs^+ mainly results from the sharp decrease in BV of the Cs^+-Obts pair, which is not immediately compensated by that of Cs^+-Ow. Moreover, this seems to be related to the sharp increase in BV of the Obts-Hw (water hydrogen) pair (Fig. 5.10b, bottom). These results imply that the hydration of Cs^+-bearing phlogopite proceeds preferentially via formation of hydrogen bonds between the water molecules and the surface Obts atoms, whereas the hydration of Na^+-bearing phlogopite results from the interaction of water molecules with Na^+ cations. This is further confirmed by careful analyses of the trajectories of interfacial water molecules, as discussed later. For K^+-bearing phlogopite, the decreasing BV of K^+-Obts/Ob pair is simultaneously compensated by the increasing BV of K^+-Ow, which presumably explains the absence of shift in both O1s and K3p as shown earlier. Such balancing infers that the K^+ cations are less affected by the water adsorption, a fact resulting from the almost perfect match between the size of the K^+ cations and that of the phlogopite ditrigonal cavities (Droste et al., 1962; Schaetzl and Anderson, 2005), which also explains the abundant natural dominance of K^+-phlogopite over other M^+-phlogopite.

The shift of the O1s main peak to a higher BE can be explained by the same reasoning. The BV sum for Obts atoms (Fig. 5.10a) exhibits a slight increase up to 1 ML coverage, irrespective of the nature of the surface cations. Contrary to the cations, the increase in BV of negatively charged O atoms indicates the loss of valence electron density, since they act as electron donors. The major contribution to the increase of BV sum for Obts atoms stems from the interaction of the Obts-Hw pair, i.e., formation of hydrogen bonds with the basal O atoms, which competes with that of the Obts-M^+ pairs. This last is reflected by the outward shifting of surface cations upon hydration, away from the interface (Fig. 5.5 left), as also observed by Wang et al. (2005). A detailed examination of interfacial water and alkali metals is discussed in the following section.

5.4.3. Detailed picture of surface hydration: what makes surface hydrophobic and what initiates water adsorption?

Surface hydrophobicity seems to be controlled by both the hydration properties of the surface cations and by the inherent structural hydrophobicity. As soon as the RH was raised, the signal from the water monolayer (532.2-532.5 eV) was observed on K^+- and Na^+-exchanged OH phlogopite at 2% and 7%, respectively (Figs. 5.2a and 5.2c). Yet it is to note that the water monolayer could have been formed at lower RH for the K^+-bearing system since the RH was raised at a larger interval. On these two surfaces, the formation of water monolayer was associated with the disappearance of the basal Obts peak (530.5 eV), followed by the formation of multilayer water at 7 and 11%, for K^+- and Na^+- OH phlogopite respectively.

For Cs^+-OH and Na^+-F phlogopite, on the other hand, the simultaneous formation of monolayer and multilayer water is observed at ~21-22% (Figs. 5.2b and 5.2d). Interestingly, on these two samples the basal Obts peak (530.5 eV) remained visible until the formation of water layers started, with a gradual shift to a higher BE. The shift of the basal Obts peak to a higher BE upon hydration (Figs. 5.2b and 5.2d) can be understood as the screening effect resulting from the formation of hydrogen bonds from the water molecules, as also confirmed by the increasing BV of the Obts-Hw pair (Fig. 5.10b). These observations seem to indicate that the Cs^+-exchanged phlogopite surface exhibits features that make it as hydrophobic as the Na^+-exchanged F phlogopite. Interestingly, however, the mechanisms dictating surface hydrophobicity on Cs^+-OH phlogopite and on Na^+-F phlogopite are rather different. This can be seen, as explained below, in the ratios of the O1s peak intensities from monolayer water and the structural oxygens, and those of the multilayer water and the structural oxygens, as shown in Figure 5.11.

The first evidence of a different origin of surface hydrophobicity stems from the fact that the contribution of the monolayer water molecules (532 eV) dominates over that of multilayer water molecules (534 eV) for Cs^+-OH phlogopite, whereas the trend is reversed for Na^+-F phlogopite (Fig. 5.11a). Instead of the intuitive growth from a water monolayer to a multilayer, as observed by (Schiros et al., 2010), the monolayer and multilayer water molecules in our system coexist for all the O1s spectra at high RH (Fig. 5.2), implying that water from these two compartments must have different origins (and therefore the labels ‘monolayer’ and ‘multilayer’ are misleading). This leads to the second evidence provided by MD simulation (Fig. 5.11b) where a careful analysis of water trajectories clearly showed different conformations for the Cs^+- and Na^+-bearing phlogopite. For the former, as indicated by the dotted lines and the arrows, the majority of water molecules point to the basal Obts atoms, forming one to two hydrogen bonds, which comprises the first hydration layer. A study by Loganathan et al. (2016) also demonstrated that a significant fraction of water molecules form hydrogen bonds with basal oxygens of hectorite in the presence of adsorbed Cs^+. At about 1.5 Å above them, a few water molecules hydrate Cs^+ cations, which comprises the second Ow layer (Fig. 5.11b), in agreement with previous studies showing that Cs^+ exhibits a small hydration energy due to its large size, which is translated into a weak interaction with water molecules (Sakuma and Kawamura, 2011; Lee et al., 2012). The presence of this second Ow layer hydrating Cs^+ is further confirmed by the observed outward shifting (Fig. 5.11b), which is concomitant to the outward shifting of the Cs^+ adsorbed as inner-sphere surface complexes (Fig. 5.5c). From this picture, we could postulate that in our system, the monolayer (532 eV) seen by NAP-XPS refers in fact to the layer of water molecules that hydrate the cations, whereas the multilayer (534 eV) refers to the multiple layers of water developed from the direct hydration of the surface that is not interfered by the presence of cations.

In the case of Na^+-bearing phlogopite, most water molecules simultaneously form hydrogen bonds with the basal Obts atoms and hydrate Na^+ cations (Fig. 5.11b), and their geometrical conformations are rapidly changing as also pointed out by Ricci et al. (2014), resulting in a single, relatively broad distribution of water molecules instead of two distinct distributions (Fig, 5.11b). Like for the Cs^+-system, this broad peak shifts outwards in a synchronized way with the adsorbed Na^+ that form both the inner-sphere and outer-sphere surface complexes (Fig. 5.5a). Reflective of this, the trajectories of Ow atoms within the first hydration layer accumulated along the simulation for Na^+-system seem more scattered as compared to the K^+- or Cs^+-bearing counterparts (Fig. 5.7b, colored in red) where dense clouds of the red-colored Ow atoms mainly sit above the Obts atoms, which also corresponds to the enhanced formation of hydrogen bonds in contrast to Na^+-bearing phlogopite (Fig. 5.11b). The existence of a strong Na^+-hydration layer confirms the observation of monolayer (532 eV) at earlier stages of hydration than for Cs^+-bearing phlogopite (Figs. 5.2b and 5.2c).

Although the MD simulations were performed only for the OH phlogopite system, the strong interaction between Na^+ and water molecules should also be present on F phlogopite, or could even be enhanced since the formation of hydrogen bonds with the surface would be reduced, as demonstrated for hydrophobic, charge-neutral talc (Wang et al., 2009) and other hydrophobic interfaces (Schwnedel et al., 2003; Steitz et al., 2003; Poynor et al., 2006; Janecek and Netz, 2007; Maccarini et al., 2007). In a similar line, a study by Dazas et al. (2013) also demonstrated that the fluorinated smectite interlayer water molecules resulted in a more ordered configuration, repelled by the adjacent smectite layers. These lines of evidence imply that the surface hydration results mainly from the interaction of water molecules with basal Obts atoms for Cs^+-bearing phlogopite, while it is the interaction of water molecules with Na^+ atoms that trigger the simultaneous hydration of basal surface, and this seems to be tuned by the inherent structural hydrophobicity as shown by NAP-XPS (Fig. 5.11a).

For K^+-bearing OH phlogopite, the number of water molecules forming hydrogen bonds with the surface and that of water molecules hydrating K^+ cations seem almost equal (Fig. 5.11b), which explains the competing contribution between surface cations and surface O atoms (Fig. 5.11a). Such a competing contribution is also seen for Na^+-bearing OH phlogopite (Fig. 5.11a), which presumably results from the fact that the water molecules simultaneously hydrate Na atoms and form hydrogen bonds with the surface as discussed earlier. At higher hydration stages, some of the surface cations completely leave the surface (Fig. S5.2), a feature more prominent in the Na^+ system. This ‘escape’ of surface cations seems to be the key in enhancing surface hydration, resulting in the formation of *rings* in the accumulated trajectories of Ow atoms above the isomorphic substitutions at 2 ML (Fig. 5.8b, indicated by circles) as compared to the distribution of water molecules at 0.22 ML (Fig. 5.7b). The formation of such rings for K^+- and Cs^+-bearing phlogopite is seen finally at 3 ML (Figs. 5.8d and 5.8g), confirming that their interaction with water molecules, which provokes the above mentioned escape, remains relatively weak. Such a specific lateral distribution of water molecules from the first hydration shell into well-defined two to three sublayers has previously been identified for K^+-muscovite mica (Park and Sposito, 2002; Wang et al., 2005; Leng and Cummings, 2006; Bourg et al., 2017) and smectite (Bourg and Sposito, 2011). In particular, those atop the basal O each form one hydrogen bonds to the siloxane surface (Bourg et al., 2017), in agreement with our observations (Fig. 5.11b).

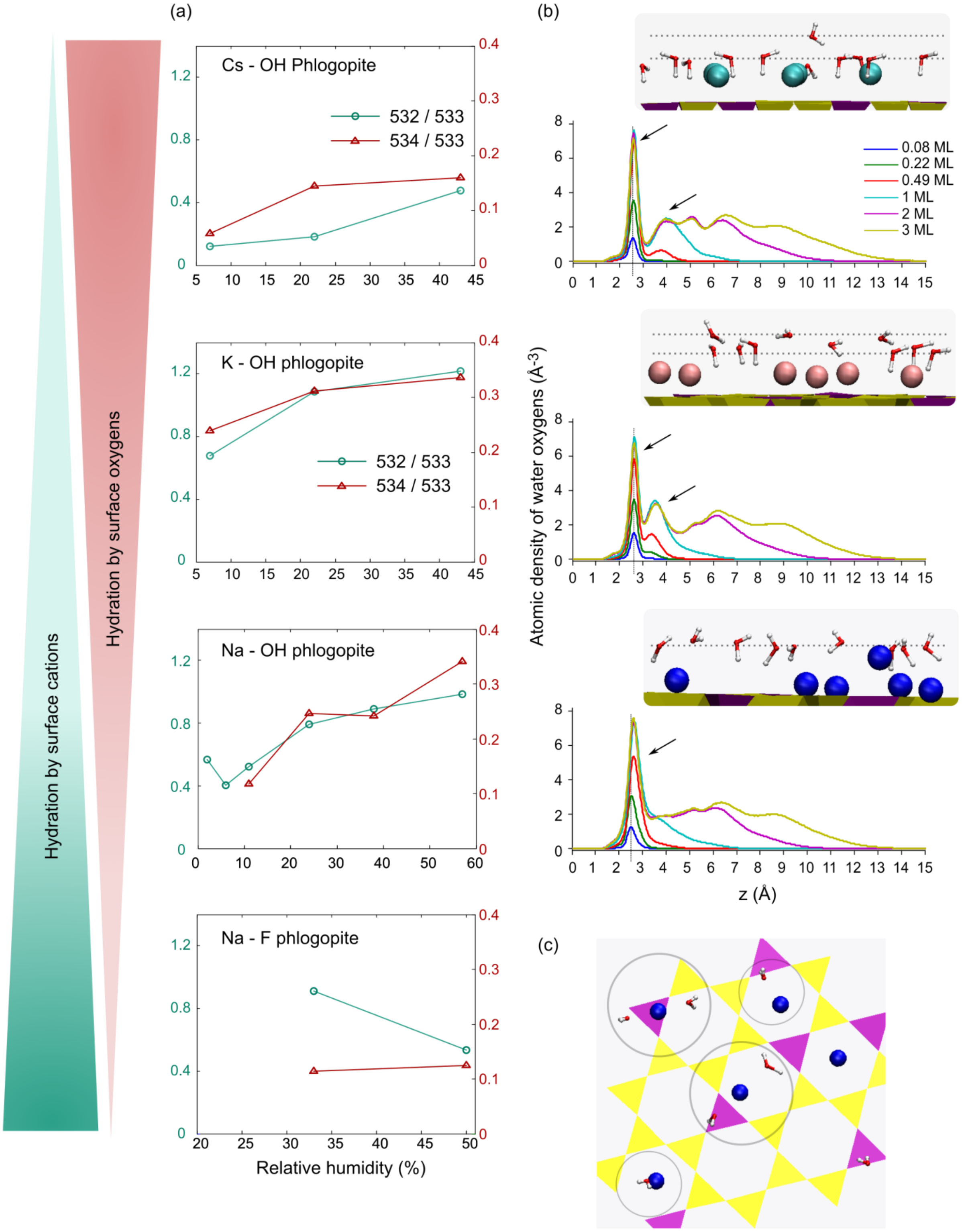

Figure 5.11. Twofold mechanism of surface hydration. **(a)** Evolution of the O1s peak ratios as a function of hydration state. The relative contributions from water molecules hydrating surface cations is represented by the peak at 532 eV. The contribution from multilayer water developed via hydrogen bonding with surface oxygens is represented by the peak at 534 eV. Both peaks are normalized by the O1s peak at 533 eV, from oxygen atoms in the phlogopite structure (533 eV). **(b)** MD simulation snapshots at 0.22 ML water coverage as well as atomic density profiles of water oxygens at increasing hydration stages. The average height of the basal O atoms was set to *z* = 0. Dotted lines in the snapshots correspond to peaks indicated by arrows in the corresponding density profiles. **(c)** Top view of Na-bearing OH phlogopite at 0.22 ML shown in b with circles indicating water molecules hydrating Na atoms. The same color scheme as in Fig. 5.5.

5.4.4. Sensitivity of classical MD simulation on predicting the shifts in binding energies

The prediction of bonding environments is conventionally performed by *ab initio* MD simulations or DFT calculations that involve electronic structure calculations (Marx and Hutter, 2000) that tend to be computationally more expensive than classical MD simulations. To name a few, Uchino et al. (1991) used ab initio MD simulations to investigate electronic structure of sodium silicate glass; Schiros et al. (2007) computed XPS, XAS and XES spectra using DFT calculations; Bickmore et al. (2004) combined molecular structures calculated by ab initio MD simulations with bond-valence analysis to determine acidity constants. A study by Bickmore et al. (2009) demonstrated that some of the water models employed by classical MD simulations, including the SPC model used in the present study, tend to underestimate the bond-valence for O atoms of liquid water by 0.13 to 0.23 v.u. with respect to the expected valence sums. Our simulation, indeed, resulted in either under- or overestimation of most of the calculated BV values (Figs. 5.9 and 5.10). Nevertheless, the predicted changes of BV at different hydration stages corresponded fairly well to the shifts of binding energies observed by NAP-XPS. In particular, the changes in the BV sum for K^+, Na^+ and Cs^+ (Fig. 5.9) agreed well with the BE shifts (Fig. 5.3). In addition, BV analyses were shown to be useful in order to obtain a larger picture of the changes in the geometrical conformations from the trends of the individual contributions to the BV sum. For instance, the steep decrease in the BV of Cs^+-Obts pair (Fig. 5.9c) as well as the sharp increase in the BV of Obts-Hw pair for the K^+- and Cs^+-systems (Fig. 5.10b middle and bottom) are well depicted in the detailed analysis of MD trajectories and the vertical density profile of Ow atoms (Fig. 5.11b): K^+ and Cs^+ cations shift outwards, leaving the surface adsorbed water molecules intact, while Na^+ atoms interact actively with the water molecules that are simultaneously hydrogen bonded to the basal Obts atoms. Classical MD and BV analyses are therefore a perfect combination to understand trends and observations from NAP-XPS experiments.

5.5. Conclusion

Two different mechanisms that control surface hydration were examined using NAP-XPS and classical MD simulation: (i) the inherent structural hydrophobicity (hydroxyl phlogopite vs. fluorinated phlogopite, both with the interfacial K^+ atoms exchanged by Na^+ atoms) and (ii) the nature of the surface alkali metals (K^+- vs. Na^+- vs. Cs^+ on OH phlogopite). Overall, our results from the two methods provided a coherent picture of the dynamical changes at the phlogopite-water interface upon surface hydration.

Water adsorption experiment by NAP-XPS demonstrated that the Na^+-bearing F phlogopite structure exhibited hydrophobic characteristics in that it suppressed the formation of water layers as compared to the OH counterpart. Among the three alkali metals, Cs^+-bearing OH phlogopite was found to be as hydrophobic as Na^+-bearing F phlogopite, due to the weak interaction of Cs^+ cations with water molecules, which hinders water adsorption. Interestingly, both NAP-XPS and MD simulation results indicate that the mechanism of surface hydration differs largely depending on the type of the surface cations: the hydration of K^+- and Cs^+-bearing phlogopite surfaces proceeds via the formation of hydrogen bonds with surface oxygen atoms, whereas that of Na^+-bearing phlogopite surfaces does so via cation hydration. To further confirm this effect on Na^+-bearing F phlogopite, MD simulation will be completed in the near future, when a set of potential for F-phlogopite will be available. We also showed that the BV analyses based on the classical MD simulation can provide sufficiently detailed information about the geometrical conformations between surface cations and interfacial water molecules, predicting changes in the binding energies of the counterions.

Supporting Information

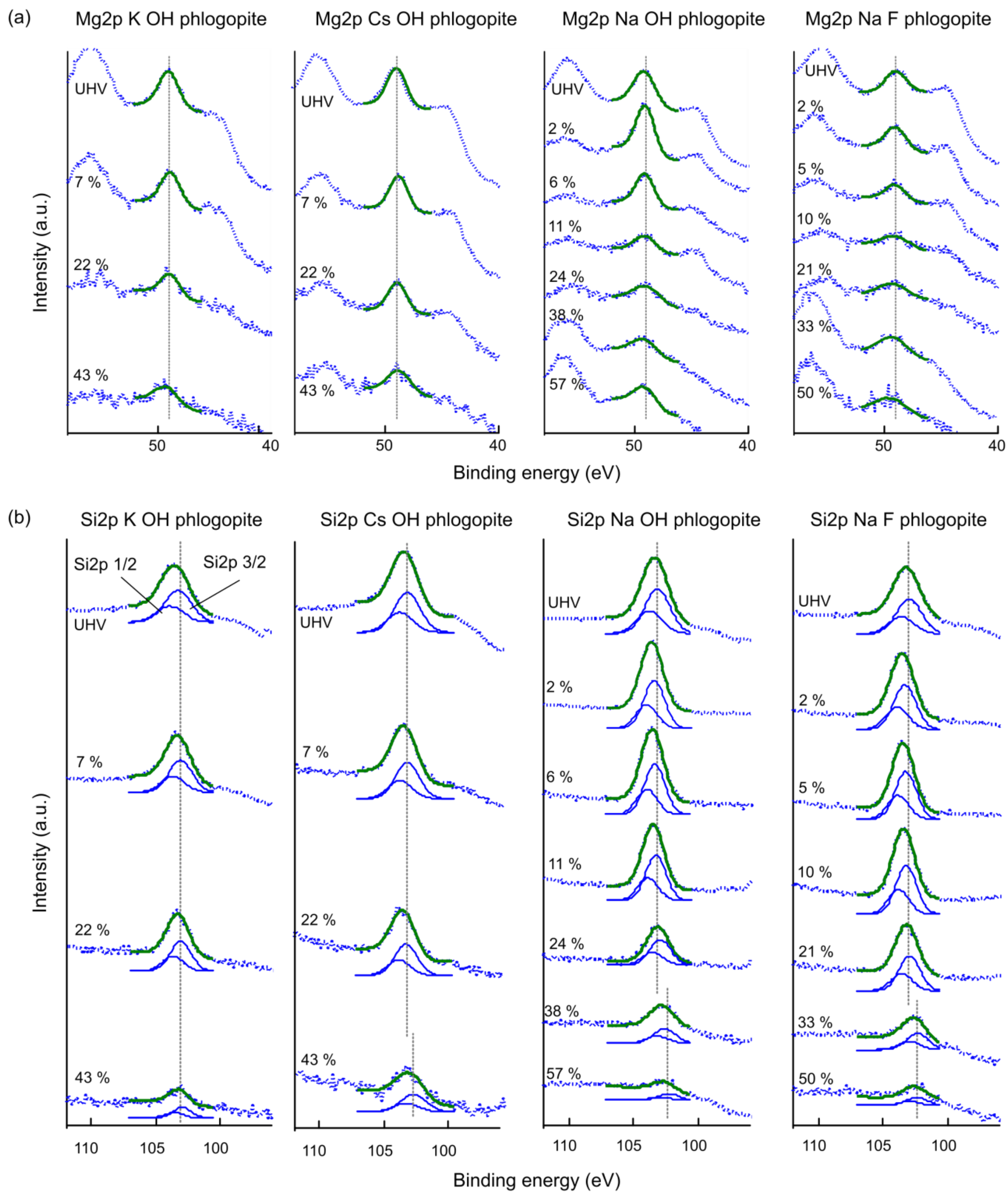

Figure S5.1. NAP-XPS spectra of **(a)** Mg2p and **(b)** Si2p for K-, Cs- and Na-exchanged OH phlogopite and Na-exchanged F-phlogopite with increasing relative humidity, measured at 750 eV incident energy. Experimental data are shown as dots and fitted results are shown as solid lines. Vertical dashed lines are inserted at the fitted peak positions as visual aids.

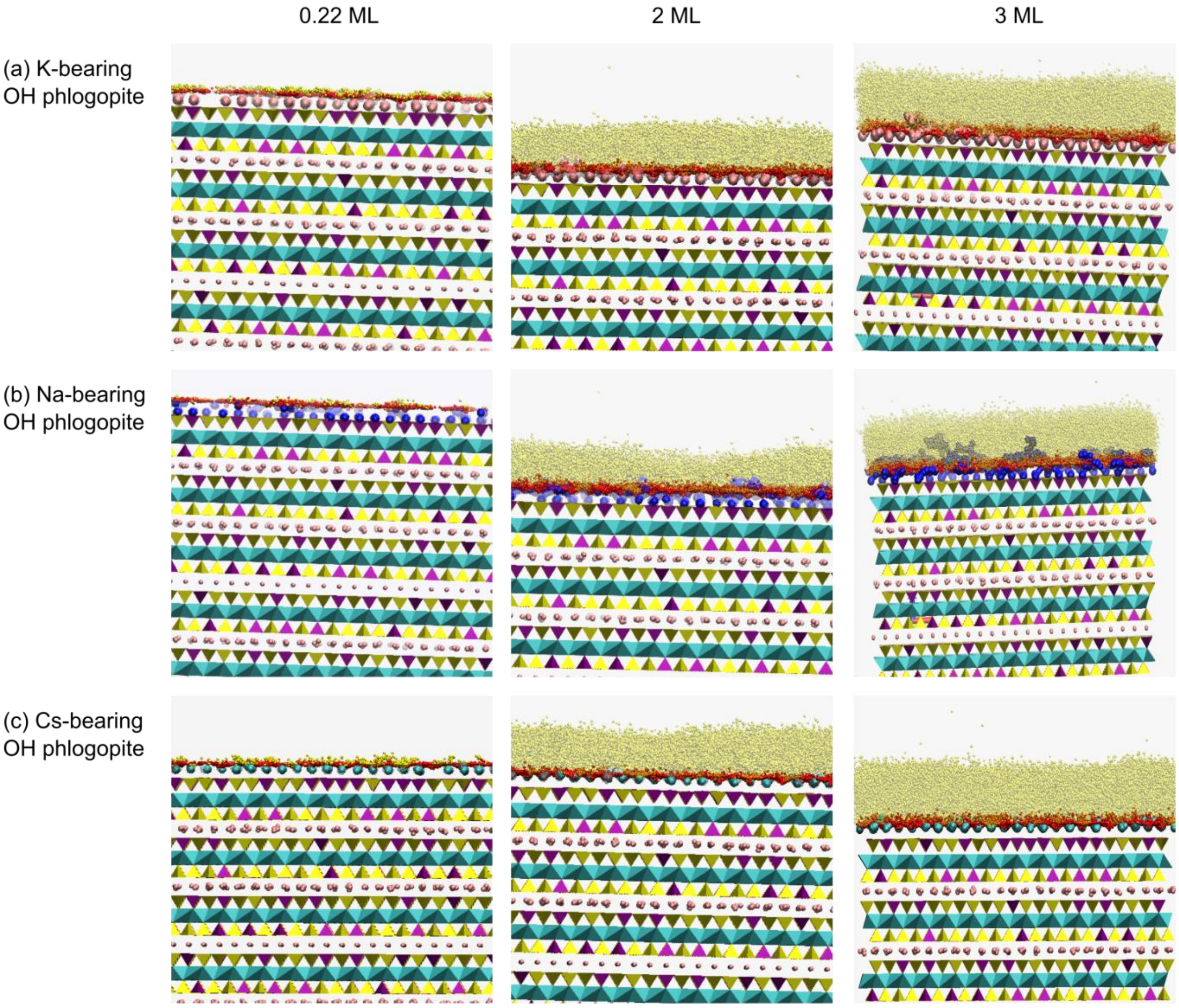

Figure S5.2. MD simulation snapshots (side view) at 0.22, 2 and 3 ML water coverage for **(a)** K-, **(b)** Na- and **(c)** Cs-bearing OH Phlogopite with trajectories of alkali metals and water oxygens (Ow) atoms accumulated during 250 ps of simulation at an interval of 2.5 ps. Ow atoms within the first Ow layer are colored in red and those outside this threshold are colored in yellow. Atoms are shown as yellow (Si), pink (Al), cyan (Mg), red (O), white (H), pink spheres (K), blue spheres (Na), cyan sphered (Cs).

References

Berendsen, H.J.C., Postma, J.P.M., van Gunsteren, W.F., Herman J. (1981) Interaction models for water in relation to protein hydration. In *Intermolecular Forces.* pp. 331–342.

Bickmore B. R., Rosso K. M., Brown I. and Kerisit S. (2009) Bond-valence constraints on liquid water structure. *J. Phys. Chem. A* **113**, 1847–1857.

Bickmore B. R., Tadanier C. J., Rosso K. M., Monn W. D. and Eggett D. L. (2004) Bond-valence methods for pKa prediction: Critical reanalysis and a new approach. *Geochim. Cosmochim. Acta* **68**, 2025–2042.

Bourg I. C., Lee S. S., Fenter P. and Tournassat C. (2017) Stern Layer Structure and Energetics at Mica-Water Interfaces. *J. Phys. Chem. C* **121**, 9402–9412.

Bourg I. C. and Sposito G. (2010) Connecting the molecular scale to the continuum scale for diffusion processes in smectite-rich porous media. *Environ. Sci. Technol.* **44**, 2085–2091.

Bourg I. C. and Sposito G. (2011) Molecular dynamics simulations of the electrical double layer on smectite surfaces contacting concentrated mixed electrolyte (NaCl-CaCl2) solutions. *J. Colloid Interface Sci.* **360**, 701–715.

Brown G. E. (2001) How Minerals React with Water. *Science* **294**, 67–70.

Brown G. E., Henrich V. E., Casey W. H., Clark D. L., Eggleston C., Felmy A., Goodman D. W., Grtzel M., Maciel G., Mccarthy M. I., Nealson K. H., Sverjensky D. A., Toney M. F. and Zachara J. M. (1999) Metal Oxide Surfaces and Their Interactions with Aqueous Solutions and Microbial Organisms Microbial Organisms. *Chem. Rev.* **99**, 77–174.

Brown I. D. and Altermatt D. (1985) Bond-Valence Parameters Obtained from a Systematic Analysis of the Inorganic Crystal Structure Database. *Acta Crystallogr.* **244**, 244–247.

Casalongue H. S., Kaya S., Viswanathan V., Miller D. J., Friebel D., Hansen H. A., Nørskov J. K., Nilsson A. and Ogasawara H. (2013) Direct observation of the oxygenated species during oxygen reduction on a platinum fuel cell cathode. *Nat. Commun.* **4**.

Cheng L., Fenter P., Nagy K. L., Schlegel M. L. and Sturchio N. C. (2001) Molecular-scale density oscillations in water adjacent to a mica surface. *Phys. Rev. Lett.* **87**, 156103.

Chevalier N. R. (2014) Do surface wetting properties affect calcium carbonate heterogeneous nucleation and adhesion? *J. Phys. Chem. C* **118**, 17600–17607.

Churakov S. V. (2013) Mobility of Na and Cs on montmorillonite surface under partially saturated conditions. *Environ. Sci. Technol.* **47**, 9816–9823.

Cygan R. T., Liang J.-J. J. and Kalinichev A. G. (2004) Molecular Models of Hydroxide, Oxyhydroxide, and Clay Phases and the Development of a General Force Field. *J. Phys. Chem. B* **108**, 1255–1266.

Damaskin B. B. and Frumkin A. N. (1974) Potentials of zero charge, interaction of metals with water and adsorption of organic substances-III. The role of the water dipoles in the structure of the dense part of the electric double layer. *Electrochim. Acta* **19**, 173–176.

Dang L. X. (1995) Mechanism and Thermodynamics of Ion Selectivity in Aqueous Solutions of 18-Crown-6 Ether: A Molecular Dynamics Study. *J. Am. Chem. Soc.* **117**, 6954–6960.

Dazas B., Lanson B., Breu J., Robert J. L., Pelletier M. and Ferrage E. (2013) Smectite fluorination and its impact on interlayer water content and structure: A way to fine tune the hydrophilicity of clay surfaces? *Microporous Mesoporous Mater.* **181**, 233–247.

Demyanova L. P. and Tressaud A. (2009) Fluorination of alumino-silicate minerals: The example of lepidolite. *J. Fluor. Chem.* **130**, 799–805.

Droste J. B., Bhattacharya N. and Sunderman J. A. (1962) CLAY MINERAL ALTERATION IN SOME INDIANA SOILS. In *Clays and Clay Minerals: Proceedings of the Ninth National Conference on Clays and Clay Minerals* (ed. A. Swineford). Elsevier. pp. 329–342.

Fenter P. and Lee S. S. (2014) Hydration layer structure at solid–water interfaces. *MRS Bull.* **39**, 1056–1061.

Giuffre A. J., Hamm L. M., Han N., De Yoreo J. J. and Dove P. M. (2013) Polysaccharide chemistry regulates kinetics of calcite nucleation through competition of interfacial energies. *Proc. Natl. Acad. Sci. U. S. A.* **110**, 9261–9266.

Gomez S. A. S. and Geiger F. M. (2014) Precipitates of Al(III), Sc(III), and La(III) at the muscovite-water interface. *J. Phys. Chem. A* **118**, 10974–10981.

Holmboe M. and Bourg I. C. (2014) Molecular Dynamics Simulations of Water and Sodium Diffusion in Smectite Interlayer Nanopores as a Function of Pore Size and Temperature. *J. Phys. Chem. C* **118**, 1001–1013.

Janecek J. and Netz R. R. (2007) Interfacial Water at Hydrophobic and Hydrophilic Surfaces: Depletion versus Adsorption. *Langmuir* **23**, 8417–8429.

Keller A., Fritzsche M., Ogaki R., Bald I., Facsko S., Dong M., Kingshott P. and Besenbacher F. (2011) Tuning the hydrophobicity of mica surfaces by hyperthermal Ar ion irradiation. *J. Chem. Phys.* **134**.

Lee S. S., Fenter P., Nagy K. L. and Sturchio N. C. (2013) Changes in adsorption free energy and speciation during competitive adsorption between monovalent cations at the muscovite (001)-water interface. *Geochim. Cosmochim. Acta* **123**, 416–426.

Lee S. S., Fenter P., Nagy K. L. and Sturchio N. C. (2012) Monovalent ion adsorption at the muscovite (001)-solution interface: Relationships among ion coverage and speciation, interfacial water structure, and substrate relaxation. *Langmuir* **28**, 8637–8650.

Lee S. S., Fenter P., Park C., Sturchio N. C. and Nagy K. L. (2010) Hydrated cation speciation at the muscovite (001)-water interface. *Langmuir* **26**, 16647–16651.

Leng Y. and Cummings P. T. (2006) Hydration structure of water confined between mica surfaces. *J. Chem. Phys.* **124**.

Loganathan N., Yazaydin A. O., Bowers G. M., Kalinichev A. G. and Kirkpatrick R. J. (2016)

Structure, Energetics, and Dynamics of Cs+ and H2O in Hectorite: Molecular Dynamics Simulations with an Unconstrained Substrate Surface. *J. Phys. Chem. C* **120**, 10298–10310.

Maccarini M., Steitz R., Himmelhaus M., Fick J., Tatur S., Wolff M., Grunze M., Janecek J. and Netz R. R. (2007) Density depletion at solid-liquid interfaces: A neutron reflectivity study. *Langmuir* **23**, 598–608.

Marx D. and Hutter J. (2000) Ab Initio Molecular Dynamics: Theory and Implementation. In *Modern Methods and Algorithms of Quantum Chemistry*, *NIC Series, Vol. 3* (ed. J. Grotendorst). pp. 329–477.

Menzel D. (2002) Water on a Metal Surface. *Science* **295**, 58.

Newberg J. T., Starr D. E., Yamamoto S., Kaya S., Kendelewicz T., Mysak E. R., Porsgaard S., Salmeron M. B., Brown G. E., Nilsson A. and Bluhm H. (2011) Formation of hydroxyl and water layers on MgO films studied with ambient pressure XPS. *Surf. Sci.* **605**, 89–94.

Nilsson A. (2002) Applications of core level spectroscopy to adsorbates. *J. Electron Spectros. Relat. Phenomena* **126**, 3–42.

Nilsson V., Van Den Bossche M., Hellman A. and Gronbeck H. (2015) Trends in adsorbate induced core level shifts. *Surf. Sci.* **640**, 59–64.

Ogasawara H., Brena B., Nordlund D., Nyberg M., Pelmenschikov A., Pettersson L. G. M. and Nilsson A. (2002) Structure and bonding of water on Pt(111). *Phys. Rev. Lett.* **89**.

Papin Ä., Sergent J. and Robert J. (1997) Intersite OH-F distribution in an Al-rieh synthetie phlogopite. *Eur. J. Mineral.* **9**, 501–508.

Park S.-H. and Sposito G. (2002) Structure of Water Adsorbed on a Mica Surface. *Phys. Rev. Lett.* **89**, 85501.

Petersen E. U., Essene E. J., Peacor D. R. and Valley J. W. (1982) Fluorine end-member micas and amphiboles. *Am. Mineral.* **67**, 538–544.

Poynor A., Hong L., Robinson I. K., Granick S., Zhang Z. and Fenter P. A. (2006) How Water Meets a Hydrophobic Surface. *Phys. Rev. Lett.* **97**, 266101–266104.

Pratt L. R. and Pohorille A. (2002) Hydrophobic Effects and Modeling of Biophysical Aqueous Solution Interfaces Hydrophobic Effects and Modeling of Biophysical Aqueous Solution Interfaces. *Chem. Rev.* **102**, 2671–2692.

Ricci M., Spijker P. and Voïtchovsky K. (2014) Water-induced correlation between single ions imaged at the solid–liquid interface. *Nat. Commun.* **5**.

Robert J.-L., Beny J.-M., Della Ventura G. and Hardy M. (1993) Fluorine in micas: Crystal-chemical control of the OH-F distribution between trioctahedral and dioctahedral sites. *Eur. J. Mineral.* **5**, 7–18.

Robert J. L., Della Ventura G. and Hawthorne F. C. (1999) Near-infrared study of short-range disorder of OH and F in monoclinic amphiboles. *Am. Mineral.* **84**, 86–91.

Rotenberg B., Marry V., Vuilleumier R., Malikova N., Simon C. and Turq P. (2007) Water and ions in clays: Unraveling the interlayer/micropore exchange using molecular dynamics. *Geochim. Cosmochim. Acta* **71**, 5089–5101.

Rotenberg B., Patel A. J. and Chandler D. (2011) Molecular explanation for why talc surfaces can be both hydrophilic and hydrophobic. *J. Am. Chem. Soc.* **133**, 20521–20527.

Sakuma H. and Kawamura K. (2011) Structure and dynamics of water on Li+-, Na+-, K+-, Cs+-, H3O+-exchanged muscovite surfaces: A molecular dynamics study. *Geochim. Cosmochim. Acta* **75**, 63–81.

Salmeron M. and Schlögl R. (2008) Ambient pressure photoelectron spectroscopy: A new tool for surface science and nanotechnology. *Surf. Sci. Rep.* **63**, 169–199.

Schaetzl R. and Anderson S. (2005) *Soils: Genesis and Geomorphology*., Cambridge University Press.

Schiros T., Näslund L.-Å., Andersson K., Gyllenpalm J., Karlberg G. S., Odelius M., Ogasawara H., Pettersson L. G. M. and Nilsson A. (2007) Structure and Bonding of the Water−Hydroxyl Mixed Phase on Pt(111). *J. Phys. Chem. C* **111**, 15003–15012.

Schiros T., Takahashi O., Andersson K. J., Öström H., Pettersson L. G. M., Nilsson A. and Ogasawara H. (2010) The role of substrate electrons in the wetting of a metal surface. *J. Chem. Phys.* **132**.

Schlegel M. L., Nagy K. L., Fenter P., Cheng L., Sturchio N. C. and Jacobsen S. D. (2006) Cation sorption on the muscovite (0 0 1) surface in chloride solutions using high-resolution X-ray reflectivity. *Geochim. Cosmochim. Acta* **70**, 3549–3565.

Schwnedel D., Hayashi T., Dahint R., Pertsin A., Grunze M., Steitz R. and Shchreiber F. (2003) Interaction of watr with slef-assembled monolayers: Neutron reflectivity measurements of the water density in the interface region. *Langmuir* **19**, 2284–2293.

Siretanu I., Ebeling D., Andersson M. P., Stipp S. L. S., Philipse A., Stuart M. C., van den Ende D. and Mugele F. (2014) Direct observation of ionic structure at solid-liquid interfaces: a deep look into the Stern Layer. *Sci. Rep.* **4**.

Sposito G. (2004) *The Surface Chemistry of Natural Particles*., Oxford University Press.

Steitz R., Gutberlet T., Hauss T., Klösgen B., Krastev R., Schemmel S., Simonsen A. C. and Findenegg G. H. (2003) Nanobubbles and their precursor layer at the interface of water against a hydrophobic substrate. *Langmuir* **19**, 2409–2418.

Tyrrell J. W. G. and Attard P. (2002) Atomic Force Microscope Images of Nanobubbles on a Hydrophobic Surface and Corresponding Force - Separation Data. *Langmuir* **18**, 160–167.

Uchino T., Iwasaki M., Sakka T. and Ogata Y. (1991) Ab initio molecular orbital calculations on the electronic structure of sodium silicate glasses. *J. Phys. Chem.* **95**, 5455–5462.

Wang J., Kalinichev A. G. and Kirkpatrick R. J. (2009) Asymmetrie hydrogen bonding and orientational ordering of water at hydrophobic and hydrophilic surfaces: A comparison of water/vapor, water/talc, and water/mica interfaces. *J. Phys. Chem. C* **113**, 11077–11085.

Wang J., Kalinichev A. G., Kirkpatrick R. J. and Cygan R. T. (2005) Structure, energetics, and dynamics of water adsorbed on the muscovite (001) surface: a molecular dynamics simulation. *J.*

Phys. Chem. B **109**, 15893–15905.

Wedepohl K. H. ed. (1978) *Handbook of Geochemistry: Vol. II/1.*, Springer-Verlag.

Yamamoto S., Bluhm H., Andersson K., Ketteler G., Ogasawara H., Salmeron M. and Nilsson A. (2008) In situ x-ray photoelectron spectroscopy studies of water on metals and oxides at ambient conditions. *J. Phys. Condens. Matter* **20**, 184025.

Zakaznova-Herzog V. P., Nesbitt H. W., Bancroft G. M., Tse J. S., Gao X. and Skinner W. (2005) High-resolution valence-band XPS spectra of the nonconductors quartz and olivine. *Phys. Rev. B* **72**.

Chapter 6

Nanoscopic dynamics of amorphous calcium carbonate: understanding the mechanisms controlling the crystallization kinetics

6.1. Introduction

Amorphous calcium carbonate (ACC) is a metastable intermediate formed during the crystallization of calcium carbonate biominerals produced by various marine organisms (Addadi et al., 2003). These organisms take advantages of the moldable character of ACC structure and its kinetic persistence against crystallization to form their shells and skeletons of intricate shapes and functionalities. Elucidating the underlying mechanisms behind this control is of particular benefit for the development of functional biomimetic materials, specifically the effective design of pharmaceutical, construction or other types of materials (Aizenberg, 2010; Rieger et al., 2014). The crystallization mechanisms of ACC into more stable polymorphs as well as the polymorph selection mechanisms are thus subject of intense study and debate. While a dissolution-reprecipitation process seems to prevail as crystallization pathway in bulk solution (Lee et al., 2007; Giuffre et al., 2015; Purgstaller et al., 2016), a solid-state crystallization, as seen in air (Ihli et al., 2014; Konrad et al., 2016), may indeed follow a dissolution-reprecipitation process initiated by physisorbed water. ACC contains a large amount of water (~1 H_2O / Ca^{2+}) that is heterogeneously distributed exhibiting distinct dynamic properties (Michel et al., 2008; Reeder et al., 2013; Schmidt et al., 2014). Reflecting this, a recent review by Fernandez-Martinez et al. (2017) suggested that the more hydrated 'nanopores' of the ACC structure could drive local dissolution and rerprecipitation processes, as it would happen in fully saturated systems. Such structural water, distributed within the solid, has been shown to acts as a thermodynamic stabilizer of the amorphous structure due to the hydrogen bonding of water molecules (Raiteri and Gale, 2010). Regarding the polymorph selection, the interactions of water with the carbonate ion have been pointed out to be responsible for the formation of proto-aragonite (Farhadi-Khouzani et al., 2016). Besides the presence of water, studies have shown that biogenic ACC contains a large variety of ions, organics and proteins, exerting unique control over its stability and crystallization in biological media (Addadi et al., 2003; Benzerara et al., 2014). In particular, the effect of Mg^{2+} on the crystallization kinetics and thermodynamics of ACC has been extensively investigated: the presence of a few percentages of Mg^{2+} (~ 0 – 20 % at.) increases the thermodynamic stability of Mg^{2+}-doped ACC (Radha et al., 2012), and it also increases its kinetic persistence, hindering crystallization both in solution (Rodriguez-Blanco et al., 2012) and in air (Politi et al., 2010; Radha et al., 2012). Politi et al. (2010) showed that the Mg-O bond lengths of Mg^{2+}-doped ACC are shorter than those of anhydrous $MgCO_3$ minerals, suggesting that the presence of Mg^{2+} reduces the average molar volume, which induces stress and therefore stabilizes the amorphous structure. A similar hypothesis was made by Xu et al. (2013), showing that reduced molar volume have strong effects on cationic ordering and kinetics of dolomite formation (Xu et al., 2013).

In spite of all these research efforts, questions remain open regarding the precise mechanisms by which Mg^{2+} controls the crystallization kinetics. In this study, we combine neutron and X-ray scattering techniques to probe the dynamics of water network and ions within a series of $Ca_{1-x}Mg_xCO_3 \cdot nH_2O$ solid samples, with x ranging from 0 (ACC) to 1 (amorphous magnesium carbonate, AMC). Specifically, incoherent inelastic neutron scattering (IINS), a powerful probe of water libration, sensitive to the hydrogen bonding environment of water molecules (Ockwig et al., 2008; Han and Zhao, 2011), is combined with X-ray photon correlation spectroscopy (XPCS), a coherent X-ray scattering technique providing relaxation dynamics in disordered systems (Giordano and Ruta, 2015; Ross, 2016). These scattering techniques, together with thermogravimetric analyses, link the nanoscopic dynamics within the solids to the molecular-scale mechanisms controlling crystallization kinetics.

6.2. Materials and Methods

6.2.1 Sample preparation

A series of Mg^{2+}-doped amorphous calcium carbonates, $Ca_{1-x}Mg_xCO_3 \cdot nH_2O$ ($x = 0$, 0.35, 0.7 and 1) were synthesized by rapidly mixing equimolar solutions of $Ca_{1-y}Mg_yCl_2$ ($y = 0$, 0.5, 0.75 and 1) and Na_2CO_3, followed by immediate quench with acetone and vacuum-filtration (Radha et al., 2012). Concentrations used were 0.02, 0.06 and 0.1 M for $y = 0$, $0 < y < 1$ and $y = 1$, respectively. When $y = 0$ (pure ACC), the pH of the mixture was adjusted to ≈13 with NaOH to favor the precipitation of an amorphous basic calcium carbonate (Kojima et al., 1993; Wang et al., 2017). Prior to the synthesis, all glassware was cleaned with 20 % HCl to remove any possible nucleation loci, and rinsed thoroughly with ultrapure water. In addition, glassware as well as all the solutions used in the synthesis were kept in a 4°C refrigerator before use. All the samples, as synthesized and confirmed to be amorphous by ATR-FTIR (Nicolet iS10), were kept in a desiccator until analysis. Additionally, a fraction of each sample was dried at 80 °C in a vacuum oven for one hour then kept in a desiccator until analysis, after being verified to be amorphous. The chemical compositions (i.e. x values) were obtained by ICP-OES (Varian 720ES) and the water contents (i.e. n values) were determined by thermogravimetry analyses (see 6.2.4).

6.2.2. Inelastic incoherent neutron scattering (IINS)

Since the ^{1}H isotope has a very large incoherent neutron scattering cross section, IINS is a unique, sensitive probe for intermolecular, rotational modes of water, called libration, occurring between 300 to 1200 cm^{-1}. IINS experiments were performed in the range of energy transfers from 21.5 to 195.3 meV with an energy resolution of ΔE/E 2-3%, using the IN1-LAGRANGE (LArge GRaphite ANalyser for Genuine Excitations) secondary spectrometer setup installed at the hot source of the high-flux reactor at the Institute Laue-Langevin in Grenoble, France (for instrumental and technical details, see Ivanov et al., 2014). The energy transfer was obtained by subtracting the analyzer energy (4.5 meV) from the energy of incident monochromatic neutrons. Under the conditions that the final momentum of the scattered neutrons, $\boldsymbol{k_f}$, is much smaller than the initial one, $\boldsymbol{k_i}$, (i.e. high $\boldsymbol{q}$), the observed intensity is directly proportional to the generalized vibrational density of states (GvDOS), that is the hydrogen partial density of states in the case of hydrogenated materials.

The samples were loaded in hollow aluminum sample holders. The spectra were recorded at 10 K in order to decrease the Debye-Waller factor. The obtained intensity was normalized to the monitor counts and then was corrected for the monitor efficiency using LAMP (Large Array Manipulation Program) package provided by ILL. The background spectrum from the cryostat and an empty sample holder was measured separately and then subtracted from the raw IINS spectrum of the sample.

6.2.3. X-ray photon correlation spectroscopy (XPCS)

XPCS technique takes advantage of a high flux coherent X-ray beam to register speckle patterns scattered from a disordered system. Time-resolved speckle patterns are collected on a 2D detector (Fig. S6.1) and their intensity fluctuations $I(\boldsymbol{Q}, t)$ provide information on the dynamics of structural rearrangements at the length scale defined by the experimental q range (q being the modulus of the momentum transfer, $q = |\boldsymbol{q}| = |\boldsymbol{k}_{\mathrm{i}} - \boldsymbol{k}_{\mathrm{f}}|$). This is evaluated by computing the intensity autocorrelation function:

$$g^{(2)}(\Delta t, q) = \frac{< I(t,q) I(t+\Delta t, q) >}{< I(t,q) >^{2}} \tag{6.1}$$

where <…> denotes the ensemble average (within an arc of $q + \Delta q$ values) for a given q. This function simply gives the correlation between intensities of a given q region within the 2D detector separated by a lag time Δt.

XPCS measurements were performed at ambient temperature under active vacuum, with an incident energy of 8 keV (λ = 1.55 Å) in a horizontal scattering geometry for a q range of 0.001 to 0.022 Å^{-1}, at the ID10 Troïka beamline at the European Synchrotron Radiation Facility (ESRF) in Grenoble, France.

The coherent part of the incoming X-ray beam (10×10 μm) was selected by a pinhole placed right in front of the sample. The samples were loaded into steel gaskets with a 100 μm-wide hole, which was then mounted vertically in the vacuum chamber. 2D speckle patterns were recorded using a Maxipix photon counting area detector with 256×256 pixels (pixel size 55 μm). Acquisition times and the number of intensity attenuators were adjusted to avoid beam damage to the samples (monitored by plotting two-time correlation functions (Bikondoa, 2017)). Acquisition times of 0.04 s were chosen for most of the samples, with a sleeping time of 1.96 s between images, thus leading to a lag time Δt of 2 s between subsequent speckle patterns. Only sample $x = 0.35$ was measured with a higher dose: 0.04 s acquisition times and 0.46 s sleeping time ($\Delta t = 0.5$ s). The static structure factor, S(q), was obtained from the same data by performing spatial averages of the speckle patterns. Intensity autocorrelation functions were generated using the pyXPCS software, provided by the Troïka beamline. The intensity autocorrelation function, or the decay of the correlation over time is fitted with a Kohlrausch–Williams–Watts (KWW) model:

$$g^{(2)}(t) = 1 + c * \exp(-2 * (t/\tau)^{\beta}) \tag{6.2}$$

where c is a set-up dependent contrast, τ is the structural 'relaxation time' and β is a 'shape factor' providing information about the nature of the relaxation processes. An ideal Brownian diffusive system will show an exponent of $\beta = 1$. Values of $\beta < 1$ are typically associated to dynamical heterogeneities in the sample, whereas values $\beta > 1$ are associated to stressed or 'jammed' systems (Ruta et al., 2013; Evenson et al., 2015).

6.2.4. Thermogravimetric and calorimetric analyses

The samples were loaded in alumina crucibles, and heated from 25 to 1100 °C at 15°C /min under a N_2 flow of 20 mL/min (Mettler Toledo TGA/DSC3+). The water content in each sample was quantified from the total weight loss and was further distributed into three types of water from the perspective of thermal stability, namely mobile, rigid and trapped. This was achieved by a rigorous determination of the first three inflection points found on the second derivatives of the TGA curves (for details, see Figs. S6.2).

6.3. Results

6.3.1. High-energy water dynamics probed by IINS

Librational spectra of Mg^{2+}-doped ACC samples are shown in Figure 6.1a. The broad spectral features are typical of disordered systems (Ockwig et al., 2008; Ockwig et al., 2009). The so-called librational edge, occurring from 300 to 600 cm^{-1}, represents the onset of librational bands. At higher frequencies (from 600 to 1100 cm^{-1}), the librational modes, namely rock, twist and wag, are very sensitive to the local H-bonding environment (Li et al., 1999). The librational edge of ACC displayed the sharpest feature, of which the slope then decreases as the Mg^{2+}/Ca^{2+} ratio increased (Fig. 6.1a). Concomitantly, there was a shift in the distribution of modes to the high frequency, proportionally to the Mg^{2+}/Ca^{2+} ratio.

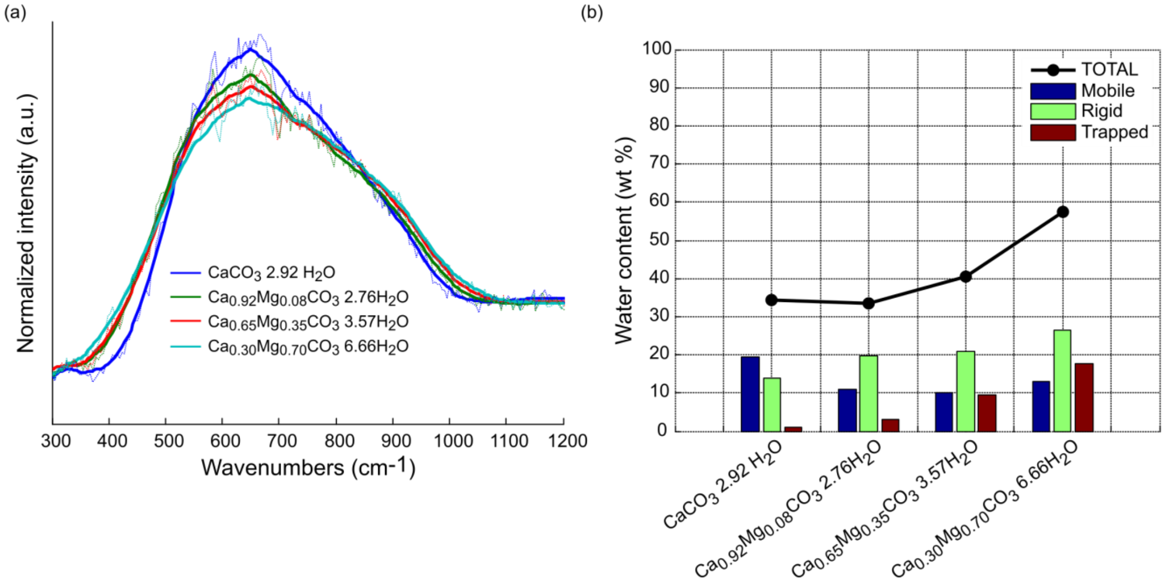

Figure 6.1. IINS spectra and thermogravimetry analysis. **(a)** Librational region of the generalized vibrational density of states (GvDOS) for pure and Mg^{2+}-doped ACC as synthesized. Intensity is normalized to the unity within the x-limit of 300 to 1200 cm^{-1}. **(b)** Water contents in the corresponding samples and their distribution into mobile, rigid and trapped regimes determined by TGA/DSC.

For the corresponding samples, the total water contents and their internal distribution (mobile, rigid and trapped regimes) are shown in Figure 6.1b. Besides the total water contents that increased as the Mg^{2+}/Ca^{2+} ratio increased, the internal distribution of the water species showed a decrease of the mobile water and an increase of the rigid and trapped water as more Mg^{2+} is doped.

Figure 6.2 compares the librational spectra and the thermogravimetry data for fresh and dried (1 hour at 80 °C) samples. When no Mg^{2+} is present, the drying process resulted in a redistribution of modes from high to intermediate frequencies (Fig. 6.2a top), together with a loss of both mobile and rigid types of water (Fig. 6.2b top). On the other hand, when Mg^{2+} is doped, regardless of its amount, the drying process did not affect the high-frequency modes above 900 cm^{-1}, while there was a decrease in the slope of the librational edge, of which the change was the most significant for $x = 0.7$ (Fig. 6.2a bottom). In addition, the drying procedure increased the fraction of water in the trapped regime, besides the loss of water in mobile and rigid regimes.

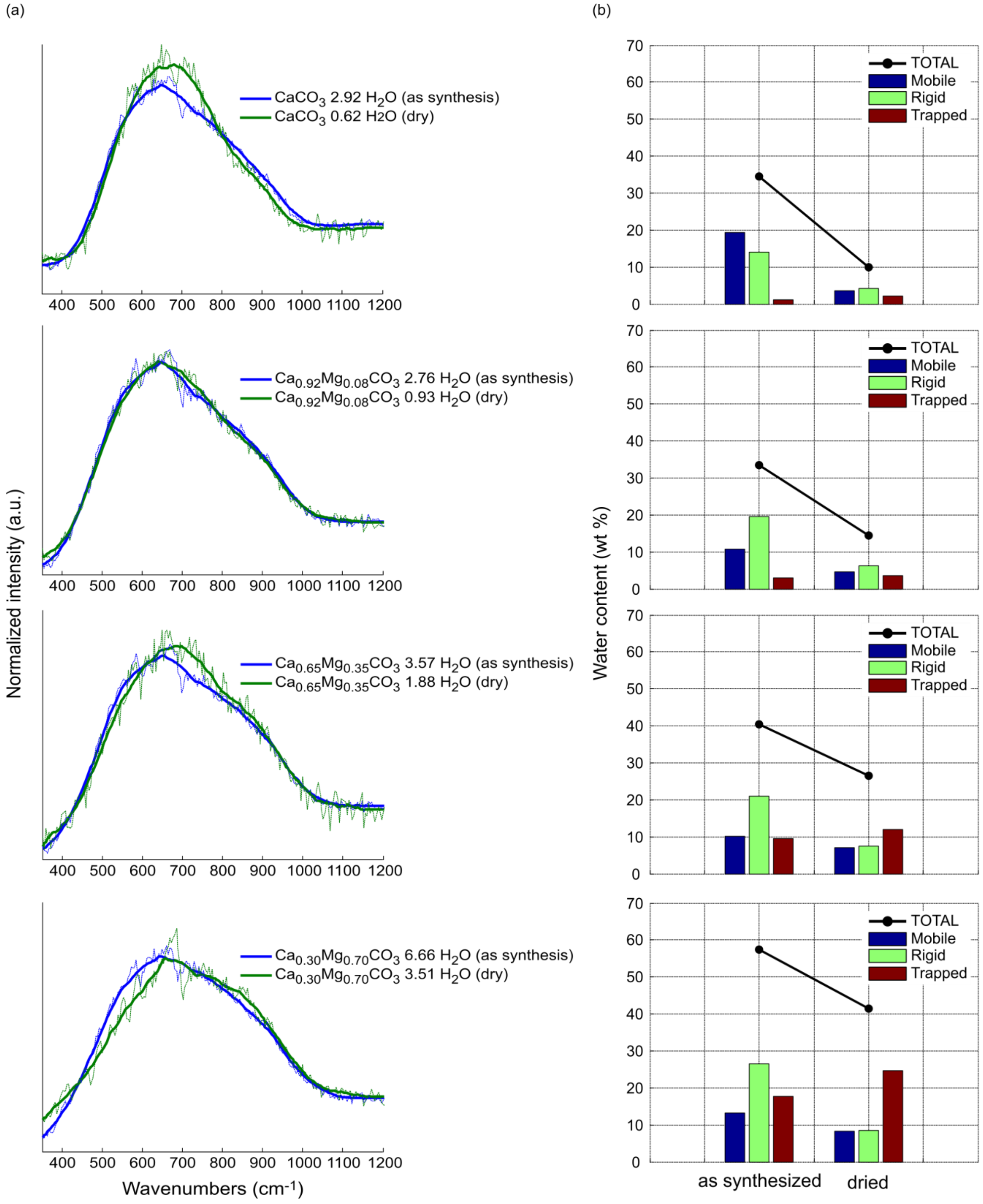

Figure 6.2. Comparison of fresh and dried samples. **(a)** Librational region of the generalized vibrational density of states (GvDOS) measured at 10 K for as-synthesized vs. dried (80°C for 1 hour) $Ca_{(1\text{-}x)}Mg_xCO_3{\cdot}nH_2O$, with x = 0, 0.08, 0.35 and 0.7. Intensity is normalized to the unity within the x-limit of 300 to 1200 cm^{-1}. **(b)** Total water contents (black points) and their distribution into mobile, rigid and trapped regimes determined by TGA/DSC.

6.3.2. Ionic dynamics probed by XPCS

The normalized intensity auto-correlation functions obtained from the first 33 minutes of XPCS measurements are shown in Figure 6.3a for samples x = 0 (ACC), 0.7 and 1 (AMC). Relaxation times,

τ, and the shape parameter, β, obtained through the fitting by the KWW model (eq. 6.2) are given in Table 6.1. The frequencies of structural re-arrangements, $\omega = 1/\tau$, (Fig. 6.3b) as a function of Mg^{2+} and water contents show a direct proportionality. In addition, the nature of the dynamics, for all the systems, was found to be hyper-diffusive or ballistic (i.e. $1/q$-dependence of the relaxation time τ; Fig. S6.3c) together with the exponent β to be larger than 1 (i.e. compressed; Table 6.1), which is indicative of an internally stressed system.

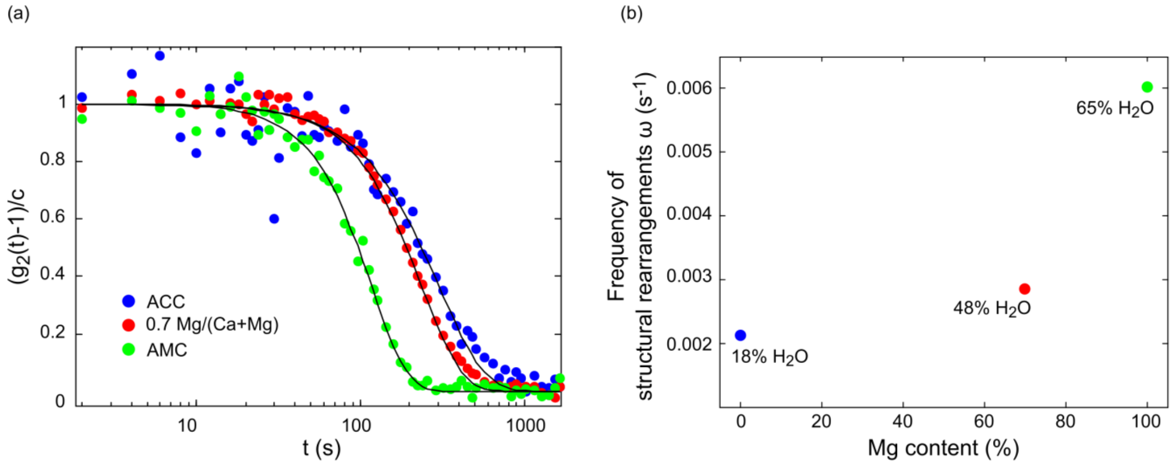

Figure 6.3. Ionic dynamics. **(a)** Normalized intensity auto-correlation functions measured at q = 0.021 Å^{-1} for $Ca_{(1-x)}Mg_xCO_3{\cdot}nH_2O$, with x = 0 (ACC), 0.7 and 1 (AMC). Fits to the data using the KWW model are represented with solid lines. **(b)** Frequency of structural re-arrangements ω (= $1/\tau$) plotted as a function of Mg^{2+} and water contents.

Table 6.1. Parameters obtained by fitting the KWW model to the intensity auto-correlation curves measured by XPCS

$Ca_{1-x}Mg_xCO_3{\cdot}nH_2O$			
x	n	τ (s)	β
0	1.2	449 ± 40	1.62 ± 0.22
0.7	4.7	349 ± 10	1.73 ± 0.09
1	8.7	171 ± 12	1.85 ± 0.24

Three samples were measured under the same condition (lag time Δt of 2 s between subsequent speckle patterns with 0.04 s of acquisition time plus 1.96 s of sleeping time).

When measuring for a long period of time (hours), a significant slowing down of the relaxation dynamics (i.e. aging) was observed for all samples (Fig. 6.4a), with no apparent changes in the static (time-averaged every 33 minutes) structure factors (Fig. 6.4b).

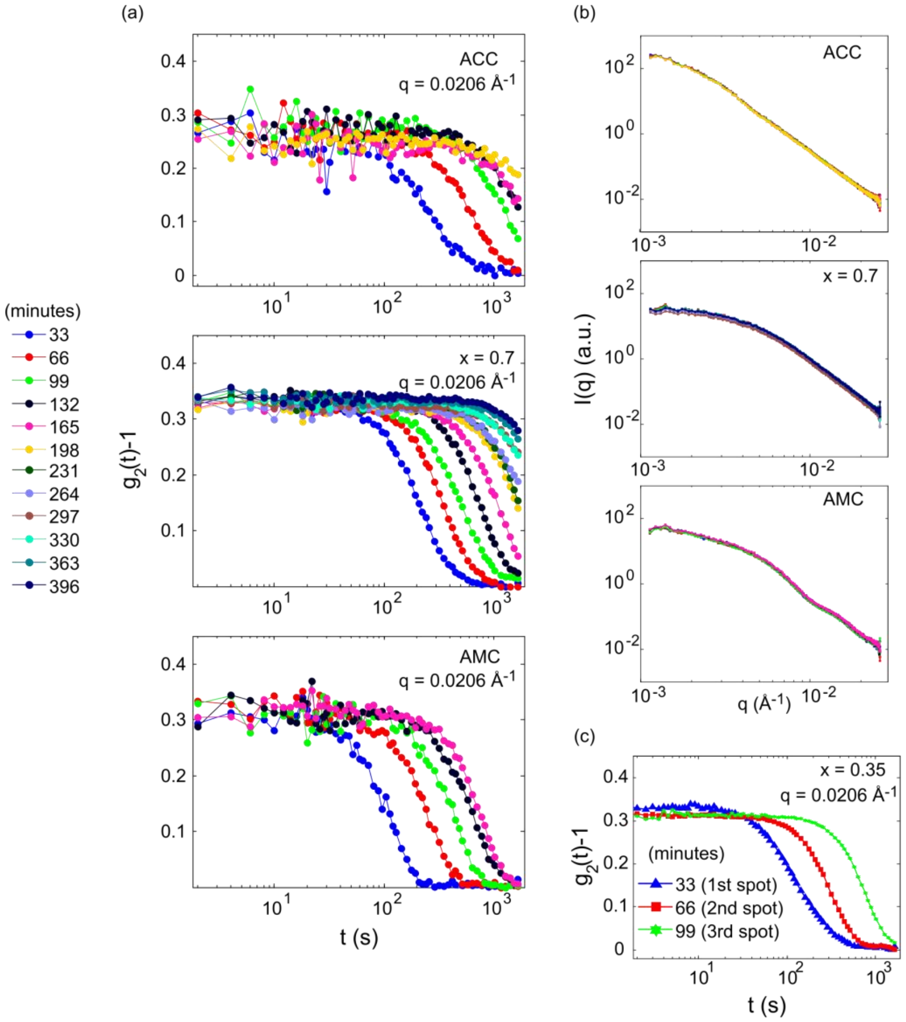

Figure 6.4. Aging dynamics. **(a)** Time-evolution of intensity autocorrelation functions for $Ca_{(1-x)}Mg_xCO_3{\cdot}nH_2O$, with $x = 0$ (ACC), 0.7 and 1 (AMC) at $q = 0.021$ $Å^{-1}$ ($d \sim 30.6$ nm), obtained for every 1000 images, corresponding to an experimental time of 33 min. (**b**) Evolution of the static structure factor, S(q), for the full q range measured ($0.001 \leq q \leq 0.023$). (**c**) Intensity autocorrelation functions for $Ca_{0.65}Mg_{0.35}CO_3$ $2.5H_2O$, measured at three different spots on the same sample but at different times.

6.4. Discussion

6.4.1. The effects of Mg^{2+} on the water dynamics

As shown in Figure S6.4, the librational spectra of water in liquid state are broad due to the disordered nature of the hydrogen bonding network, and at temperatures below zero degrees, the spectra display sharp features since the hydrogen bonding network is in very well-defined order (i.e. ice). The decrease in the slope of the librational edge (Fig. 6.1a) therefore indicates that the order of the hydrogen bonding network is less defined as Mg^{2+}/Ca^{2+} ratio increases. In other words, the presence of Mg^{2+} results in the distribution of modes (i.e. degeneration of modes), disrupting the typical ordering of water network. To this point, the increase in the water in the rigid and trapped regimes (Fig. 6.1b) may be responsible, acting as structural water that does not behave like ice. At the same time, the redistribution of modes toward higher frequencies (Fig. 6.1a) points to an increase in the stiffness of the hydrogen bonds. Due to its small size, Mg^{2+} has a higher enthalpy of hydration as compared to other divalent ions such as Ca^{2+}, Ba^{2+} or Sr^{2+} (Noyes, 1962). This translates into a much slower water exchange rate in its first hydration shell, specifically three orders of magnitude slower than that of Ca^{2+} (Di Tommaso and de Leeuw, 2010), which is reflected in the observed formation of strong hydrogen bonds. One may also note that the libration measured here results from the H-bond interactions of water molecules with neighboring water molecules and ions. The shift in the distribution of modes towards higher frequencies thus shows that the presence of a strong center of charge such as Mg^{2+} not only enhances the enthalpic interaction of the ions with water molecules, but also that of the bonded water with its neighboring water molecules. Other divalent ions with larger ionic radii, such as Ba^{2+} or Sr^{2+}, have lower electronic density. Increasing Ba^{2+}/Ca^{2+} ratio decreased the order of the hydrogen bonding network but the stiffness of H-bond interactions remained the same (Fig. S6.5a) and increasing Sr^{2+}/Ca^{2+} ratio had no effect on the water dynamics (Fig. S6.5b). The increase in the stiffness of the H-bonding interactions therefore seems unique to Mg^{2+}.

It is also necessary to discern how the different types of water contribute to the librational spectra. When Mg^{2+} was absent, the change in the librational spectra before and after the drying process resides in the redistribution of modes from the high to intermediate frequencies (Fig. 6.2a top), referring to the reduction in the stiffness of the hydrogen bonding interactions, which can be linked to the loss of water in mobile and rigid regimes (Fig. 6.2b top). Interestingly, for all the Mg^{2+}-doped samples, the drying process did not affect the stiffness as there is no change above 900 cm^{-1}. Provided that there was also the loss of both the mobile and rigid water, this resistance could be attributed to the trapped water, of which the proportion increased as dried (Fig. 6.2b). The non-negligible presence of such trapped water, unique to the Mg^{2+}-doped amorphous samples and proportional to the Mg^{2+}/Ca^{2+} ratio, thus confirms that the presence of Mg^{2+} increases the structural water that is responsible for the disorder in the hydrogen bonding network, as discussed above. Overall, our experimental data successfully demonstrate that the kinetic hindrance to crystallization is linked to the stiff hydrogen bonding interactions.

6.4.2. Amorphous carbonates as highly dynamics soft matter systems

XPCS is sensitive to structural changes within the material, with a weight factor that is proportional to the atomic number of each atom and to its concentration (Als-Nielsen and McMorrow, 2011). We performed the measurements in a *q*-range that covers small angles, corresponding to distances of ~25 to 630 nm. The observed dynamics are therefore not atomic-scale, but they cover a range that corresponds to density fluctuations within individual particles of amorphous calcium and magnesium carbonate, which have typical sizes in the order of tens to hundreds of nanometers (Radha et al., 2012). It is important to note that test experiments performed at higher *q* (atomic scale) were unsuccessful since the dynamics were too fast (data not shown) and was out of the measurable range available to the technique. This highly dynamic character of these amorphous carbonate solids, measured at scale of individual particles as discussed above, are comparable to the slower dynamics present in other amorphous and glassy systems such as covalent-like metallic glasses exhibiting relaxation times that are at least four orders of magnitude longer (Horbach et al., 2002; Ruta et al., 2012). Amorphous carbonates can therefore be considered as 'soft systems', as described also by the self-diffusivity of Ca^{2+} determined by computer simulations, which is close to that of molecular species in organic solvents (Wallace et al., 2013).

At the scale of tens of nanometers (d~30.6 nm), there was an increase in the relaxation dynamics when samples are doped with Mg^{2+} (Fig. 6.3 and Table 6.1). Given the isotropic character of the amorphous carbonates, and the lack of recognizable higher order or hierarchical structural arrangements (Fig. 6.4b), it seems logical to think that the same behavior can be extrapolated to the Å-scale. The observed dynamic behavior can therefore be interpreted as a proxy for the atomistic dynamics. Indeed, relaxation times τ can be interpreted here as the lifetimes of a given structural configuration. Thus the number of structural rearrangements in a unit of time (i.e. ω) is the number of conformational trials in a series of structural configurations that eventually lead the system toward crystallization. In this perspective, relaxation dynamics proved here allows to establish a link to the crystallization kinetics.

6.4.3. Linking solid state dynamics and crystallization kinetics

Unique combination of neutron and X-ray scattering techniques demonstrated here that the presence of Mg^{2+} induces an unexpected coexistence of the stiffening of hydrogen bond networks and the accelerated relaxation dynamics, which together brings about the barrier to crystallization. For a solid-state nucleation process (i.e. crystallization), the change in the free energy associated to the formation of a new bulk phase is proportional to the difference in the chemical potential $\Delta\mu$ between the initial states and final states and to the interfacial free energy of the newly created interface:

$$\Delta g = -\left\{\frac{\frac{4}{3}\pi r^3}{\Omega}\right\}(\mu_\mathrm{i} - \mu_\mathrm{f}) + 4\pi r^2 \alpha \tag{6.3}$$

where Ω is the molar volume of the new phase, r is the size of the nucleus and α is the interfacial free energy corresponding, in case of solid-state nucleation process, to the interface created between the amorphous matrix and the crystalline nucleus. When the nucleation barrier is high enough compared to the thermal energy, $K_\mathrm{B}T$, the metastable state of the system contains thermal fluctuations that are well described by a Boltzmann distribution. Sometimes, some of these fluctuations will reach and overcome the critical size. According to CNT, they can then continue to grow so as to become more and more stable. CNT assumes that the system reaches a steady-state and stable nuclei then appear at a rate given by:

$$J_\mathrm{n} = A\mathrm{e}^{-\frac{\Delta g}{K_\mathrm{B}T}} = f^{*}ZC_0\mathrm{e}^{-\frac{\Delta g}{K_\mathrm{B}T}} \tag{6.4}$$

where f^* is the rate at which a critical cluster grows, Z is the Zeldovich factor and C_0 is the concentration of particles (ions) in the system. The factor f^* depends on the nucleus growth mechanism. The Zeldovich factor is determined by the energy profile around the particle of the critical size (it is therefore proportional to dg/dr). Critical clusters experience random size variations that cause some of them to re-dissolve and to fall out of the stable region (Kashchiev, 2000). The Zeldovich factor accounts for the probability of success where only some of these clusters will continue to grow. It is a factor that effectively decreases the nucleation rate by $f^*\cdot C_0\cdot\exp(-\Delta g/K_\mathrm{B}T)$. As shown by Clouet (2010), under the assumption that the critical cluster growth is controlled by the long-range diffusion of solute atoms, the nucleus growth rate f^* can be expressed as:

$$f^{*} = 4\pi r \frac{D}{\Omega}\frac{x^0}{y^e} \tag{6.5}$$

where x^0 and y^e are fractions of atoms diffusing in the metastable (initial) and stable (final) phases, respectively, and D is the diffusion coefficient of the particles feeding the crystalline nucleus (under the approximation that the diffusion of a single species is limiting the growth process). This expression links therefore the diffusivity of the species being added to the growing cluster to the nucleation rate. The diffusivity, D, in eq. (6.5) is the self-diffusivity of a single species within the solid. To this point, as described in chapter 3, the diffusivity associated to the structural relaxation measured by coherent X-rays is the so-called ‘coherent diffusivity’, which measures the relative displacement of one species with respect to any other (Binder and Kob, 2011; Ross et al., 2014). In the case of solid state nucleation within disordered materials, such as the case for the crystallization of amorphous carbonates, the coherent diffusivity is more representative of the physical mechanisms underlying the crystallization process. It is therefore reasonable to replace the f^* in eq. (6.4) by:

$$f^{\mathrm{coh}} = \frac{D_{\mathrm{coh}}}{\Omega} = \frac{1}{\Omega\tau q^2} = \frac{\omega}{\Omega q^2} \tag{6.6}$$

Using $\omega = 1/\tau$, equation (6.4) then becomes:

$$J_{\mathrm{n}} = \frac{\omega}{\Omega q^2} Z C_0 \mathrm{e}^{-\frac{\Delta g}{\mathrm{k}_B T}} \tag{6.7}$$

Note that the proportionality with q^2 is only true for a Brownian diffusive system. Other diffusion mechanisms are present in jammed or strained systems that show compressed exponentials in the relaxation functions, with different q-dependencies (e.g., $D \propto q^{-1}$). Our results show that the nature of the diffusivity in the amorphous carbonates is not that of an ideal Brownian system, but it displays compressed exponents ($\beta > 1$), with $1.23 < \beta < 1.85$. The q-dependence of the relaxation times also shows deviations from the ideal Brownian diffusivity (Fig. S6.3c). Under these circumstances, the results of these experiments are analyzed here in a qualitative way, by comparing relaxation times of different samples measured at the same value of q (= 0.021 Å^{-1} (d ~ 30.6 nm)), independently of the nature of the diffusion mechanism. A detailed analysis of the evolution of the compressed exponents β with the Mg^{2+} concentration is thus beyond the scope of this thesis.

We shall now analyze the unexpectedly accelerated relaxation dynamics within Mg^{2+}-doped amorphous carbonates, with ACC showing a frequency of structural re-arrangement at least two times slower than that of AMC. A detailed examination of all the factors in eq. (6.7) is required to understand which factor controls the crystallization kinetics. In view of the kinetic, pre-exponential factors in eq. (6.7), the higher value of ω for AMC indicates that this has to be compensated by a smaller Zeldovich factor, Z, so that J_{n} becomes higher for ACC than for AMC. The Zeldovich factor is proportional to the probability that structural rearrangements within the sample result in successful crystallization events. Different structural factors could explain this. Namely, the presence of more strongly bonded water molecules in Mg^{2+}-doped amorphous carbonates than in pure ACC (Fig. 6.1a) could be posing steric impediments for the formation of crystalline nuclei. Indeed, Mg^{2+} dehydration has been cited in the past as a factor hindering the formation of ordered Ca-Mg-carbonates such as dolomite (Arvidson and Mackenzie, 1999; Wang et al., 2009). The small molar volume of the Mg^{2+} ion, which creates internal strain impeding the mobility and decreasing the entropy of the Mg-CO_3 units, has also been indicated as a possible steric factor (Xu et al., 2013; Pimentel and Pina, 2014). This last may also explain the measured stressed character of the Mg^{2+}-doped amorphous carbonates ($\beta > 1$). It is yet to note that J_{n} depends also on the thermodynamic, exponential term (eq. 6.7), controlled by the distance to the equilibrium, $\Delta\mu$, and by the interfacial free energy, α, that remains unknown, since $\Delta\mu$ and α depend strongly on the crystalline phases considered.

An additional element limiting the discussion is the fact that the concentration of water in the samples increases proportionally to the Mg^{2+} concentration. Determining the factor in controlling water and ionic dynamics thus remain thus elusive. To cope with this ambiguity, future experiments should be designed such that samples doped with different Mg^{2+} concentrations contain the same concentration of water (and vice versa).

6.4.4. Aging dynamics

It is striking that the structure factor of the different amorphous samples did not show significant changes during the course of the experiments whereas the aging proceeded by almost one order of magnitude during the same length of time (Figs 6.4a and 6.4b). In addition, the aging behavior seems to reflect the persistence of AMC and Mg^{2+}-doped amorphous carbonates in comparison to that of ACC. As shown in Figure S6.3a, the time-evolution of the measured relaxation times τ, particularly the increase of the τ values (i.e. aging), shows that ACC displays the most dramatic changes with a five-fold increase. The fact that the Mg^{2+}-doped samples are less prone to age may refer to their stability in comparison to that of pure ACC.

Aging phenomena are typical in systems that are out-of-equilibrium, such as metal glasses (Ruta et al., 2012; Giordano and Ruta, 2015), supported silica particles (Shinohara et al., 2010) or peptide gels (Dudukovic and Zukoski, 2014). For our case, different reasons can be responsible for the aging behavior:

(i) The aging is due to partial dehydration during the course of the XPCS experiments. Samples were kept in a dry desiccator then transferred to the experimental chamber where they undergo an active primary vacuum (~5 mbar). In order to check whether (and when) these processes caused significant dehydration, we reproduced the conditions under which samples were subjected to experience and monitored the water contents. The results show that most of the dehydration takes place during the first ~12 hours, which corresponds to the time spanned between the end of the synthesis and the start of the XPCS during which the corresponding sample was in a dry desiccator (Fig. S6.6; $x = 0.7$). Active vacuum resulted in only a slight dehydration (maximum change of 2%). For samples $x = 0$, 0.35 and 1, only the water loss in a dry desiccator is reported (Fig. S6.7) since the loss of water under active vacuum can be negligible. Nevertheless, as shown by Giordano and Ruta (2015) for the case of metallic glasses, small structural changes (~1% change in the lattice parameter) can be responsible for large changes in the relaxation dynamics (~ one order of magnitude) . We therefore cannot exclude that this small dehydration under active vacuum was responsible for the observed aging behavior, which neither allows one to discern the reason why the aging was less prominent for AMC and Mg-dopes ones.

(ii) The aging is due to X-ray beam induced dynamics. A strong coupling between the samples and the 8 keV X-rays used for these measurements could be responsible for the slowing down of the dynamics, including possible X-ray induced dehydration. A recent study has shown that relaxation dynamics of covalent glasses are affected by X-ray beams, and that this effect can even be used as a probe to accelerate the system dynamics, given their reversibility (Ruta et al., 2017). In order to test whether this could be the case, three experiments were performed using sample x = 0.35, lasting 50 minutes each, on three different spots with a minimum spacing of 100 µm (Fig. 6.4c). The intensity autocorrelation functions at these three spots exhibited a similar trend (i.e. slowing down) as for samples x = 0, 0.7 and 1 (Fig. 6.4a), indicating that the slowing down is not limited locally on the irradiated spot, inferring that the beam-induced aging can *a priori* be excluded.

6.5. Conclusions

The kinetic stabilizing effect of Mg^{2+} in amorphous carbonates has been previously reported and is considered as one of the most important mechanisms possibly regulating biomineral crystallization processes (Rodriguez-Blanco et al., 2012). The presence of a few molar Mg^{2+} is known to exert a thermodynamic effect stabilizing calcite (Navrotsky and Capobianco, 1987) as well as Mg^{2+}-doped amorphous calcium carbonate (Radha et al., 2012). Previous studies have also reported the influence of the water network as a stabilizer of the amorphous structure (Raiteri and Gale, 2010). However, the precise mechanisms of stabilization remained unknown. Here, a combination of neutron and X-ray scattering techniques probing the dynamics of the amorphous systems has, for the first time, experimentally unraveled the explicit factors controlling the crystallization kinetics. On one hand, inelastic neutron scattering experiments have shown that the presence of water, brought by Mg^{2+}, a strong center of charge, strengthens the H-bonding interactions within the water network. On the other hand, X-ray scattering experiments showed that Mg^{2+}-doped ACC displayed a enhanced dynamic character as compared to ACC. These results point to the coexistence of a stiff water network and the accelerated nanoscopic dynamics within the kinetically persistent Mg^{2+}-doped ACC, which together invokes the presence of steric barriers to crystallization induced by the presence of Mg^{2+}.

Supporting information

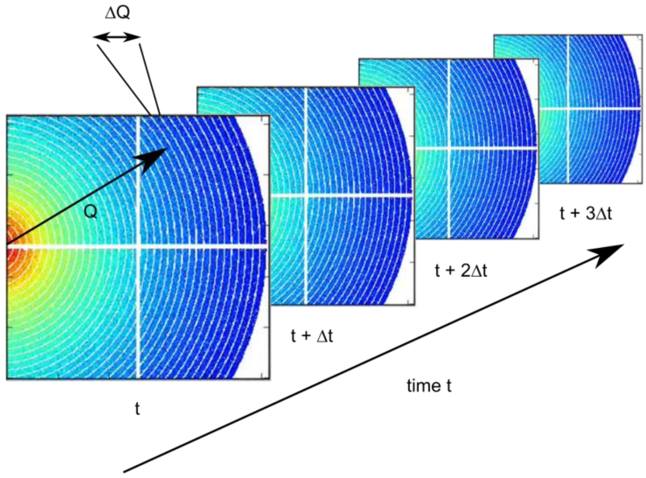

Figure S6.1. Representative 2D speckle patterns and schematic illustration of XPCS data analysis . The intensity autocorrelation functions were computed from an ensemble of these time-resolved images at a given *q* with a certain width.

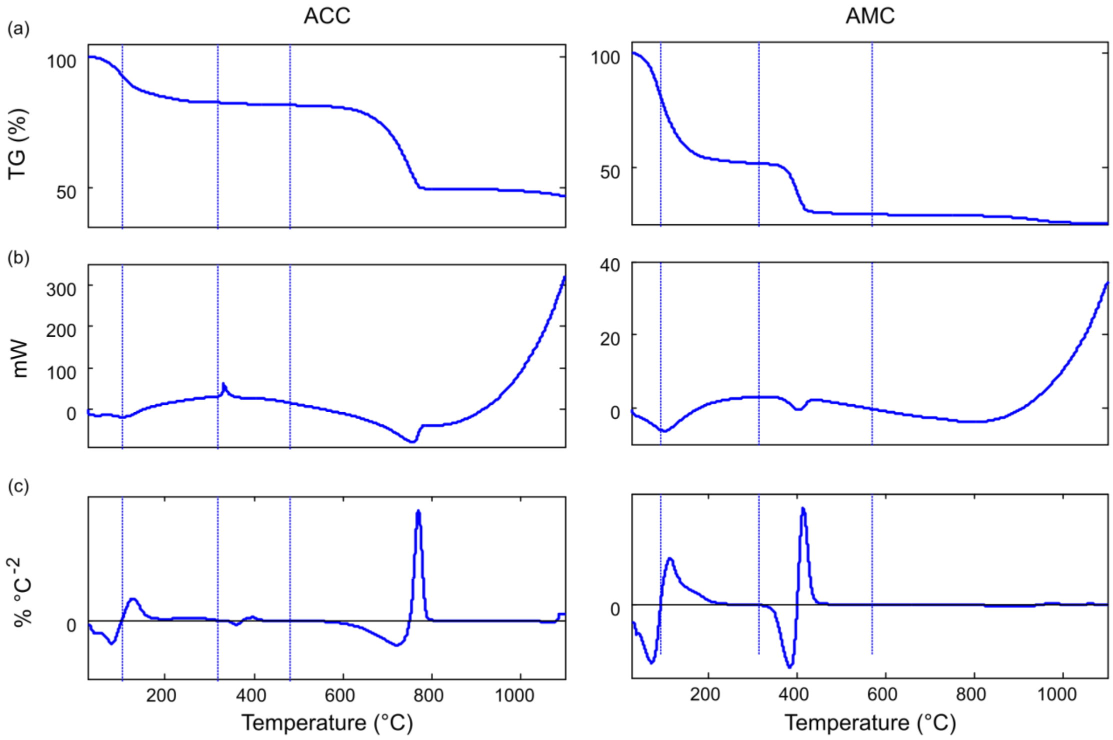

Figure S6.2. Determination of mobile, rigid and trapped water regimes for ACC (left) and AMC (right). **(a)** TGA, **(b)** DSC, and **(c)** TGA second derivative curves. Three regimes were determined based on the first three inflection points found on (c), indicated by dotted guidlines. The DSC curve of ACC generally exhibits two endothermic peaks: a first broad peak at around 100°C, indicative of a dehydration of adsorbed water, and a second at around 750°C, indicative of decarbonation from calcite to CaO. The sharp exothermic peak, observed at around 320 °C, indicates crystallization of ACC into calcite. For Mg-doped ACCs, absence of sharp crystallization peaks and the presence of two endothermic peaks (one at ~100 °C for dehydration and the other at ~400 °C for decarbonation) were the common features of DSC curves. The limit between mobile and rigid water regimes typically falls between 80 – 150 °C and that between rigid and trapped regimes falls between 290 – 350 °C, depending on the hydration states and the Mg^{2+}/Ca^{2+} ratio.

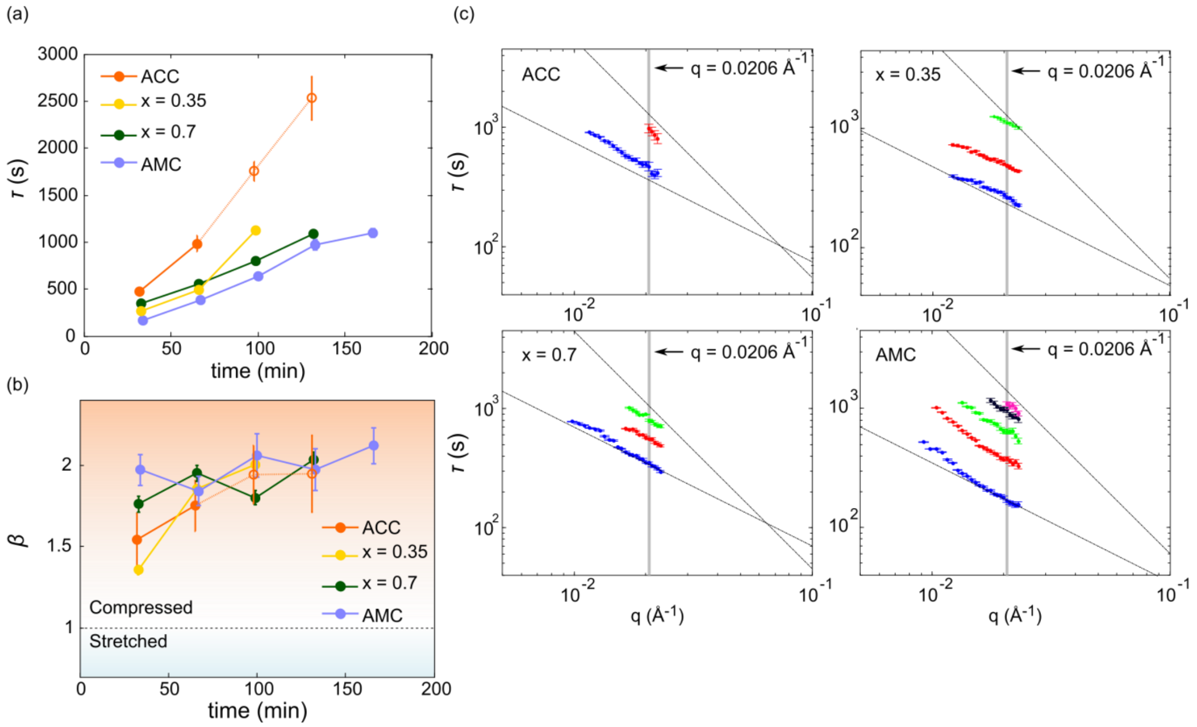

Figure S6.3. Time-evolution of **(a)** relaxation time τ, **(b)** shape parameter β and **(c)** q-dependence. Data fitted using the KWW model at q = 0.0206 $Å^{-1}$ (d = 30.6 nm). **(a, b)** t = 0 corresponds to the starting time of each measurement. Extrapolated values (from incomplete intensity auto-correlation functions) are indicated by empty circles and dotted lines. **(c)** q-dependence of the relaxation time for $Ca_{(1-x)}Mg_xCO_3 \cdot nH_2O$, with x = 0 (ACC), 0.35, 0.7 and 1 (AMC). The vertical grey lines indicate the q value (= 0.0206 $Å^{-1}$) used for the evaluation of τ and β. The dotted lines indicate the theoretical q-dependence for a purely Brownian diffusion (q^{-2}) and for a so-called ballistic dynamics (q^{-1}).

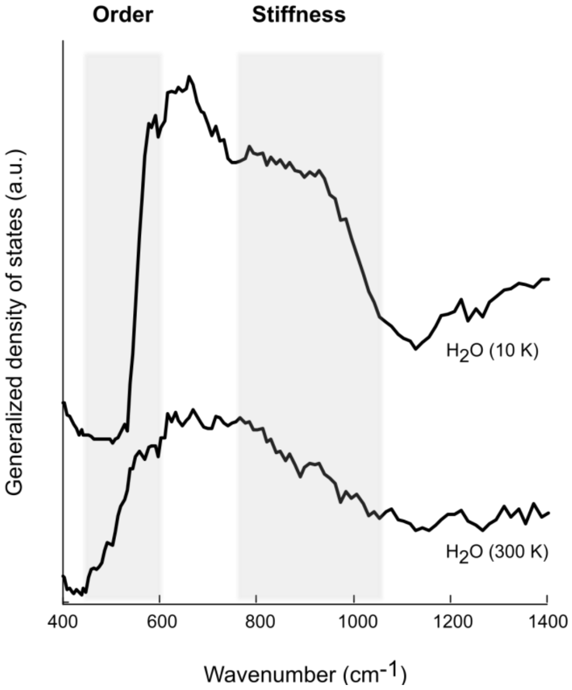

Figure S6.4. Librational region of the generalized vibrational density of states (GvDOS) for water measured at 10 and 300 K.

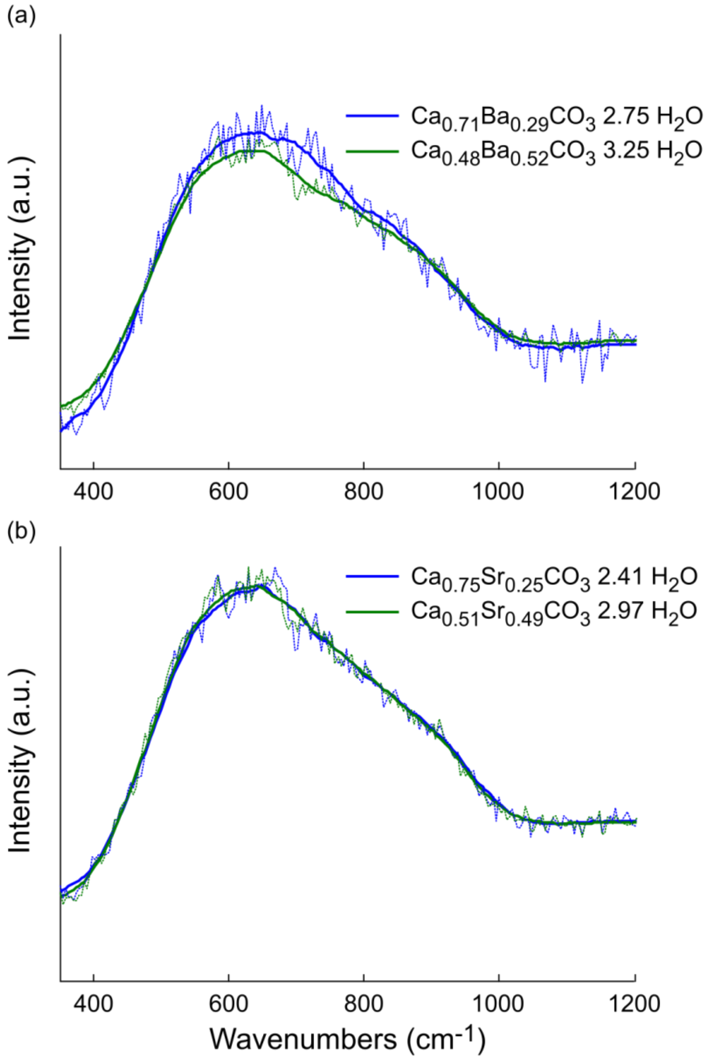

Figure S6.5. Librational region of the generalized vibrational density of states (GvDOS) for **(a)** Ba^{2+}- and **(b)** Sr^{2+}-doped ACC.

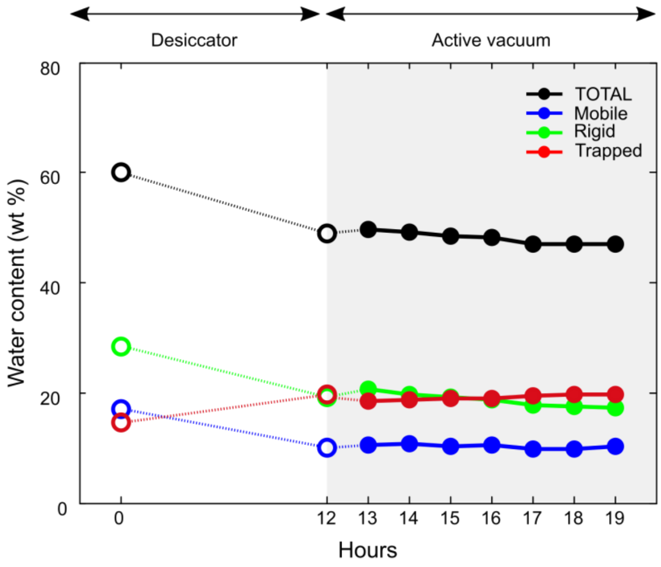

Figure S6.6. Time-evolution of water loss and water distribution between mobile, rigid and trapped regimes determined from TGA/DSC data for $Ca_{0.3}Mg_{0.7}CO_3$ nH_2O ($7.45 \geq n \geq 4.40$). The XPCS data for the corresponding sample was collected after 12 hours from the synthesis, during which the sample was stored in a dry desiccator at ambient temperature. This figure combines two separate TGA/DSC measurements which reproduced the conditions for XPCS measurements; a first sample stored as synthesized in a desiccator (empty circles and dotted lines) and a second, another sample placed under active vacuum (filled dots and solid lines) as synthesized, for 7 hours. The *x*-axis shows the time evolution from the synthesis of the sample (stored in the desiccator) to the XPCS measurements (light grey region).

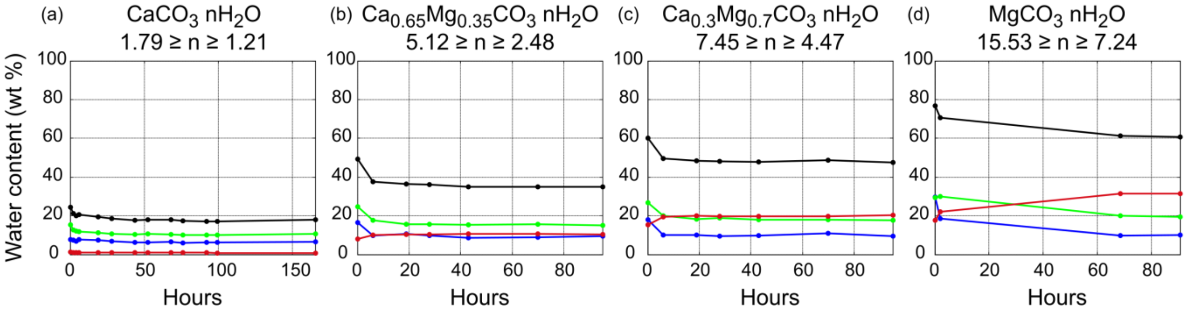

Figure S6.7. Time-evolution of water loss and water distribution between the mobile, rigid and trapped compartments of samples stored in a dry desiccator, determined by TGA/DSC for $Ca_{(1-x)}Mg_xCO_3{\cdot}nH_2O$ with (**a**) $x = 0$ ($1.79 \geq n \geq 1.21$), (**b**) $x = 0.35$ ($5.12 \geq n \geq 2.48$), (**c**) $x = 0.7$ ($7.45 \geq n \geq 4.47$), and (**d**) $x = 1$ ($15.53 \geq n \geq 7.24$).

References

Addadi L., Raz S. and Weiner S. (2003) Taking advantage of disorder: Amorphous calcium carbonate and its roles in biomineralization. *Adv. Mater.* **15**, 959–970.

Aizenberg J. (2010) New Nanofabrication Strategies: Inspired by Biomineralization. *MRS Bull.* **35**, 323–330.

Als-Nielsen J. and McMorrow D. (2011) *Elements of Modern X-ray Physics*., Wiley.

Arvidson R. S. and Mackenzie F. T. (1999) The dolomite problem; control of precipitation kinetics by temperature and saturation state. *Am J Sci* **299**, 257–288.

Benzerara K., Skouri-Panet F., Li J., Ferard C., Gugger M., Laurent T., Couradeau E., Ragon M., Cosmidis J., Menguy N., Margaret-Oliver I., Tavera R., Lopez-Garcia P. and Moreira D. (2014) Intracellular Ca-carbonate biomineralization is widespread in cyanobacteria. *Proc. Natl. Acad. Sci.* **111**, 10933–10938.

Bikondoa O. (2017) On the use of two-time correlation functions for X-ray photon correlation spectroscopy data analysis. *J. Appl. Crystallogr.* **50**, 357–368.

Binder K. and Kob W. (2011) *Glassy materials and disordered solids: An introduction to their statistical mechanics*., World Scientific.

Clouet E. (2010) Modeling of Nucleation Processes. In *ASM Handbook Vol. 22A, Fundamentals of Modeling for Metals Processing* (eds. D. U. Furrer and S. L. Semiatin). pp. 203–219.

Dudukovic N. A. and Zukoski C. F. (2014) Nanoscale dynamics and aging of fibrous peptide-based gels. *J. Chem. Phys.* **141**.

Evenson Z., Ruta B., Hechler S., Stolpe M., Pineda E., Gallino I. and Busch R. (2015) X-ray photon correlation spectroscopy reveals intermittent aging dynamics in a metallic glass. *Phys. Rev. Lett.* **115**.

Farhadi-Khouzani M., Chevrier D. M., Zhang P., Hedin N. and Gebauer D. (2016) Water as the Key to Proto-Aragonite Amorphous CaCO $_3$. *Angew. Chemie Int. Ed.* **55**, 8117–8120.

Fernandez-Martinez A., Lopez-Martinez H. and Wang D. (2017) Structural Characteristics and the Occurrence of Polyamorphism in Amorphous Calcium Carbonate. In *New Perspectives on Mineral Nucleation and Growth: From Solution Precursors to Solid Materials* (eds. A. E. S. Van Driessche, M. Kellermeier, L. G. Benning, and D. Gebauer). Springer. pp. 77–92.

Giordano V. M. and Ruta B. (2015) Unveiling the structural arrangements responsible for the atomic dynamics in metallic glasses during physical aging. *Nat. Commun.* **7**, 1–8.

Giuffre A. J., Gagnon A. C., De Yoreo J. J. and Dove P. M. (2015) Isotopic tracer evidence for the amorphous calcium carbonate to calcite transformation by dissolution–reprecipitation. *Geochim. Cosmochim. Acta* **165**, 407–417.

Han K.-L. and Zhao G.-J. (2011) *Hydrogen Bonding and Transfer in the Excited State*., John Wiley &

Sons Ltd.

Horbach J., Kob W. and Binder K. (2002) Dynamics of Sodium in Sodium Disilicate: Channel Relaxation and Sodium Diffusion. *Phys. Rev. Lett.* **88**.

Ihli J., Wong W. C., Noel E. H., Kim Y.-Y., Kulak A. N., Christenson H. K., Duer M. J. and Meldrum F. C. (2014) Dehydration and crystallization of amorphous calcium carbonate in solution and in air. *Nat. Commun.* **5**.

Ivanov A., Jimenéz-Ruiz M. and Kulda J. (2014) IN1-Lagrange-the new ILL instrument to explore vibration dynamics of complex materials. *J. Phys. Conf. Ser.* **554**.

Kashchiev D. (2000) *Nucleation: Basic Theory with Applications*., Butterworth-Heinemann, Oxford.

Kojima Y., Kawanobe A., Yasue T. and Arai Y. (1993) Synthesis of Amorphous Calcium Carbonate and Its Crystallization. *J. Ceram. Soc. Japan* **101**, 1145–1152.

Konrad F., Gallien F., Gerard D. E. and Dietzel M. (2016) Transformation of Amorphous Calcium Carbonate in Air. *Cryst. Growth Des.* **16**, 6310–6317.

Lee J. R. I., Han T. Y. J., Willey T. M., Wang D., Meulenberg R. W., Nilsson J., Dove P. M., Terminello L. J., Van Buuren T. and De Yoreo J. J. (2007) Structural development of mercaptophenol self-assembled monolayers and the overlying mineral phase during templated CaCO3 crystallization from a transient amorphous film. *J. Am. Chem. Soc.* **129**, 10370–10381.

Li J.-C., Londono D., Ross D. K., Finney J. L., Bennington S. M. and Taylor a D. (1999) Inelastic incoherent neutron scattering study of ice Ih, II, IX, V and VI in the region from 50-500 meV. *J. Phys. Condens. Matter* **4**, 2109–2116.

Michel F. M., MacDonald J., Feng J., Phillips B. L., Ehm L., Tarabrella C., Parise J. B. and Reeder R. J. (2008) Structural characteristics of synthetic amorphous calcium carbonate. *Chem. Mater.* **20**, 4720–4728.

Navrotsky A. and Capobianco C. (1987) Enthalpies of formation of dolomite and of magnesian calcites. *Am. Mineral.* **72**, 782–787.

Noyes R. M. (1962) Thermodynamics of Ion Hydration as a Measure of Effective Dielectric Properties of Water. *J. Am. Chem. Soc.* **84**, 513–522.

Ockwig N. W., Cygan R. T., Hartl M. A., Daemen L. L. and Nenoff T. M. (2008) Incoherent inelastic neutron scattering studies of nanoconfined water in clinoptilolite and heulandite zeolites. *J. Phys. Chem. C* **112**, 13629–13634.

Ockwig N. W., Greathouse J. A., Durkin J. S., Cygan R. T., Daemen L. L. and Nenoff T. M. (2009) Nanoconfined Water in Magnesium-Rich 2:1 Phyllosilicates. *J. Am. Chem. Soc.* **131**, 8155–8162.

Pimentel C. and Pina C. M. (2014) The formation of the dolomite-analogue norsethite: Reaction pathway and cation ordering. *Geochim. Cosmochim. Acta* **142**, 217–223.

Politi Y., Batchelor D. R., Zaslansky P., Chmelka B. F., Weaver J. C., Sagi I., Weiner S. and Addadi L. (2010) Role of magnesium ion in the stabilization of biogenic amorphous calcium carbonate: A structure-function investigation. *Chem. Mater.* **22**, 161–166.

Purgstaller B., Mavromatis V., Immenhauser A. and Dietzel M. (2016) Transformation of Mg-bearing amorphous calcium carbonate to Mg-calcite - In situ monitoring. *Geochim. Cosmochim. Acta* **174**, 180–195.

Radha A. V., Fernandez-Martinez A., Hu Y., Jun Y.-S., Waychunas G. A. and Navrotsky A. (2012) Energetic and structural studies of amorphous Ca1−xMgxCO3·nH2O (0⩽x⩽1). *Geochim. Cosmochim. Acta* **90**, 83–95.

Raiteri P. and Gale J. D. (2010) Water is the key to nonclassical nucleation of amorphous calcium carbonate. *J. Am. Chem. Soc.* **132**, 17623–17634.

Reeder R. J., Tang Y., Schmidt M. P., Kubista L. M., Cowan D. F. and Phillips B. L. (2013) Characterization of Structure in Biogenic Amorphous Calcium Carbonate: Pair Distribution Function and Nuclear Magnetic Resonance Studies of Lobster Gastrolith. *Cryst. Growth Des.* **13**, 1905–1914.

Rieger J., Kellermeier M. and Nicoleau L. (2014) Formation of nanoparticles and nanostructures-an industrial perspective on CaCO3, cement, and polymers. *Angew. Chemie - Int. Ed.* **53**, 12380–12396.

Rodriguez-Blanco J. D., Shaw S., Bots P., Roncal-Herrero T. and Benning L. G. (2012) The role of pH and Mg on the stability and crystallization of amorphous calcium carbonate. *J. Alloys Compd.* **536**, S477–S479.

Ross M. (2016) *Atomic Diffusion in Glasses Studied with Coherent X-Rays.*, Springer.

Ross M., Stana M., Leitner M. and Sepiol B. (2014) Direct observation of atomic network migration in glass. *New J. Phys.* **16**.

Ruta B., Baldi G., Monaco G. and Chushkin Y. (2013) Compressed correlation functions and fast aging dynamics in metallic glasses. *J. Chem. Phys.* **138**.

Ruta B., Chushkin Y., Monaco G., Cipelletti L., Pineda E., Bruna P., Giordano V. M. and Gonzalez-Silveira M. (2012) Atomic-scale relaxation dynamics and aging in a metallic glass probed by X-ray photon correlation spectroscopy. *Phys. Rev. Lett.* **109**.

Ruta B., Zontone F., Chushkin Y., Baldi G., Pintori G., Monaco G., Rufflé B. and Kob W. (2017) Hard X-rays as pump and probe of atomic motion in oxide glasses. *Sci. Rep.* **7**.

Schmidt M. P., Ilott A. J., Phillips B. L. and Reeder R. J. (2014) Structural Changes upon Dehydration of Amorphous Calcium Carbonate. *Cryst. Growth Des.* **14**, 938–951.

Shinohara Y., Kishimoto H., Yagi N. and Amemiya Y. (2010) Microscopic Observation of Aging of Silica Particles in Unvulcanized Rubber. *Macromolecules* **43**, 9480–9487.

Di Tommaso D. and de Leeuw N. H. (2010) Structure and dynamics of the hydrated magnesium ion and of the solvated magnesium carbonates: insights from first principles simulations. *Phys. Chem. Chem. Phys.* **12**, 894–901.

Wallace A. F., Hedges L. O., Fernandez-Martinez A., Raiteri P., Gale J. D., Waychunas G. A., Whitelam S., Banfield J. F. and De Yoreo J. J. (2013) Microscopic evidence for liquid-liquid separation in supersaturated CaCO3 solutions. *Science* **341**, 885–889.

Wang D., Wallace A. F., De Yoreo J. J. and Dove P. M. (2009) Carboxylated molecules regulate magnesium content of amorphous calcium carbonates during calcification. *Proc. Natl. Acad. Sci. U. S. A.* **106**, 21511–21516.

Wang H.-W., Daemen L. L., Cheshire M. C., Kidder M. K., Stack A. G., Allard L. F., Neuefeind J., Olds D., Liu J. and Page K. (2017) Synthesis and structure of synthetically pure and deuterated amorphous (basic) calcium carbonates. *Chem. Commun.* **53**, 2942–2945.

Xu J., Yan C., Zhang F., Konishi H., Xu H. and Teng H. H. (2013) Testing the cation-hydration effect on the crystallization of Ca-Mg-CO3 systems. *Proc. Natl. Acad. Sci. U. S. A.* **110**, 17750–17755.

Chapter 7

Conclusions

Conclusions are divided into three sections (7.1, 7.2. and 7.3), following the order of research chapters (Chapters 4, 5 and 6). Research questions and hypotheses are recalled for each section. New hypotheses and related discussions resulting from this work can be found in section 7.4.

7.1. Heterogeneous nucleation of calcium carbonate: effect of surface hydrophobicity

Research question #1

Effect of substrate hydrophobicity on $CaCO_3$ heterogeneous nucleation

Objective 1: to perform $CaCO_3$ heterogeneous nucleation on two substrates exhibiting distinct differences in α_{ls} and high similarity in α_{sc}.
Objective 2: to ascertain the possibility of multistep nucleation pathways during the heterogeneous nucleation of $CaCO_{3.}$

The likelihood of heterogeneous nucleation is associated to the lowering of the effective interfacial free energy, α'. This stems from a complex interplay of three interfacial free energies between liquid, crystal and substrate (α_{lc}, α_{sc} and α_{ls}). In particular, for heterogeneous nucleation to be favored, α' must be lower than α_{lc}, the interfacial free energy controlling homogeneous nucleation. The extent of heterogeneous nucleation is therefore strongly regulated by the physico-chemical interactions between the substrate, the nucleating crystal and the surrounding solution. Hydrophobicity has been demonstrated to enhance nucleation by lowering the nucleation barrier, as it favors wetting by the solid phase rather than by the fluid. Engineered solutions to increase the extent of heterogeneous nucleation are based on surface functionalization using a wide range of organic monolayers. Here, instead, the effect of substrate hydrophobicity on $CaCO_3$ heterogeneous nucleation was addressed using phlogopite mica as substrates with varying hydrophobicity (different α_{ls}). An advantage of this solution was the fact that the phlogopite hydrophobicity results from fluorine substitution, thus minimum differences in terms of surface structure are found, limiting the variation in α_{sc}. The effect of substrate hydrophobicity was therefore directly studied, contributing to a predicting understanding of heterogeneous nucleation as a function of surface property. Based on the results of previous studies, it was hypothesized that the more hydrophobic substrate will show a lower barrier to nucleation, thus yielding a distinctively lower value for the effective interfacial energy (hypothesis 1). The existence of multistep nucleation pathways has been confirmed for homogeneous nucleation of $CaCO_3$ by recent studies. Their relevance, however, remains elusive for the case of heterogeneous nucleation. Considering the hydrous nature of ACC, one of the intermediates present in these multistep pathways, it was hypothesized that ACC would form more favorably on hydrophilic substrate and crystalline $CaCO_3$ polymorphs on the hydrophobic substrate (hypothesis 2).

Heterogeneous nucleation experiments of $CaCO_3$ were performed using *in situ* time-resolved GISAXS technique. Contrary to the hypothesis (1), results yielded identical values for effective interfacial energy, irrespective of substrate hydrophobicity, suggesting that the $CaCO_3$ system exhibits no thermodynamic preference for nucleating on either hydrophilic or hydrophobic substrate (same nucleation barrier). For the two phases considered, calcite and ACC, the obtained values for α' were 33-34 and 9 mJ/m^2, respectively. Interestingly, however, the *ex situ* observation by FTIR demonstrated that the initial nucleating phase is ACC on both hydrophilic and hydrophobic substrates (same nucleation pathway), but the kinetic persistence of ACC is enhanced on the former (different crystallization kinetics). This was further confirmed by the *ex situ* AFM study where the nucleated particles demonstrated distinctively different morphologies. In particular, the hydrophilic substrate was fully covered by a thin layer of ACC along with heterogeneously nucleated crystalline particles while the inter-particle surface of the hydrophobic substrate was left clean. A detailed analysis of the effective interfacial energies obtained from the GISAXS data suggests that there might be thermodynamic drivers for the formation of ACC on the hydrophilic substrate and their rapid crystallization on the hydrophobic substrate, in agreement with the hypothesis (2).

Given the difference in the crystallization kinetics controlled by the surface hydrophobicity, the fact that both the hydrophilic and hydrophobic substrates display the same nucleation barrier points to the structural flexibility of the $CaCO_3$ system, in its ability to adapt to different surfaces. A proxy to understand this structural flexibility is the fact that the $CaCO_3$ exhibits a high degree of polymorphism. The multiple structural conformations reflect a complex potential energy surface with numerous local minima in the configuration space, supporting the observed ability to adapt to remarkably different environments such as those provided by OH and F phlogopite substrates.

7.2. Surface hydrophobicity and properties of interfacial water

Research question #2

Atomistic view of surface hydrophobicity: what does define the hydrophobic properties of fluorinated phlogopite in the presence of adsorbed cations?

Hydrophobic surfaces are generally characterized by the depletion of interfacial water density, which results from the asymmetric hydrogen bonding due to the suppression of interaction sites with water molecules (see section 2.2). Previous studies have demonstrated that the asymmetric hydrogen bonding, more specifically the net deficiency of accepted H-bonds, develops a negative electric field at the hydrophobic interface, which supposedly attracts cations (Wang et al., 2009). The presence and the type of surface cations, however, can alter this conformation and the dynamics of interfacial water. Properties of interfacial water are relatively well documented at the muscovite mica-water interface, representative model for a hydrophilic mineral interface. On the other hand, little is known about how the properties of the interfacial water would be affected by fluorine substitutions in negatively charged mica minerals such as muscovite or phlogopite where a range of counterions can be present at the interface to screen the surface charge. This is relevant to naturally occurring hydrophobic substrates since fluorine substitution in phyllosilicates is commonplace. The postulated hydrophobic properties of the F-bearing mica are hypothesized to be defined through a competition between the hydration properties of counterions and inherent structural hydrophobicity.

Water adsorption was studied *in situ* using NAP-XPS allowing for speciation of adsorbed water species, aiming at examining the effect of counterions (K^+- vs. Na^+- vs. Cs^+-bearing OH phlogopite substrates) and of fluorine substitution (Na^+-bearing OH^- and F^- phlogopite). The presence of adsorbed water was observed at relatively early hydration stages for K^+- and Na^+-bearing OH phlogopite (7 and 2% of relative humidity, respectively) as compared to Cs^+-bearing OH and Na^+-bearing F phlogopite (22 and 21%, respectively). Interestingly, while these results underline the inherent hydrophobic character of F-phlogopite, the observed shift in binding energies was inversed for Na^+ and Cs^+, indicating that these two samples may have different hydration mechanisms. Furthermore, K^+-bearing substrates displayed no shift in binding energies of O1s (water species) as well as K3p, which suggests that K^+ is not affected by the water adsorption. MD simulation provided further molecular explanation to these observations. A detailed analysis of MD trajectories revealed that the surface hydration of Na^+-bearing OH phlogopite was initiated by the water molecules hydrating Na^+ that simultaneously formed hydrogen bonds with the basal oxygen atoms, while for K^+- and Cs^+-bearing phlogopite it was via the interfacial water molecules that were hydrogen bonded solely to the basal oxygen atoms. The surface charge distribution of phlogopite, further altered by F substitution, is closely coupled to the hydration property of counterions, which together succeeds into specific interactions at the phlogopite-water interface.

Hydrophobicity is a property known to enhance heterogeneous nucleation, at least, of solids that show little structural flexibility (unlike $CaCO_3$). This work highlights the inherent complexity of mineral surface such as mica, a priori ‘simple’ mineral that is abundant in natural and engineered environments.

The results from this detailed analysis of the hydration mechanisms are non-negligible and in particular open new questions about the loci of heterogeneous nucleation. Concepts such as conformation of hydrogen bonds with respect to counterions and surface charge distribution at the interface and the adjacent water structures are encouraged to be integrated in the atomistic picture and mechanistic description of heterogeneous nucleation processes.

7.3. Nanoscopic dynamics of amorphous calcium carbonate: understanding the mechanisms controlling the crystallization kinetics

Research question #3

Linking the atomistic dynamics and crystallization kinetics in ACC: how does the presence of water and Mg^{2+} control ACC crystallization kinetics?

ACC, an intermediate in the crystallization processes of the $CaCO_3$ system, is a known precursor to a variety of biominerals exhibiting advanced functionalities. Biogenic ACC displays enhanced kinetic persistence, which has been shown to be closely associated to its structural water, organic and inorganic additives as well as the presence of heterogeneous biophysical boundaries. The presence of water and Mg^{2+} is also known to stabilize ACC thermodynamically. Studies have shown that the different types of water of varying thermal stability and dynamical character within ACC, as well as their distribution with respect to carbonate ions, can be the key in locally controlling the crystallization processes (Reeder et al., 2013; Schmidt et al., 2014). Provided its lower hydration energy, we hypothesized that Mg^{2+} enhances the kinetic persistence of ACC via formation of strong hydrogen bonds within the water network and in doing so, slowing down the rate of structural rearrangements (i.e. Brownian diffusivity) through which crystallization is achieved.

A unique combination of X-ray and neutron scattering techniques was employed to study dynamical characters of solid amorphous carbonates. Results from IINS, sensitive probe for hydrogen dynamics, indicated a stiffening of hydrogen bonding interactions within the water network present in Mg^{2+}-doped ACC, in agreement with the hypothesis and the known kinetic stabilization effects of Mg^{2+}. Results from XPCS, interestingly, indicated that the presence of Mg^{2+} accelerated the relaxation dynamics within the Mg^{2+}-doped ACC, with its coherent diffusivity or the rate of structural rearrangements at least two times faster than pure ACC. Provided the smaller volume imposed by Mg^{2+} ions, the presence of Mg^{2+} may introduce kinetics barriers of steric nature, as in the conformational restraints in the Mg-CO_3 binding environments and in the stiff hydrogen bonding network. Among different factors controlling the crystallization kinetics, these steric barriers may contribute to reduce the probability of success (Zeldovich factor) of structural rearrangements which dictates the kinetics of crystallization.

In addition to the fundamental understanding of nucleation and crystallization pathways, of particular importance in elucidating the mechanisms and processes of formation of biominerals as well as the role of additives, is their potential to the synthesis of novel biomimetic materials. The fact that a highly dynamic yet kinetically persistent precursor can be designed, by a simple additive such as Mg^{2+}, is therefore of high relevance. Future studies may focus on the rheological properties of these precursors in order to assess their potential impacts for industrial applications.

7.4. New hypotheses

7.4.1. Multistep heterogeneous nucleation pathway

One of the main findings of this Ph.D. thesis is that the $CaCO_3$ system exhibits no preference for nucleating on hydrophilic or hydrophobic substrates, on both of which ACC is the primary nucleating phase, with enhanced kinetic persistence on hydrophilic substrate (Chapter 4). This has been demonstrated by three major lines of evidence: (1) identical values of effective interfacial energy irrespective of substrates; (2) observation of ACC on both substrates with different crystallization pathways and kinetics; (3) morphological distinctiveness of $CaCO_3$ precipitates, in particular the presence of ACC layer on the hydrophilic substrate.

7.4.1.1. Amorphous precursor strategy: insights from the interfacial water structure

One must underline that the systems studied here were additive free, indicating that ACC can be stabilized heterogeneously in absence of organic matrix or stabilizers such as Mg^{2+}. The most plausible mechanism of stabilization stems from the interaction between the hydrophilic substrate and the water molecules within the ACC particles through the formation of hydrogen bonds, as also pointed out by Xu et al. (2004) for a OH-terminated substrate. As demonstrated in Chapter 5, phlogopite surface displays various adsorption sites, in particular the basal Obts atoms, bearing negative charge, accept hydrogen bonds from water molecules. This process was shown to initiate surface hydration, in particular in presence of large cations such as K^+ and Cs^+ for their weak interaction with water molecules, as opposed to Na^+, to which water molecules would be hydrogen bonded, or in other words, would interfere with the formation of hydrogen bonds with the substrate itself.

Phlogopite substrates used here for the heterogeneous nucleation experiments bear K^+, thus the hydrophilic substrate surface itself is readily hydrated, developing well-structured layers of water molecules up to ~10 Å, dictated by the substrate. This may suggest that the observed formation of ACC can be viewed as an adapted strategy facing the ‘necessity’, in the interest of the intended crystalline product to lower α_{sc} in contact with the fully hydrated substrate. By following this pathway, the system was able to nucleate on a hydrophilic substrate as much as on hydrophobic counterpart, as demonstrated by the identical values for effective interfacial energy. This adaptability of $CaCO_3$ at the ACC-substrate interface is certainly an advantage for the nucleation in the confined, hydrated environments present in biominerals, where ACC acts as precursor of different polymorphs (Addadi et al., 2003). Examples include transformation of ACC to calcite in sea urchin larval spicule (Beniash et al., 1997; Raz et al., 2003; Politi et al., 2004; Politi et al., 2008) or to aragonite in nacre (Devol et al., 2015). Note however that the transformation mechanism is different; biomineralization in sea urchin occur intracellularly in contact with the forming cells (Beniash et al., 1999; Vidavsky et al., 2014), while in nacre it takes place extracellularly where assumingly ACC precursors must be stabilized by sulfate, Mg^{2+} or organic substances (Farre et al., 2011; Dauphin et al., 2014; Devol et al., 2015). Devol et al. (2015) make additional note that the crystallization of ACC into aragonite is dictated by the pre-existing crystals, thus requires no pre-structure, in line with the fact that proto-aragonite has not been observed.

7.4.1.2. Role and formation of ACC layer

If the water molecules within the ACC layer are able to form hydrogen bonds with the hydrophilic substrate, then it is logical to think that they do so with the surrounding water molecules, thus decreasing α_{lc}, although the definition of ‘interface’ is not straightforward. This lowering of the interfacial energy is certainly the cause that ACC is the first formed precipitate, as suggested by Navrotsky (2004). There seems to exist an allegedly accepted idea that ACC forms homogeneously, most likely by aggregation of ion polymers, and only then deposits onto surface (Politi et al., 2004; Pouget et al., 2009; Gal et al., 2014; Rodriguez-Navarro et al., 2016). However, recent evidence tends to show that heterogeneous nucleation of ACC can also be possible. The existence of an ACC layer has been observed on the surfaces of the primary building blocks of aragonite and around aragonite platelets in nacre (Nassif et al., 2005a; Nassif et al., 2005b). Authors attribute this to a ‘coating’ that prevents the direct contact of aragonite with water, thus effectively increased the stability of aragonite that is otherwise prone to recrystallize in contact with water. They also note the unexpected stability of the ACC coating. Reflective of this, our finding that ACC can be the initial nucleating phase irrespective of the substrate hydrophobicity can be the result of different scenarios: (1) ACC particles form on hydrophobic substrate but are metastable, thus short-lived, which is explained by a the α_{sc} penalty if a direct contact was to be made or maintained with a hydrophobic substrate bearing restricted access for water to form hydrogen bonds; (2) ACC particles do not form in direct contact with the hydrophobic substrate itself but only on the surface of the crystalline particles as a coating. Despite its hydrous nature, this can be rationalized from the fact that the interfacial energy between a crystalline particle and ACC would still be lower than that between crystalline particle and water itself. This scenario lowers α_{cl} between the crystalline particles and water, with a minimum penalty between ACC and crystalline particles; (3) ACC particles form on both the hydrophobic substrate and the crystalline particles. The former may quickly dissolve (due to the metastability caused by α_{sc}) resulting in an increase in the interfacial supersaturation which in turn is favorable for the formation of crystalline particles, together with α_{cl} (crystalline particle-water) that is maintained low thanks to the ACC coating as in scenario (2).

A recent study by Mass et al. (2017) reports that coral skeleton forms by attachment of ACC particles inside the tissue and behind tightly sealed membranes. Interestingly, authors also note that the memory of particle attachment seems to be retained in the crystalline aragonite. The possible existence and relevance of these ACC layers on top of crystalline phases needs to be explored in detail both on biominerals and on idealized systems, so the accurate crystallization mechanisms can be elucidated, which is indeed the underlying question.

7.4.2. Coexistence of accelerated dynamics and stiff hydrogen bond networks

Another main finding of this Ph.D. thesis is the unexpected coexistence of accelerated dynamics and the stiffening of hydrogen bond networks, which together translates into the hindrance of crystallization (Chapter 6). Given the known kinetic persistence of Mg^{2+}-doped ACC, the observed accelerated dynamics, thus increased frequency of structural rearrangements, is not *a priori* intuitive since it is via these structural rearrangements that an amorphous solid can crystallize. In fact, Mg^{2+} seems to induce steric factors that effectively reduce the probability of successful structural rearrangements (the Zeldovich factor).

7.4.2.1. Topological distribution and network of water components

The probed scale by XPCS in our study ranges from ~25 to 630 nm, which covers dynamics within the individual amorphous particles that are in the order of tens to hundreds of nanometers (Radha et al., 2012). Question remains open as to whether there exists a certain topological distribution of Ca^{2+}, Mg^{2+} or CO_3^{2-} ions with respect to the types of water regimes at this scale. Let us start by postulating the plausible topological distribution of water components within ACC. It seems reasonable to assume that (1) mobile water, due to their ease of access, resides near the solid-air interface; (2) rigid water resides within individual particles with partial access to mobile water or to the solid-air interface; (3) trapped water resides within individual particles, thus structural, with no access to other regimes or air unless crystallization. A similar view is proposed by Ihli et al. (2014).

The terms ‘mobile’, ‘rigid’, and ‘trapped’ refer to the responses to the thermal treatment. In dynamical terms, a combined study of NMR and TGA by Schmidt et al. (2014) suggest that the thermally ‘mobile’ regime (1) corresponds indeed to a mixture of fluidlike, restrictedly mobile and rigid water components, and the thermally ‘rigid’ regime (2) to a mixture of restrictedly mobile and rigid water components. They also identified the thermally ‘trapped’ water component that is released upon crystallization, thus definition of (3) ‘trapped’ water stands alone. Indeed, these combined interpretations imply that there might be a certain degree of connectivity in between the fluidlike, restrictedly mobile and rigid water within this ‘mobile’ regime, since otherwise the simultaneous loss of the three components, as reported, would not have been achieved. Similarly, a connection between the restrictedly mobile and rigid water within the ‘rigid’ regime seems plausible, and only the trapped regime bears physical disconnectivity.

Reflecting this connectivity, the same authors (Schmidt et al., 2014) note a possible exchange between these water components, based on the observation that crystallization temperature has been elevated when samples underwent isothermal measurements. Along a similar line, an interesting observation in our study was that during the dehydration, there is an increase in the fraction of trapped water molecules at the expense of mobile and rigid compartments observed for all the samples. This effect was more prominent as increasing the Mg^{2+} contents, and less pronounced for pure ACC. Two explanations are possible: (i) a change in the nature of some of the water components in the mobile and rigid compartments, possibly through changes in the structural organization such as the sealing of pore connectivity upon dehydration. Since the trapped regime assumingly bears no physical connectivity to the other components, the only possibility to increase the fraction of the trapped regime is to create new trapped molecules. However, the static structure factor remained almost intact, and it has been shown that structural changes accompanying dynamical ones can be subtle (Giordano and Ruta, 2015); (ii) the trapped compartment is not completely inaccessible, thus exchange, or migration in our case, of water components are possible within all the compartments. Question remains elusive as to whether the increased fraction of trapped regime can be linked to the aging dynamics, in particular for Mg^{2+}-doped ACC given that the trapped fraction seems to increases proportionally to Mg^{2+}/Ca^{2+}.

7.4.2.2. Plausible scenario for the accelerated dynamics as opposed to the hindered kinetics

In presence of Mg^{2+}, we observed a coexistence of accelerated dynamics and the stiffening of hydrogen bond network together with the increase of the water components in trapped, inaccessible regime. By comparing fresh and partially dried samples of the same composition (Fig. 6.2), for pure ACC, the intensity at high frequencies dropped when dried, mainly due to the loss of mobile and rigid regimes, since trapped regime was barely present. When Mg^{2+} is present, despite the observed water loss of the mobile and especially rigid regimes, solely the degeneration of modes is pronounced with the stiffness (the intensity at high frequencies) remained intact, which infers the contribution from the trapped compartment. Therefore, one may speculate that the H-bonding network within the mobile and rigid regimes could be loose compared to that of trapped regime. Thus it seems reasonable to relate the enhanced stiffness of the water network, in particular of the trapped water molecules, to the hindered crystallization kinetics, and the relatively loose H-bond network within the mobile and rigid regimes to the dynamic properties of the solid. The fact that $x = 1$ (AMC) sample exhibits the most dynamic nature could be explained by the relatively larger fraction of water within the mobile regime as compared to pure ACC and the other Mg^{2+}-doped ACC (Fig. 6.1b). Interestingly, though, the final states of samples $x = 0.7$ and 1 at ~ 80 hours from the synthesis (Fig. S6.7) exhibit similar distributions of water, with ~10% of mobile and ~20% of rigid regimes, which might suggest that there is a threshold of water contents within these regimes, whereas no such limit seems to appear for the trapped regime. This may points to the fact that the water components within these two regimes belong only partly to the structure of ACC per se.

7.4.2.3. Topological distribution of Ca^{2+}, Mg^{2+}, CO_3^{2-} with respect to the water components

The enhanced stiffness observed in the trapped regime, together with the slower water exchange rate of Mg^{2+} in its first hydration shell (Di Tommaso and de Leeuw, 2010), seems to indicate that the structural, trapped water resides in a close vicinity to Mg^{2+} ions. Previous studies have shown that water molecules are strongly coupled to CO_3^{2-} ions within ACC (Saharay et al., 2013; Farhadi-Khouzani et al., 2016). Of particular interest, a study by Reeder et al. (2013) showed that mobile, fluidlike water was absent in the vicinity of CO_3^{2-} in biogenic ACC, suggesting that limited access of mobile water component to CO_3^{2-} may be the key in impeding the crystallization. This steric barrier could be behind the decreased probability of successful structural rearrangements (Zeldovich factor), in addition to the related steric barriers discussed in Chapter 6. Clearly, more work is needed to ascertain how different factors mentioned here control crystallization kinetics, in particular by further investigating:

- how different additives present in biogenic ACC affect the water distribution, in particular their dynamical and thermal nature
- the universality of the enhanced H-bond network as a stabilizer agent of amorphous precursors
- existence of exchange between water components and its link to the ionic and aging dynamics

Isothermal measurements by TGA/DSC at relatively low temperatures, combined with NMR study, could provide relevant information on activation energy of exchange processes and their mechanisms. Coherent X-ray Scattering and Inelastic neutron scattering techniques used in Chapter 6 can be of additional advantage, if available. It is also necessary to perform thermal analyses at different rates of heating to verify that the dynamics of water components are truly related to the inherent mechanisms and not thermally induced.

References

Addadi L., Raz S. and Weiner S. (2003) Taking advantage of disorder: Amorphous calcium carbonate and its roles in biomineralization. *Adv. Mater.* **15**, 959–970.

Beniash E., Addadi L. and Weiner S. (1999) Cellular control over spicule formation in sea urchin embryos: A structural approach. *J. Struct. Biol.* **125**, 50–62.

Beniash E., Aizenberg J., Addadi L. and Weiner S. (1997) Amorphous calcium carbonate transforms into calcite during sea urchin larval spicule growth. *Proc. R. Soc. B Biol. Sci.* **264**, 461–465.

Dauphin Y., Cuif J.-P. and Salomé M. (2014) Structure and composition of the aragonitic shell of a living fossil: Neotrigonia (Mollusca, Bivalvia). *Eur. J. Mineral.* **26**, 485–494.

Devol R. T., Sun C. Y., Marcus M. A., Coppersmith S. N., Myneni S. C. B. and Gilbert P. U. P. A. (2015) Nanoscale Transforming Mineral Phases in Fresh Nacre. *J. Am. Chem. Soc.* **137**, 13325–13333.

Farhadi-Khouzani M., Chevrier D. M., Zhang P., Hedin N. and Gebauer D. (2016) Water as the Key to Proto-Aragonite Amorphous CaCO3. *Angew. Chemie - Int. Ed.* **55**, 8117–8120.

Farre B., Brunelle A., Laprévote O., Cuif J. P., Williams C. T. and Dauphin Y. (2011) Shell layers of the black-lip pearl oyster Pinctada margaritifera: Matching microstructure and composition. *Comp. Biochem. Physiol. - B Biochem. Mol. Biol.* **159**, 131–139.

Gal A., Kahil K., Vidavsky N., Devol R. T., Gilbert P. U. P. A., Fratzl P., Weiner S. and Addadi L. (2014) Particle accretion mechanism underlies biological crystal growth from an amorphous precursor phase. *Adv. Funct. Mater.* **24**, 5420–5426.

Giordano V. M. and Ruta B. (2015) Unveiling the structural arrangements responsible for the atomic dynamics in metallic glasses during physical aging. *Nat. Commun.* **7**, 1–8.

Ihli J., Wong W. C., Noel E. H., Kim Y.-Y., Kulak A. N., Christenson H. K., Duer M. J. and Meldrum F. C. (2014) Dehydration and crystallization of amorphous calcium carbonate in solution and in air. *Nat. Commun.* **5**.

Mass T., Giuffre A. J., Sun C.-Y., Stifler C. A., Frazier M. J., Neder M., Tamura N., Stan C. V., Marcus M. A. and Gilbert P. U. P. A. (2017) Amorphous calcium carbonate particles form coral skeletons. *Proc. Natl. Acad. Sci.* **114**, E7670–E7678.

Nassif N., Gehrke N., Pinna N., Shirshova N., Tauer K., Antonietti M. and Cölfen H. (2005a) Synthesis of stable aragonite superstructures by a biomimetic crystallization pathway. *Angew. Chemie - Int. Ed.* **44**, 6004–6009.

Nassif N., Pinna N., Gehrke N., Antonietti M., Jäger C. and Cölfen H. (2005b) Amorphous Layer around Aragonite Platelets in Nacre. *Proc. Natl. Acad. Sci. U. S. A.* **102**, 12653–12655.

Navrotsky A. (2004) Energetic clues to pathways to biomineralization: precursors, clusters, and nanoparticles. *Proc. Natl. Acad. Sci. U. S. A.* **101**, 12096–12101.

Politi Y., Arad T., Klein E., Weiner S. and Addadi L. (2004) Sea Urchin Spine Calcite Forms via a

Transient Amorphous Calcium Carbonate Phase. *Science* **306**, 1161–1164.

Politi Y., Metzler R. A., Abrecht M., Gilbert B., Wilt F. H., Sagi I., Addadi L., Weiner S. and Gilbert P. U. P. A. (2008) Transformation mechanism of amorphous calcium carbonate into calcite in the sea urchin larval spicule. *Proc. Natl. Acad. Sci. U. S. A.* **105**, 17362–17366.

Pouget E. M., Bomans P. H., Goos J. A., Frederik P. M. and Sommerdijk N. A. (2009) The Initial Stages of Template-Controlled CaCO3 Formation Revealed by Cryo-TEM. *Science* **323**, 1455–1458.

Radha A. V., Fernandez-Martinez A., Hu Y., Jun Y.-S., Waychunas G. A. and Navrotsky A. (2012) Energetic and structural studies of amorphous Ca1−xMgxCO3·nH2O (0⩽x⩽1). *Geochim. Cosmochim. Acta* **90**, 83–95.

Raz S., Hamilton P. C., Wilt F. H., Weiner S. and Addadi L. (2003) The transient phase of amorphous calcium carbonate in sea urchin larval spicules: The involvement of proteins and magnesium ions in its formation and stabilization. *Adv. Funct. Mater.* **13**, 480–486.

Reeder R. J., Tang Y., Schmidt M. P., Kubista L. M., Cowan D. F. and Phillips B. L. (2013) Characterization of Structure in Biogenic Amorphous Calcium Carbonate: Pair Distribution Function and Nuclear Magnetic Resonance Studies of Lobster Gastrolith. *Cryst. Growth Des.* **13**, 1905–1914.

Rodriguez-Navarro C., Burgos Cara A., Elert K., Putnis C. V. and Ruiz-Agudo E. (2016) Direct Nanoscale Imaging Reveals the Growth of Calcite Crystals via Amorphous Nanoparticles. *Cryst. Growth Des.* **16**, 1850–1860.

Saharay M., Yazaydin A. O. and Kirkpatrick R. J. (2013) Dehydration-induced amorphous phases of calcium carbonate. *J. Phys. Chem. B* **117**, 3328–3336.

Schmidt M. P., Ilott A. J., Phillips B. L. and Reeder R. J. (2014) Structural Changes upon Dehydration of Amorphous Calcium Carbonate. *Cryst. Growth Des.* **14**, 938–951.

Di Tommaso D. and de Leeuw N. H. (2010) Structure and dynamics of the hydrated magnesium ion and of the solvated magnesium carbonates: insights from first principles simulations. *Phys. Chem. Chem. Phys.* **12**, 894–901.

Vidavsky N., Addadi S., Mahamid J., Shimoni E., Ben-Ezra D., Shpigel M., Weiner S. and Addadi L. (2014) Initial stages of calcium uptake and mineral deposition in sea urchin embryos. *Proc. Natl. Acad. Sci. U. S. A.* **111**, 39–44.

Wang J., Kalinichev A. G. and Kirkpatrick R. J. (2009) Asymmetrie hydrogen bonding and orientational ordering of water at hydrophobic and hydrophilic surfaces: A comparison of water/vapor, water/talc, and water/mica interfaces. *J. Phys. Chem. C* **113**, 11077–11085.

Xu X., Han J. T. and Cho K. (2004) Formation of Amorphous Calcium Carbonate Thin Films and Their Role in Biomineralization. *Chem. Mater.* **16**, 1740–1746.

APPENDIX A

Complementary information for Chapter 4 (heterogeneous nucleation of calcium carbonate: effect of surface hydrophobicity)

A.1. Introduction

Appendix A provides additional *ex situ* data to Chapter 4. It consists of microscopic imaging of heterogeneously nucleated $CaCO_3$ precipitates by scanning electron microscopy (SEM) and stereo microscopy followed by phase identification by ATR-FTIR.

A.2. Materials and Methods

Ex situ characterization by SEM

Heterogeneous nucleation experiments were performed on OH and F phlogopite under conditions I (Table 4.2). Freshly cleaved substrates were placed vertically in a freshly mixed, metastable, supersaturated solution. The substrates were sampled at 30 minutes and 6 hours, gently quenched with ethanol and characterized by SEM. Detailed description of samples and preparation procedure can be found in Chapter 4, Materials and Methods section.

Ex situ characterization by stereo microscope followed by ATR-FTIR

Heterogeneous nucleation experiments were performed on OH and F phlogopite under conditions I and III (Table 4.2). Detailed description of samples can be found in Chapter 4, Materials and Methods section. Freshly cleaved substrates were fixed vertically inside a cuvette with a small amount of vacuum grease and 5 mL of a freshly mixed, metastable, supersaturated solution was introduced. After four days, substrates were imaged using a stereo microscope (DP25, Olympus). Unlike all other *ex situ* characterizations by AFM (Chapter 4), ATR-FTIR (Chapter 4) and SEM, microscope images were collected under the supersaturated solution without quenching. Then, substrates were removed from the cuvettes, gently quenched with ethanol and characterized by ATR-FTIR (Nicolet iS10). Spectra were collected in the range of 650 – 4000 cm^{-1}, by averaging 100 scans at a resolution of 4 cm^{-1}. FTIR peaks were assigned accordingly to the literature cited in Chapter 4.

A.3. Results and Discussion

Figure A1 compares the SEM images of $CaCO_3$ precipitates on F and OH phlogopite after 30 minutes under condition I. The particle population is clearly denser on F phlogopite, and the size distribution also seems narrower, as compared to OH phlogopite (a-1 and b-1). No preferred plane of nucleation can be recognized on both substrates. One may also note the distinctive morphological differences. $CaCO_3$ crystals on F phlogopite displays clean and sharp lines and shapes that allow one to readily identify calcite (a-2, 3), aragonite (a-4) and vaterite (a-5). On OH phlogopite, on the other hand, most of the $CaCO_3$ particles exhibit rough surface features and/or morphologies with combined phases (b-2, 3). Interestingly, many of the $CaCO_3$ particles on OH phlogopite were partially covered by gel-like precipitates (b-2, 4, 5), while on F phlogopite no such features were observed, although a small trace may be recognized (a-3, 5).

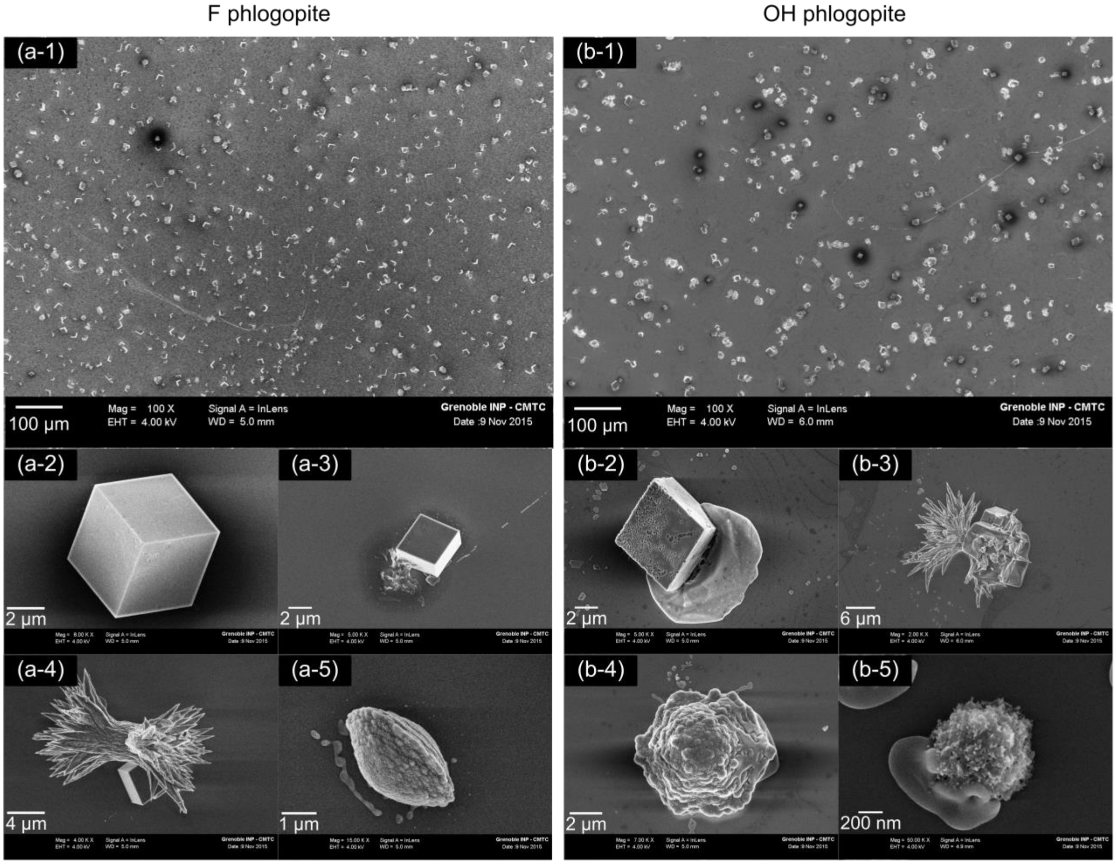

Figure A1. SEM images of $CaCO_3$ precipitates on **(a)** F and **(b)** OH phlogopite after 30 minutes under condition I (σ_{calcite} = 3.97; σ_{ACC} = 2.04).

As demonstrated in Chapter 4, $CaCO_3$ system follows multistep heterogeneous nucleation pathways regardless of surface hydrophobicity where the initial nucleating phase is ACC. This last bears an enhanced kinetic persistence on OH phlogopite (i.e. hydrophilic), while on F phlogopite (i.e. hydrophobic) the crystallization of ACC is more favorable due to the interfacial penalties provided its hydrous nature. Reflective of this, the gel-like precipitates as mentioned above could be identified as ACC. This can further be supported by the observation of ACC after 1 hours on both F and OH phlogopite under the same condition (Fig. S4.5). The fact that the gel-like precipitates are more prominent on OH phlogopite is also in agreement with its enhanced kinetic persistence on OH phlogopite. Similarly, the enhanced metastability of ACC on F phlogopite may have contributed to the denser particle population as their dissolution leads to a higher supersaturation at the interface, which in turn favors the crystallization.

After 6 hours (Fig. A2), the population and the overall size distribution of $CaCO_3$ particles seems comparable between F and OH phlogopite (a-1, 5 and b-1, 4), with an exception that on OH phlogopite a non-negligible number of newly formed, relatively small vaterite (a few ~ 5 µm) were observed (b-1, 4, 5). Moreover, a small fraction of gel-like precipitates, presumably ACC as discussed above, were incorporated in most of the vaterite ‘flower-like’ structures seem on OH phlogopite (b-2, 3), which further supports the persistence of ACC on hydrophilic substrate and possibly their transformation into vaterite which is the most likely pathway for vaterite formation (Pouget et al., 2010; Radha et al., 2010; Xiao et al., 2010; Rodriguez-Blanco et al., 2011). Like at 30-minute stage, no epitaxial growth was observed on both substrates.

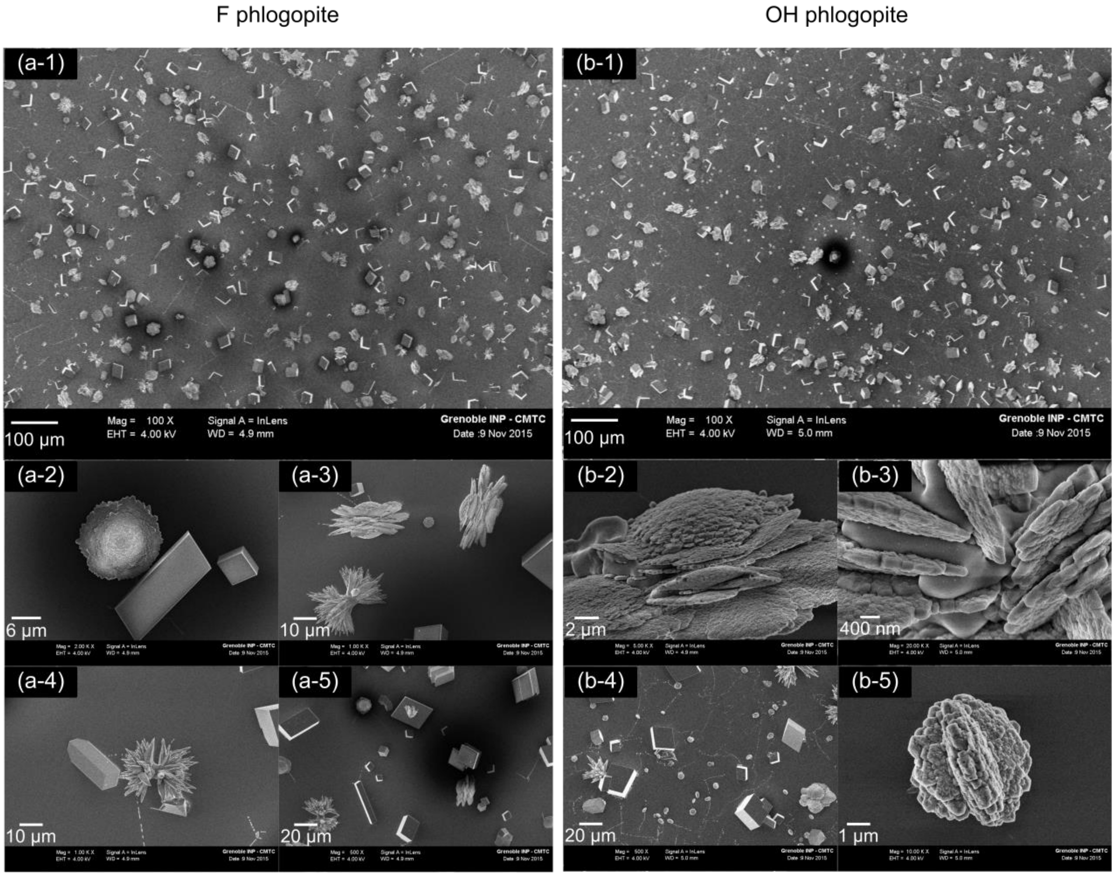

Figure A2. SEM images of $CaCO_3$ precipitates on **(a)** F and **(b)** OH phlogopite after 6 hours under condition I ($\sigma_{calcite}$ = 3.97; σ_{ACC} = 2.04).

After four days, under condition I, calcite seems to be the most predominant phase for both F and OH phlogopite, although other phases can be recognized (Fig. A3). Since the substrates were in solution, imaging at higher resolution was not achievable. FTIR spectra of the corresponding samples also indicate calcite (1395 cm^{-1}; v_3) as the main phase. Under condition III, however, calcite does not appear to be the most prevailing. This is further confirmed by the corresponding FTIR spectra where vaterite (743 cm^{-1}; v_4) and ACC (1475 and 1417 cm^{-1}; v_3) seems to be the main nucleating phases, respectively, on F and OH phlogopite (Fig. A4).

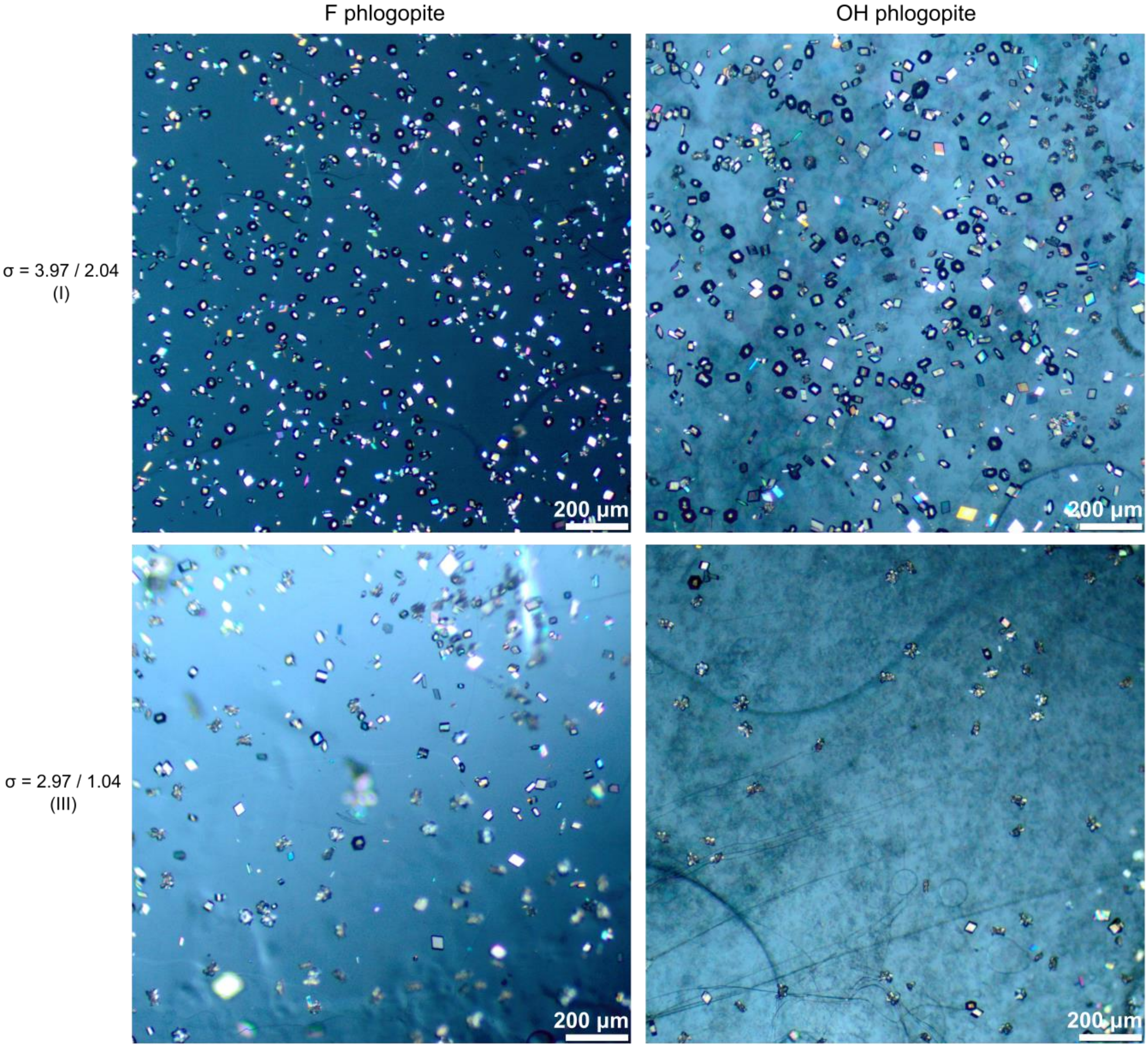

Figure A3. Stereo microscope images of $CaCO_3$ precipitates on F and OH phlogopite after 4 days under conditions I ($\sigma_{calcite}$ = 3.97; σ_{ACC} = 2.04) and III ($\sigma_{calcite}$ = 2.67; σ_{ACC} = 0.74).

Apparently no ACC was observable microscopically, and particularly, only a few particles were formed on OH phlogopite under condition III (Fig. A3). This could infer that the ACC observed by FTIR could have resulted from the quenching process, although, at the same time, the presence of a ‘dense layer’ composed of Ca-CO_3-H_2O on the surface is necessary to produce ACC when quenched. Whether this layer shall be called ACC or another, the ‘invisible’ inter-particle $CaCO_3$ precipitates, as was the case for AFM observations, must be identified, for instance, by performing *in situ* TEM or *in situ* confocal Raman spectroscopy.

The number of nucleated particles is proportional to the supersaturation (Fig. A3; I > III). In terms of the particle size, particles are clearly larger on OH phlogopite under condition I as compared to those on F counterpart. This is in line with the particle size difference, though to a lesser extent, between F and OH phlogopite, as discussed earlier, observed by SEM after 30 minutes under condition I (Figs. A1a-1, b-1). In the framework of CNT, particle size is inversely proportional to the supersaturation (see eq. 1.13). This suggests that the interfacial supersaturation may be lower for OH than for F phlogopite, which in turn infers (i) the enhanced metastability of ACC on F phlogopite (i.e. dissolution) as was demonstrated in Chaper 4 and/or (ii) promoted adsorption of cations on F phlogopite due to the asymmetric hydrogen bonding (Wang et al., 2009) resulting in a negative field on the substrate side (for a detailed description see Chapter 2, section 2.2). As for SEM observations, however, it is important to recall that the SEM imaging is performed under high vacuum that is susceptible to modify the crystallization pathway and kinetics. This, again, underlines the necessity of performing *in situ* experiments and characterizations.

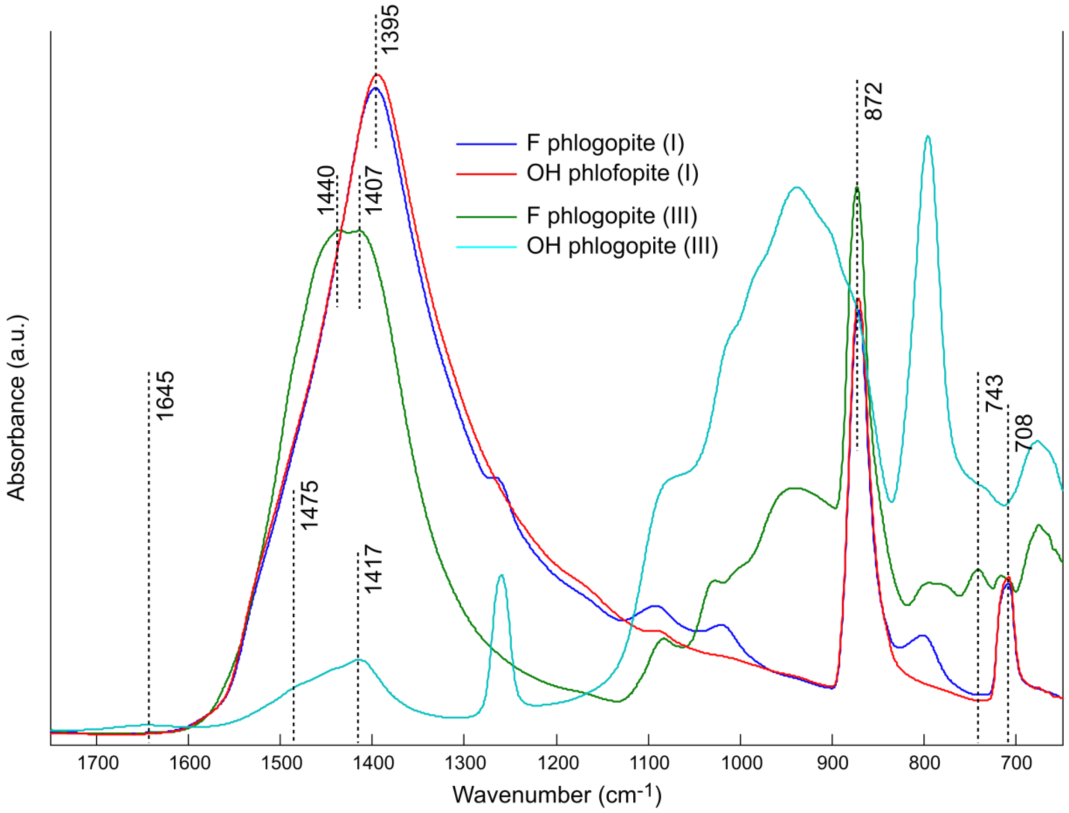

Figure A4. ATR-FTIR spectra for F and OH phlogopite after 4 days under conditions I (σ_{calcite} = 3.97; σ_{ACC} = 2.04) and III (σ_{calcite} = 2.67; σ_{ACC} = 0.74).

A.4. Conclusion

Microscopic characterization of $CaCO_3$ precipitates on F and OH phlogopite was performed at different stages on the course of their heterogeneous nucleation. The data support the formation of ACC as the initial nucleating phase on both hydrophobic and hydrophilic substrates and the role of surface hydrophobicity as governor of the crystallization kinetics of the ACC layer, in agreement with the main findings of Chapter 4. Further *in situ* analysis is necessary to fully elucidate the effects of surface hydrophobicity on the nucleation and crystallization dynamics of the CaCO3 system, without interfering with the kinetics of reactions such as quenching process or active vacuuming.

References

Pouget E. M., Bomans P. H. H., Dey A., Frederik P. M., de With G. and Sommerdijk N. A. J. M. (2010) The Development of Morphology and Structure in Hexagonal Vaterite. *J. Am. Chem. Soc.* **132**, 11560–11565.

Radha A. V., Forbes T. Z., Killian C. E., Gilbert P. U. P. A. and Navrotsky A. (2010) Transformation and crystallization energetics of synthetic and biogenic amorphous calcium carbonate. *Proc. Natl. Acad. Sci. U. S. A.* **107**, 16438–16443.

Rodriguez-Blanco J. D., Shaw S. and Benning L. G. (2011) The kinetics and mechanisms of amorphous calcium carbonate (ACC) crystallization to calcite, viavaterite. *Nanoscale* **3**, 265–271.

Wang J., Kalinichev A. G. and Kirkpatrick R. J. (2009) Asymmetrie hydrogen bonding and orientational ordering of water at hydrophobic and hydrophilic surfaces: A comparison of water/vapor, water/talc, and water/mica interfaces. *J. Phys. Chem. C* **113**, 11077–11085.

Xiao J., Wang Z., Tang Y. and Yang S. (2010) Biomimetic mineralization of CaCO3 on a phospholipid monolayer: From an amorphous calcium carbonate precursor to calcite via vaterite. *Langmuir* **26**, 4977–4983.

APPENDIX B

Publications

Ma, Bin, Fernandez-Martinez, Alejandro, Grangeon, Sylvain, Tournassat, Christophe, Findling, Nathaniel, Carrero, Sergio, Tisserand, Delphine, Bureau, Sarah, Elkaim, Erik, Marini, Carlo, Aquilanti, Giuliana, **Koishi, Ayumi**, Marty, Nicolas, Charlet, Laurent. (2017) Selenite uptake by Ca-Al LDH: a description of intercalated anion coordination geometries. Accepted.

Dai C., Stack A. G., **Koishi A.**, Fernandez-Martinez A., Lee S. S. and Hu Y. (2016) Heterogeneous Nucleation and Growth of Barium Sulfate at Organic–Water Interfaces: Interplay between Surface Hydrophobicity and Ba 2+ Adsorption. *Langmuir* **32**, 5277–5284.

Ma B., Fernandez-Martinez A., Grangeon S., Tournassat C., Findling N., Claret F., **Koishi A.**, Marty N. C. M., Tisserand D., Bureau S., Salas-Colera E., Elkaïm E., Marini C. and Charlet L. (2017) Evidence of Multiple Sorption Modes in Layered Double Hydroxides Using Mo As Structural Probe. *Environ. Sci. Technol.* **51**, 5531–5540.